Pre-ionization Studies on the Modular θ-Pinch Experiment for Field-Reversed Configuration Applications

Ian Alexander Bean

Dissertation submitted to the Faculty of the
Virginia Polytechnic Institute and State University
in partial fulfillment of the requirements for the degree of

Doctor of Philosophy
in
Applied Physics in Aerospace Engineering

Colin S. Adams, Chair
Bhuvana Srinivasan
Wayne A. Scales
Thomas E. Weber

October 15, 2024
Blacksburg, Virginia

Keywords: Pre-ionization, Seed Ionization, Inductively-Coupled Breakdown, FRC

Pre-ionization Studies on the Modular θ-Pinch Experiment for Field-Reversed Configuration Applications

Ian Alexander Bean

(ABSTRACT)

A new semi-empirical model is introduced for the quantification of inductively-coupled breakdown systems. The model is informed by breakdown studies conducted on the Modular Theta-pinch eXperiment (MTX). Observations made of inductively-coupled breakdown behaviour are consistent with the model's expectations, indicating that the model can be used to aid in design of inductively-coupled pre-ionization systems. The model is further found to be capable of quantifying the efficacy of seed ionization in inductively-coupled systems. Comparisons are made between the standard ringing-theta and a new field-aligned dipole pre-ionization systems. In the presence of sufficient seed ionization, no physical reason was observed for selection of one method over the other, leaving only engineering considerations as the determining factor for selection of an appropriate pre-ionization system. This work is supported by the Institute for Critical Technology and Applied Science (ICTAS) at Virginia Tech and the National Nuclear Security Administration of the U.S. Department of Energy.
LA-UR-24-31269

Pre-ionization Studies on the Modular θ-Pinch Experiment for Field-Reversed Configuration Applications

Ian Alexander Bean

(GENERAL AUDIENCE ABSTRACT)

A new experiment at Los Alamos National Laboratory called the Modular Theta-pinch eXperiment (MTX) has been constructed to explore a variety of applications of Field-Reversed-Configurations (FRCs). An FRC is a plasma torus with a unique magnetic field configuration that has potential applications for astrophysical shock studies, fusion energy, and space proplusion. The first step in forming an FRC is the pre-ionization step, in which a plasma is created with a magnetic field diffused throughout its volume. The first purpose of this study is to better characterize inductively-coupled breakdown. Breakdown refers to the transition of a gas into a plasma (the fourth state of matter). To do this using inductively-coupled methods means that oscillating magnetic fields are used to induce electric fields in the gas, which cause electrons to gain energy and eventually collide with gas particles, creating a plasma. The second purpose of this study is to compare the more common ringing-theta pre-ionization method to a field-aligned method. Ringing-theta systems have been observed to encounter difficulties with diffusion of magnetic field into the pre-ionized plasma and field-aligned methods are a potential alternative that can circumvent the problems that ringing-theta systems encounter. Together, these studies should allow for other experimentalists to more easily design pre-ionization systems for both FRC experiments and general plasma physics experiments.

Dedication

This work is dedicated to my family, friends, and Nicole. She has stood by me during the most challenging parts of this work.

Acknowledgments

Of those who assisted with the experiment directly, I would like to offer my profound thanks to (in order of appearance) John Dunn, Lesia Luviano, John Lamar, Lawrence Simons, John Boguski, Ezra Hutterer, Martin Ward, Evan Loftin, and Jason Sweeney. You all know how you helped me get this done and I greatly appreaciate your efforts. Of those who assisted me in maintaining sanity outside of the lab, there are too many names to acknowledge. You know who you are and if you're reading this while wondering if I mean you, I mean you. And yes, it means you're invited to the next chicken party. Thank you all so much for all of your help.

Contents

Chapter 1

Introduction and Motivation

Efforts are underway at Los Alamos National Laboratory to construct a new experimental platform capable of studying various aspects and applications of Field Reversed Configurations (FRCs). Such applications include fusion energy, space propulsion, and astrophysical shock studies. Thus, the new experiment has been titled the Modular θ-pinch eXperiment (MTX), given that it must be modular in nature in order to study a variety of FRC applications. To do this, it is necessary for the experiment to be able to form FRCs with as wide a range of parameters as possible. The first step in forming in an FRC is the "pre-ionization" phase, in which a neutral gas is initially ionized prior to FRC formation. Pre-ionization quality has long been considered a vital aspect of FRC formation and equilibrium [1][2] but to date, few dedicated studies have been performed [3][4][5] to investigate it. Historically, most studies have varied pre-ionization methods and parameters to yield the longest lifetime FRC their respective devices were capable of (commonly referred to as "formation recipes") but most of the work was empirical and not described in any reproducible detail. Due to this, there is a gap in knowledge of FRC pre-ionization where basic quantitative comparison is difficult to perform. It was found during the initial design of MTX's pre-ionization unit that field configuration requirements for inductively-coupled breakdown systems could not be found in published literature. This fact motivated the first goal of this study, which to provide a basic theoretical framework for inductively-coupled breakdown that can be easily applied for a number of field configurations. This takes the form of a

semi-empirical model which is informed by experiments conducted on MTX. The intention of the model is that it can be used to aid in the design of any future inductively-coupled breakdown systems.

The second goal of the present study requires a brief discussion of some fundamental aspects of FRC physics. Figure 1 displays a conceptual image of an FRC where the solid black lines represent magnetic field lines, the blue solid objects are θ-coils that carry an azimuthal current, and the gradiated orange solid represents a plasma. The external axial field lines are produced by the azimuthal current in the coils while an oppositely directed azimuthal current inside the FRC itself produces the poloidal closed magnetic field configuration inside of the axial field lines.

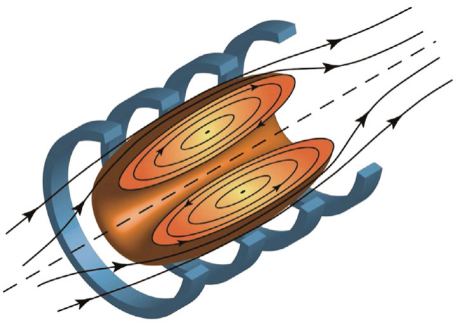

Figure 1: FRC conceptual image. Reprinted from the U.S. Fusion Energy Sciences Advisory Committee: Report of the FESAC Toroidal Alternates Panel.[6]

In figure 2, a cross section of an FRC is shown with several key features labeled that are commonly used in discussion of FRCs. The separatrix is the boundary between the closed poloidal magnetic field lines and the external axial field lines. The O-point is the magnetic null of the FRC where its azimuthal current is centered. The X-point is the location where external field lines and internal field lines diverge (to form an almost X-like shape with the field lines).

Formation of an FRC occurs in four primary steps, as shown in figure 3. First, (and the focus of this study) is the pre-ionization step. Here, a plasma is created with an axial magnetic field penetrating its volume. This field is generally referred to as the "bias" field. In this figure the pre-ionized plasma is spatially uniform but azimuthal and radial non-uniformities are common in practice. The next step (sub image b) is field reversal in which the field being produced by the external coils is rapidly reversed.

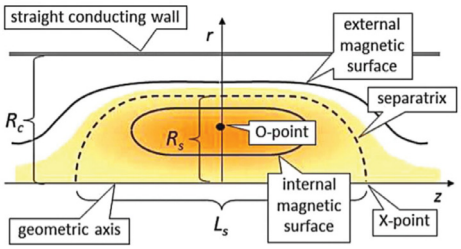

Figure 2: Structure of an FRC. Reproduced from [Loren C. Steinhauer. Review of field-reversed configurations. Physics of Plasmas, 18 (7), 2011. ISSN 1070-664X 1089-7674. doi: 10.1063/1.3613680.] with the permission of AIP publishing.[2]

By $\nabla \times \vec{E} = -\frac{\partial \vec{B}}{\partial t}$, a rapid reversal of the field in the axial direction induces a current in the plasma in the azimuthal direction. During this, the plasma resists the diffusion of the externally reversed magnetic field.

The field lines opposing the externally applied field then reconnect and close in on themselves (sub figure c), forming the isolated magnetic structure of the FRC. Finally, the FRC contracts radially and axially (sub figure d) into an equilibrium state. Once formed, the stability of the equilibrium FRC has been shown to depend strongly on the ratio of the average ion gyro-orbit radius to the FRC's separatrix radius ($\frac{r_{gryo}}{r_s}$), commonly referred to as the "s" parameter of the FRC. Lower s values tend to yield more stable and longer-lived FRCs[1][2][7].

The axial bias flux that was imbedded in the plasma prior to the reversal of the external field is the absolute maximum amount of flux that can exist in the FRC post-formation (no new poloidal flux is generated during the formation process). FRC equilibrium temperature is strongly dependent on the formation scheme and the rise time of MTX's reversal field ($\tau_{\frac{1}{4}} \approx 1\,\mu s$) is expected to produce higher temperature FRCs, which will require a higher

flux to maintain particle confinement as ion-gyro orbit sizes scale directly with temperature and indirectly with magnetic field strength. Thus keeping the s parameter within a stable range will require higher fluxes at higher temperatures so that maximizing the trapped flux (which requires optimization of the pre-ionization process) of the FRC will be necessary for forming high temperature FRCs.

Historically, a ringing-θ pre-ionization method has been the most commonly used technique in FRC experiments. In this method, the bias field is rung at a high frequency to cause breakdown in the gas prior to reversal. Figure 4 displays an example of an axial magnetic field measurement of a ringing-θ discharge prior to the reversal step. The ringing axial magnetic field induces an azimuthal electric field which accelerates free electrons and causes ionization via electron impact with neutrals. The drawback is that the energy imparted to electrons via this electric field is capped by the presence of the bias field (the maximum velocity of an electron in this configuration is $2E_\theta/B_z$). Therefore, ionization tends not to occur until the bias field is almost 0. For FRC formation, it is imperative that flux be diffused through the pre-ionized plasma but in this ringing-θ case, a plasma is formed with little to no bias flux in it. Researchers have achieved flux diffusion by allowing multiple oscillations of the ringing-θ field before reversal, where

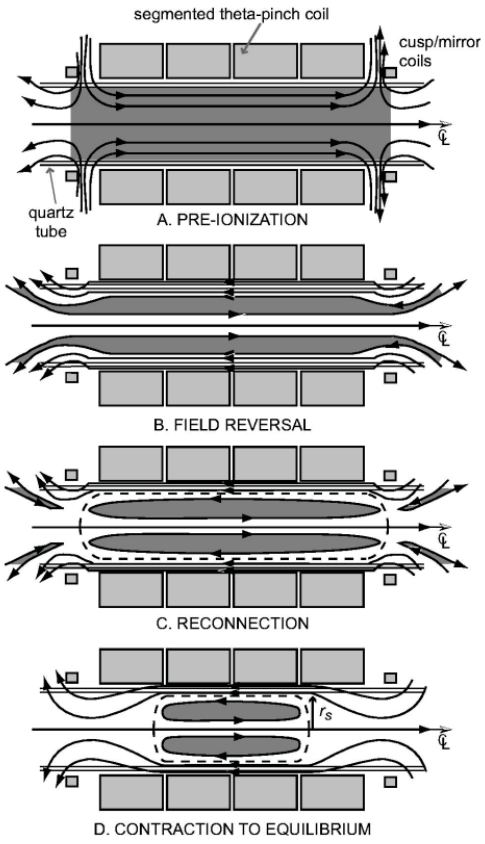

Figure 3: FRC formation process. Reproduced from [J. M. Taccetti, et al. FRX-L: A field-reversed configuration plasma injector for magnetized target fusion. Reviewof Scientific Instruments, 74(10), 2003. doi: 10.1063/1.1606534] with the permission of AIP publishing.[8]

more flux tends to be diffused with each oscillation. However, the oscillations cause the plasma to contract and then expand against the tube wall, which tends to introduce more impurities to the plasma and lead to lower quality FRCs[3].

Ringing-θ pre-ionization systems encounter another difficulty when considering dynamic formation of FRCs. Dynamic formation refers to formation of an FRC while also accelerating it in an axial direction. Ringing-θ pre-ionization systems tend to eject plasma in these conditions prior to formation[4], which can produce lower quality FRCs. As the purpose of MTX is to study a variety of FRC applications, this is an undesirable trait in a pre-ionization system.

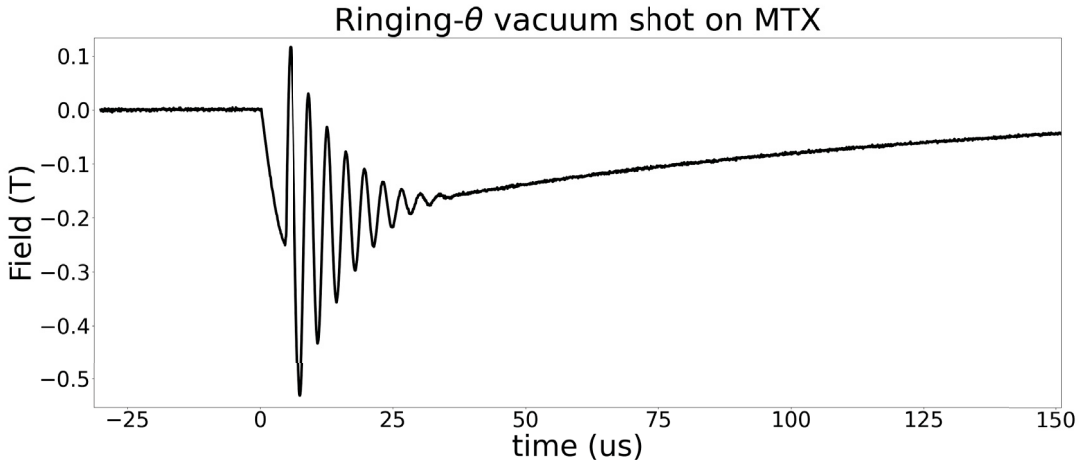

Figure 4: An example of a ringing-θ discharge field profile on MTX. The trace reperesents a measurement of the axial magnetic field strength just inside the θ-coils.

Field-aligned pre-ionization methods are a potential alternative to the classical ringing-θ approach. Field aligned pre-ionization methods refer to field configurations that induce axial electric fields, aligned with the bias magnetic field, so that ionization can be performed without reducing the strength of the bias field. Although some studies have been performed with field-aligned pre-ionization systems, a direct comparison between ringing-θ and field-

aligned methods has not been published. Thus, the second goal of this study is to asses MTX's field-aligned pre-ionization system and compare its performance to the more standard ringing-θ system.

The remainder of this document is organized as follows: Chapter 2 discusses pre-ionization in the context of FRC studies, covering general ionization techniques as well as detailing relevant information from prior literature on FRC pre-ionization methods; Chapter 3 details the modeling approach for inductively-coupled breakdown, beginning with discussion of the base relevant physics, making simplifying assumptions, and proposing a semi-empirical model that (once informed with experimental data) can be used to aid design of other pre-ionization systems; Chapter 4 gives an overview of the experiments, including the coil systems, the discharge bank properties, and the diagnostics available to perform measurements with; Chapter 5 details the experimental campaigns performed to obtain the data for the present study and the methods used; Chapter 6 analyzes the data obtained in the campaigns for both inductively-coupled breakdown studies, and comparison of the ringing-θ and field-aligned pre-ionization methods; Chapter 7 summarizes the primary findings of the study and identifies avenues of future work relevant to the present study.

Chapter 2

Review of Literature

This chapter begins with a brief introduction to pre-ionization methods, followed by more detailed reviews focusing on past research of ringing-θ and Z-discharge pre-ionization methods. Although other pre-ionization methods have been used on FRC experiments (as shown in table 1) they were not described in enough detail to allow any discussion other than that of their existence. Thus, quantitative information to review regarding pre-ionization in FRC experiments is lacking, which only further motivates the present work. Note that a review of the general history of FRC research is included in appendix A. The historical review focuses primarily on experiments that form FRCs using the field-reversed θ-pinch method as this is the formation method most relevant to the present pre-ionization work.

2.1 General ionization methodologies

Before proceeding with the more focused literature review of pre-ionization work, it is important to discuss the most basic challenges of pre-ionization for FRC formation. The first step to creating an FRC is creating a plasma with an axial magnetic field imbedded in it. All methods of achieving this effectively fall into two categories, ionizing neutral gas where an axial magnetic field is already present, or diffusing a magnetic field into a plasma. Because a plasma is conductive, diffusing a magnetic field into it can be problematic, but creating a plasma inside of an existing magnetic field has its own challenges. It is not yet clear if one approach is superior to the other.

In some experiments, researchers employ more than one method to pre-ionize the plasma. These staged approaches usually consist of a "seed" ionization method that ionizes a small fraction of the gas, followed by a "Pre-Ionization" (PI) method that is intended to fully ionize the gas.

While several different methods of PI have been investigated, quantitative data regarding the plasma parameters and configuration prior the field reversal are rare. The effectiveness of the PI method is usually determined by comparing the FRC parameters during the equilibrium phase (stability, trapped-flux, lifetime, etc.) While this approach is not without merit for any given experiment, it makes quantitative cross-comparison between different experiments difficult, if not impossible. This lack of data is part of the motivation for the present research; this dissertation project is intended to introduce a framework of quantitative comparisons to which future PI techniques can be compared.

Experimental methods of ionization can be broken down into four basic categories: photon induced, capacitively coupled, electrode driven, and inductively coupled. While photon induced ionization is common outside of FRC experiments, there are few examples of its use within the FRC community. An experiment at the University of Tokyo [9] used a laser to create a plasma prior to applying a reversal field but no quantitative data regarding the pre-ionized plasma were provided. A clear advantage of photon induced ionization is that no impurities are introduced into the plasma, but implementation of laser-based ionization systems can be complex and expensive.

Capacitively coupled electric fields can be used to ionize neutral gases but the energy that can be transmitted to a gas/plasma is limited by the capacitance and the voltage of the system. On the size scales that FRCs are commonly explored (5-20 cm scale diameters), the electrodes that would be used to transmit energy to the plasma will tend towards very low capacitances ($\lesssim$ 10 nF). Therefore, capacitively coupled systems are more applicable

for seed ionization rather than full PI. One benefit is that with careful implementation and proper materials, capacitively coupled seed ionization can be achieved with lower impurity introduction than electrode driven systems. They can also be relatively inexpensive and straight-forward to implement. Despite this, it is difficult to find any FRC experiments that have published on their use of capacitively coupled seed ionization.

Electrode driven ionization has been employed in several FRC experiments [10], [3], [7], [4]. Because of the broad range of energies and configurations that are possible with electrode driven ionization, it is suitable for both seed ionization and as a full PI system. Z-discharge is a commonly referenced PI method for FRC systems wherein an electrode discharge is initiated across the axial length of the tube prior to field reversal. Coaxial rail guns are another common method of injecting plasma into a bias field. These PI systems are straightforward to implement but can introduce high-Z impurities through ablation of the electrode material.

Finally, the most commonly used method of PI for FRC experiments, are inductively coupled systems [8], [7], [4], [11], [12], [13], [14], [15]. These systems transmit the energy required for ionization through oscillating magnetic fields. The energy that can be transmitted is limited by the inductance and voltage of the system ($\nabla \times \vec{E} = -\frac{\partial \vec{B}}{\partial t} \propto \frac{\partial \vec{j}}{\partial t}$). Ringing-$\theta$ (Rθ), Oscillating Magnetic Field (OMF), and Radio Frequency (RF) are all types of inductively coupled PI techniques that are used for FRC experiments and will be discussed in more detail in the next section. Inductively coupled PI systems tend to be a practical choice for FRC PI due to the fact that most of the technology and expertise needed to implement it is already present in FRC labs. Further, inductively coupled systems tend to introduce lower levels of impurities compared to electrode driven systems. However, due to the necessity of a bias field being present, inductively coupled PI systems can have their own set of limitations and complexities based on their implementation.

Table 1: A list of prior FRC experiments and their ionization techniques stated in publication

FRC Experiments and their ionization methodology				
Experiment	Year	Institution	Seed Ionization Method	PI Method
FRX-A [16]	1979	Los Alamos	RF	Rθ, OMF
FRX-B [11]	1981	Los Alamos	none	Rθ
FRX-C [14]	1983	Los Alamos	none	Z-discharge, Rθ
TRX-I [10]	1982	Spectra Technology	none	Z-discharge
TRX-II [3]	1987	Spectra Technology	OMF	Z-discharge, Rθ
LSX [7]	1990	STI Optronics	OMF	Z-discharge, Rθ
FRX-L [8]	2003	Los Alamos	none	Rθ
MSX [4]	2015	Los Alamos	coaxial rail guns	Rθ
C-2U [17]	2017	TAE	none	Rθ
Yingguang-I [15]	2017	CAEP	none	Rθ
C-2W [17]	2019	TAE	none	OMF
KMAX [5]	2022	USTC	coaxial rail guns	Rθ

Because the previous work done hasn't followed any clear evolution or any identifiable progression, the following discussion will be organized by method of PI, with a general introduction to the method and any unique information that has been published on the topic. Table 1 gives a general overview of FRC experiments that discuss their PI methodology in enough detail to be useful to this work. It should be noted that the experiments listed in table 1 may have tested other pre-ionization methods as well but the listed methods are those discussed with the most detail in published material. The experiments listed in table 1 serve as the primary source of information on PI methods for the following review.

2.2 Ringing-θ pre-ionization

Ringing-θ is a method of pre-ionization that rings the bias field prior to reversal in order to ionize the neutral gas present in the tube and is the most common method used for PI for FRC formation [8], [7], [4], [11], [12], [13], [14], [15]. Figure 5 displays how a ringing-θ PI system was employed on the FRX-B experiment [11]. A measurement of the

axial magnetic field strength is shown where a bias field is applied (< -15 μs) and then the field is oscillated at a high frequency (-15 μs to -5 μs). The high frequency oscillation of the field strength in the axial direction induces electric fields in the azimuthal direction which accelerate electrons and cause ionization via impact. However, the energy that can be transmitted to the electrons by the ringing field is inhibited by the presence of the bias field (more on this in chapter 3) and so most of the ionization actually occurs near the first zero crossing of the field strength. This means that the plasma is actually formed when there is little to no bias field inside of the plasma (and thus falls into the category of diffusing a field into the plasma). Over the next 15 μs the field ideally diffuses into the plasma prior to field reversal and FRC formation. During these remaining oscillations the plasma annulus that is formed cyclically contracts and expands into the tube wall (see figure 6 but note that these images are not from the same shot as figure 5), which introduces impurities with each contact [8].

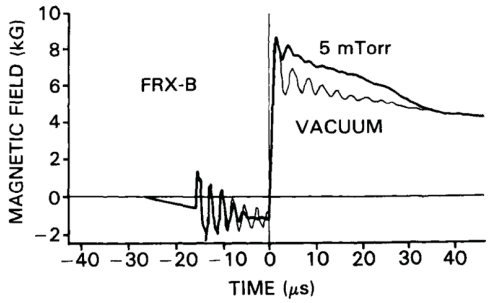

Figure 5: Axial field measurement of a ringing-θ PI system. Reproduced from [W. T. Armstrong, et al.. field-reversed experiments (frx) on compact toroids. Physics of Fluids, 24(11):2068–2089, 1981.] with the permission of AIP publishing.[11]

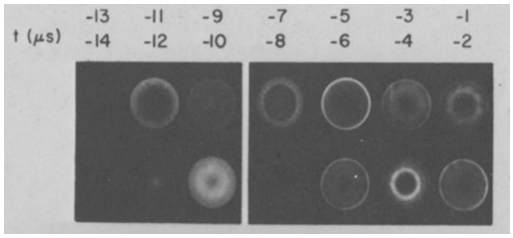

Figure 6: Framing camera images of the pre-ionized plasma on FRX-B. Reproduced from [C.W. Hartman. Summary of U.S. Compact Torus Experiments, pages 441–461. Geneva, Switzerland, 1982].[18]

Despite the clear dominance of Rθ as a PI method (see table 1) there is not much quantitative data available in the literature, nor discussions of the process leading to breakdown. A

model for analyzing the annulus of plasma initially formed by a Rθ PI system was introduced by Armstrong [19]. This "snowplow" model assumes the existence of a fully ionized annulus of plasma that contracts and expands radially as the external magnetic field is oscillated. The model was shown to match experimental measurements on FRX-B of the plasma annulus' radius relatively well when proper fitting coefficients were applied. The overall result showed that one can expect to get about 50% of the initial bias flux into the plasma annulus prior to field reversal when using the standard Rθ method (where the B_z strength must approach or cross the 0 point).

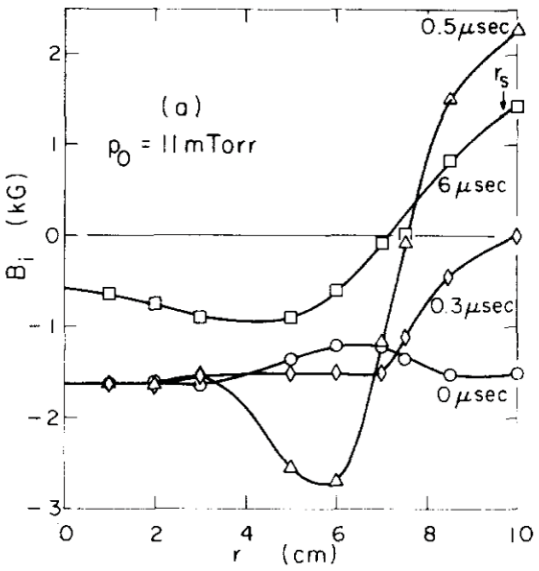

Figure 7: Axial field measurements on HBQM prior to field reversal. Reproduced from [S. O. Knox. Reversed-field flux-trapping in a low-compression theta pinch. Physics of Fluids, 25(2), 1982. ISSN 00319171. doi: 10.1063/1.863756.] with the permission of AIP publishing.[12]

The High Beta Q Machine (HBQM) [12] also used a Rθ PI approach and measured the radial distribution of axial magnetic field strength of their plasma prior to reversal. Figure 7 dispalys these measurements. The reduced magnitude of the bias field around the 6 cm position could be inferred as the presence of a plasma annulus that is excluding flux from its volume. Of particular interest for the present context is the $t = 0$ line (circles indicators) that show the field distribution within the plasma prior to field reversal. The measurements indicate almost full flux trapping compared with the external magnetic field strength. These measurements show the diffusion of flux into the plasma and the timescales on which diffusion occurs.

Further publication of quantitative analysis of Rθ systems occurred in 2015 when Weber [4] explored the use of an annular array of coaxial plasma rail guns to provide seed ionization for a Rθ PI system on the Magnetized Shock eXperiment (MSX). Density measurements of a single one of these railguns were taken and an inferred distribution of seed ionization from the array of guns is displayed in figure 8. Combining this method of seed ionization with a Rθ PI system was shown to consistently yield higher trapped flux for a formed FRC than either method alone. A similar method of combining rail gun seed ionization with a Rθ PI system was explored on the Keda Mirror with Axisymmetry (KMAX) [5] device at the University of Science and Technology of China (USTC) and yielded similar favorable results for increasing trapped flux.

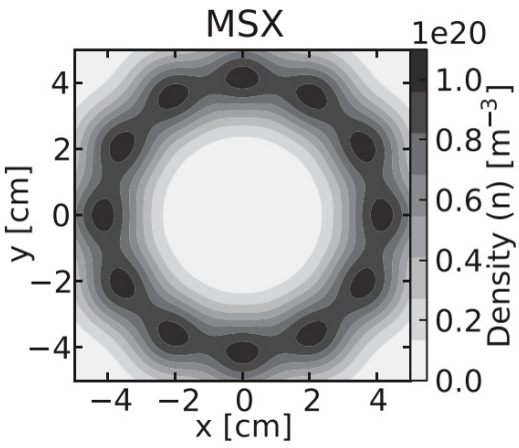

Figure 8: An inferred distribution of seed ionization from the annular array of coaxial railguns on MSX based on single gun density measurements. Reproduced from [T. E. Weber, T. P. Intrator, and R. J. Smith. Plasma-gun-assisted field-reversed configuration formation in a conical θ-pinch. Physics of Plasmas, 22(4), 2015. ISSN 1070-664X1089-7674. doi: 10.1063/1.4919262.] with the permission of AIP publishing.[4]

A recent study on the Yingguang-I device at the China Academy of Engineering Physics (CAEP) explored the Rθ pre-ionization more quantitatively, measuring both induced electric fields of the PI system and the densities of plasmas produced by it. The primary test performed on the PI system was to increase bias field strength while holding the Rθ system at a constant strength. In figure 9, it can clearly be seen that as the bias field strength is increased, ionization of the gas is suppressed.

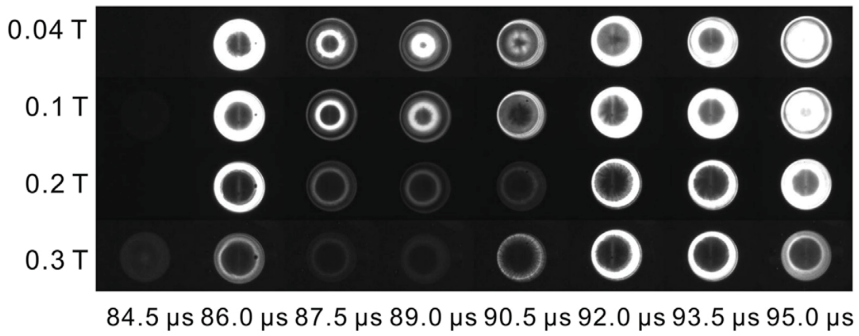

Figure 9: Framing camera images of the Rθ process on the Yingguang-I for varying bias field strengths. Reproduced from [[15]] which is published under a CC BY-ND-ND license: Copyright ©2017 Science and Technology Information Center, China Academy of Engineering Physics.

2.3 Z-discharge pre-ionization

In literature, a Z-discharge PI system generally refers to an annular electrode discharge across the tube in which the FRC is formed. Thus, the plasma distribution pre-reversal is in the shape of a hollow cylinder. Using this method, nearly 100% of the bias flux present in the tube can be contained inside of the pre-reversal plasma. However, two primary challenges exist with this method. The first is that higher levels of currents are necessary to achieve higher percentages of pre-ionization but higher currents can tend to pinch down and become a radially centered column of plasma as opposed to a hollow cylinder. Thus, ionization percentage is limited with this method. The second challenge is that when not pinched, the plasma will tend to form along the surface of the tube, introducing high levels of impurities (not even counting for the impurities introduced by the electrodes themselves). It is also worth noting that initiating a Z-discharge across large distances can be a challenging engineering project, though sufficient seed ionization may help alleviate this challenge.

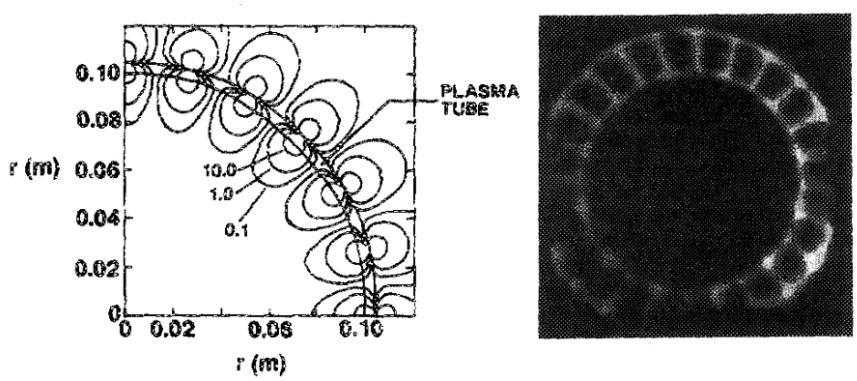

Figure 10: Framing camera image from TRX-II displaying the separation of the Z-discharged plasma from the tube wall by the high-order multipole field. Reproduced from [J. T. Slough. Experimental study of the formation of field-reversed configurations employing high-order multipole fields. Physics of Fluids B, 2(4), 1990.] with the permission of AIP publishing.[3]

The Triggered Reconnection eXperiment-I (TRX-I) [10], TRX-II [3], and Large-S eXperiment (LSX) [7] all employed Z-discharge PI systems. In order to move the discharge away from the wall and lower impurity content the researchers on TRX-II also employed high-order multipole fields (see figure 10). However, it was stated that achieving both a high percentage of ionization and radial/azimuthal uniformity was difficult (due to the challenges stated in the paragraph above). The researchers also explored the use of a Rθ PI system in conjunction with ionization by the multipole fields. Although they state that this combination yielded the best results, only a brief discussion is given in an appendix [3] regarding ionization by multipole fields. It is clear from the literature that much effort was put into achieving an ideal pre-ionized plasma for FRC formation on these experiments, however almost all of the information presented in the literature is qualitative and gives no basis for reproduction or comparison.

2.4 Summary of literature

Drawing any clear conclusions from the prior work is difficult because almost all of the previous work performed regarding PI methods for FRC formation is qualitative. This is likely due to the complex nature of the problem, but the absence of any analytical or quantitative analysis provides clear motivation for the present work. A framework of analytic modeling and quantitative experimental comparison/verification must be created to allow a more structured approach to the problem of pre-ionization for FRC formation.

A common thread between all of these experiments is that all the researchers describe how the PI systems were generally tuned to very specific amplitudes and firing times, resulting in a variety of pre-ionization "recipes". Despite the many methods explored, the most popular is still the Rθ approach, which most easily provides a uniform annulus of plasma (despite the flux diffusion challenges). Therefore, it can be hypothesized (but not concluded) that having a radially and azimuthally uniform pre-ionized plasma promotes FRC stability.

Chapter 3

Pre-ionization Modeling

Ionization of a gas can be broken down into several distinct stages: the first stage is breakdown when the amount of ionized particles present is negligible and they do not significantly affect the distribution of applied electric and magnetic fields; the second stage is a partially ionized plasma in which the field dynamics are coupled to the plasma and ionization/recombination rates must be accounted for to determine the plasma parameters; the final stage is that of a fully ionized plasma in which ionization and recombination rates are equalized. Each of these stages require different modeling approaches that vary greatly based on the specific conditions and although some models exist for the second phase and many for the third phase for FRCs, there are presently no models for the most commonly employed inductively coupled breakdown methods used for pre-ionization in FRC experiments. The primary goal of this work will be to introduce semi-empirical models for the breakdown phase in a number of commonly used inductively coupled systems that will be informed with data. The models will be compared to experimental results and refined as necessary.

For inductively coupled PI methods, breakdown of a neutral gas into a plasma is caused by induced electric fields which accelerate free electrons. These accelerated electrons eventually impact neutral gas particles and if the impact occurs with sufficient energy, ionization will occur. Two primary parameters determine whether a particle is ionized by an electron impact. The first parameter is the energy of the electron at the time of impact and the second is the cross section of the electron impact ionization reaction (there are many types

of interactions that can occur upon electron impact). The electron energy at the time of impact depends on both the strength of the electric field that accelerates the electrons and the mean-free-path (λ_{mfp_e}) that the electron travels within this field before a collision. Prior to breakdown and for very low ionization percentages, the effect that ionized particles have on a field's distribution may be neglected. Therefore, an electron's average energy in these conditions can be determined using single particle motion analysis coupled with collision cross section statistics. However, once a sufficient number of particles have been ionized, the field distribution and evolution become coupled to the plasma dynamics and different models are necessary to properly describe the system. For example, a snow-plow model similar to that described in section 2.2 may be useful in the Rθ case.

Before continuing, it should be noted that some of the following discussion employs results used from a Boris Pusher simulation. The Boris Pusher algorithm is a standard modeling tool that is used to model charged particle motion under the influence of electric and magnetic fields. A full discussion of the model can be found in Birdsall and Langden's text[20]. For the purposes of this study, a source code was obtained freely online from the PlasmaPy community's available resources[21]. This algorithm required only minor modification for its use in these analyses and was a very convenient resource to have freely available.

3.1 Townsend Discharge and Paschen's Law

The Townsend discharge condition and Paschen's law represent a classic example of breakdown prediction that is worth presenting here in order to pull any related concepts for the development of an electrodeless breakdown model. Townsend's discharge model describes the breakdown of a gas into a plasma when subjected to a uniform electric field between two plates. A diagram of the problem setup with coordinate definitions is shown in figure 11.

The model starts by assuming that electrons present in the gap (in practice there is always a small population of free electrons) are accelerated by the electric field and ionize neutral particles when they collide with them (provided they have enough energy to cause ionization). Therefore, the electron flux will increase exponentially in the x direction, or stated mathematically,

$$\frac{d\Gamma_e}{dx} = \alpha\Gamma_e \tag{3.1.1}$$

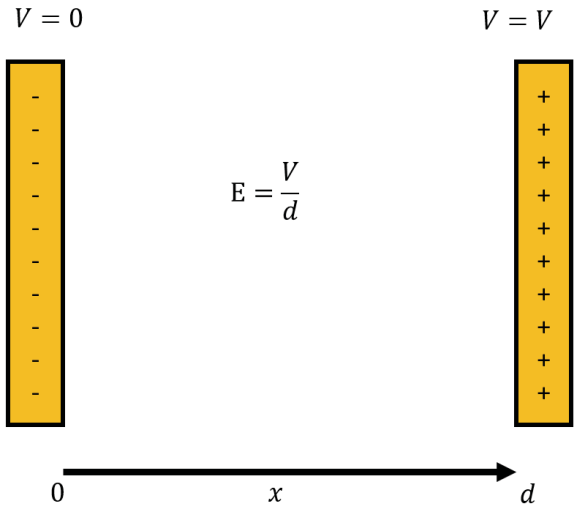

Figure 11: Diagram of Townsend discharge model setup.

Where $\boldsymbol{\alpha}$ is the number of ionizing collisions that occur per unit length and is known as the "1st Townsend Coefficient." Note that this model neglects diffusion, recombination, and assumes that $\boldsymbol{\alpha}$ is not a function of space. This differential equation has the solution of

$$\Gamma_e(x) = \Gamma_e(0)e^{\alpha x} \tag{3.1.2}$$

Next is the determination of the electron flux at the cathode ($x = 0$). The model assumes that the primary source of electrons generated at the cathode is due to ions impacting the cathode surface. This is referred to as secondary emission and it is assumed that each ion impact releases $\boldsymbol{\gamma_{se}}$ electrons (the "2nd Townsend Coefficient") and takes the form

$$\Gamma_e(0) = \gamma_{se}\Gamma_i(0) + \Gamma_{e0} \tag{3.1.3}$$

Where $\boldsymbol{\Gamma_i(0)}$ is the ion flux at the cathode and $\boldsymbol{\Gamma_{e0}}$ is any other source of electrons (UV radiation, thermionic emission, field emission, etc.). In the Townsend discharge model, it is assumed that $\boldsymbol{\Gamma_{e0} = 0}$ so that the only source of electrons at the cathode is due to secondary emission. To determine the ion flux at the cathode, note that every ionizing collision that occurs in the gap will produce an ion that will be drawn to the cathode. The number of ionizing collisions that occur in the gap will be $\boldsymbol{\Gamma_e(d) - \Gamma_e(0)}$. i.e., the total number of ions produced in the gap will be equal to the total number of additional electrons produced in the gap due to ionizing collisions. Therefore,

$$\Gamma_i(0) = (\Gamma_e(d) - \Gamma_e(0)) + \Gamma_{i0} \tag{3.1.4}$$

Where $\boldsymbol{\Gamma_{i0}}$ represents any other source of ions other than ionizing collisions. This is again assumed to be 0 for the Townsend model. Plugging equations 3.1.2 and 3.1.3 into equation 3.1.4, and recalling that it is assumed that $\boldsymbol{\Gamma_{e0} = 0}$ and $\boldsymbol{\Gamma_{i0} = 0}$, the relation below is obtained.

$$\Gamma_i(0) = \Gamma_e(0)e^{\alpha d} - \gamma_{se}\Gamma_i(0) \tag{3.1.5}$$

Using equation 3.1.3 for the $\boldsymbol{\Gamma_e(0)}$ term in 3.1.5,

$$\Gamma_i(0) = \gamma_{se}\Gamma_i(0)e^{\alpha d} - \gamma_{se}\Gamma_i(0) = \gamma_{se}\Gamma_i(0)(e^{\alpha d} - 1) \tag{3.1.6}$$

Here, $\boldsymbol{\Gamma_i(0)}$ divides out and the relation can be re-arranged to obtain

$$\boxed{\alpha d = ln\left(1 + \frac{1}{\gamma_{se}}\right)} \tag{3.1.7}$$

Equation 3.1.7 is known as the Townsend discharge condition. It is a condition that is satisfied for conduction of current through a gas/plasma in a uniform field between two plates where the only source of electrons is from secondary emission at the cathode and the only source of ions is due to ionizing collisions in the gap.

Recall from the beginning of this section that $\boldsymbol{\alpha}$ is the number of ionizing collisions per unit length. In order to ionize upon collision with another particle, an electron must travel a certain distance while under the influence of the electric field to gain sufficient kinetic energy. In order to understand the number of ionizing collisions per unit length in this system, the probability distribution of how far an electron will travel before impacting a neutral must be determined. Let $\boldsymbol{n(x)}$ be the number of electrons at position x that **have not yet collided** and let $\boldsymbol{n(0) = n_0}$. Further, define the average distance between collisions **that remove all kinetic energy from an electron in the x direction** as $\boldsymbol{\lambda}$ (note that there are many types of collisions that will be discussed in 3.2). Now the number of particles that have yet to collide at position $x + dx$ can be modeled as

$$n(x + dx) = n(x) - n(x)\frac{dx}{\lambda} \tag{3.1.8}$$

Note that the sign is negative because particles that have not yet collided are removed from $n(x)$. Once a collision occurs, they are subtracted from $n(x)$. Using the basic identity of differential calculus, the left hand side of equation 3.1.8 can be represented as

$$n(x + dx) = n(x) + \frac{dn}{dx}dx \tag{3.1.9}$$

Substituting equation 3.1.9 into equation 3.1.8 yields the differential equation

$$\frac{dn}{dx} = -\frac{1}{\lambda}n(x) \tag{3.1.10}$$

and using the boundary condition as stated above that $n(0) = n_0$, this equation has the solution of

$$n(x) = n_0 exp\left(\frac{x}{\lambda}\right) \tag{3.1.11}$$

Equation 3.1.11 represents the distribution of electrons that will travel distance x before a collision. Therefore, the **probability** that an electron will travel distance x before collision is simply

$$P_x = \frac{n(x)}{n_0} = exp\left(\frac{x}{\lambda}\right) \tag{3.1.12}$$

The above derivation can be easily be repeated with an energy gained in an electric field before collision instead of distance traveled to yield the probability of an ionizing collision occurring as[22]

$$P_{\xi_i} = exp\left(\frac{\xi_i}{E\lambda}\right) \tag{3.1.13}$$

where $\boldsymbol{\xi_i}$ is the ionization energy of the neutral particle and $\boldsymbol{E}$ is the strength of the uniform electric field. This is the probability that an electron will gain sufficient kinetic energy before collision to cause ionization. The **average** number of ionizing collisions per unit length is given by multiplying the probability of an ionizing collision occurring by the number of mean free paths **within a unit length**. Therefore, α can be represented as

$$\alpha = \frac{1}{\lambda}exp\left(\frac{\xi_i}{E\lambda}\right) \tag{3.1.14}$$

Since this model is dealing with averages, ξ_i can be assumed a constant (even for mixtures). Further, noting that the mean-free-path is inversely proportional to the gas pressure p, (i.e.,

$\boldsymbol{\lambda \propto p^{-1}}$), the relation can be re-written with new constants of $\boldsymbol{Ap = 1/\lambda}$ and $\boldsymbol{Bp = \xi_i/\lambda}$. Finally, if the field strength is expressed in terms of voltage (uniform field between two plates) as $E = V/d$, then α can be represented as

$$\boxed{\alpha = A\,p\,exp\left(\frac{Bpd}{V}\right)} \tag{3.1.15}$$

Note here that A and B[22] are the familiar constants from Paschen's Law. Note that these "constants" are actually energy dependent due to the fact that mean-free-path depends on collision cross-sections, which are energy dependent. To get the Paschen's law relation from the Townsend model, plug equation 3.1.15 into equation 3.1.7 to get

$$\boxed{V_{\text{BD}} = \frac{Bpd}{ln[A\,p\,d] - ln\big[ln[1 + 1/\gamma_{se}]\big]}} \tag{3.1.16}$$

Although Paschen's Law and the Townsend discharge model rely too heavily on the presence of electrodes to be easily adapted to inductively coupled systems, it is worth noting that mean free paths for ionizing collisions in a uniform electric field can be estimated with the Paschen coefficient, $Ap = \frac{1}{\lambda}$. This may be useful for inductively coupled systems that produce a uniform electric field on the length-scales of the system. Further, these models can be directly applied for determining Z-discharge breakdown conditions, though some modification may be necessary for the barrier-field modified Z-discharge system like those used on the TRX [10], [3] experiments.

3.2 Basic Breakdown Modeling

To begin with, this work will consider ionization of a gas in three separate phases as shown in the flow charge in figure 12. The first is the "Pre-Breakdown" phase, in which the

skin depth of the plasma is very large compared to the system's size. This effectively means that the distribution of applied magnetic and electric fields are unmodified by the presence of charged particles. The second phase is that of a partially ionized plasma in which plasma dynamics signficantly affect distribution of applied fields but ionization and recombination rates are not equilibrated. The final phase, which is a common starting assumption for many plasma models, is that of a fully ionized plasma in which the population of neutral gas particles is negligible. Breakdown is defined as the point when a gas transitions from being an electrical insulator into an electrical conductor. Effectively, this transition spans the "Pre-breakdown" regime so that the conditions leading to breakdown can be studied in the "Pre-breakdown" regime. This means that single particle motion models can be used to study behavior of electrons in inductively-coupled breakdown.

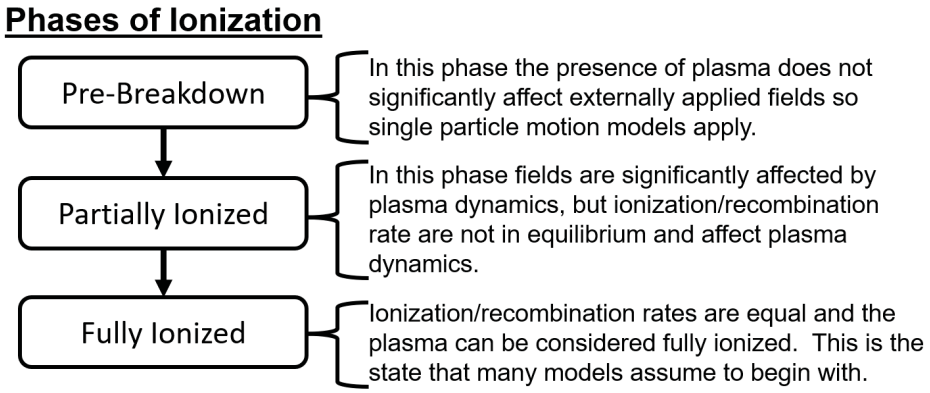

Figure 12: A flow chart that breaks ionization of a gas into three separate phases.

Inductively-coupled breakdown is generally achieved using ringing magnetic fields and the sooner a gas breaks down the more efficiently energy can be transferred from the ionizing system into the gas (energy cannot be transferred until the gas becomes conductive). Therefore, this study further simplifies the breakdown problem by separating it into two cases. Consider "Prompt Breakdown" to be defined as breakdown that occurs within the first 8th of a ringing cycle ($T/8$ where T represents the ringing cycle's period). Breakdown

that occurs after this time is considered "delayed breakdown." Figure 13 displays this graphically using an example magnetic field measurement of a ringing system made on the MTX machine. In most cases for experimentalists using inductively-coupled breakdown, prompt breakdown will be preferred so that this work focuses on studying the conditions required to yield prompt breakdown in a gas.

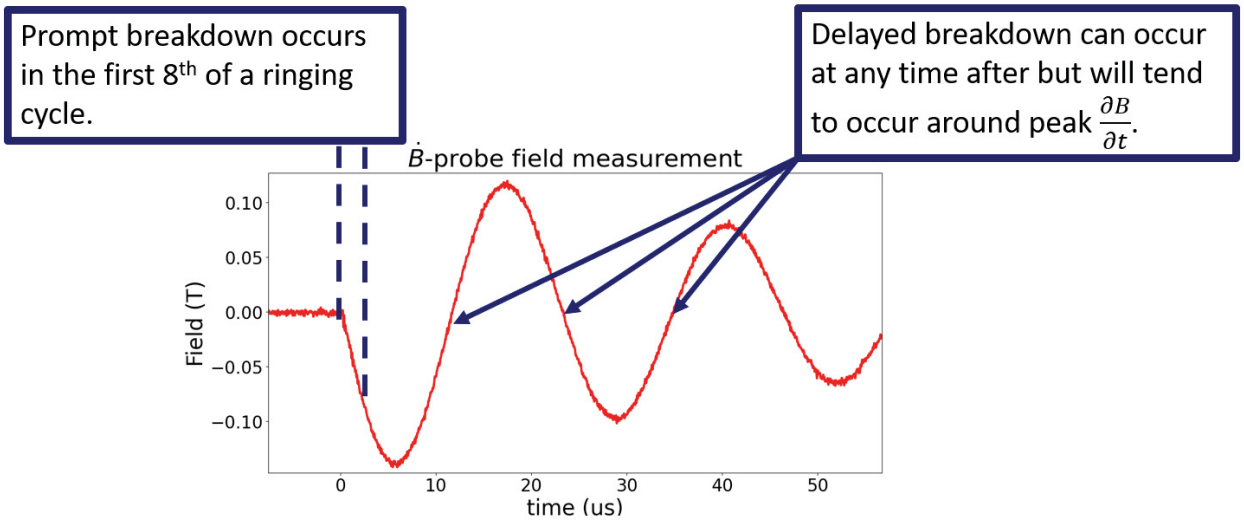

Figure 13: An example measurement of a ringing discharge from MTX, labeling the prompt and delayed breakdown regions.

To begin with, it is assumed that electron impact ionization is the dominant method of ionization in an inductively-coupled system. This means that the growth rate of electron population in a gas can be modeled as

$$S_e = \frac{dn_e}{dt} = S_{\text{Ion}} - S_{\text{Rec}} \tag{3.2.1}$$

where n_e represents electron number density, S_{Ion} represents the ionization rate, and S_{Rec} represents the recombination rate. For breakdown to occur (a rapid change in the ionization percentage of the gas), it is necessary that the ionization rate is much greater than the

recombination rate ($S_{\text{Ion}} >> S_{\text{Rec}}$). Therefore, for present purposes the recombination rate is considered to be negligible ($S_{\text{Rec}} \approx 0$). This is the first primary assumption made in the development of the model at-hand. With negligible recombination rate, the electron growth rate simplifies to

$$S_e = \frac{dn_e}{dt} = n_e n_n \sigma_{\text{Ion}}(v_e) v_e \tag{3.2.2}$$

where n_e represents the electron number density, n_n represents the neutral particle number density, $\sigma(v_e)$ represents the electron impact ionization cross section (which is a function of electron energy), and v_e represents the electron velocity. Integration of this gives the electron number density as a function of time.

$$n_e = n_{e0} e^{n_n \sigma_{\text{Ion}}(v_e) \int_0^t v_e} \tag{3.2.3}$$

where n_{e0} represents the initial electron number density. Note that appendix B gives an introductory discussion of cross sections and also describes how these rate and growth equations can be derived. The second primary assumption is that the starting electron number density is approximately constant between the separate conditions tested here for a given gas ($n_{e0} \approx$ Constant).

In these inductively-coupled breakdown studies, only a few initial free electrons are accelerated by the induced electric fields (n_{e0} in this case). Thus, for breakdown to occur, it is necessary that these few initial free electrons are able to interact with the neutral gas and transfer energy from the induced electric field to the gas. Energy can be transferred with any collision that transfers momentum. Therefore, the momentum-transfer cross section of electron impact with neutral particles is actually the cross section of primary interest (as opposed to purely the ionization cross section which is only one component of the total momentum transfer cross section). Using data from Yoon's[23] work, the momentum-transfer

cross section for electrons in hydrogen gas is seen to vary with electron energy as shown in figure 14. Due to the low mass of electrons, they tend to be rapidly excited to very high energy in inductively-coupled systems (particularly in plasma experiments where pressures tend to be low which yield large mean-free-paths). As an example, figure 15 depicts the expected energy of an electron over time that has been accelerated by one of MTX's weaker systems (specifically the firing of a bias bank at its minimum voltage as described in section 4.1.1). Note that this simulation is performed using the Boris Pusher algorithm described at the beginning of this chapter. It is clear when comparing figures 14 and 15 that electrons are rapidly accelerated past the resonance region of the momentum transfer cross section and beyond into regions where the author could not find data for momentum transfer cross sections. Although it is not known exactly how the cross section behaves in higher energy regimes, it can be said with some degree of reasoning that it is likely to be slowly varying with electron energy. Therefore, the third primary assumption made for the prompt breakdown model is that the momentum transfer cross section is effectively constant at the electron energy ranges of interest in the present studies.

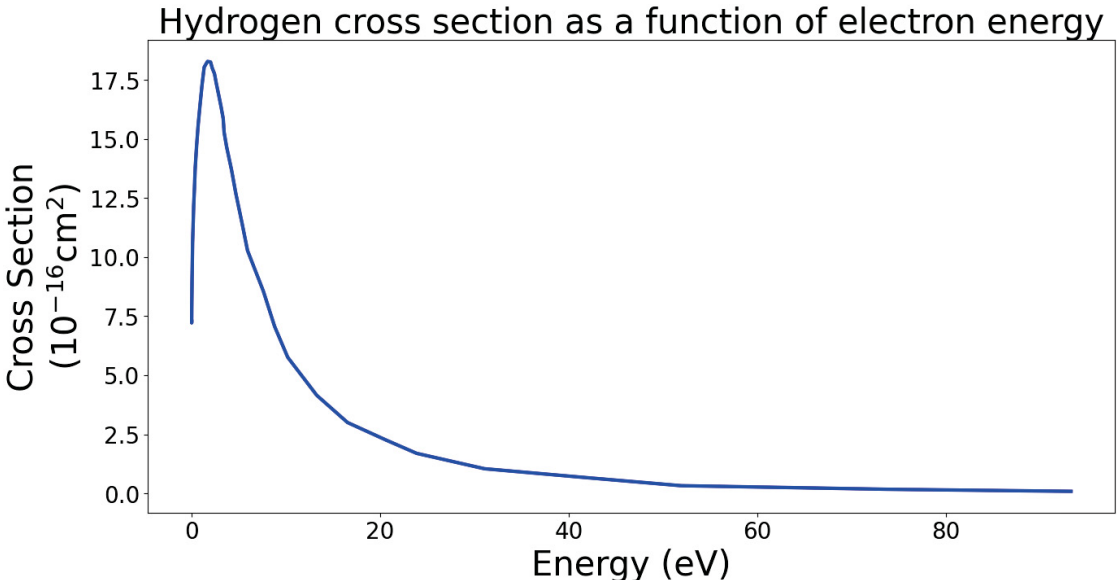

Figure 14: A plot of the momentum transfer cross section of electrons in hydrogen gas, generated using Yoon's[23] data

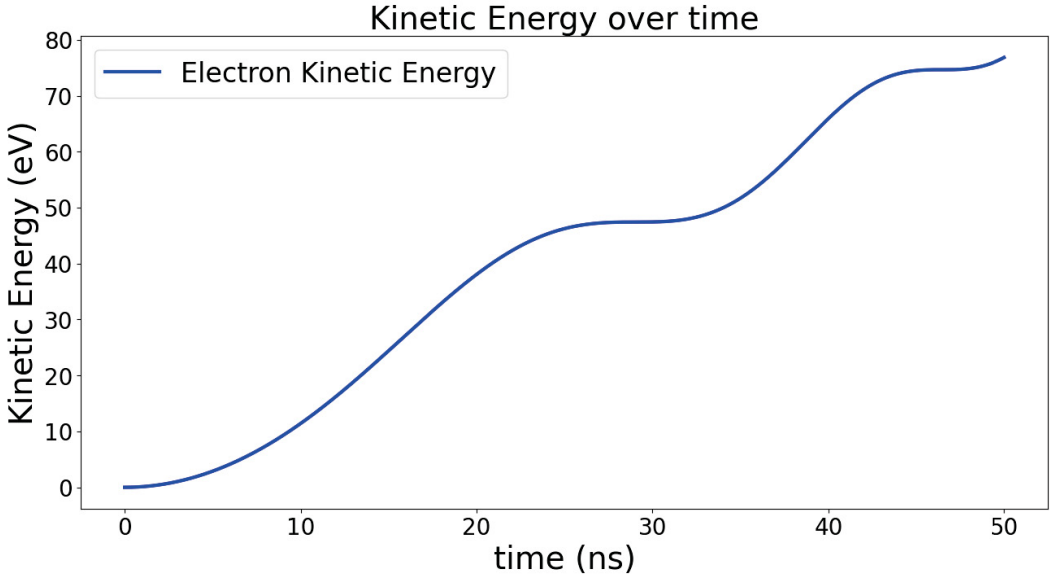

Figure 15: A plot depicting simulated electron kinetic energy as accelerated by the firing of MTX's low strength bias field.

Thus, there are three primary assumptions being made for the present model.

- Assumption 1: Recombination rates are negligible at breakdown conditions.
- Assumption 2: Initial electron density (n_{e0}) is constant between experiments.
- Assumption 3: Collisional cross section is approximately a constant at electron energy ranges of interest.

Combining these three assumptions with equation 3.2.3 above, one can say that dominant factors affecting prompt breakdown will be neutral number density, and electron velocity. Noting that neutral number density is directly proportional to gas pressure and that electron velocity is proportional to electron energy, it can then be said that prompt breakdown of a given gas in inductively-coupled systems should primarily be a function of only two variables. Thus,

$$S_e = f(n_n, v_e) = f(p, K.E._{e^-}) \tag{3.2.4}$$

This implies that breakdown of a gas at a given pressure should occur once electrons have obtained the required energy. In general, electron kinetic energy in the system will be a function of the induced field configuration. It is proposed here that it is sufficient to consider only how electron energy scales in a given field configuration (field configurations such as θ-pinch, multi-pole fields, etc.). What this means is that it is not necessary to determine the exact path and energy profile of a statistical distribution of free electrons. Further, since the transition from gas into plasma occurs during the pre-breakdown phase, simple single particle motion models can be used to determine electron kinetic energy scaling for a given field configuration. Therefore, the approach here is to determine a scaling model for electron kinetic energy in a given field configuration and measure the "scaling energy" required to

cause breakdown of a gas at a given pressure. It is common in literature for ionization experiments to normalize electron energy by the ionization energy of the experimental gas, therefore consider the definition of a breakdown factor here as

$$\alpha^* = \frac{\text{K.E.}_{e^-}}{\xi_{\text{Ion}}} \tag{3.2.5}$$

where K.E._{e^-} is the electron kinetic energy at time of breakdown as determined by the scaling model, ξ_{Ion} is the ionization energy of the given gas, and α^* is now defined as the breakdown factor. Note that this term is similar to the concept of "normalized energy" used in other ionization studies. The key distinction here is that normalized energy is normally calculated using a very well measured electron kinetic energy, whereas breakdown factor is the ratio of only a scaling model for electron energy to ionization energy. It can now be said that breakdown will behave as a function of gas pressure and breakdown factor so that

$$S_e = f(p, \alpha^*) \tag{3.2.6}$$

At this point, a very simple semi-empirical model for breakdown of gases in inductively-coupled systems has been established. The proposal is that inductively-coupled breakdown will behave as a function of gas pressure and breakdown factor. Pressure can be measured using simple and widely available transducers. Breakdown factor is a function of the field configuration of a given inductively-coupled system and will be a function of field geometry, magnetic field strength, discharge frequency, and time. These models are derived later in this chapter for the configurations explored in this study. It is worth noting expectations of breakdown behavior in the face of the present physics being considered. First, it is noted that all breakdown experiments conducted here are expected to be in a collision-rate limited regime. Figure 16 depicts the mean-free-path of an electron exposed to a low voltage

θ-pinch discharge on MTX in hydrogen gas at 100 mTorr (mean-free-path is calculated using momentum transfer cross section data in hydrogen gas from Yoon[23]). Even when simulating the weakest discharge on the MTX device, the electron's mean-free-path exceeds the experiment's scale size within 30 ns (the discharge tube on MTX has a 5.0 cm radius). Thus, it is expected that collision-rates, rather than electron energy, will be the limiting factor on causing breakdown for these experiments.

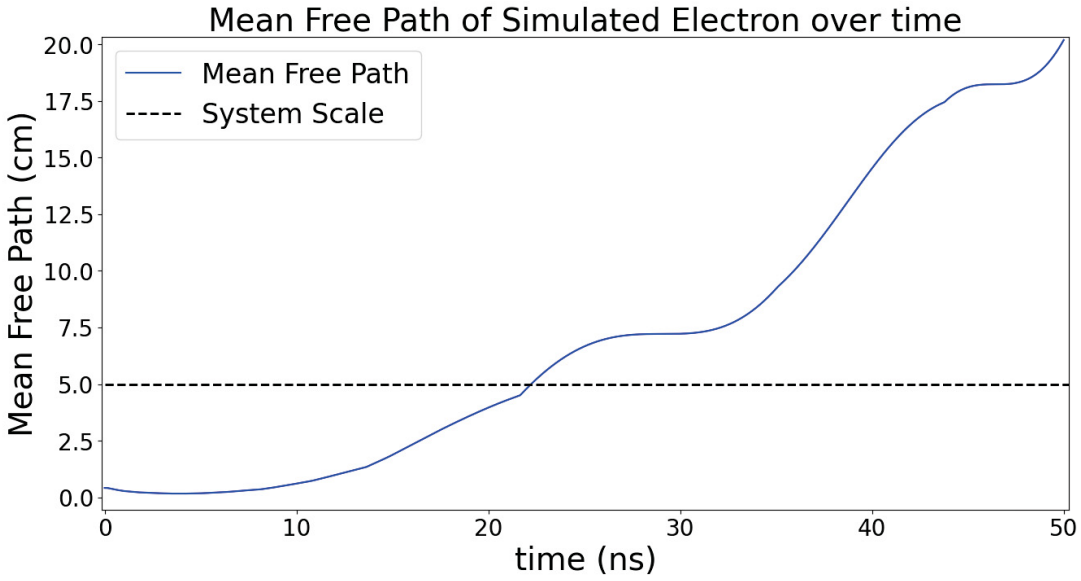

Figure 16: A plot depicting simulated mean-free-path of an electron (based on its kinetic energy) in a low voltage θ-pinch discharge on MTX. Mean-free-path is calculated using momentum transfer cross section data in hydrogen gas from Yoon[23] and a pressure of 100 mTorr.

Using the semi-empirical model considered so far, and the fact the experiments at hand will take place in a collision-rate limited environment, several expectations on behavior of the studies can be projected. First, since electrons will generally be traveling large distances under the influence of electric fields prior to collision, it is expected that measured breakdown factors will be much greater than unity ($\alpha^* >> 1$). Second, since collision rates are the

limiting factor for breakdown in the present study and higher pressure will increase collision rates, it is expected that lower breakdown factors will be measured at higher pressures. Finally, according to equation 3.2.3, electron density is exponentially dependent on neutral density, so that measured breakdown factor is expected to be exponentially higher for lower gas pressures. These expectations are summarized below.

- Expectation 1: Breakdown factors should be much greater than unity ($\alpha^* >> 1$).
- Expectation 2: Measured breakdown factors should decrease at higher gas pressures.
- Expectation 3: Measured breakdown factors should be exponentially higher at lower gas pressures.

3.3 General solution for particle motion in static $\vec{E} \times \vec{B}$ fields

It is worthy to present here the general solution of particle motion in spatially and temporally invariant crossed electric and magnetic fields for both context and the fact that the general solution is still applicable to more complex configurations after making some simplifying assumptions. To begin, let a constant and uniform magnetic field exist in the $\hat{x}$ direction (B_x) and a constant and uniform electric field exist in the $\hat{z}$ direction (E_z). From the general equation of motion for a charged particle,

$$m\frac{\partial \vec{v}}{\partial t} = q(\vec{E} + \vec{v} \times \vec{B}) \tag{3.3.1}$$

two coupled equations emerge for the motion of an electron, one in the $\hat{y}$ direction

$$\dot{v}_y = \frac{qB_x}{m_e} v_z = \omega_{ce} v_z \tag{3.3.2}$$

where m_e is the mass of an electron and ω_{ce} is the cyclotron frequency of an electron, and the other force is in the $\hat{z}$ direction,

$$\dot{v}_z = \omega_{ce}\left(\frac{E_z}{B_x} - v_y\right) \tag{3.3.3}$$

To solve this system, differentiate equation 3.3.2 with respect to time and substitute it into equation 3.3.3 to obtain

$$\ddot{v}_y = \omega_{ce}^2\left(\frac{E_z}{B_x} - v_y\right) \tag{3.3.4}$$

This represents a second order ordinary differential equation whose solution can be determined by combining the homegeneous solution ($v_y(t) = C_1 sin(\omega t) + C_2 cos(\omega t)$) and the particular solution ($v_y(t) = \frac{E_z}{B_x}$). So that the velocities have the solution

$$v_y(t) = C_1 sin(\omega_{ce} t) + C_2 cos(\omega_{ce} t) + \frac{E_z}{B_x} \tag{3.3.5}$$

in the $\hat{y}$ direction and

$$v_z(t) = C_1 cos(\omega_{ce} t) - C_2 sin(\omega_{ce} t) \tag{3.3.6}$$

in the $\hat{z}$ direction. Letting the initial velocity of the particle be 0 in both directions, the constants can be solved so that

$$\boxed{v_y(t) = \frac{E_z}{B_x} sin(\omega_{ce} t) + \frac{E_z}{B_x} cos(\omega_{ce} t) + \frac{E_z}{B_x}} \tag{3.3.7}$$

and

$$\boxed{v_z(t) = \frac{E_z}{B_x} cos(\omega_{ce} t) - \frac{E_z}{B_x} sin(\omega_{ce} t)} \tag{3.3.8}$$

This is the general motion of an electron in crossed electric and magnetic fields with

no initial velocity. It is basically a cyclotron motion of velocity magnitude $\frac{E}{B}$ and a drift velocity of $\frac{E}{B}$ in the $\vec{E} \times \vec{B}$ direction. An important note here is that an electron starting from rest that is exposed to crossed electric and magnetic fields will achieve a maximum velocity of no greater than $\frac{2E}{B}$. Thus, the energy that can be transmitted to an electron by an electric field is limited by the presence of a perpendicular magnetic field. Further, in the present ringing-θ experimental setup the maximum magnitude of $\frac{E}{B}$, and therefore an electron's kinetic energy, is greatest at the coil's maximum radius.

3.4 Ringing-θ breakdown modeling

The first step for developing a model for the ringing-θ configuration is to define the electric and magnetic fields. The initial condition is a circular coil carrying a current in it (commonly referred to as a θ coil), producing a uniform magnetic field in an enclosed area (as seen in figure 17). For this problem setup it is assumed that the bias current and fields are constant in time when compared to the frequency of the ringing-θ discharge so that

$$B_z(t) \approx B_{bias} + B_{R\theta} sin(\omega_{R\theta} t) \tag{3.4.1}$$

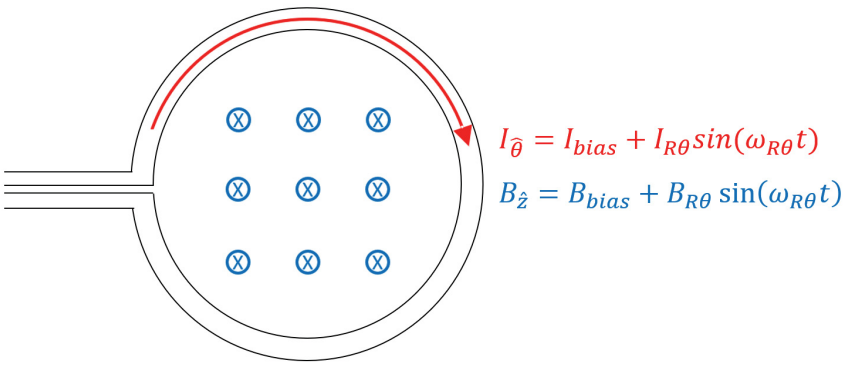

Figure 17: Ringing-θ field setup

Where $B_{R\theta}$ is the peak field strength of the ringing unit and B_{bias} is the field strength of the bias unit (assumed constant in time with respect to the ringing unit). This is a case in which the general Stokes' theorem can be applied as

$$\iint \nabla \times \vec{E} = \oint_C \vec{E} \cdot dl = \iint -\frac{\partial \vec{B}}{\partial t} ds \tag{3.4.2}$$

so that

$$\int_0^r \int_0^{2\pi} -\frac{\partial B}{\partial t} r dr d\theta = -\pi r^2 \frac{\partial B}{\partial t} = \oint_C \vec{E} \cdot dl = V \tag{3.4.3}$$

Because the determined voltage is in a circumferential loop around the enclosed magnetic flux, the electric field strength is simply

$$E\hat{\boldsymbol{\theta}} = \frac{\partial V}{\partial c}\hat{\boldsymbol{\theta}} = \frac{\pi r^2 \frac{\partial B_z}{\partial t}}{2\pi r}\hat{\boldsymbol{\theta}} = \frac{r}{2}\frac{\partial B_z}{\partial t}\hat{\boldsymbol{\theta}} \tag{3.4.4}$$

where c is the circumference differential. Now that the fields have been determined, the next step is to determine the path of an electron in such a configuration. The equation of motion for an electron (neglecting axial motion of the electron) is

$$m_e \frac{\partial v_r}{\partial t}\hat{\boldsymbol{r}} = q(\vec{E} + \vec{v} \times \vec{B})\hat{\boldsymbol{r}} = q v_\theta B_z(t)\hat{\boldsymbol{r}} \tag{3.4.5}$$

$$m_e \frac{\partial v_\theta}{\partial t}\hat{\boldsymbol{\theta}} = q(\vec{E} + \vec{v} \times \vec{B})\hat{\boldsymbol{\theta}} = q(E_\theta(r) + v_r B_z(t))\hat{\boldsymbol{\theta}} \tag{3.4.6}$$

Taking the time derivative of the equation 3.4.5 and substituing equation 3.4.6 yields

$$\frac{\partial^2 v_r}{\partial t^2}\hat{\boldsymbol{r}} = \left(\frac{q}{m_e}\right)^2 \dot{B}_z(E(t) + v_r B_z(t))\hat{\boldsymbol{r}} \tag{3.4.7}$$

The full equation fits the form of a non-homogeneous 2nd order ordinary differential equation with variable coefficients. However, using the work from section 3.3, a simplified model for the ringing-θ configuration can be developed that is still applicable in the parameter regime of interest.

First, the results of section 3.3 show that electron velocity in a ringing-θ configuration is greatest at the coil's maximum radius ($v_e \propto E/B \propto r$). Thus, breakdown is expected to first occur at or very near the vacuum tube's maximum radius (where the vacuum tube's maximum radius is usually very close to the radius of the θ coil). Therefore, the electron energy scaling model for a ringing-θ system should use $r = r_{tube}$. For these conditions, the results from equations 3.3.7 and 3.3.8 apply directly and the magnitude of an electron's velocity over a cyclotron orbit will vary from 0 to $2\frac{E}{B}$. Therefore, a reasonable reference velocity for determining the scaling of the electron kinetic energy in a ringing-θ configuration is simply $v_{\text{ref}} = 2E_\theta/B_z$ where B_z is given by

$$B_{\hat{z}} = B_{\text{bias}} + B_{R\theta} sin(\omega_{R\theta} t) \tag{3.4.8}$$

and $E_{\hat{\theta}}$ is given by substituing in the appropriate time derivative in equation 3.4.4 to obtain

$$E_{\hat{\theta}} = \frac{B_{R\theta}\omega_{R\theta} r_{tube}}{2} cos(\omega_{R\theta} t)\hat{\boldsymbol{\theta}} \tag{3.4.9}$$

Using these magnetic and electric field strengths, the kinetic energy of an electron in a ringing-θ system prior to breakdown can be modeled as

$$K.E._{scale} = \frac{m_e}{2}\left(\frac{B_{R\theta}\omega_{R\theta} r_{tube} cos(\omega_{R\theta} t)}{B_{Bias} + B_{R\theta} sin(\omega_{R\theta} t)}\right)^2 \tag{3.4.10}$$

Now, using equation 3.2.5 for the definition of breakdown factor, α^* can be determined

as

$$\alpha^*_{R\theta} = \frac{K.E._{e^-}}{\xi_{\text{Ion}}} = \frac{m_e}{2\xi_{\text{Ion}}}\left(\frac{B_{R\theta}\omega_{R\theta}r_{tube}cos(\omega_{R\theta}t)}{B_{Bias} + B_{R\theta}sin(\omega_{R\theta}t)}\right)^2 \tag{3.4.11}$$

Where $\xi_{\text{ionization}}$ is the ionization energy of the gas and $\alpha^*_{R\theta}$ is the breakdown factor for a ringing-θ system. For breakdown studies in a ringing-θ configuration, determination of $\alpha^*_{R\theta}$ requires only a measurement of the time at which breakdown occurs and knowledge of the field configuration (i.e., measurements of $B_{R\theta}$, $\omega_{R\theta}$, etc.). It should be noted particularly here when applying this model that an area-averaged field strength out to r_{tube} should be used for the numerator of equation 3.4.11 while the point measurement at r_{tube} should be used for the denominator. This is due to the fact that the field values in equation 3.4.11 represent E_θ/B_z, where E_θ depends on the rate of change of the enclosed flux (which can be determined using an area-averaged field strength), and B_z is the field strength value at the location of interest (r_{tube}) in this case.

3.5 Dipole Breakdown Modeling

As with the ringing-θ breakdown model, the first step for the ringing-multipole breakdown model is to determine the field distribution. For the experiments conducted on MTX, a dipole coil will be used and an example of the expected field distribution can be seen in figure 18. Note that the field distribution of higher order poles can be roughly estimated using super-position of the Biot-Savart equation (this neglects mutual inductance between poles and other coils which becomes more significant with higher numbers and proximities of poles).

Although direct measurements of magnetic field strength will be used for later analysis, a rough approximation of the dipole's field distribution can be determined by assuming the magnetic field is uniform in the region between the two coils. The dipole coil will have a

rectangular shape extending along the formation section in the axial direction as shown in figure 19.

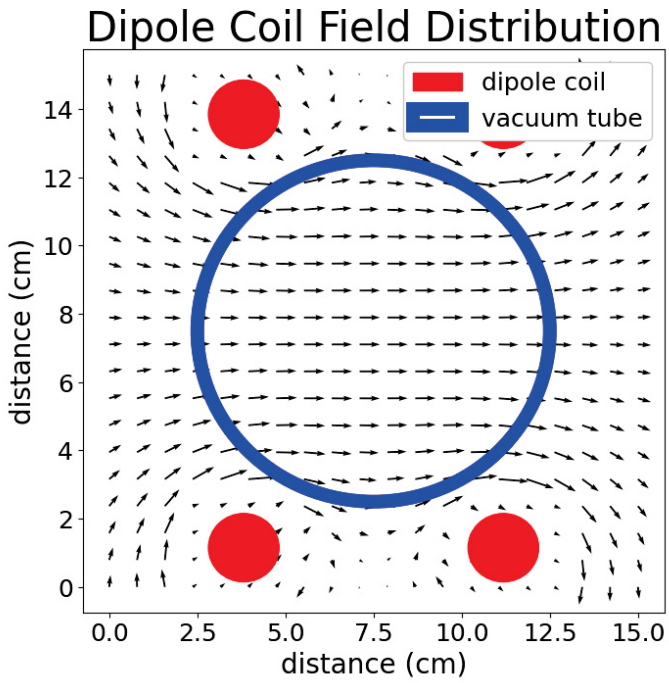

Figure 18: Field distribution of MTX's dipole coil, approximated as superimposed Biot-Savart wire source.

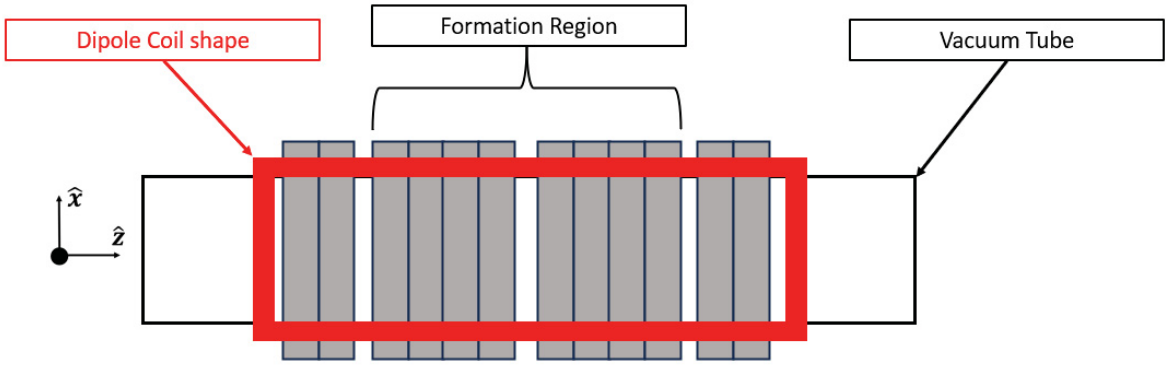

Figure 19: Diagram displaying a top-down view of the dipole coil's shape installed on MTX.

To define the field distribution for this configuration, a rectangular coordinate system as shown in figure 19 with its origin at the center of the formation chamber is convenient. Assuming a uniform magnetic field inside of the dipole coils (to reiterate, this is a rough estimation of the field) the magnetic field will be

$$B_{\hat{y}} = B_{\mathrm{OMF}} sin(\omega_{OMF} t)\hat{y} \tag{3.5.1}$$

The electric field distribution can again be determined by applying Stokes' theorem as

$$\nabla \times \vec{E} = -\frac{\partial B}{\partial t} = B_{\mathrm{OMF}} \omega_{OMF} cos(\omega_{OMF} t)\hat{y} \tag{3.5.2}$$

Using a coordinate system centered on the coilset, the voltage can be determined as

$$V = \oint_C \vec{E} \cdot dl = \int_{-z}^{z} \int_{-x}^{x} B_{OMF} \omega_{OMF} cos(\omega_{OMF} t) dx dz \tag{3.5.3}$$

so that

$$V = B_{OMF} \omega_{OMF} cos(\omega_{OMF} t) xz \tag{3.5.4}$$

The electric field is just the voltage divided by the path vector of interest which is in the $\hat{x}$ and $\hat{z}$ directions for this application. Thus, the total path length in the $\hat{x}$ direction will obviously be $2x$, and the same applies for the $\hat{z}$ direction. Dividing 3.5.4 by these vector path lengths will yield the field at any point in the $x - z$ plane as

$$\vec{E}_{\mathrm{dipole}} = B_{OMF} \omega_{OMF} cos(\omega_{OMF} t) \left[\frac{z}{2}\hat{x} + \frac{x}{2}\hat{z} \right] \tag{3.5.5}$$

Further, if $z >> x$ as is the case for MTX then the $\hat{x}$ component of the electric field will be negligible in the formation region and the electric field can be assumed to be primarily in the axial direction, varying across the $\hat{x}$ direction as given in equation 3.5.5.

The primary region of interest is the axial center of the formation chamber and the induced electric field will have the greatest strength near the tube wall, i.e., at $z = 0$, $x = r_{tube}$. With this field strength, a scaling model for electron energy can be determined using kinematics. Consider that for a charged particle exposed to an electric field the resulting force is given as, $F = qE$ (where q is the particle's charge). Thus, the acceleration of the electron in an electric field then, is simply

$$a = \frac{q_e E}{m_e} \tag{3.5.6}$$

where a is the electron's acceleration, q_e is electron charge, E is the electric field strength, and m_e is the electron mass. Plugging in equation 3.5.5 for the electric field strength, electron velocity can then be determined by taking the time integral of equation 3.5.6 as

$$v_e = \int_0^t a dt = \int_0^t \frac{qE(t)}{m_e} = \frac{q r_{\text{tube}} B_{\text{dipole}} sin(\omega_{\text{dipole}} t)}{2 m_e} \tag{3.5.7}$$

Using equation 3.5.7, the kinetic energy of an electron in a dipole coil discharge can be determined as (using K.E. $= 0.5mv^2$)

$$\text{K.E.}_{e^-} = \frac{q r_{\text{tube}} B_{\text{dipole}} sin(\omega_{\text{dipole}} t)}{8 m_e} \tag{3.5.8}$$

and thus the breakdown factor for a dipole configuration can be determined as

$$\alpha^*_{\text{dipole}} = \frac{q r_{\text{tube}} B_{\text{dipole}} sin(\omega_{\text{dipole}} t)}{8 m_e \xi_{\text{Ion}}} \tag{3.5.9}$$

3.6 θ-Pinch Breakdown Modeling

Although not commonly used in modern experiments, a θ-pinch pre-ionization approach was widely used in early FRC experiments [1]. In this approach, ionization occurs during the initial rise of the bias field when the magnetic field strength is low but dB/dt (and therefore E_θ) is high. It was found that the MTX was unintentionally causing seed ionization through a θ-pinch method using a bias discharge with a quarter cycle time of approximately 6 μs and a peak field strength of approximately 0.2 T. Thus, breakdown using a θ-pinch system will be explored on the MTX in the same fashion as the preceding inductively coupled PI methods.

The field distribution of a θ-pinch configuration is approximated as that of an ideal solenoid so that the magnetic field inside of the coil is given as

$$B_z(t) = -B_{\theta P} sin(\omega_{\theta P} t) \tag{3.6.1}$$

and the electric field is given by the same result obtained for equation 3.4.9 as

$$E_\theta = \frac{B_{\theta P}\omega_{\theta P} r}{2} cos(\omega_{\theta P} t) \tag{3.6.2}$$

where $B_{\theta P}$ represents the peak field strength of the θ-pinch discharge and $\omega_{\theta P}$ is its discharge frequency. From the standard equation of motion for a charged particle

$$m_e \frac{d\vec{v}}{dt} = q(\vec{E} + \vec{v} \times \vec{B}) \tag{3.6.3}$$

and assuming the $\vec{v} \times \vec{B}$ term can be neglected in early time, the acceleration in the $\hat{\theta}$

direction is given as

$$\frac{dv_\theta}{dt} = \frac{qB_{\theta P}\omega_{\theta P} r_{\text{tube}} cos(\omega_{\theta P} t)}{2m_e} \tag{3.6.4}$$

Again, it is sufficient to consider only how an electron's energy scales in a given configuration. Therefore, it is not necessary to consider how a change in radial position (a θ-pinch discharge tends to pull electrons inward with a small radial velocity due to the magnetic field it produces) affects an electron's actual kinetic energy and it is sufficient to simply integrate equation 3.6.4 over time to determine a scaling velocity. Thus,

$$v_\theta = \frac{qB_{\theta P} r_{\text{tube}} sin(\omega_{\theta P} t)}{2m_e} \tag{3.6.5}$$

Using this velocity, the scaling model for an electron's kinetic energy in a θ-pinch configuration can be determined as

$$\text{K.E.}_{e^-} = \frac{1}{2} m_e v^2 = \frac{(qB_{\theta P} r_{\text{tube}} sin(\omega_{\theta P} t))^2}{8m_e} \tag{3.6.6}$$

and the breakdown factor for a θ-pinch configuration is then directly given as

$$\alpha^*_{\theta P} = \frac{(qB_{\theta P} r_{\text{tube}} sin(\omega_{\theta P} t))^2}{8m_e \xi_{\text{Ion}}} \tag{3.6.7}$$

Note the similarity of breakdown factor models for the θ-pinch here (equation 3.6.7) and that for the dipole configuration (equation 3.5.9). This is because electron kinetic energy scales the same in both configurations. However, it should be noted that the θ-pinch configuration accelerates electrons azimuthally and pulls them inward to lower radii while the dipole configuration accelerates electrons axially, thus forcing them towards the outer regions of the experiment. Effectively, this means that θ-pinch discharges will keep accelerated electrons in the system for logner than a dipole configuration.

3.7 Modeling Summary

To summarize this chapter, a model has been proposed which states that breakdown of a gas with inductively-coupled systems will behave primarily as a function of gas type, gas pressure, and the newly introduced term, "breakdown factor." Three primary assumptions for the model are made which are listed here.

- Assumption 1: Recombination rates are negligible at breakdown conditions.
- Assumption 2: Initial electron density (n_{e0}) is constant between experiments.
- Assumption 3: Collisional cross section is approximately a constant at electron energy ranges of interest.

Electron density is then observed to scale as

$$n_e = n_{e0} e^{n_n \sigma_{\mathrm{Ion}}(v_e) \int_0^t v_e} \tag{3.7.1}$$

which, when given the above assumptions, identifies gas number density (directly proportional to gas pressure) and electron kinetic energy as the dominant varying factors. Thus, growth rate of electrons (i.e., breakdown) is expected to behave primarily as a function of gas pressure and electron kinetic energy. As breakdown is the transition of a gas from being electrically insulative to electrically conductive, electron energy induced by imposed fields can be determined using single particle motion models, due to the fact electron number density is too low to affect imposed field distribution prior to breakdown (i.e., breakdown occurs before the plasma's skin depth is shorter than the scale length of the system). It is sufficient to consider only how electron energy scales in a given configuration but models used for electron kinetic energy of a given configuration must be consistent for results to be

compared. Given the above considerations and the fact that these experiments will be conducted in a collision-rate limited regime, three primary expectations on breakdown behavior are projected.

- Expectation 1: Breakdown factors should be much greater than unity ($\alpha^* >> 1$).
- Expectation 2: Measured breakdown factors should decrease at higher gas pressures.
- Expectation 3: Measured breakdown factors should be exponentially higher at lower gas pressures.

The concept of a breakdown factor is introduced, which is defined as the ratio of the scaling model of electron energy in a given configuration to the ionization energy of the gas.

$$\alpha^* = \frac{\text{K.E.}_{e^-}}{\xi_{\text{Ion}}} \tag{3.7.2}$$

Three separate configurations are considered for the present study and models for breakdown factors of each are introduced. In a ringing-θ configuration, breakdown factor is calculated as

$$\alpha^*_{R\theta} = \frac{K.E._{e^-}}{\xi_{\text{Ion}}} = \frac{m_e}{2\xi_{\text{Ion}}}\left(\frac{B_{R\theta}\omega_{R\theta}r_{tube}cos(\omega_{R\theta}t)}{B_{Bias} + B_{R\theta}sin(\omega_{R\theta}t)}\right)^2 \tag{3.7.3}$$

Breakdown factors for dipole configurations are given as

$$\alpha^*_{\text{dipole}} = \frac{qr_{\text{tube}}B_{\text{dipole}}sin(\omega_{\text{dipole}}t)}{8m_e\xi_{\text{Ion}}} \tag{3.7.4}$$

Finally, breakdown factors for θ-pinch configurations are given as

$$\alpha^*_{\theta P} = \frac{(qB_{\theta P}r_{\text{tube}}sin(\omega_{\theta P}t))^2}{8m_e\xi_{\text{Ion}}} \tag{3.7.5}$$

In total, this means that for a given gas, at a given pressure, a breakdown factor can be determined by measuring the time at which breakdown occurs in a given field configuration. Effectively, breakdown factor is a function of field parameters and time but once field parameters are defined, it is a monotonic function of time. So for a given configuration whose field parameters are well known, a line can be generated as a function of time. The time at which breakdown occurs can be measured, and will thus correspond to a specific breakdown factor. Figure 20 shows an example of this for a θ-pinch discharge on the MTX machine. In this case, two lines are shown, each for a different field strength of θ-pinch. The scatter points indicate the actual measured time of breakdown for these configurations but are presented here only to provide context for how breakdown factor behaves, and how it can be measured. This is the method that will be used to analyze breakdown in this study.

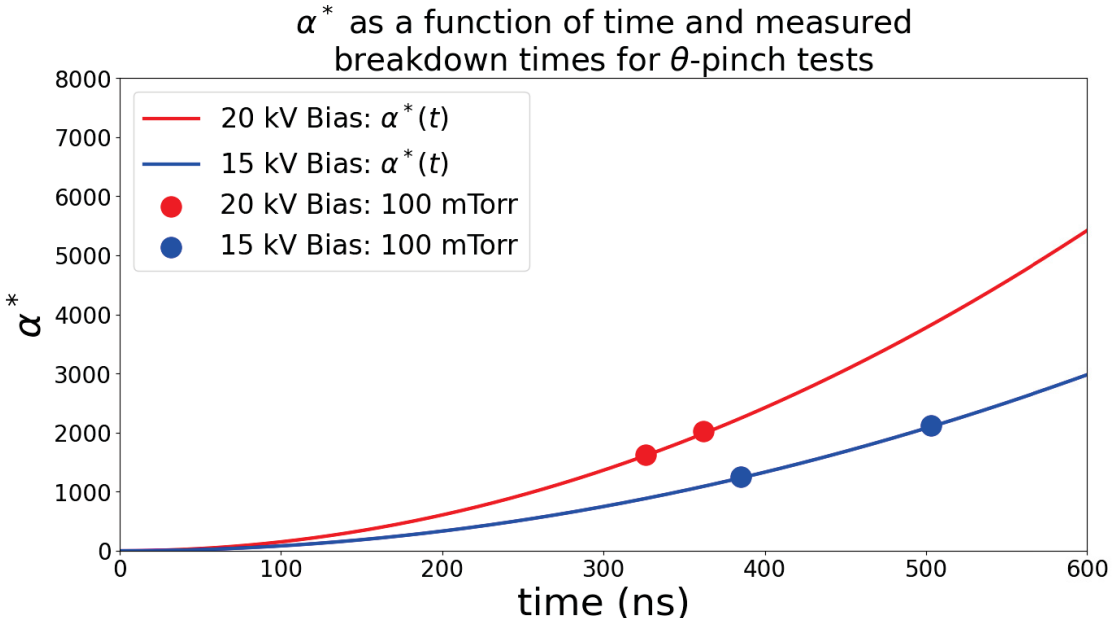

Figure 20: An example plot, showing breakdown factor as a function of time for a θ-pinch configuration. Also shown are measured times of breakdown, which correspond to a specific breakdown factor value.

Chapter 4

Experiment Overview

4.1 MTX: Pulsed Power Design

To achieve the independent firing capabilities, it must be possible that one coil is able to fire without triggering neighboring coil modules or even other banks connected to the same coil. Unintentional triggering of separate units is commonly referred to as "pre-firing" in pulsed-power parlance and is a common problem for many pulsed-power experiments. Commercially available pulsed-power systems are not directly capable of providing the desired performance and were prohibitively expensive for the modularity required for the project's goals. Therefore, a campaign was carried out by the MTX researchers to develop new pulsed-power systems to meet the project's needs.

4.1.1 MTX Coil Modules

MTX presently consists of two formation coils and two cusp coils for basic formation studies. The field shape is somewhat similar to the setup shown in figure 3 which displays four formation coils and two cusp coils. Each coil on the MTX machine has its own separate pulsed power module and the design of each module depends on the pulse shape the specific coil must produce. A simplified schematic of a cusp coil and its associated pulsed power module can be viewed in figure 21. The cusp coils must produce a magnetic field that

decays on a slow time scale compared to FRC timescales and the fields must be oriented oppositely to the bias fields (as shown on the smaller edge coils in part A of figure 3). Once the start switch is fired the charged capacitor discharges through the circuit to produce the axial magnetic field in the machine. The isolation inductor shown in the schematic serves to increase the pulse length of the discharge. The crowbar switch then fires when the current is (ideally) at its peak value, effectively isolating the load side of the circuit from the capacitor. Figure 22 displays a plot showing a standard ringing discharge compared to its "crowbarred" version for clarity. Succesfully firing the crowbar switch at the peak current changes the discharge from an LRC ringing decay to a smoother LR decay. This produces the desired pulse shape and magnetic field strength using far less capacitive energy than would be required by a standard LRC circuit.

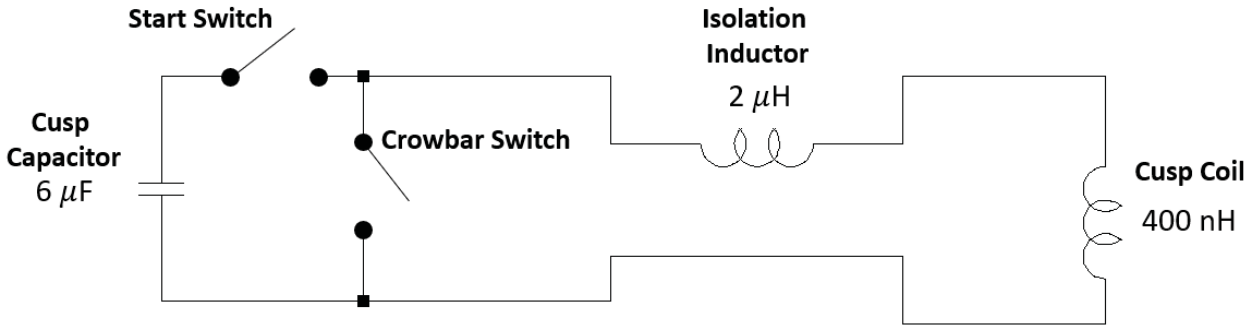

Figure 21: Simplified schematic of a cusp coil module

The bias and reversal fields are produced in the same formation coil so the design of its associated pulsed power module is slightly more complex. Figure 23 displays a schematic of bias/reversal module. The bias side of the unit is very similar to the schematic for the cusp unit shown in figure 21. However, the inductor now labeled "isolation inductor" serves to increase the pulse duration and two other purposes. It additionally serves to isolate the voltage produced by the firing bias switch from the reversal switch and vice-versa which

prevents pre-firing of the reversal unit and overvoltaging of the bias switch.

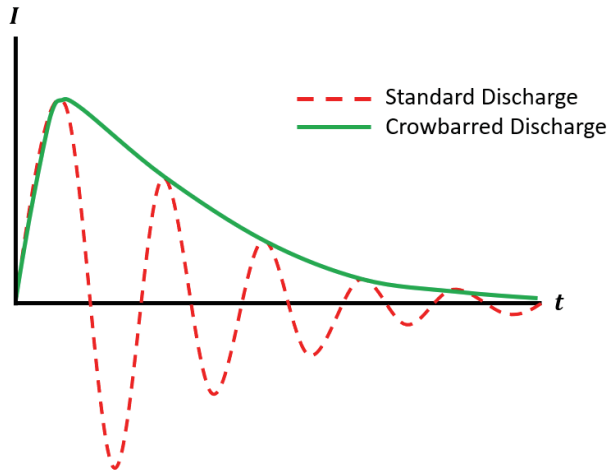

Figure 22: Conceptual plot of current over time for a standard LRC discharge vs. its crowbarred LR ringdown

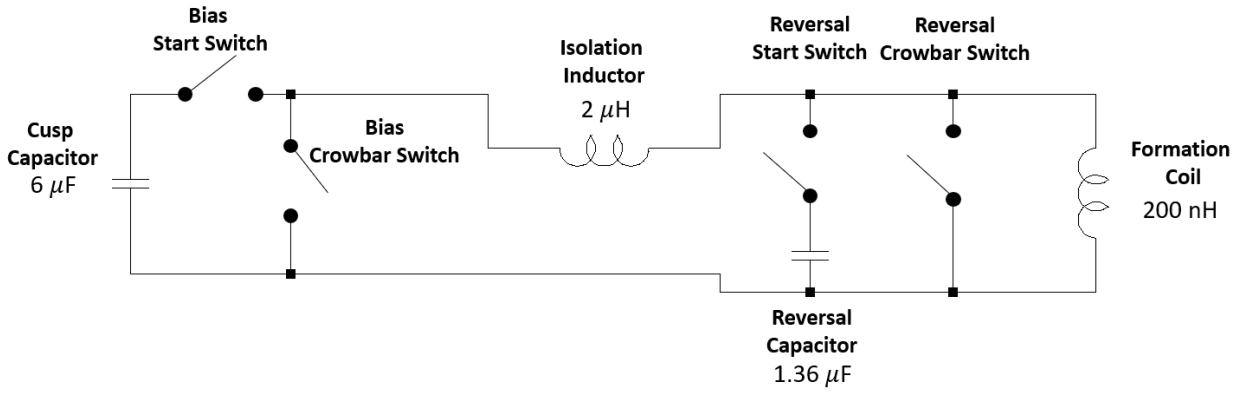

Figure 23: Simplified schematic of a formation coil module

The isolation inductor also ensures that most of the current produced by the reversal switch is fired into the coil rather than going back through the bias switch to reach ground. Initially the bias start switch fires, producing a negatively oriented magnetic field in the formation chamber (as shown again in part A of figure 3). When the bias unit reaches peak

current, its crowbar switch is fired, preventing ringing. The reversal start switch is generally fired at the same time as the bias crowbar switch or soon thereafter, allowing the reveral capacitor to discharge through the coil and rapidly reverse the magnetic field's orienation. Finally, the reversal's crowbar switch is fired, preventing the ringing of the reversal field (note that the reversal field still decays much faster than the bias field).

The final unit on the present incarnation of the machine is the OMF module which fires the dipole coil for pre-ionization. The dipole coil is outlined in figure 24 and a schematic of the module is shown in figure 25 (note the lack of a crowbar switch because the unit must ring to function). This module is designed to fire a transverse magnetic field through the formation chamber . This, in-turn, produces axial electric fields which cause pre-ionization prior to the firing of the reversal field (see section 3.5 for more details).

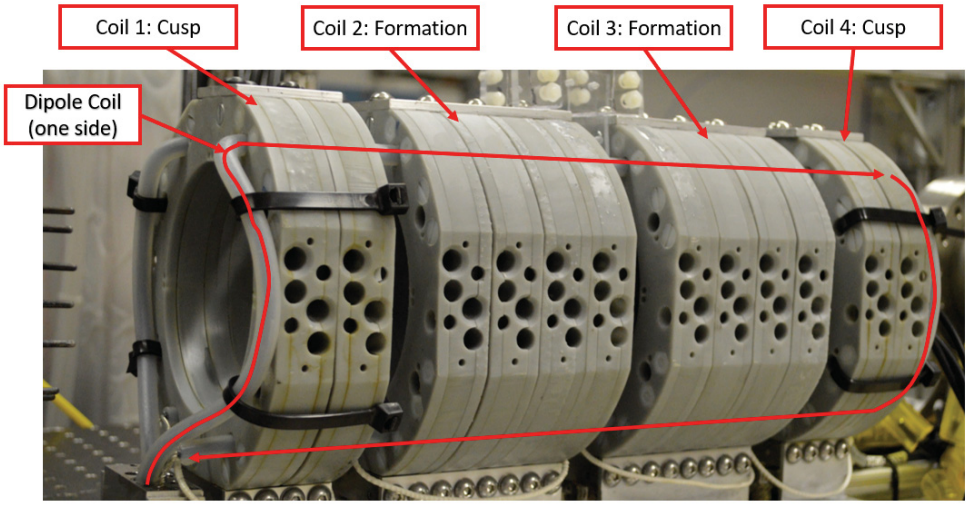

Figure 24: Outline of the dipole coil in the present incarnation of MTX

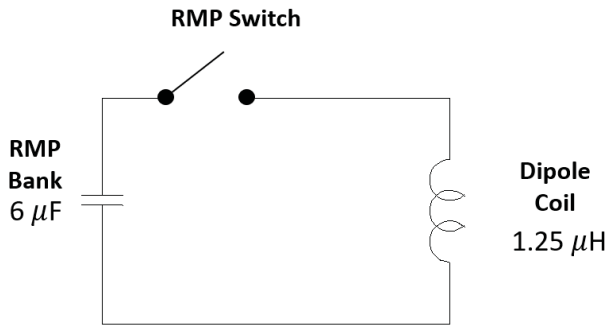

Figure 25: Simplified schematic of the dipole coil module

Table 2 summarizes the voltages, field strengths, and frequencies of MTX's discharge banks.

Table 2: This table summarizes the bank parameters. Note that the magnetic field values presented are the tube-area-averaged field strength.

Bank parameters for breakdown studies			
Bank	**Voltage Range (kV)**	**Field Range (mT)**	**Frequency (kHz)**
Cusp	10 to 20	150 to 300	43
Bias	10 to 20	-110 to -225	43
Reversal	20 to 40	300 to 600	320
Dipole	20 to 40	105 to 215	140

4.2 Diagnostics

In order to perform prompt breakdown studies and comparison of ringing-θ and biased dipole pre-ionization methods, several parameters need to be measured. First and foremost the magnetic fields generated by the pulsed power system needed to be measured, including the total flux generated in the formation chamber, the magnetic field strengths produced

inside the θ coils (external to the vacuum system), and the current through the θ-coils. Firing timing is measured using magnetic field measurements for prompt breakdown studies. Additionally, to better understand diffusion of magnetic flux through the plasma for pre-ionization method comparison, it is beneficial measure magnetic field strengths inside the plasma. The flux array was designed for this purpose.

In order to measure the time at which breakdown occurs it is necessary to have visible light photodiodes to detect light signals generated at breakdown. Gas fill pressures are measured with a an MKS brand, model 626 capacitance manometer with a stated accuracy of $\pm$ 0.5% of the acquired reading. Two photodiodes are also fitted with H-α and H-β band-pass filters so that temperature estimates up to 10 eV in deuterium plasma could be made. A 12-frame high-speed visible light imaging camera which takes images along the axial axis of the chamber is used to observe plasma structures and make estimations of plasma uniformity. Finally, an interferometer is also used to measure line-integrated plasma density. Note RG-223 coaxial cable was used for transmission of all electric signals in these diagnostics, as the extra outer braiding was seen to yield better noise shielding than the single braided RG-58. Details on all of these diagnostics are given in the following subsections.

4.2.1 Magnetic Diagnostics

The term magnetic diagnostics is used here to represent a class of probes that measure either current, magnetic field, or flux through voltage induced on electric circuits via Faraday's law. Thus, these magnetic diagnostics can only be used to measure time-varying signals (which is sufficient for the purposes of this study). Three types of these probes are used on the MTX experiment. The first is a flux loop which measures the total flux in the formation chamber. The second are $\dot{B}$-probes, which are used to measure magnetic field

strength inside of the θ-coil outside of vacuum tube. These are also used in a number of other instances including field mapping of the coils systems (see section 5.1) and in the flux array for measuring magnetic field distribution insided the plasma. Finally, Rogowski probes are used to measure current passing through the coils in the experimental region (θ coils and dipole coil). Note that signficantly more detail on these diagnostics is given in appendix C, covering topics such as basic physics, parastic considerations, basic analytic and spice modeling, calibration methods, and signal processing. Therefore the details presented here in the main body of text are intended to give an overview sufficient for understanding the function, location, basic circuit, and accuracy of the diagnostic.

Flux Loop

A flux loop functions by Faraday's law where an electric field generated by a changing magnetic flux induces a voltage on a circuit (see figure 26). The voltage induced is given as

$$\frac{\partial \phi(t)}{\partial t} = V(t) \tag{4.2.1}$$

where ϕ is the flux in the loop area and V is the voltage induced by the time-varying flux. This voltage can be measured and integrated with respect to time to determine the the magnetic flux in the loop. Combining a measurement of total flux in the formation chamber with spatially resolved magnetic field strength measurements can allow one to determine if flux is being excluded from plasma in the chamber. Effectively, if flux is being excluded from the plasma, a higher magnetic field strength will be measured outside of the plasma for the same given flux. MTX uses a flux loop positioned around the vacuum tube in the formation chamber between the formation coils as shown in figure 27. Note that the flux loop is positioned off-center closer to coil 3. This is intended to allow light-based diagnostics

to make measurements in the exact axial center of the formation chamber. The effects of the flux measurement on this positioning are covered in section 5.1.1.

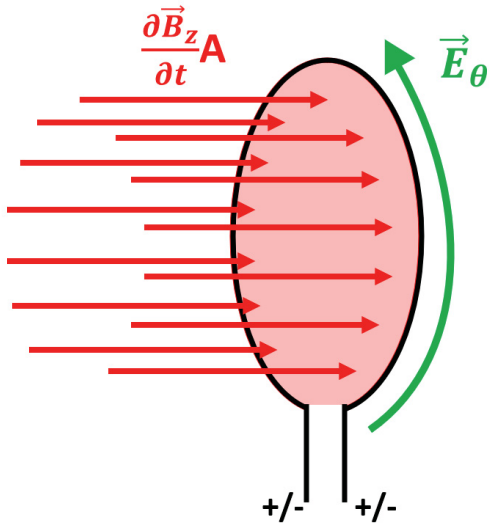

Figure 26: A basic representation of Faraday's law, where a changing magnetic flux enclosed by a conducting loop will induce a voltage along that loop.

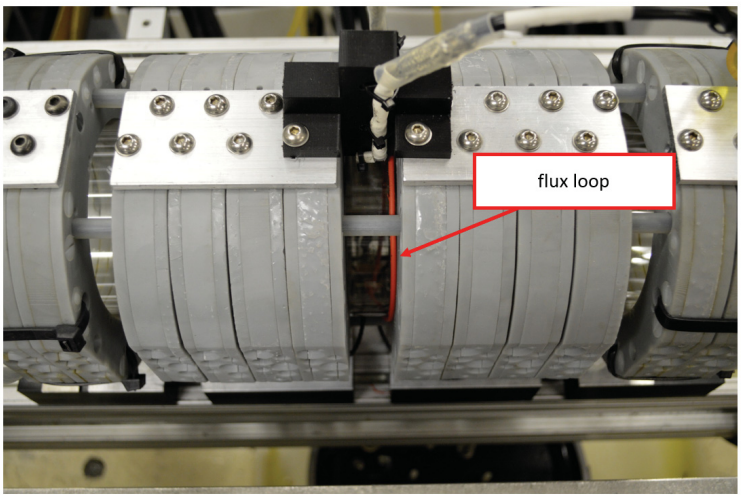

Figure 27: Annotated photo displaying the location of the flux loop on the MTX formation chamber.

The raw signal from the flux loop is resistively divided and sent back to a shielded

oscilloscope via BNC cable. A passive integrator is used to filter out high-frequency noise from switch firing on the pulsed power system. Note that due to the high voltages that were induced on the flux loop, select resistors that maintained a steady impedance under high voltage were used (see appendix C for more details). The spice model used for the circuit to deconvolve the signal is shown in figure 28. Sources of error include the parasitic inductance in the divider circuit and measurement accuracy of the flux loop's area. In total the flux loop measurement is expected to be better than 5% accurate up frequencies of 350 kHz.

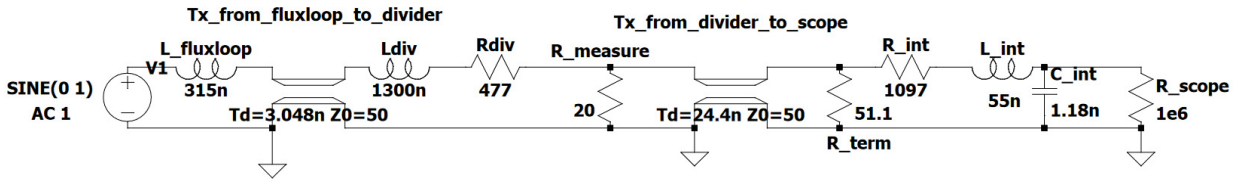

Figure 28: Spice model of the measuring circuit used for the flux loop.

$\dot{B}$ Probes

$\dot{B}$-probes also function by measuring the induced voltage due to changing magnetic flux in a conducting loop (see figure 29). The voltage induced in a $\dot{B}$-probe is given as

$$V(t) = \frac{\partial \phi(t)}{\partial t} = NA\frac{\partial B(t)}{\partial t} \tag{4.2.2}$$

where ϕ is the flux in the probe's loops, N is the number of loops, A is the area of the loops, and V is the voltage induced by the time-varying flux. Magnetic field strength at the probe's location (assuming it's uniform over the length and area of the probe) can be determined by integrating the voltage signal with respect to time. The primary difference between $\dot{B}$-probes and flux loops is that while flux loops measure magnetic flux over a large area (usually on the scale of the system size), $\dot{B}$-probes are intended to measure magnetic

field in a small region to provide an estimate of magnetic field strength at a point location. $\dot{B}$-probes are installed inside the each of the θ coils of the MTX machine as shown in figure 30. $\dot{B}$-probes are also used for the field mapping campaign described in section 5.1 and ceramic-shielded $\dot{B}$-probes are used to measure the magnetic field inside of the plasma in the flux array campaign described in section 5.3.

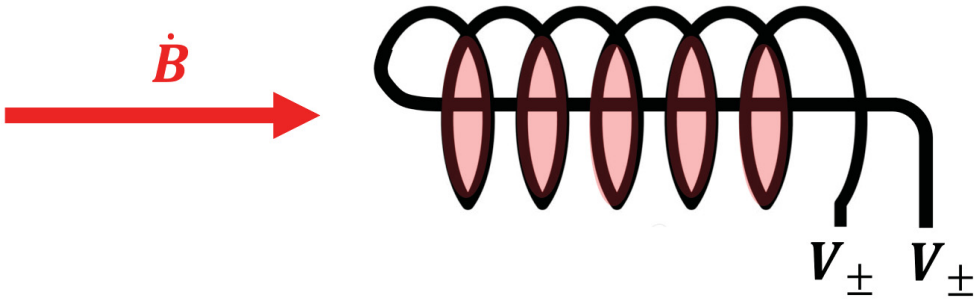

Figure 29: A diagram showing the general shape and function of a $\dot{B}$-probe.

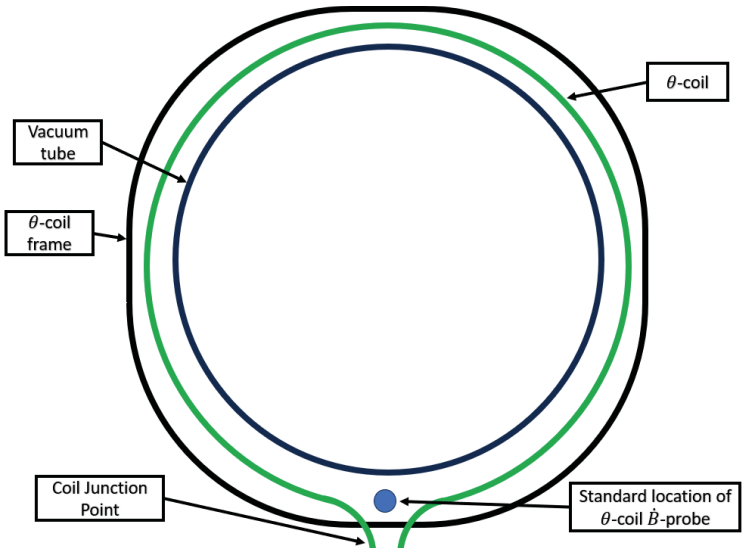

Figure 30: Diagram showing the general location of the θ-coil $\dot{B}$-probes.

The signal induced on the $\dot{B}$-probe is transmitted via RG-223 coaxial cable to a shielded oscilloscope for measurement. A passive low-pass circuit is used to filter out noise picked

up from the firing the pulsed power system's switches. An example of the spice model used for the circuit to deconvolve the signal is shown in figure 31 (note that circuit values vary slightly from probe to probe). Sources of error in the $\dot{B}$-probes include parasitic inductance/-capacitance affecting the frequency response and uncertainties in the calibration process (see appendix C for details). Overall, the $\dot{B}$-probes used in these studies are expected to be better than 5% accurate up to frequencies of 1 MHz.

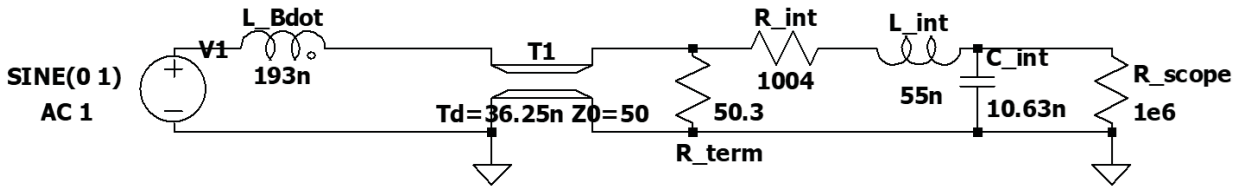

Figure 31: Spice model of the measuring circuit used for $\dot{B}$-probes.

Rogowski Coils

Rogowski probes also function by measuring the induced voltage due to changing magnetic flux in a conducting loop. In this particular case the field inducing a voltage signal is that produced by a current passing through an exposed wire. A Rogowski coil is essentially a solenoid that is wrapped around a current carrying wire as shown in figure 32. r_{minor} represents the area of the individual loops and r_{major} represents the radius of the solenoid's curvature as it is wrapped around the current carrying wire to be measured. If $r_{\text{major}} >> r_{\text{minor}}$, then the magnetic field in the minor loops can be assumed constant across their area and using a Biot-Savart approxmation for the magnetic field generated by the current carrying wire, one can arrive at the relation

$$V(t) = \frac{\mu_0 N A_{\text{minor}}}{2\pi r_{\text{major}}} \frac{\partial I(t)}{\partial t} \tag{4.2.3}$$

where μ_0 is the permeability of free space, N is the number of turns in the Rogowski probe, A_{minor} is the area of the Rogowski probe's loops, r_{major} is the radius of the Rogowski probe as it wrapped around the current carrying wire, and $I(t)$ is the time-varying current in the wire. Thus, the voltage signal from the Rogowski probe can be integrated with respect to time to determine the current in the primary line. Rogowski probes are installed on each θ coil on the MTX machine as well as one on the dipole coil as shown in figure 33

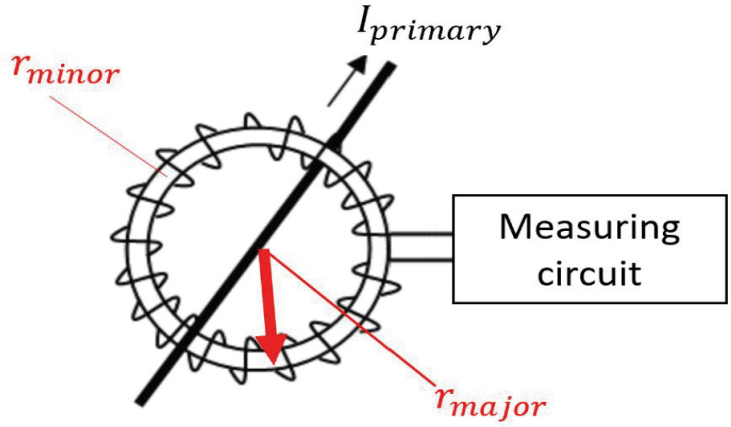

Figure 32: A diagram showing the general shape and function of a Rogowski probe.

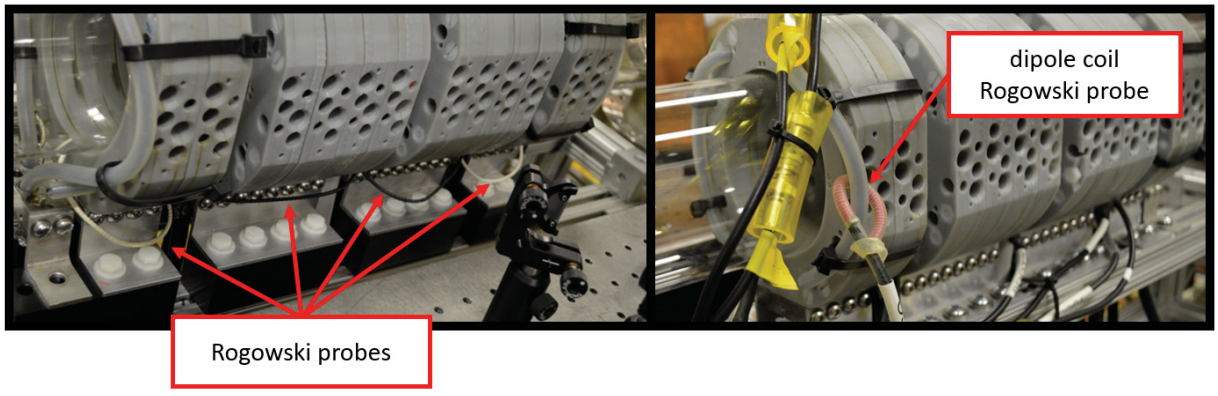

Figure 33: Diagram showing the location Rogowski probes with θ-coil probes shown on the left and the dipole coil's Rogowski probe shown on the right.

The signal picked up by the Rogowski probes are transmitted through RG-223 coaxial cable back to a shielded oscilloscope where passive integrator are again employed to filter out high-frequency noise from the firing of the pulsed power system. An example of the spice models used for the Rogowski probe circuits is shown in figure 34 (the particular model shown is for the dipole coil's Rogowski probe). Sources of error include parasitic capacitance on the Rogowski probes' windings as well as some error from positioning. Note that the θ-coil Rogowski probes used for these studies were uncalibrated as they primarily served only as debugging signals for the pulsed power system. However, the Rogowski probe used on the dipole coil is a calibrated probe. This measurement was used to determine magnetic field strength produced by the dipole coil (see section 5.1.1 for details). Details on its calibration process are given in appendix C and it is expected to be accurate to better than 10% up to frequencies of 350 kHz.

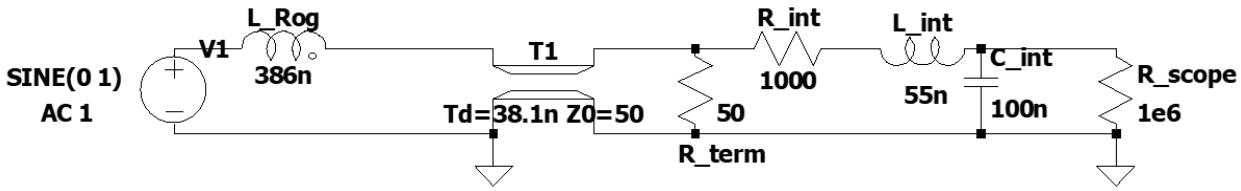

Figure 34: Spice model of the measuring circuit used for dipole coil's Rogowski probe.

Flux Array

The flux array is a custom device made to measure axial magnetic fields internal to the plasma and determine the flux diffusion characteristics of the ringing-θ and biased dipole pre-ionization methods. It is composed of five separate $\dot{B}$-probes that are shielded with ceramic tubes, positioned at various radial and azimuthal locations (see figure 35) and can be inserted to the formation chamber.

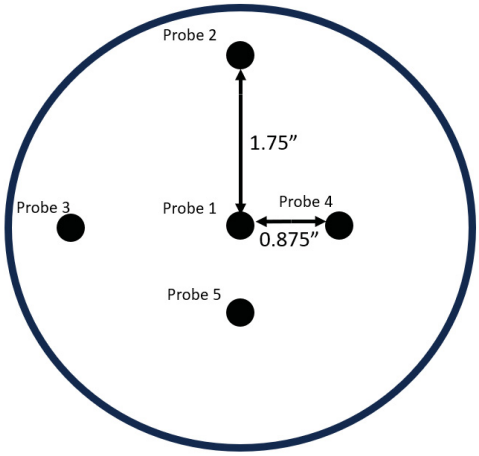

Figure 35: A diagram detailing the radial and azimuthal positions of the flux array's ceramic tubes.

Figure 36 displays two photos of the flux array. The left side of the image shows the ceramic shields fed through an adapter plate but not installed on the MTX machine while the right side displays a photo of installed. Note that because of its installation location, use of the flux array precludes the use of the high-speed imaging camera (which is set up to take photos along the same axis). The ceramic tubes are closed on the side inserted into the vacuum chamber and open on the end exposed to air so that a $\dot{B}$-probe can be inserted into it. The ceramic tubes can be adjusted in the axial direction so that they can be positioned in the formation chamber to measure field strengths or pulled out to prevent interference with the plasma by the ceramic tube. Figure 37 displays a simplified diagram of the flux array installed in the chamber with one of the ceramic tubes pulled out of the formation region as an example. The $\dot{B}$-probes used with the flux array are consistent with the description given in the $\dot{B}$-probe section above and are expected to be accurate to better than 5% up to frequencies of 1 MHz. However, it should be noted that because these ceramic shielded probes are perturbitive in nature, the magnetic field strength without the probe's presence cannot be known for certain. Section 5.3 provides details on flux array measurements and

how they may be intererpreted in light of their perturbative nature. For details on $\dot{B}$-probe calibration, see appendix C.

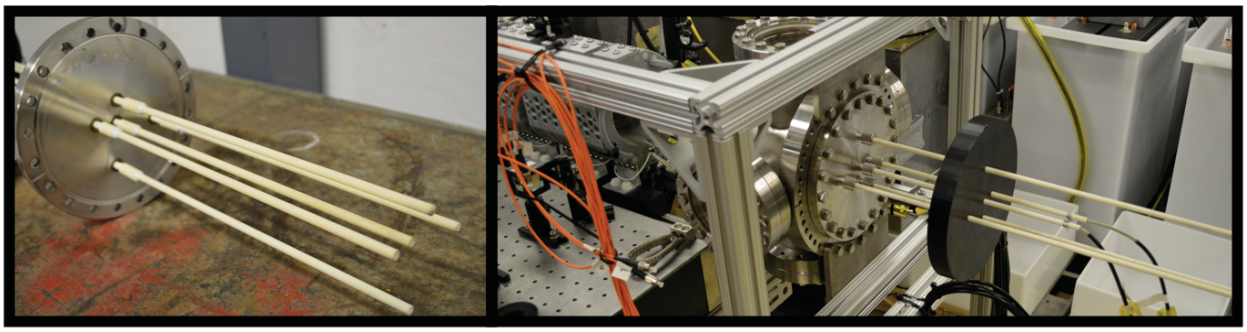

Figure 36: Left: A photo of the end-plate and ceramic tubes of the flux array, not yet installed on the machine. Right: A photo of the flux array installed on the machine with $\dot{B}$-probes positioned in the ceramic tubes for measurement.

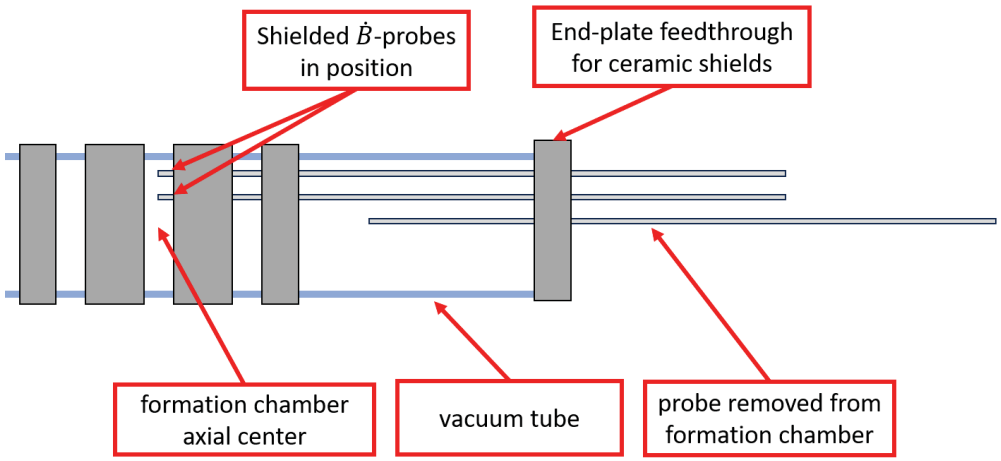

Figure 37: A diagram displaying how ceramic tubes are inserted into the formation chamber to allow for measuring of magnetic field with $\dot{B}$-probes..

4.2.2 Visible Light Diagnostics

Several visible light diagnostics are employed for this study. Figure 38 displays four collimation units that are directed at the axial and radial center of the formation chamber. Note that one collimator is not shown in figure 38 which focuses on the region between coils 3 and 4 (see figure 24) for a total of five collimation units on the experiment. The light is transmitted via multimode fiber optic cable to an EMI shielded enclosure containing the visible light diagnostic electronics. Varying strengths of neutral density filters are used on all collimators depending on the expected light signal in order to pretect diagnostics from being damaged by over-saturation. Practically, this limits the minimum signal that can be detected.

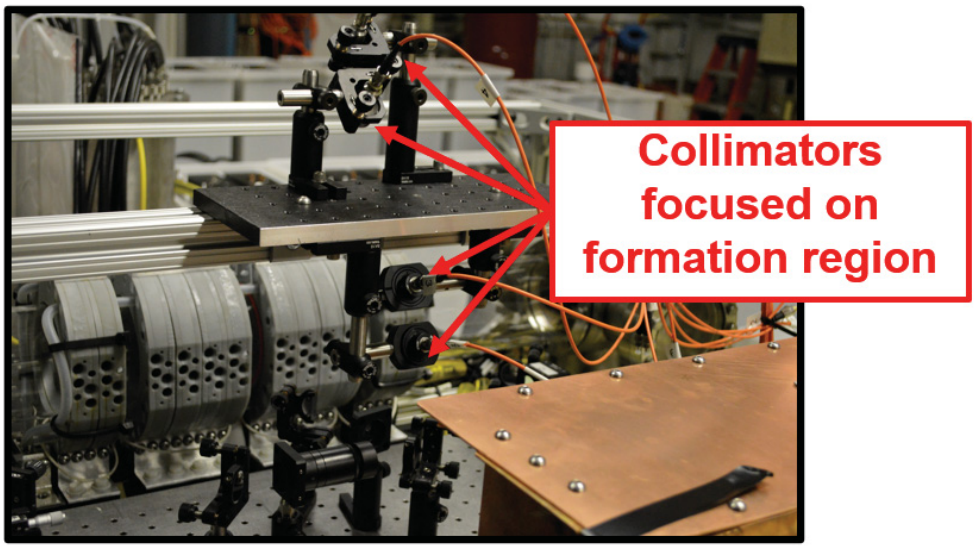

Figure 38: An array of collimators focused on the formation region that send light signals back to visible light diagnostics.

One of the signals is sent back to a broadband spectrometer for impurity detection (specifically a Thorlabs brand CCS100 with a bandwidth range of 350-700 nm). During

deuterium studies, the spectrometer's collimator is fitted with a 650 nm low-pass filter in order to filter out H-α line emission. This is intended to allow for lower neutral density filtering and a higher chance of detecting impurtiy emission. All other signals discussed henceforth are sent to Menlo brand photodiodes, capable of detecting line in the wavelength range of 400-1000 nm with a frequency range of DC to 600 MHz (specifically model number: FPD610-FC-VIS). One of the collimators focused on the formation region and the collimator focused on the region between coils 3 and 4 use no wavelength dependent filtering and therefore send a full visible wavelength signal back. One of the collimators on the formation region uses a band-pass filter (660 $\pm$10 nm fwhm) to observe H-α line emission from the deuterium gas during breakdown. The final collimator focused on the formation region uses another band-pass filter (488 $\pm$10 nm fwhm) to observe H-β line emission. The ratio of line intensities of the H-α and H-β emission can be used to make temperature estimates in a plasma up to temperatures of approximately 10 eV. At this measurement is made in real time, measurement error is dependent on the rate of change of line intensity. For more details on how line-ratio temperature estimates are implemented in these studies, see appendix D ([24], [25], [26], [27], [28]).

The final visible light diagnostic used in these studies is a Hadland brand, UHSi24 high-speed imaging camera. The camera is used to take up to 12 sequential frames of images at frequencies in the range from 225 kHz to 2 MHz (the camera is capable of up to 200 MHz frequency). Exposure lengths used in these studies ranged from 50 to 200 ns. The camera is fitted with a Sigma brand, 50-500mm, 1:4-6.3 APO lens and sits approximately 15 ft away from the experiment and takes images down the axial line-of-sight of the formation chamber, as shown in figure 39.

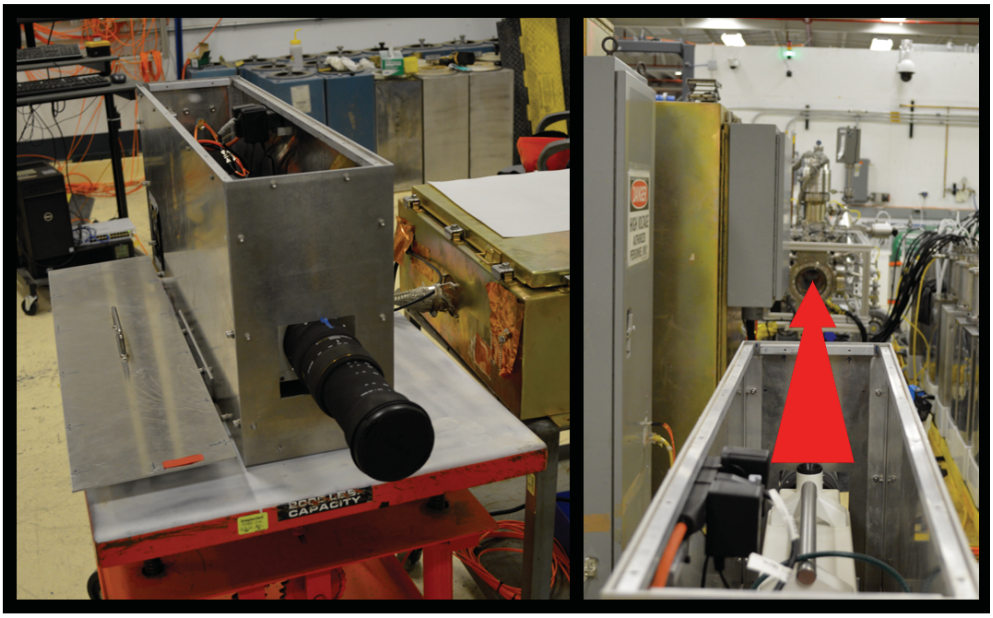

Figure 39: Left: A photo of the framing camera inside of its EMI enclosure (without the top on). Right: An annotated photo displaying the line-of-sight of the camera with regard to the formation chamber.

4.2.3 Polarization Interferometer

Ther interferometer used for these studies is the same style of interferometer design presented by Weber[29]. It is a homodyne interferometer which makes use of polarization state information from the interfered beams to solve the phase ambiguity problem. Effectively, one beam is split into two where one is passed through the plasma (the scene beam) and the other is not (the reference beam). Before recombintation, both beams are then polarized (to maximum signal strength) and rotated to a 45° polarization angle using $\lambda/2$ waveplates. At a 45° polarization angle each beam is effectively composed of a horizontal component ($\vec{p}$) and a vertical component ($\vec{s}$). The reference beam is passed through a $\lambda/4$ wave plate which phase shifts its $\vec{p}$ component by 90°. The two beams are then interfered and once again split using a polarizing beam splitter, each going to one photodiode. With this approach,

each photodiode sees a variation in the intensity of the combined beam but the intensity variations are 90° out of phase with one another. Thus, this approach resolves the phase ambiguity problem inherent in homodyne interferometers.

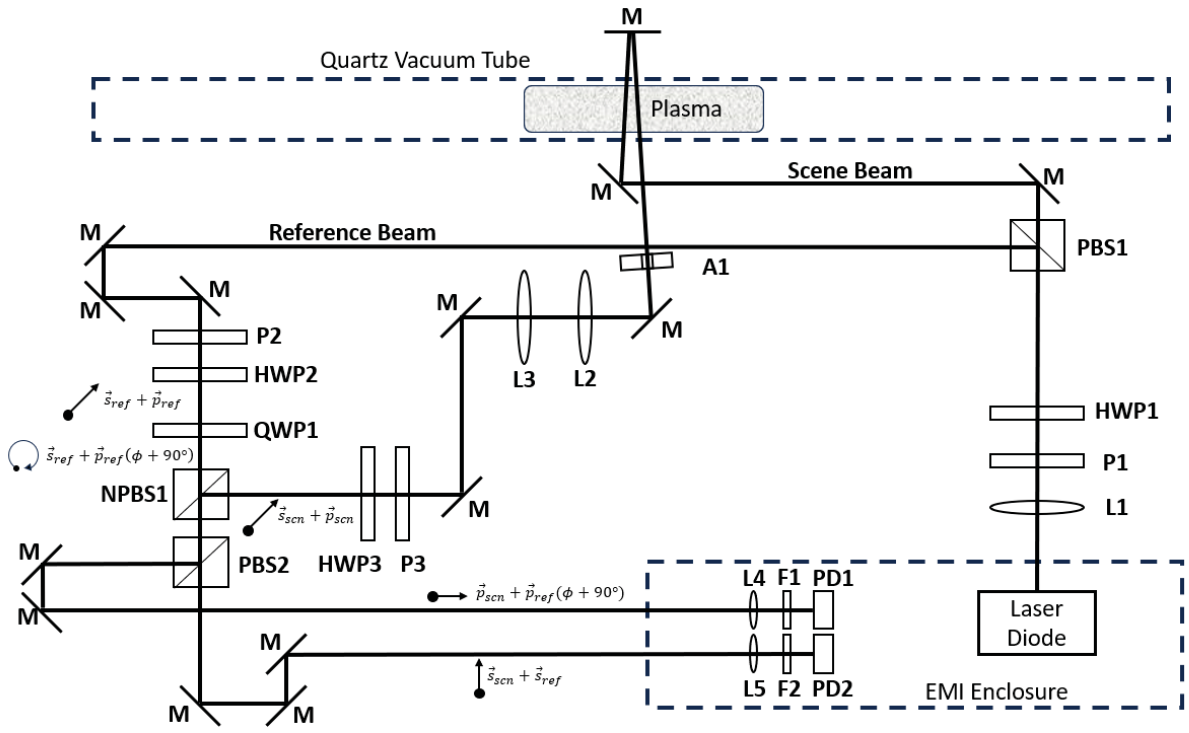

Figure 40: Diagram of the interferometer as it is used for these studies. L=Lens, P=Polarizer, HWP = half-wave-plate, PBS = polarizing beam splitter, M = mirror, A = aperture, QWP = quarter-wave-plate, NPBS = non-polarizing beam splitter, F = spectral filter, PD = photodetector

Figure 40 displays a diagram of how this interfermoeter is implemented for this study. Figure 41 shows an annotated photo of the diagnostic on the MTX machine. The laser source for this diagnostic is a Thorlabs model DJ532-10 laser diode which is housed in a Thorlabs model TCLDM9 laser diode mount. The detectors used (PD1 and PD2 in the diagram) are Thorlabs model DET10A photodiodes. During this study transimpedance amplifiers were installed in the EMI shield seen in figure 41 in order to boost signal and allow higher frequency measurements. The transimpedance amplifiers used were Femto model DHPCA-

100 devices. Figure 42 displays the expected sensitivity of this interferometer for the pressure ranges explored in this study. The relatively low sensitivity means that the interferometer is not able to measure small percentages of ionization for this study. Note that signficantly more detail is given on the physics, setup, error estimation, and post-processing of this diagnostic in appendix E ([30], [31], [32], [29], [33]). The line-integrated density measurement obtained using this diagnostic is expected to be accurate to better than 15%.

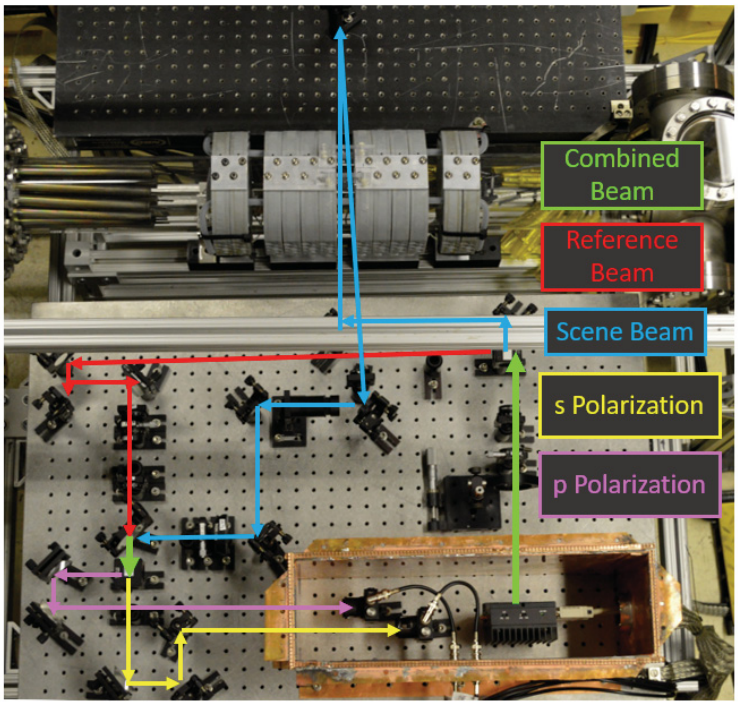

Figure 41: Top down view of the interferometer with various beam paths labeled.

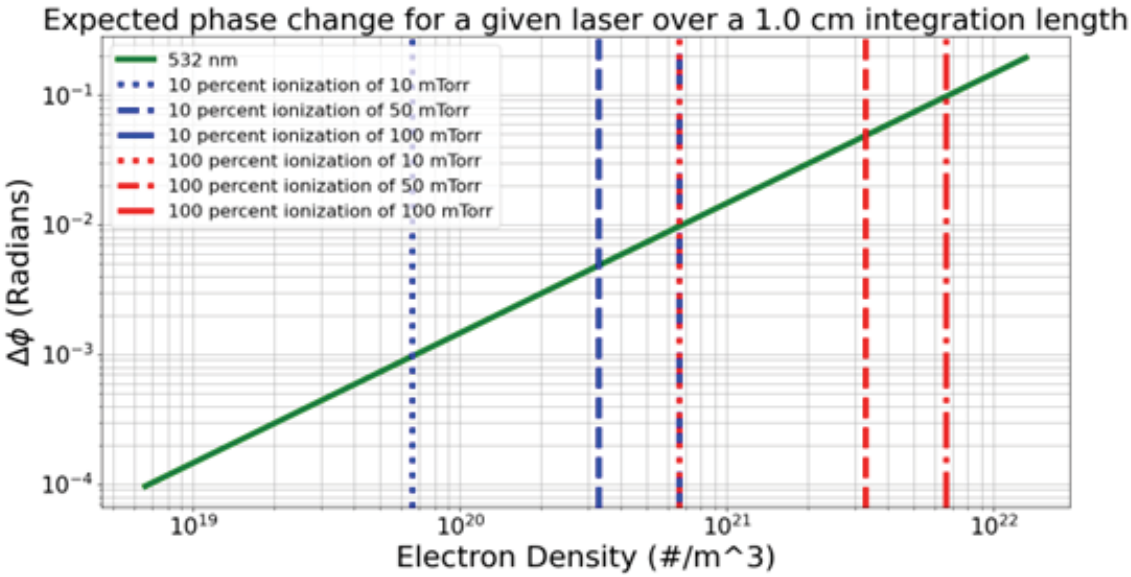

Figure 42: Expected beam phase difference vs. electron density in the pressure ranges explored in this study.

Chapter 5

Experimental Campaigns

The total set of experiments conducted in this study were comprised of three major portions. The first was a "field-mapping" campaign in which special frames and magnetic probes were created with the express purpose of accurately determining the strength and distribution of the magnetic fields produced by the MTX machine. This is one part of the information is necessary for the calculation of breakdown factors. The second was a "breakdown" campaign in which bulk data was collected regarding the field strengths and static pressures capable of causing both prompt and delayed breakdown. In cases where prompt breakdown was achieved, additional data was taken with tuned-in diagnostics to allow for calculation of breakdown factors. Finally, the "Flux Array" campaign was conducted, in which the flux array (discussed in section 4.2.1) was installed in order to compare the field-diffusion properties of both ringing-θ and biased dipole pre-ionization methods. Each of these campaigns is discussed in more detail below.

5.1 Field Mapping Campaign

Calculation of a breakdown factor requires both a measurement of the time at which breakdown occurred as well as accurate measurements of the magnetic field distribution in the system. A short campaign was performed to map out the fields produced by the MTX machine using $\dot{B}$-probes and 3-D printed frames to hold the probes in precise locations. The campaign consisted of two primary portions: The first set of shots maps out the field

strength and distribution of the four main θ-coils; the second set maps out the strength and distribution of the dipole coil.

The field mapping of both coil sets was performed using 5 $\dot{B}$-probes made specifically for this task (see figure 43). The probes were constructed by wrapping turns around a #10 bolt with a diameter of approximately 0.165" and had 12 turns of 26 AWG magnet wire. A twisted pair of approximately 0.5" length connects the probe to an RG-223 coaxial cable and metal braid soldered to the outer conductor of the cable extends over the twisted pair in order to reduce noise pickup. All 5 of the probes used were constructed in this fashion and have an average inductance of about 190 nH with an average calibrated area-turns factor of approximately $1.6 * 10^{-4}$ m^2. The calibration was no worse than 5% accurate. Note that general shot-to-shot variance was found to be less than 3% in terms of field strength.

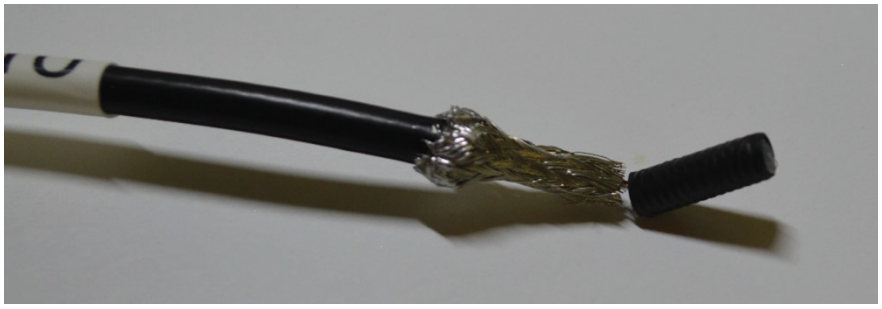

Figure 43: Photo of one of the $\dot{B}$-probes used in the field mapping campaign.

5.1.1 θ-Coil Field Mapping

In order to better understand the field strength and distribution produced by the main banks of the system (bias, reversal, and cusp banks) a short campaign of shots was performed with different combinations of firing banks to determine the field strengths and distributions of the 2-formation/2-cusp coil system. The two primary locations of intersest are the center of the formation chamber between coils 2 and 3 (see figure 44) and the field null point

between coils 3 and 4. Note that the separation between all coils is measured as 1".

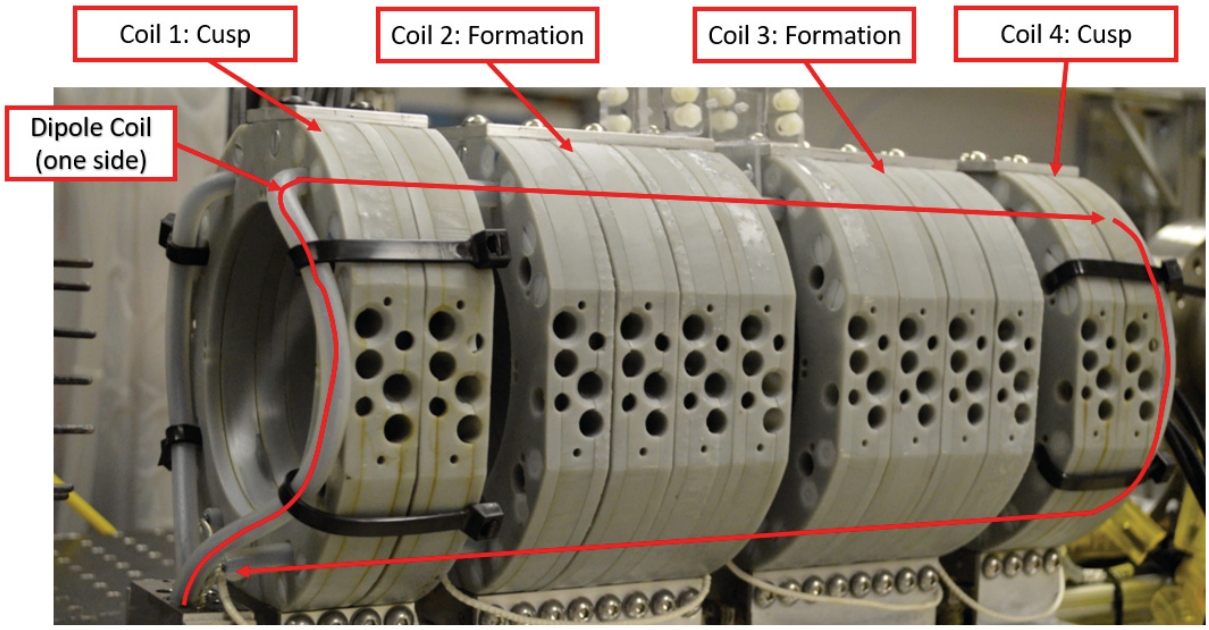

Figure 44: Annotated photo of the MTX coil set.

A 3-D printed probe frame was designed with the intention of measuring axial field strength at multiple radial and azimuthal locations. Figure 45 displays two different pictures of the probe-frame, labeling out the points where the probes are held. Figure 46 is a diagram of the probe frame showing the dimensions for the radial and axial locations for the probes during the shots.

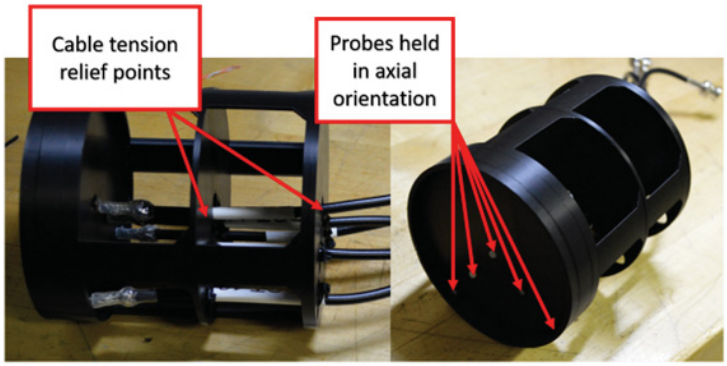

Figure 45: Annotated photo of 3-D printed probe frame used to map θ-coil field distribution

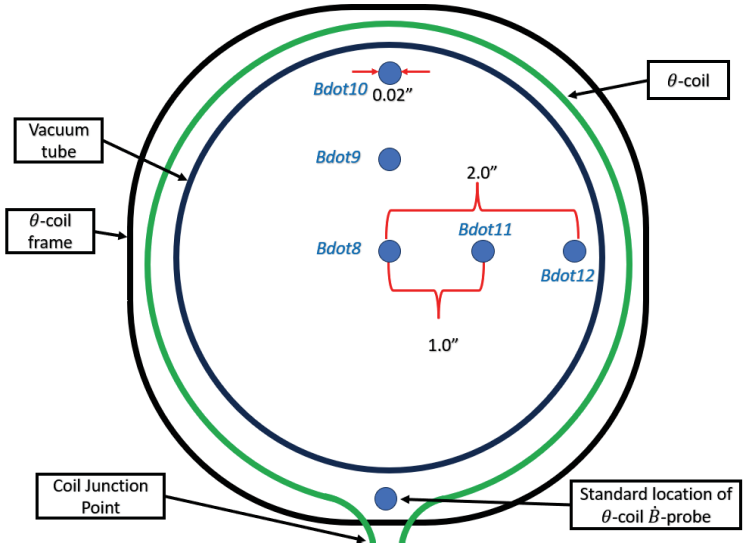

Figure 46: Diagram of the θ-coil field mapping probe frame.

Four primary axial positions were surveyed; the center of the formation chamber between coils 2 and 3, the center of coil 3, the mid-point between coils 3 and 4, and the center of coil 4. See figure 44 above for context on these four locations. At each primary position, the bias banks, cusp banks, and reversal banks were all fired individually as well as a combination of the bias with cusp, and finally firing the bias, cusp, and reversal banks all together. Thus five separate shots were performed for each primary axial location. Additional shots

were taken to locate the field null between coils 3 and 4 which only fired the bias and cusp banks. Only the data from the above campaign relevant to this study is presented here.

The first set of shots explored the azimuthal field symmetry in the center of the formation chamber between coils 2 and 3. Thus, the $\dot{B}$-probe frame was rotated 90° clockwise relative to figure 46 so that $\dot{B}$-12 was measuring the field strength closest to the θ-coil junction point (note that all other shots in this study were performed with the probe orientation as shown in figure 46). Inspection of the data shown in figure 47 revealed an azimuthal variation of approximately 10% from the coil junction to a position 90° off. Azimuthal variation between 90° and 180° off of the coil junction was found to be negligible. Azimuthal variation in field strength at the 1" radius measuements ($\dot{B}$-probes 9 and 11) was found to be less than 3%.

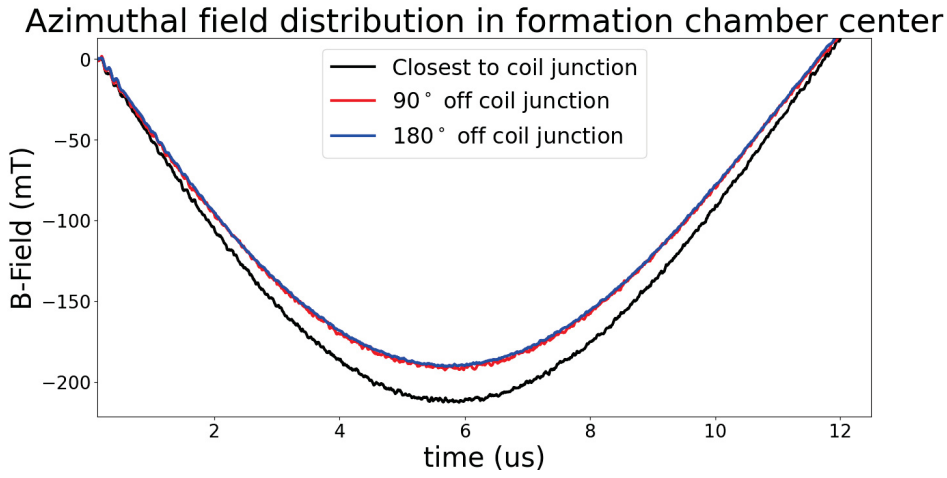

Figure 47: Plot showing azimuthal asymmetry of field distribution in the formation chamber.

A series of shots were also performed to locate the field null point between coils 3 and 4. Figure 48 presents the magnetic field strength at the radial center of the θ-coils for several axial positions between coils 3 and 4. The data shows a field null point slightly closer to coil 3 than coil 4, which makes sense due to coil 4's tendency to produce a denser magnetic field

than coil 3. This yields an overall length of the formation chamber of approximately 9.5” or 24 cm.

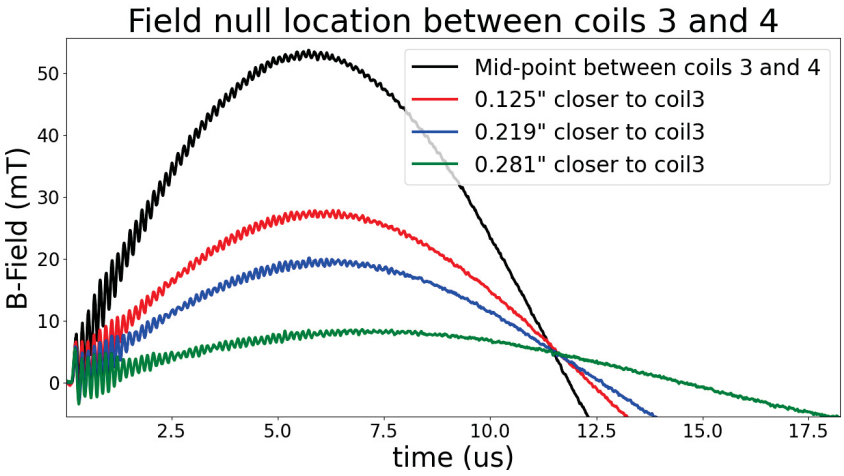

Figure 48: Plot displaying measurements used to determine the location of the field null between coils 3 and 4.

The field distribution between coils 2 and 3 was found to be signficantly different when compared to the field distribution in the axial center of coil 3. Figure 49 shows that while magnetic field strength tends to increase with increasing radius inside the axial center of coil 3, the field strength tends to decrease with increasing radius in the formation chamber center. This is due to the 1” gap between coils 2 and 3 left for diagnostic access.

In calculation of the breakdown factor, it is reasonable to use an average field strength determined from these measurements. Using a partially quadratic fit as shown in figure 50, an average field strength of 0.227 mT is determined. This is a factor of 0.778 off of the measurement made by $\dot{B}$-3, which is installed in the axial center of coil 3 near the coil junction point as shown in figure 46. Thus, in calculation of breakdown factors, field strengths are determined using this factor applied to the measurement of $\dot{B}$-3.

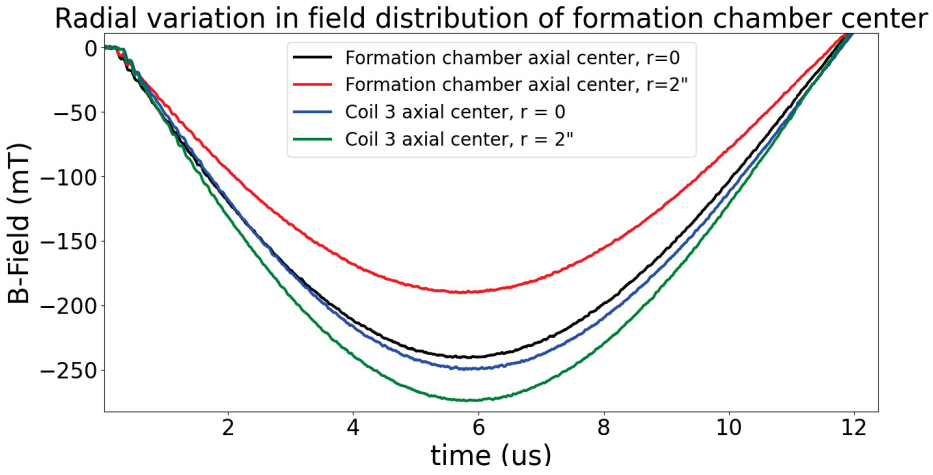

Figure 49: Plot displaying the difference in radial field distribution between the formation chamber center and the axial center of coil 3.

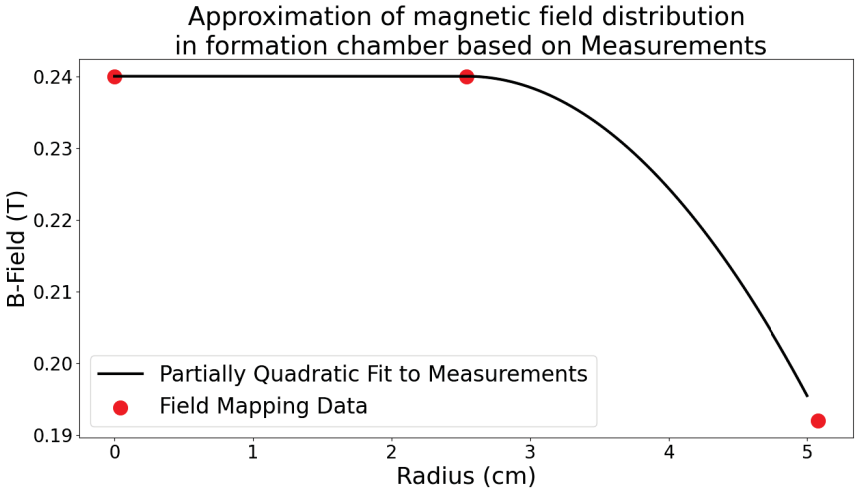

Figure 50: Plot displaying partially quadratic fit to the field mapping measurements of radial field distribution in the center of the formation chamber.

It should be noted here that the off-set placement of the flux loop (as seen in figure 27 in section 4.2.1), causes more flux to pass through the flux loop than if it were placed at the exact center of the formation chamber where these field mapping measurements take place. Measurements of the flux loop in this campaign display a consistent factor of 1.3 higher

flux measured by the flux loop than is estimated using the field distribution approximation shown in figure 50. This information is needed to properly understand results from the flux array campaign analyzed in section 6.3.1.

5.1.2 Dipole Coil Field Mapping

The mapping of the dipole coil's field distribution was performed using the 3-D printed frame shown in figure 51. A diagram of the probe's positions within the frame is shown in figure 52. Shot-to-shot variance in field strength measurements was again found to measure less than 3% difference.

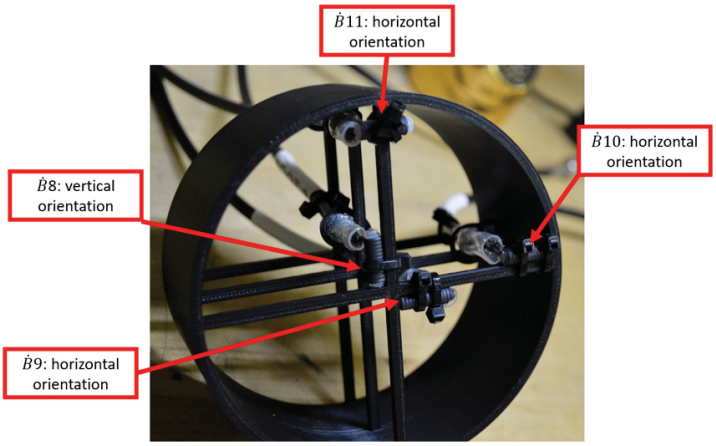

Figure 51: Annotated photo of the frame and probe positioning used to map the dipole coil's field distribution.

Figure 53 shows measurements taken the radial center of the tube in different axial positions. The measurements indicate that the dipole coil's field strength does not vary signficantly within the foramtion region. A simple Biot-Savart approximated field solver (distribution seen in figure 54) was compared to the measured field strengths (scaled to the measurement at the center of the chamber) and was found to provide reasonable agreement

(within 5%) as shown in figure 55. Thus, using the Rogowski coil on the dipole coil (accurate to within 10% as described in section 4.2.1), the field strength generated by the dipole coil in the system can be determined.

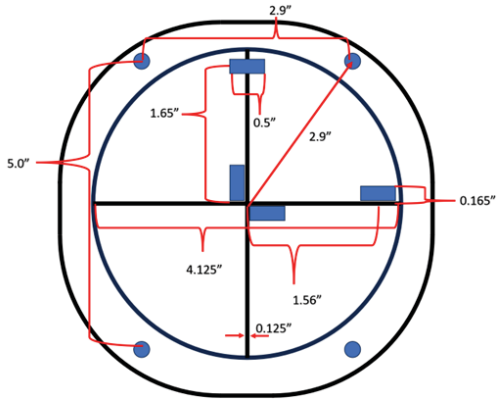

Figure 52: Diagram of probe positioning used for mapping the dipole coil's field distribution.

Using the these measurements and a Biot-Savart approximation, an average field strength of 105 mT for a 20 kV discharge and an average field strength of 215 mT were determined. Note that these values are higher than the measurements depicted in figure 55 due to the fact that the pre-ionization capacitor bank was changed early in the data gathering campaigns. This change is discussed in more detail in section 5.2.

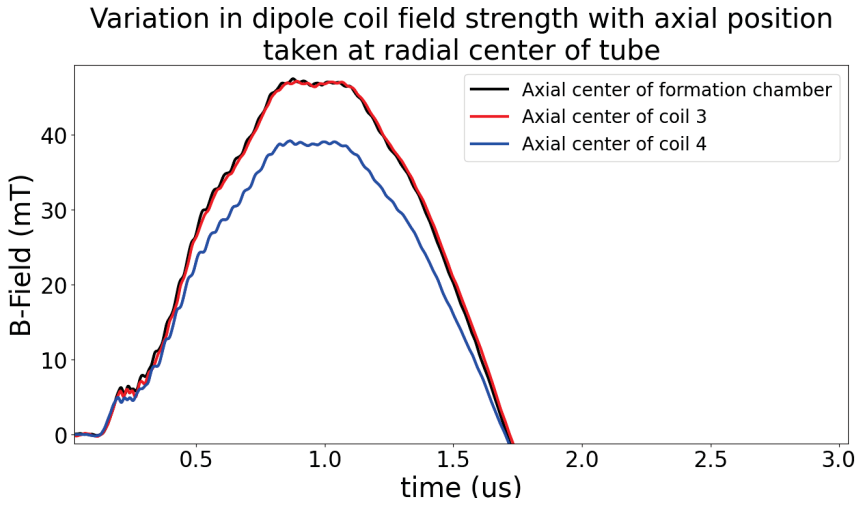

Figure 53: Plot displaying the variation of transverse field strength of the dipole coil at various axial locations.

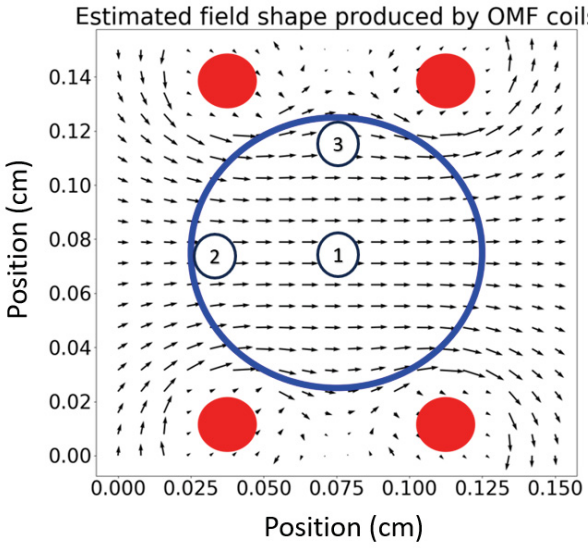

Figure 54: Plot of a Biot-Savart approximated dipole coil field with labeled measurement positions. $\dot{B}$-9 is at location 1, $\dot{B}$-10 is at location 2, and $\dot{B}$-11 is at location 3. for the measurements shown in figure 55.

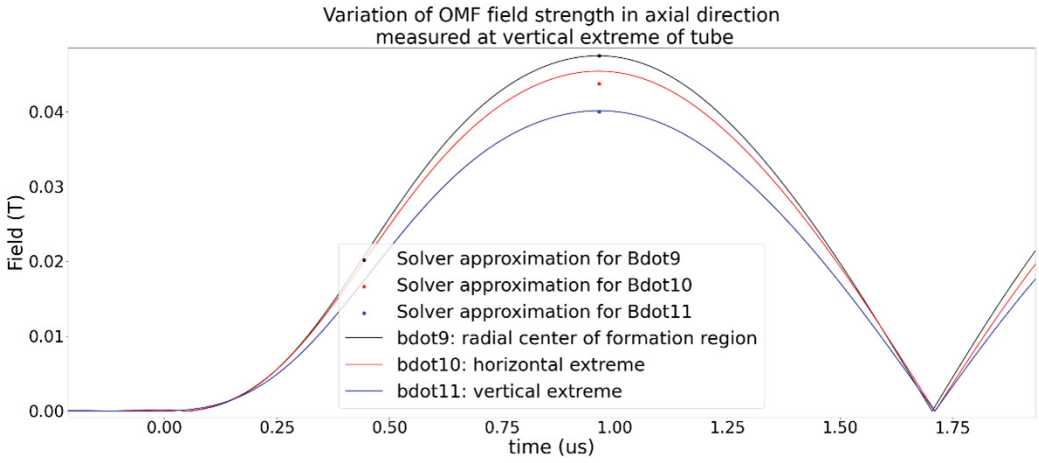

Figure 55: Plot comparing measured field strengths to those predicted by the Biot-Savart approximation.

5.1.3 Field Mapping Campaign Summary

Precise measurements were taken of the field strengths and distributions of the θ-coils and dipole coil so that accurate field strength values could be used in calculation of breakdown factors for the breakdown campaign (see section 5.2).

The θ-coils were found to vary less than 10% in strength azimuthally and the radial field distribution in the formation chamber center was measured and can be reasonably approximated with a partially quadratic fit. The functional length of the formation region was found to extend just past the formation coils for a total length of approximately 9.5" or 24 cm. Given the known accuracy of the $\dot{B}$-probes, the shot-to-shot variance, and the estimated error in the partially quadratic fit, the overall error in the measured field strength used to calculate breakdown factors can be considered no worse than 10% accurate.

The dipole coil's field distribution was found to vary negligibly within the formation region and a simple Biot-Savart field approximation was shown to predict the field accurately

within 5%. Given the known accuracy of the $\dot{B}$-probes and the Rogowski coil that will be used to measure current in the dipole coil, the overall error in the field strength used to calculate breakdown factors can be considered no worse than 15% accurate.

Measurements were combined with calculation and basic simulation to determine average magnetic field strengths for the purpose of calculating electric field strengths for breakdown factors.

5.2 Breakdown Campaign

The purpose of the breakdown campaign was to record data on what conditions yielded prompt breakdown, delayed breakdown, and no breakdown at all. Deuterium gas and Helium gas in a range of 25-100 mTorr were studied for this purpose. Four primary field configurations relevant to breakdown were identified and studied on the MTX system. The first was the θ-pinch as described in section 3.6. The second and third configurations that can be studied are the unbiased dipole and the biased dipole (note that the breakdown model is the same between these two conditions because the induced electric field is aligned with the bias field as discussed in section 3.5). The final configuration is the ringing-θ, as discussed in section 3.4.

As stated in section 3.6, it was discovered that discharging of the bias and cusp fields on MTX produced ionization in deuterium gas. Thus, the unbiased dipole and θ-pinch configurations are the only ones that can be studied on MTX without seed ionization which means that the biased-dipole and ringing-θ configurations cannot be studied without seed ionization. Therefore, the two primary categories of study are seeded breakdown and unseeded breakdown.

In initial testing it was seen with spectrometer data that impurity presence tended to

decrease over a number of discharges of the reversal bank. Figure 56 shows this tendency of decreasing impurity presence with repeated shots. Note that the sharp line around 486 nm represents the H-β line, which is expected for breakdown of deuterium gas (recall from section 4.2.2 that the spectrometer was fitted with a 650 nm low pass filter to block reception of H-α emission). For the campaigns discussed here where data was collected, impurity line strengths comparable to H-β emission were not detected using the wideband spectrometer.

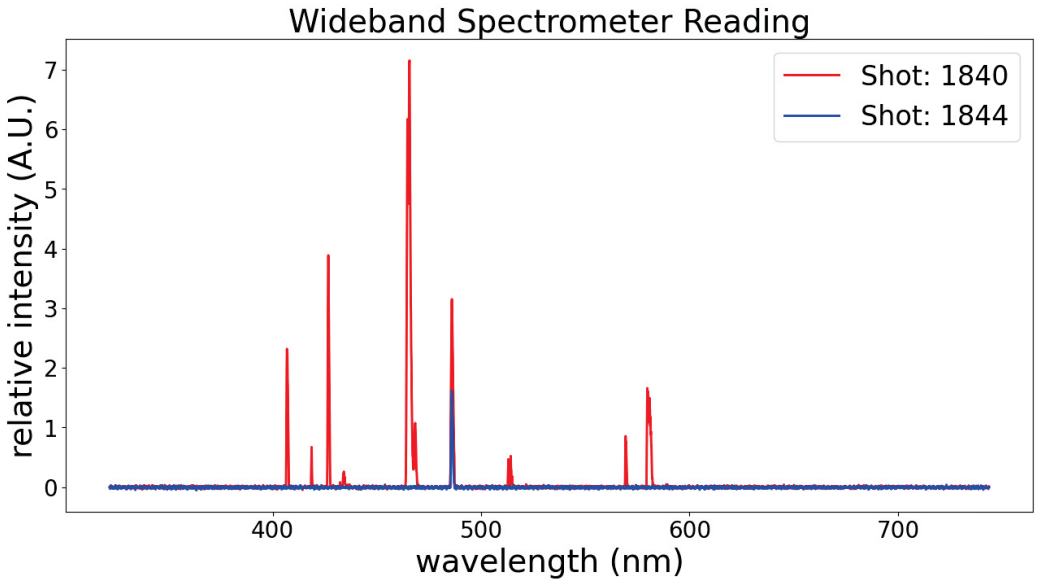

Figure 56: Comparison of impurity lines detected in earlier vs. later discharges as measured by the wideband spectrometer.

5.2.1 Breakdown Campaign Parameters

The parameters of each bank are summarized in table 3. Note that these values are averaged over the tube area, as determined by the field mapping campaign discussed in section 5.1. To gather data for the unbiased dipole configuration, only the dipole bank would be fired and allowed to ring down naturally. For biased dipole data either the bias

alone or the bias and cusp would be fired and crowbarred close to peak field strength (4.6 μs) to provide a background field. The dipole bank would then be fired at 10 μs into a tube-area-averaged background field strength of approximately 162 mT and allowed to ring down naturally. To gather θ-pinch breakdown data firing of the bias banks alone was sufficient for Deuterium studies. Prompt breakdown could not be achieved in helium using the any of the banks for an unseeded configuration. Finally, ringing-θ data was gathered by firing both bias and cusp banks and crowbarring them at 4.6 μs. The reversal banks would also be fired at 4.6 μs and allowed to ring down naturally. Note that ringing-θ data was only taken at one set of bank voltages (specifically the upper ranges of the cusp/bias banksand the lower range of the reversal bank) as these were the only available settings that allowed for a ringing-θ profile with a small 0 crossing as used in previous FRC experiments (see section 2.2).

Table 3: This table summarizes the bank parameters. Note that the magnetic field values presented are the tube-area-averaged field strength.

Bank parameters for breakdown studies			
Bank	**Voltage Range (kV)**	**Field Range (mT)**	**Frequency (kHz)**
Cusp	10 to 20	150 to 300	43
Bias	10 to 20	-110 to -225	43
Reversal	20 to 40	300 to 600	320
Dipole	20 to 40	105 to 215	140

Early on in the campaign it was found that the bank powering the dipole coil was insufficient to cause breakdown. It originally consisted of a bank with 160 nF, an overall inductance of 1.25 μH, and a discharge frequency of 350 kHz. This bank was swapped out with a Scyllac style capacitor with a capacitance of 1.36 μF. This also lowered inductance by 1/3 to a value of 800 nH and the discharge frequency decreased to 140 kHz. Do note that table 3 lists the new bank parameters as this was the bank used for all data presented

in later sections. Note that for a simple discharging capacitor bank the rate of change of current is dependent only on the capacitor voltage and discharge inductance so that, $\frac{dI}{dt} = \frac{V}{L}$. Further, since $E \propto \frac{dB}{dt} \propto \frac{dI}{dt}$, it can be inferred that this bank change increased the initial induced electric field strength by roughly 30%.

Using the bank parameters and configurations discussed henceforth, Deuterium and Helium gas were swept through pressures from 25-100 mTorr. Photodiodes and the high-speed imaging camera were the primary diagnostics used to determine if breakdown had occurred during a shot. It is important to find the minimum conditions (field strengths and pressures) capable of causing breakdown so that minimum requirements can be identified for the design of inductively-coupled ionization systems. To do this, a series of approximately 250 shot sequences were performed to establish general baselines for which conditions yielded prompt, delayed, or no breakdown. Once these baselines had been established, another series of approximately 100 shots were performed in order to find minimum breakdown conditions for the four primary configurations. These later shots comprise the bulk of the data that is analyzed in section 6.1.

5.2.2 Breakdown Factor Calculation

For all conditions except θ-pinch, breakdown factor was calculated in the following fashion. A signal from the visible light photodiode aimed at the center of the formation chamber that was above the noise level was taken to be the presence of breakdown. The time at which the system fired was determined from either $\dot{B}$-probes for θ-coil discharges or the dipole coil's Rogowski probe for dipole discharges. An example of these traces for an unbiased dipole shot can be seen in figure 57. Since this was a dipole discharge, breakdown factor was then calculated using equation 3.5.9. Breakdown timing was determined as the

difference between the photodiode signal and the fire time of the dipole bank as shown by the Rogowski signal. Magnetic field strength was determined using the field mapping information discussed in section 5.1.2.

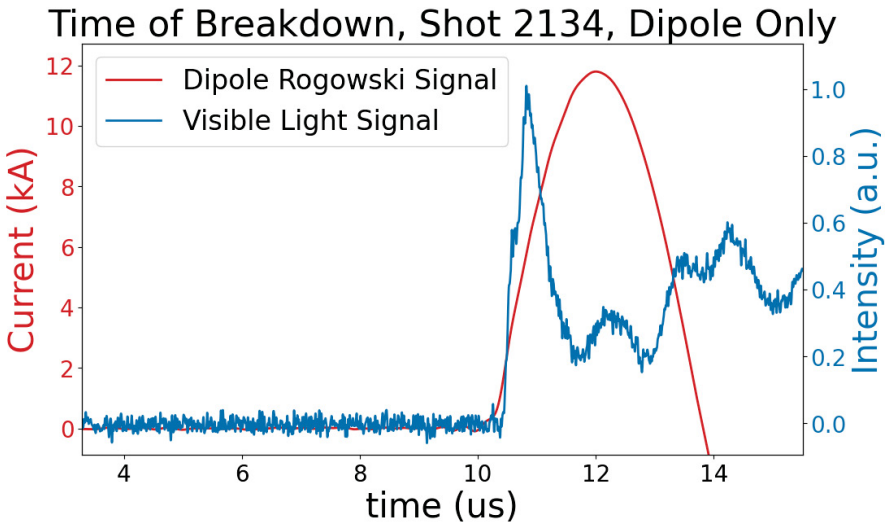

Figure 57: Plot that shows fire timing of dipole coil relative to the time at which breakdown occurred. This was done with Deuterium gas at 100 mTorr, and the dipole coil discharging at its minimum field strength.

In the case of θ-pinch discharges, the light signal was generally too weak to be picked up by photodiodes except in a few cases. Therefore, the high-speed imaging camera was the primary diagnostic used to determine breakdown timing, albeit with less time resolution than the photodiodes. Figure 58 displays photodiode signals for a θ-pinch discharge in 100 mTorr of Deuterium. Here, a small signal can be seen in the formation chamber and no signal is detected in the cusp region (between coils 3 and 4). Further, the timing of the high-speed imaging camera is overlayed on the plot. The images taken by the camera can be seen in figure 59 and show plasma in the same time that signal is seen by the photodiode (note that no light was seen in frames prior to the one shown in figure 59). This is an important

distinction as in all other configuration tested, breakdown first occurs in the cusp region so that the high-speed imaging camera cannot be used for prompt breakdown detection in the center of the formation region. Thus, for all θ-pinch prompt breakdown studies, the high-speed imaging camera is used for determination of breakdown timing.

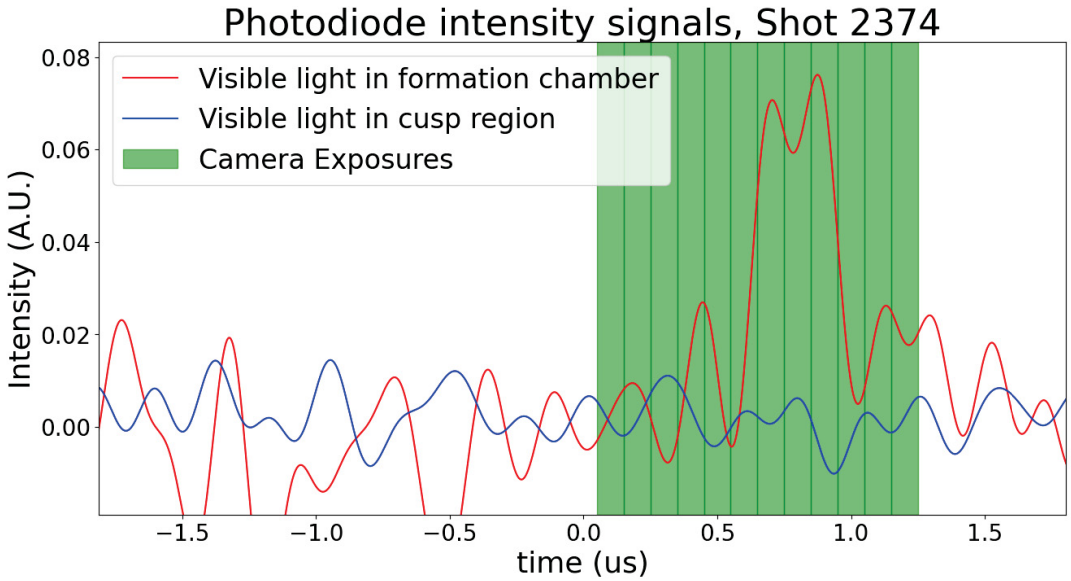

Figure 58: Plot showing photodiode traces of a θ-pinch discharge in 100 mTorr D_2 overlayed with timing of the high-speed imaging camera.

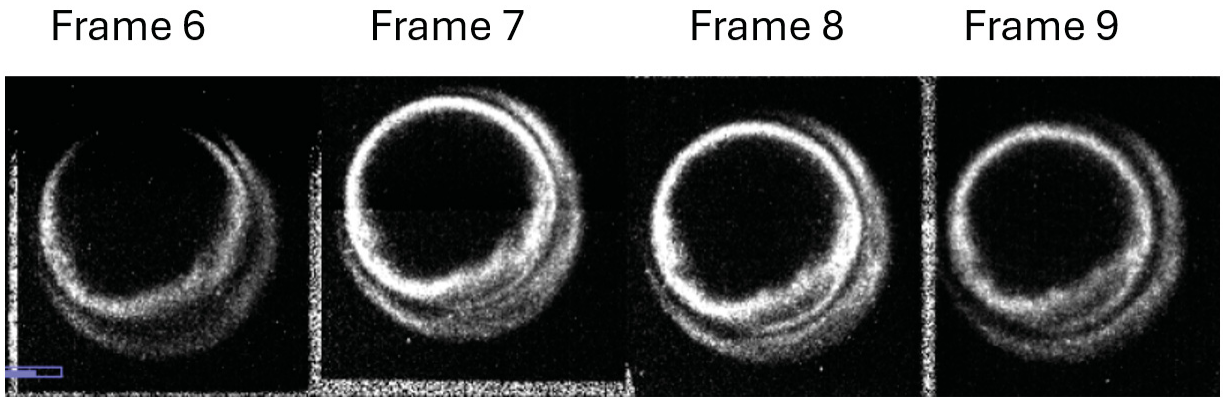

Figure 59: Frames obtained by the high-speed imaging camera, show existence of plasma that coincides with the photodiode signal shown in figure 58.

5.3 Flux Array Campaign

The primary purpose of the flux array campaign was to study flux diffusion in the biased dipole and ringing-θ configurations, as these are the configurations most applicable to FRC pre-ionization. Additional parameters of interest include the plasma density, plasma temperature, and overall flux as measured by the external flux loop. Using table 3 as a reference, the biased dipole shots were performed by firing the bias and cusp banks at their peak field strengths and crowbarring them at 4.6 μs. The dipole coil was then fired at 10 μs and allowed to ring down naturally. For a ringing-θ shot, the bias and cusp banks were fired at their peak field strengths and crowbarring them at 4.6 μs. The reversal bank was then fired and allowed to ring down naturally. Data was gathered using these two configurations with the flux array installed for pressures of 25, 50, and 100 mTorr using Deuterium and helium gas.

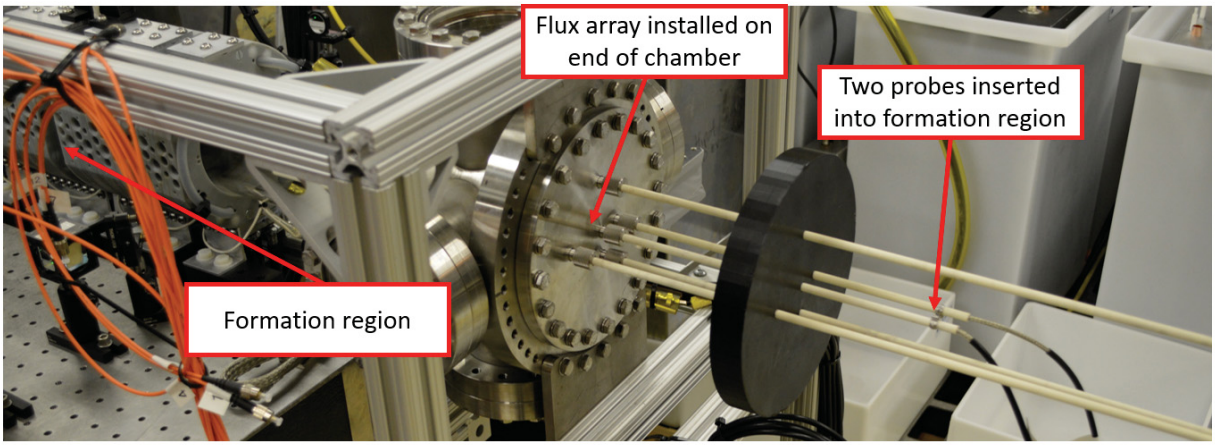

Figure 60: Annotated photo of the flux array installed on the MTX machine.

For the flux array campaign, the flux array (see section 4.2.1 for details) was installed in the main chamber as seen in figure 60. This precluded the use of the high-speed imaging

camera as the flux array blocks its line-of-sight. Measurements from the external $\dot{B}$-probes and flux loop in the formation chamber were observed to not be affected by the presence of the flux array when vacuum and plasma shots were compared. However, measurements from the photodiodes and the interferometer were seen to be significantly affected during the ringdown of both the biased dipole and ringing-θ configurations. Figure 61 depicts an example of this where peak values of the ringing-θ compressions are signficantly higher in the presence of the flux array. The same tendency was seen with photodiodes measurements so that neither accurate measurement of light or integrated line density can be done during the ringdown of either configuration. However, figure 61 also shows overlapping density values after the ringdown phase, which is the primary region of interest because this is where a the reversal field would most likely be fired to form an FRC. Therefore, light based measurements may still be considered useful after the ringdown phase for comparisons of interest.

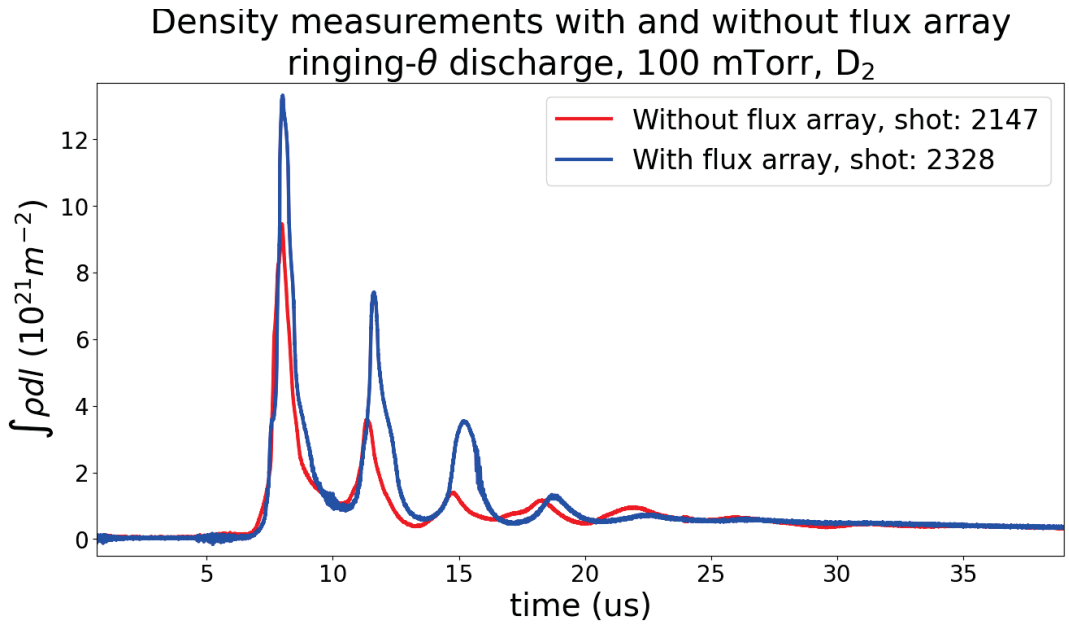

Figure 61: Plot comparing interferometer traces with and without the flux array installed.

Chapter 6

Analysis

First, the results of the breakdown studies are presented, detailing the conditions in which prompt breakdown could be achieved and how the expectations set forth by the prompt breakdown models compare to the experimental results. The effects of seed ionization are analyzed within the context of breakdown factors and how breakdown requirements are affected. Then, the observed conditions for which prompt and delayed breakdown are tabulated for use in future pre-ionization system design. Finally, measurements of the ringing-θ and biased dipole pre-ionization configurations are compared and contrasted to determine benefits and/or drawbacks between the two methods.

6.1 Prompt Breakdown Results

The θ-pinch and unbiased dipole breakdown experiments conducted on MTX were unassisted by seed ionization and therefore represent pure case studies on breakdown of gases by inductively coupled fields. The biased dipole and ringing-θ configuration, however, are both seeded by the firing of the bias and cusp fields prior to the primary discharge. Table 4 summarizes this. It will be seen in the analysis that the presence of seed ionization significantly affects breakdown properties. Therefore, it is better to analyze them separately before direct comparison with seeded conditions. As a final note, the minimum field conditions required to cause prompt breakdown are generally the most interesting for system design purposes, so the study was primarily focused on identifying these conditions. Identification of these

conditions generally required tuning in optical diagnostics, which was a time consuming process. Therefore, data on breakdown at higher-than-necessary field conditions is generally not explored for prompt breakdown.

Table 4: Four primary conditions are analyzed. This table displays which cases are unseeded and which cases are seeded.

Unseeded	**Seeded**
unbiased dipole	biased dipole
θ-pinch	ringing-θ

6.1.1 Unseeded Breakdown

The unbiased dipole tests consist simply of firing the pre-ionization bank through the dipole coil (see figure 44) without any other banks, which produced a transverse field through the tube area. The θ-pinch tests performed consisted of firing only the bias banks through the two central formation coils (coils 2 and 3 as shown in figure 44). See sections 5.1.2 and 5.1.1 for details on field mapping on both of these configurations, respectively. Since both of these configurations are fired independent of any other systems, they represent case studies of unseeded breakdown testing and are thus analyzed prior to seeded conditions.

Unbiased Dipole Analysis

The unbiased dipole tests consisted of firing the dipole coil with an area-averaged field range of 105-215 mT (corresponding to 20 and 40 kV bank charge, respectively) at a discharge frequency of 140 kHz. Section 5.1.2 gives explicit field mapping details. First, it is noted that minimum field requirements for prompt breakdown of 25 mTorr D_2 gas for the unbiased dipole configuration could not be established as the maximum field settings were incapable of

causing prompt breakdown. Further, this configuration could not cause prompt breakdown of helium at any pressure.

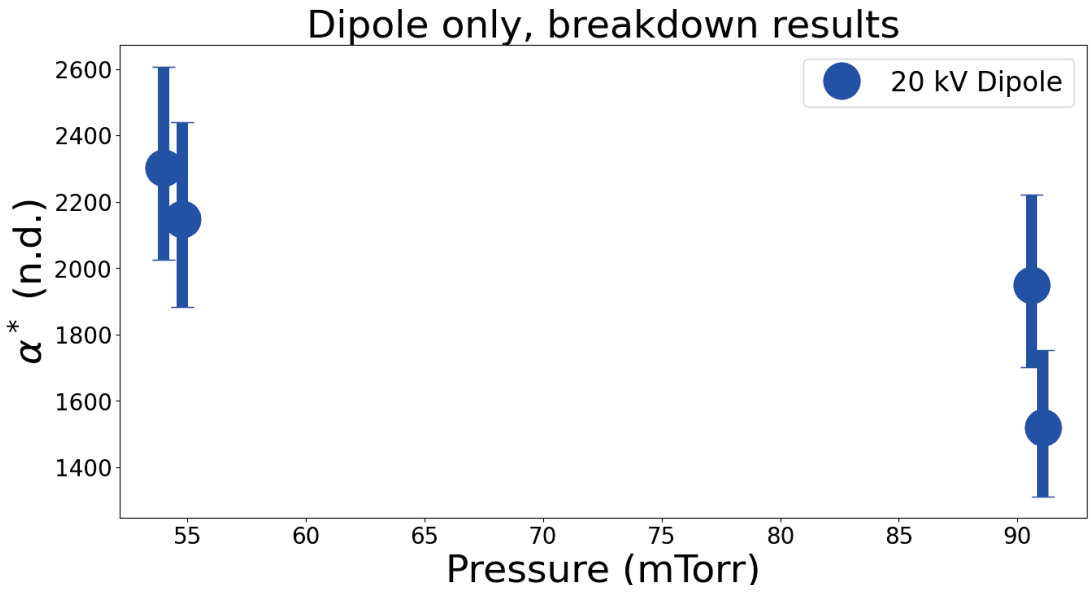

Figure 62: Plot displaying measured breakdown factors for the unseeded dipole configuration.

Figure 62 displays the breakdown factors measured using a 20 kV charge on the dipole coil for D_2 gas. First, it is noted that the measured breakdown factors are much greater than unity ($\alpha^* >> 1$). Further, lower breakdown factors are measured at higher pressures. These general results are both consistent with model expectations. Figure 63 shows the "null" data points at 25 mTorr. Although prompt breakdown could not be achieved, these points on the plot display the theoretical breakdown factor that the system is capable of at its defined maximum of 1/8th the cycle time (900 ns in this case). This strongly implies an exponential dependence of field strength requirements on gas pressure, which is also consistent with model expectations.

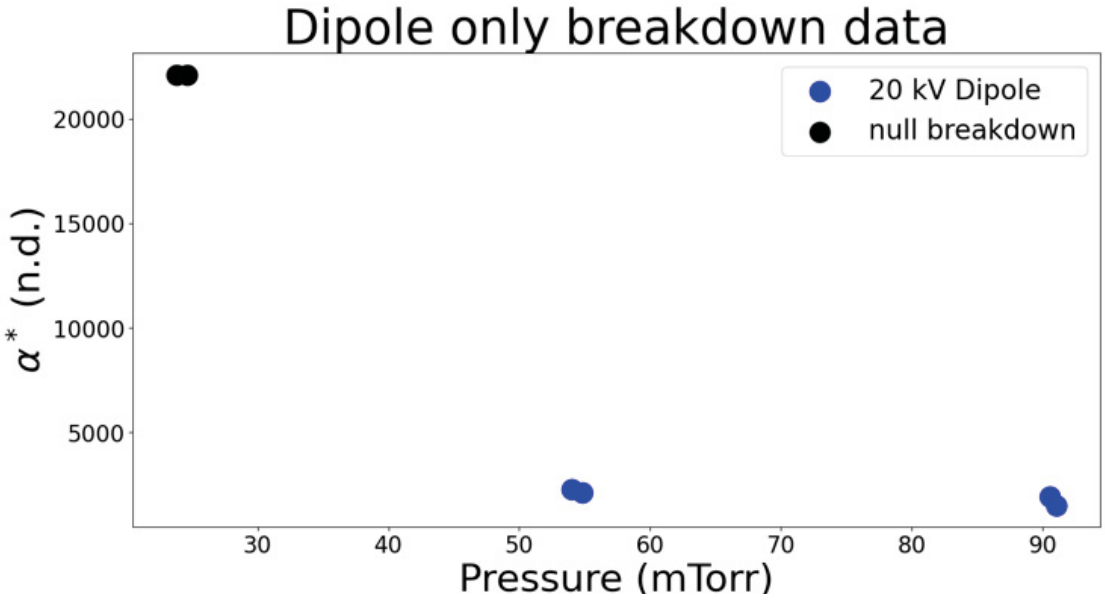

Figure 63: Plot displaying measured breakdown factors for the unseeded dipole configuration.

θ-Pinch Analysis

The θ-pinch discharges were formed by firing the bias banks into coils 2 and 3 as shown in figure 44. The tube-area-averaged field strength varied from 110-225 mT (corresponding to 10 and 20 kV bank charge, respectively) at a discharge frequency of 43 kHz. Section 5.1.1 gives explicit details on field mapping. Similar to the unbiased dipole results, prompt breakdown could not be achieved in D_2 at 25 mTorr or in helium at any pressure using the maximum range of the bias banks. Note that the data presented here was obtained using the high-speed imaging camera as discussed in section 5.2.2. Therefore, this data is obtained with a lower temporal resolution than other configurations and is subject to higher overall error.

Discharges of 225 mT (20 kV charge on the bias banks) into the formation coils resulted in consistent prompt breakdown at 100 mTorr and 50 mTorr, albeit with higher variance

than seen in the unbiased dipole results above. Discharges of 170 mT (15 kV charge on the bias banks) achieved prompt breakdown in approximately 50% of shots (delayed breakdown was seen in the other 50%). Figure 64 summarizes these results.

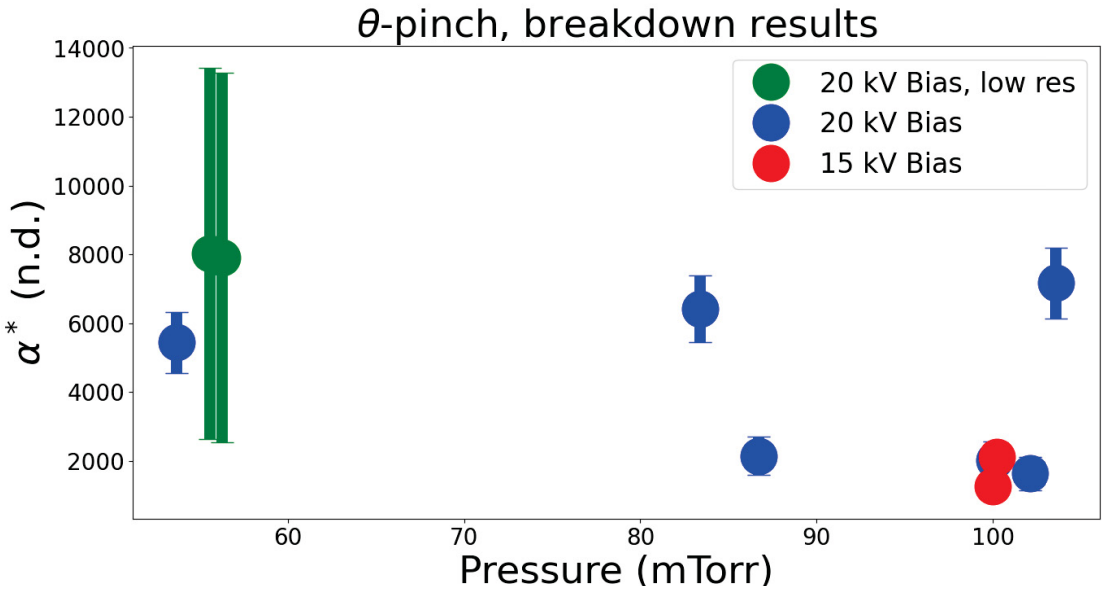

Figure 64: Plot displaying measured breakdown factors for the θ-pinch configuration.

The fact that the 15 kV bias discharge did not break down consistently indicates that this condition is close to the absolute minimum field requirement to cause prompt breakdown. Further, prompt breakdown could not be achieved with a 15 kV bias discharge at 50 mTorr despite the fact that it is capable of injecting the same amount of energy that caused breakdown at the 20 kV charge. This implies that rate of energy injection (i.e., power) becomes an important factor, which then implies the assumption that the recombination rate is negligible may be violated at this condition. However, it is worth noting that breakdown factors overlap at the 100 mTorr condition indicating that the model is working as intended in these specific conditions.

The higher variance in the θ-pinch breakdown factors can be analyzed more closely

using the Boris Pusher algorithm discussed at the beginning of chapter 3. Using a starting point near the tube edge (4 cm radius) and simulating its path for 50 ns, it is seen that an electron under the influence of a 225 mT θ-pinch discharge at 43 kHz will be pulled in radially as shown in figure 65 below. Here it is seen that the electric field does not accelerate electrons out of this system in this configuration, unlike all other configurations tested in this study, so that free electrons will only be lost on timescales relative to thermal velocity. This could be why a higher variance is seen in breakdown factor for the θ-pinch, since electrons are confined longer and therefore have a longer chance to interact and impart energy to the gas through collisions.

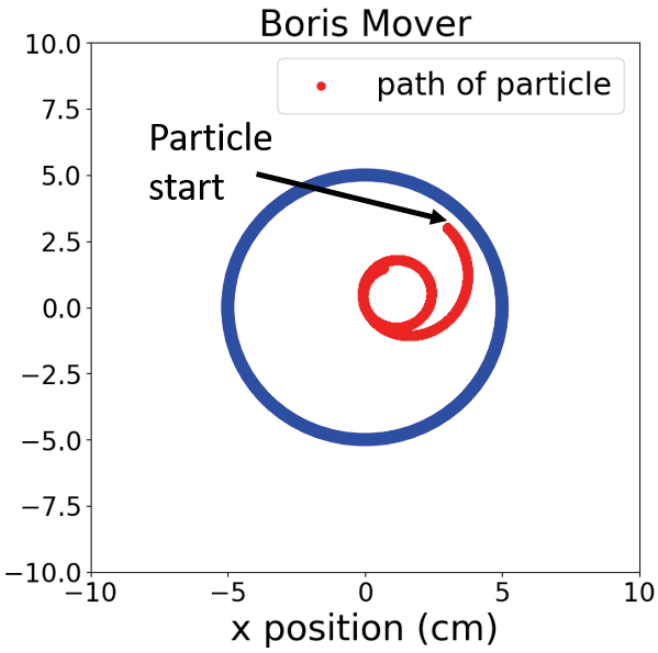

Figure 65: Plot displaying the path of an electron in a bias discharge (225 mT peak field at 43 kHz) simulated using a boris pusher.

Overall, the higher variance makes it more challenging to pull specific conclusions from this data, but there does seem to be a general decreasing trend in breakdown factor as pressure increases. The fact that 25 mTorr could not be broken down also implies non-linearly

increasing breakdown factor at lower pressures. These observations are still consistent with model expectations.

Finally, it is worth noting that breakdown factors measured for both θ-pinch discharges and unbiased dipole discharges at 100 mTorr show are within similar ranges ($1500 < \alpha^* < 2000$) with exception to a single θ-pinch data point where breakdown occurred signficantly later in time. This could imply that breakdown factors are also useful for comparing different configurations to one another, but more data would be needed to make any certain conclusions.

6.1.2 Seeded Breakdown

The two seeded breakdown cases consist of the biased-dipole and ringing-θ configurations. In a biased dipole shot, the bias banks were fired into coils 2 and 3 while the cusp banks were fired into coils 1 and 4 (see figure 44 for coil locations). These banks were crowbarred at approximately 4.6 μs and the pre-ionization bank was then fired into the dipole coil at 10 μs into a tube-area-averaged background field strength of approximately 162 mT and allowed to ring down naturally. For a ringing-θ discharge, the bias and cusp banks are fired in the same manner as the biased dipole configuration, but instead of firing the dipole coil the reversal banks were discharged into coils 2 and 3 at 4.6 μs (the same time at which the bias and cusp banks are crowbarred) into a tube-area-averaged background field value of 175 mT.

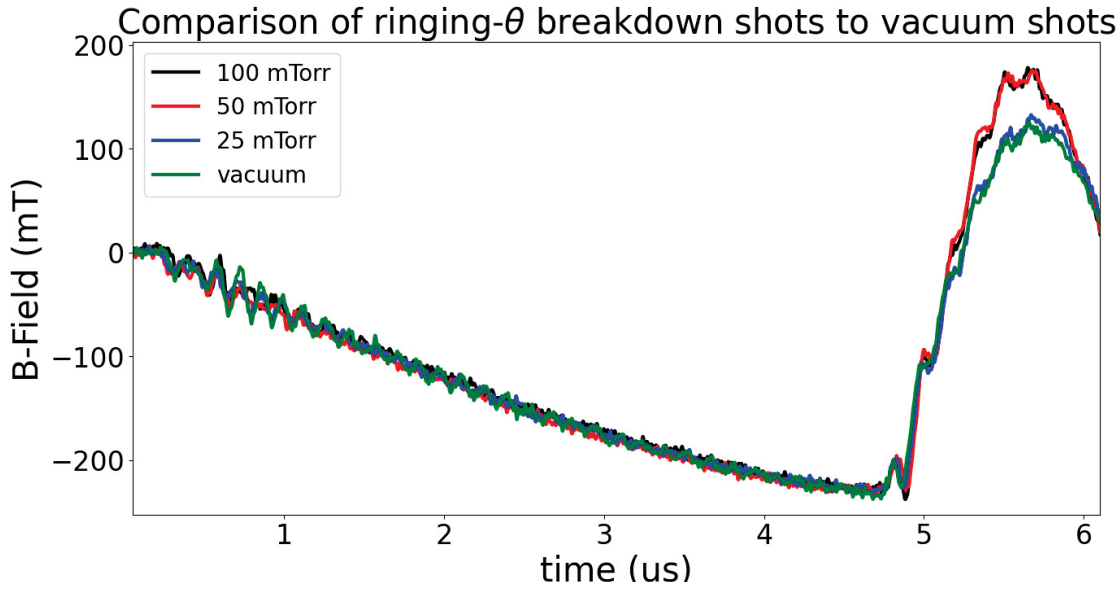

Figure 66: Comparison of external field measurements for ringing-θ discharges in D_2 to vacuum.

The bias banks are discharged for both the biased dipole and ringing-θ configurations, which were seen in the θ-pinch results above to produce prompt breakdown for D_2 at 50 and 100 mTorr. It is important to know whether the θ-pinch discharge is producing enough plasma to affect field distribution, because if the field distribution is changed by the presence of this plamsa, then the breakdown models no longer apply. Figure 66 shows a comparison of external magnetic field measurements on coil 3 for ringing-θ for a range of pressures (note that the trace labeled "vacuum" was measured to have a pressure on the order of 1 μTorr). These results clearly indicate that the plasma created by the initial θ-pinch discharges are not significantly affecting field distribution at the time of the reversal banks' firing. Further, images from the high-speed imaging cameras confirm that significant plasma presence is quenched by the time the reversal banks fire (due to the lower electric field strength near the peak of the θ-pinch discharge).

While the field geometry produced by the cusp coils firing independently is not covered by the models, it is worth noting the results of a short campaign of shots that studied their prompt breakdown capabilities. It was observed that the cusp fields were able to produce visible prompt breakdown with weaker tube-averaged-field strengths when compared to the bias discharges. The same field mapping analysis as summarized for the formation chamber in figure 50 in section 5.1.1 was performed for the cusp coils with the results seen in figure 67 below. Comparing the two field distributions, the cusp coils clearly produce an overall stronger magnetic field than is produced in the formation chamber for 20 kV charges (note that they were designed with this intention for the purpose of containing an FRC). However, the cusp banks discharged at 10 kV still produced weaker electric fields than those produced by the 20 kV bias discharges but were observed to yield prompt breakdown in conditions where the bias discharges could not. Essentially, the cusp fields were able to cause breakdown with significantly weaker fields than the bias fields (prompt breakdown could even be observed in 100 mTorr of Helium with the cusp fields). The primary difference between the bias and cusp fields is the curvature of the fields in the axial direction. Therefore, it is possible that $\nabla\vec{B}$ and curvature drift have a signficant impact on breakdown. It is also possible that more impurities exist on the tube surface in the cusp region (as both the bias and cusp fields pass through the tube at this location), which may be affecting the prompt breakdown characteristics in this region. Regardless, two major points were elucidated in this short study. The first is that the cusp fields generate more seed ionization than the bias fields. Secondly, the affects of field curvature relative to electron motion on prompt breakdown characteristics should be studied in the future.

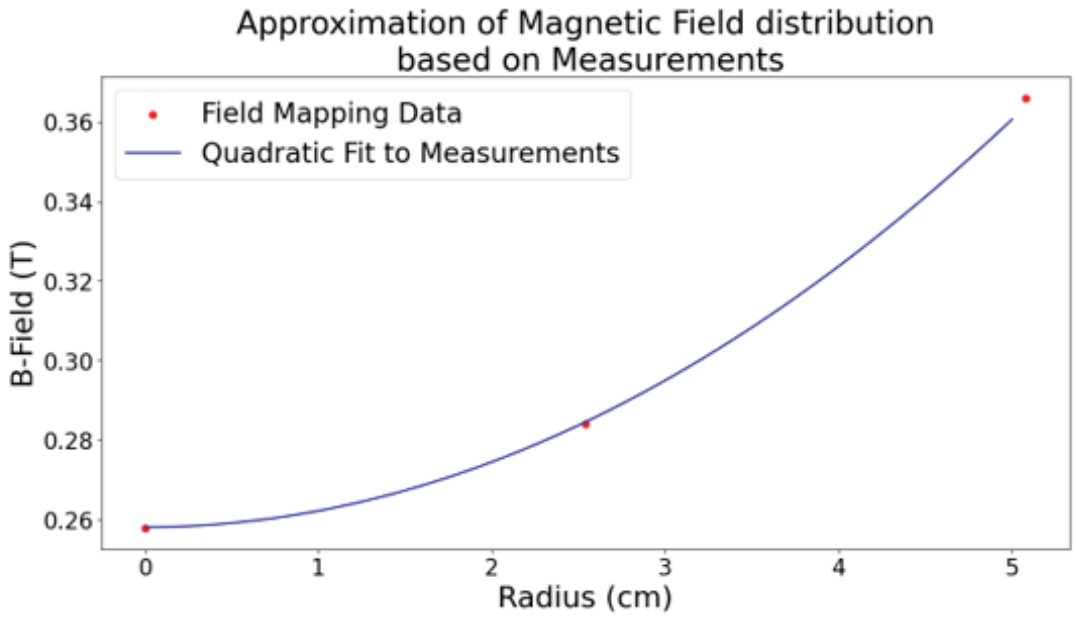

Figure 67: Partially quadratic fit to the cusp coils' field distribution based on field mapping measurements.

Biased Dipole Analysis

It was found that the biased dipole configuration was able to cause prompt breakdown at all tested pressures of D_2 (25 - 100 mTorr). Figure 68 shows the measured breakdown factors for a biased dipole configuration fired with a 20 kV charge on the bias, cusp, and dipole banks. It should be noted that the range of measured breakdown factors here is on the order of measurement error in the diagnostics so that relative comparisons between these low values cannot be made. However, it is clear that the measured breakdown factors for this configuration are significantly lower than its unbiased equivalent (see figure 69 for comparison).

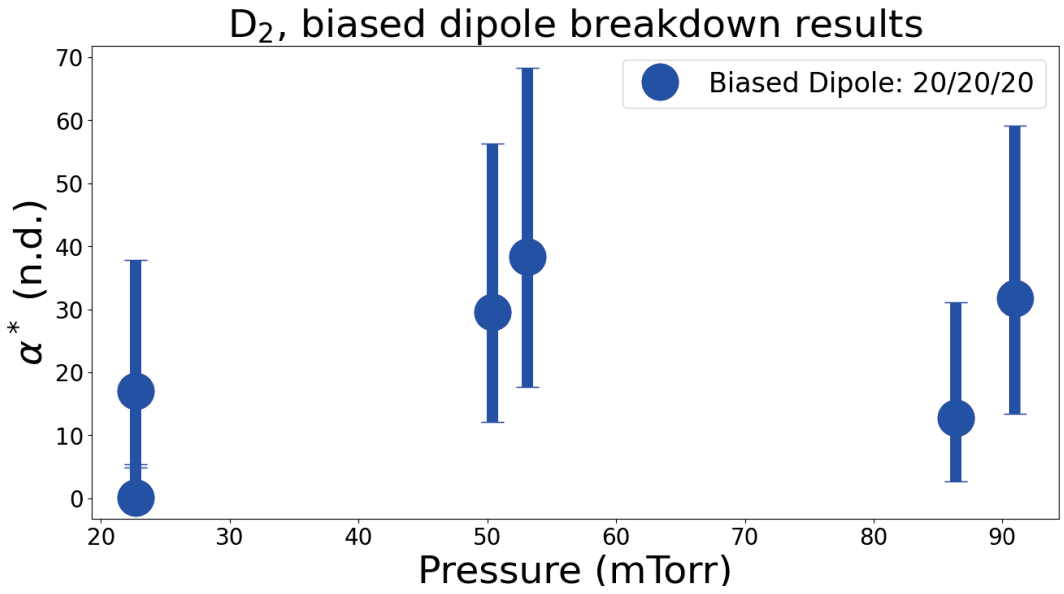

Figure 68: Measured breakdown factors of biased dipole configuration in D_2, fired with a 20 kV charge on the bias, cusp, and dipole banks.

Given the expectations based on the general electron density equation 3.2.3 (which states $n_e = n_{e0} e^{n_n \sigma_{\text{Ion}}(v_e) \int_0^t v_e}$), it is probable that this exponential decrease in measured breakdown factor with pressure is due to the presence of more charged particles at the time of the discharge which significantly increase the bulk cross section of the gas. However, without a measurement of electron density (such low densities cannot be measured with the present experiment's interferometer), it cannot be stated for certain if the increased electron density is not the primary factor.

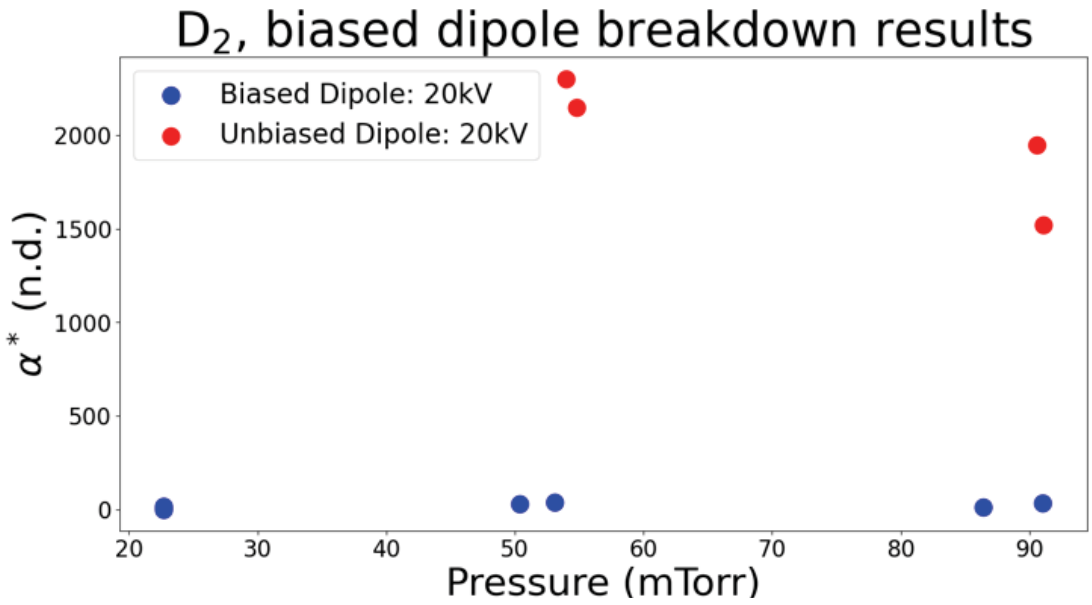

Figure 69: Comparison of the measured breakdown factors for an unbiased dipole configuration to the biased dipole configuration.

Since it was hypothesized that seed ionization from the bias and cusp banks were causing the change in measured breakdown factor, another set of data was taken using weaker field strengths on the bias and cusp fields. It was theorized that weaker bias and cusp discharges should yield less seed ionization, which should increase measured breakdown factors relative to those seen in figure 68. This comparison is presented below in figure 70 which shows similar measured breakdown factors except in the case of a 25 mTorr static fill where one of the two data points is measured with a significantly higher breakdown factor. While more data would be needed to be sure of this relationship, it is still consistent with the expectations based on the hypothesis. In the cases of 50 and 100 mTorr, it is possible that the 10 kV bias and cusp discharges still provide suffient seed ionization to significantly alter the breakdown timing of the biased dipole.

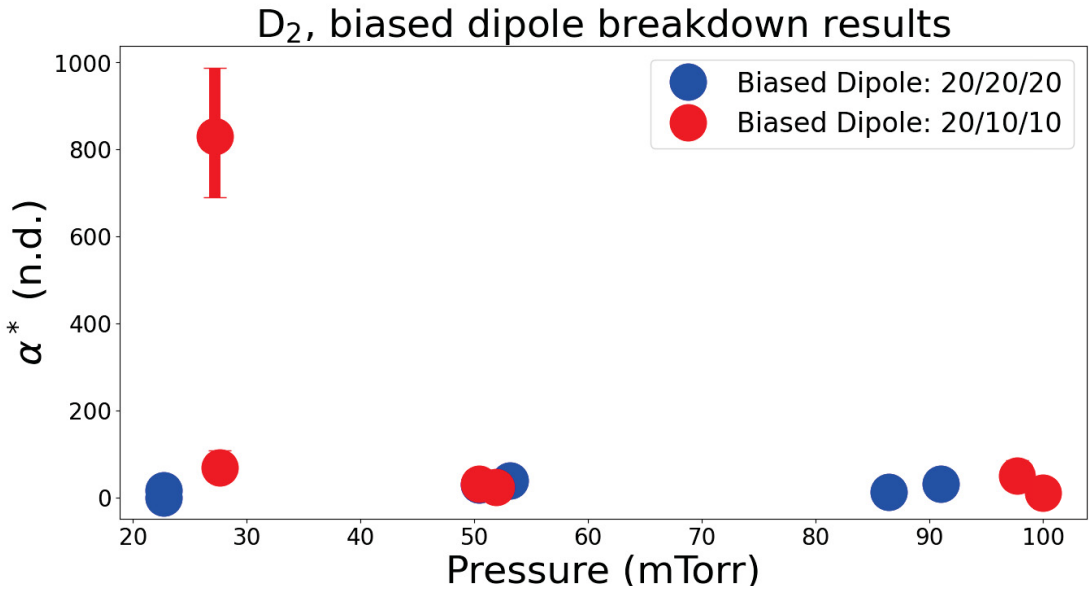

Figure 70: Comparison of bias and cusp field strength on breakdown factor in D_2.

As seed ionization is expected to be a dominant factor in prompt breakdown, it is worth discussing the results of helium tests since it has the highest first ionization energy requirement of any known element. Figure 71 displays measured breakdown factors for helium exposed to a biased dipole configuration with each bank charged to 20 kV. Again, it is clearly seen that the seed ionization has a signficant effect on prompt breakdown properties. Recall that the dipole bank, even when charged to its maximum 40 kV capacity, could not promptly breakdown helium at any pressure. Figure 71 shows that with seed ionization, helium promptly breaks down at all pressures tested. However, a noticeable outlying data point with a measured breakdown factor over 600 can be observed at the 100 mTorr range. Of the three data points at 100 mTorr, two were obtained using the same degree of filtering on the visible light photodiode aimed at the center of the formation chamber. Figure 72 presents the intensity measured over time for these two data points. A small, but noticeable signal is seen on one trace vs. the other between 4 μs and 10 μs, indicating the presence of

detectable seed ionization (recall that the dipole bank is fired at 10.6 μs). This indicates at least that the outlying data point was subject to weaker seed ionization than its counterpart. This further indicates that breakdown factors can be used as a proxy for determining efficacy of seed ionization. It should be noted that the reason for weaker seed ionization in one shot vs. another was determined to be due to a difference in bias crowbar timing of one switch, which allowed for weaker seed ionization in the outlying shot.

Tests were then performed using weaker seed ionization by discharging the bias and cusp fields at 10 kV (as opposed to the previous 20 kV charge) while contintuing to discharge the dipole bank at 20 kV. These results are shown in figure 73 and compared to the results of firing the bias and cusp banks at 20 kV. While prompt breakdown could be achieved with a 100 mTorr fill, it could not be achieved at 50 or 25 mTorr under these conditions. This again implies that seed ionization has a strong affect on prompt breakdown capabilites.

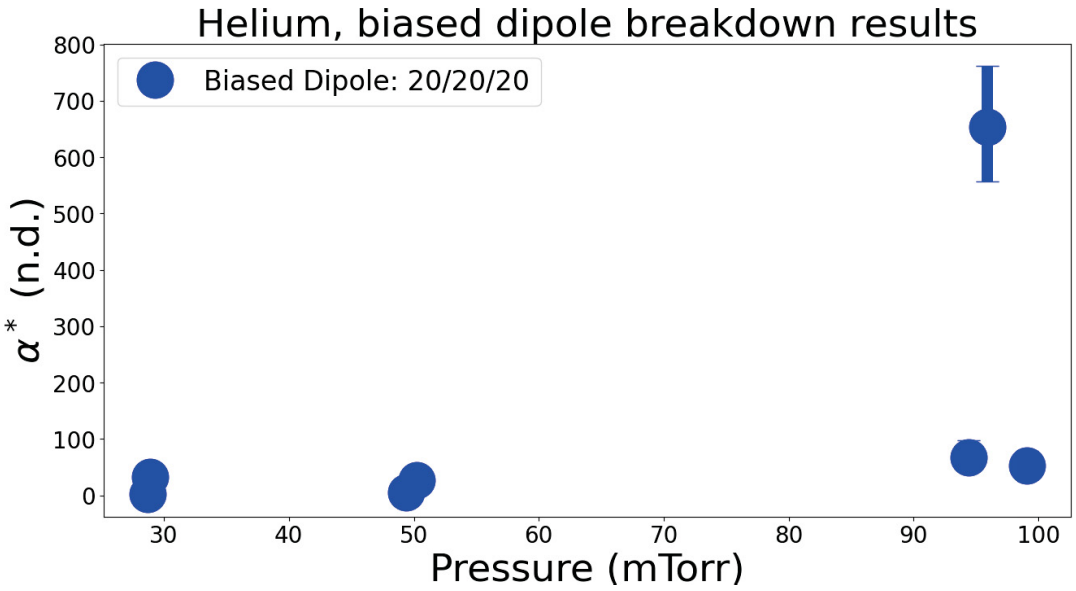

Figure 71: Measured breakdown factors of biased dipole configuration in helium, fired with a 20 kV charge on the bias, cusp, and dipole banks.

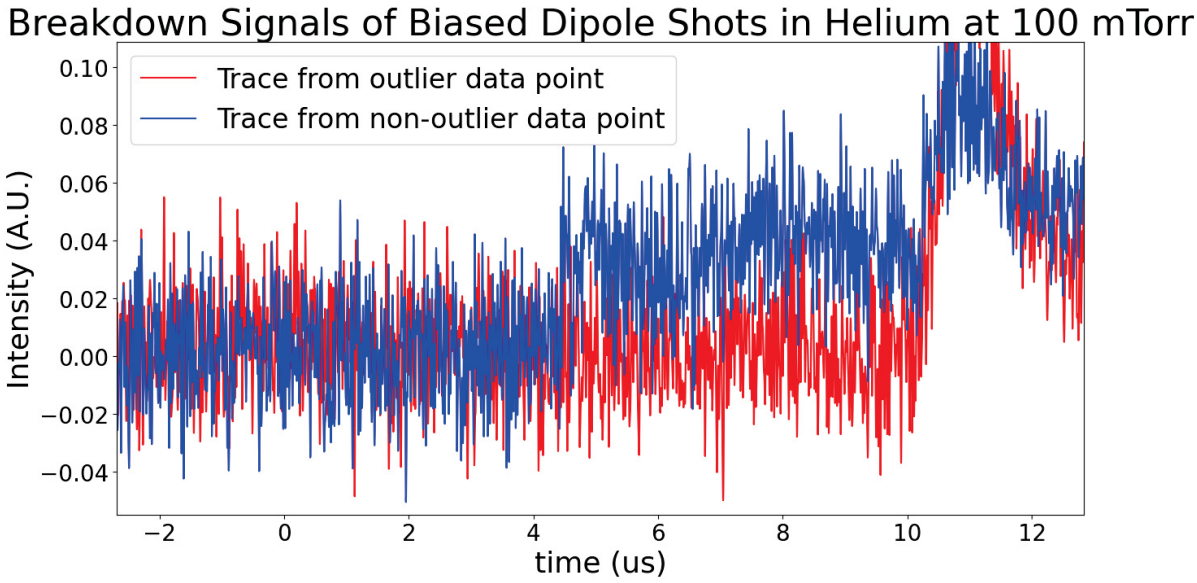

Figure 72: A plot depicting the chamber center photodiode signal for two of the three 100 mTorr data points seen in figure 71, including the outlying data point.

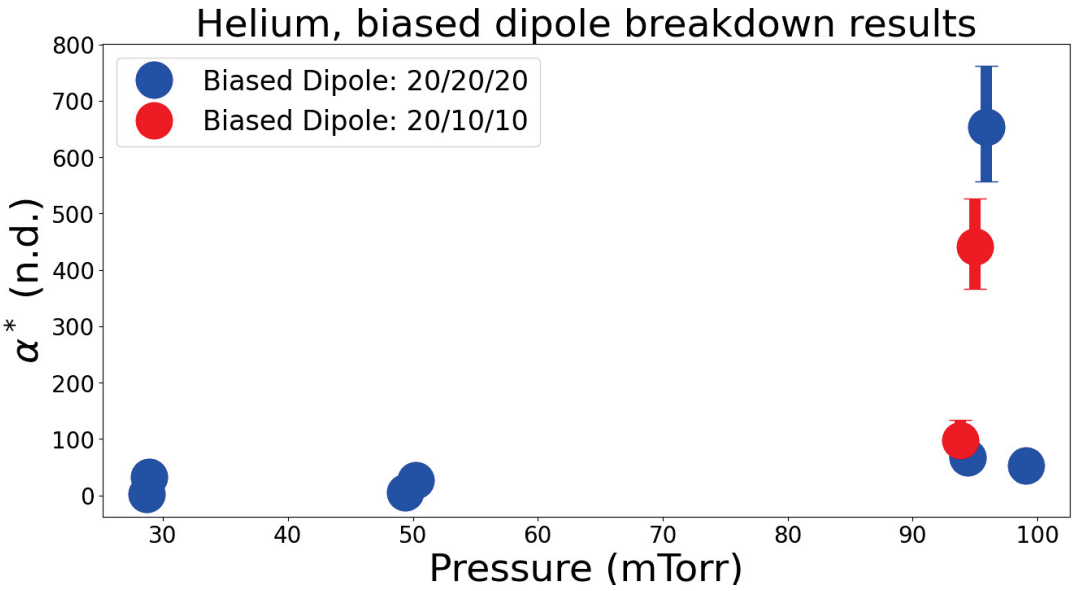

Figure 73: Comparison of bias and cusp field strength on breakdown factor in Helium. Dipole bank discharged at 20 kV while bias and cusp fields are discharged at 10 kV.

On a final note regarding the seeded breakdown results, it is worth considering how seeding electrons into a gas may change the expected breakdown behaviour. Recall equation 3.2.3, which gives the electron growth rate due to ionizing collisions as $n_e = n_{e0} e^{n_n \sigma_{\text{Ion}}(v_e) \int_0^t v_e}$. Clearly, seeding a gas with electrons will increase the initial electron density, n_{e0}. Additionally, when a gas is given seed ionization, it is expected that some electrons in neutral atoms will be excited into higher energy orbitals. Figures 74 displays both the mometum transfer cross section of ground state hydrogen ([23]) as well as the ionization cross section of hydrogen energized to the 2S state ([34]). It is clear that the interaction cross sections for high energy electrons are significantly higher than for ground state particles, particularly given that fact the that electron impact ionization cross section is only one component of the overall momentum transfer cross section. A similar plot showing the electron impact momentum transfer cross section ([35]) and electron impact ionization cross section of helium in the 2S state ([36]) is displayed in figure 75. When considering the effects of seed ionization on breakdown properties of a gas, the change in cross sections of excited gases should not be discounted.

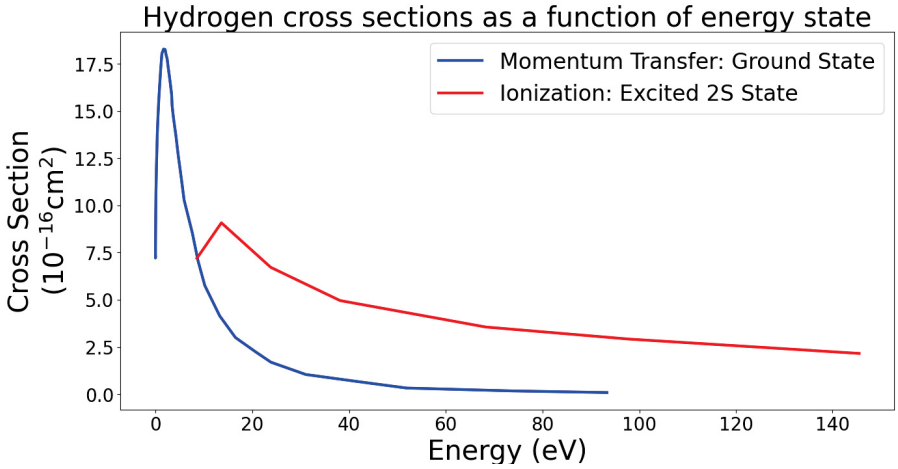

Figure 74: Comparison of hydrogen electron impact cross sections for momentum transfer at ground state to ionization cross section at an excited state. Produced using data from Yoon's[23] and Dixon's[34] studies.

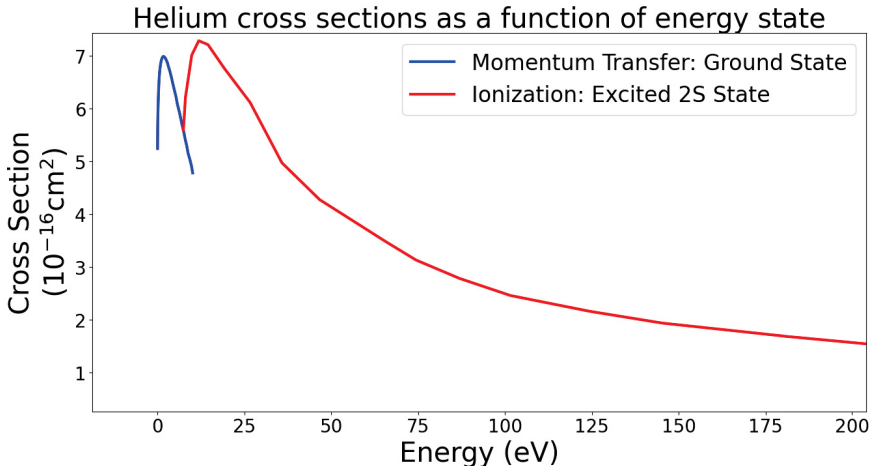

Figure 75: Comparison of hydrogen electron impact cross sections for momentum transfer at ground state to ionization cross section at an excited state. Produced using data from Itikawa's[35] and Dixon's[36] studies.

Ringing-θ Analysis

Recall from the derivation of electron energy scaling in section 3.4 that the energy that can be transferred to electrons in a ringing-θ system is signficantly limited by the pre-existing bias field. Although the ringing-θ system on MTX was able to break down promptly for D_2, figure 76 shows that much lower breakdown factors than expected are observed. This effectively means that breakdown is occurring before electrons are expected to acquire kinetic energy on the order of the ionization energy of the gas.

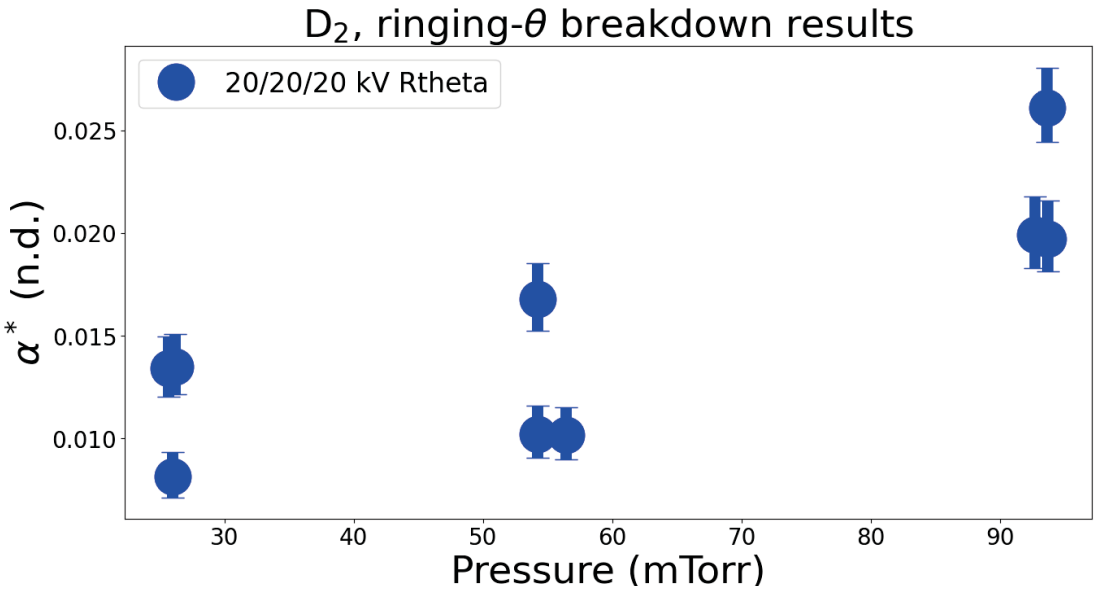

Figure 76: Measured breakdown factors of a ringing-θ system in D_2, fired with 20 kV on the bias, cusp, and reversal banks.

The Boris Pusher simulation was used at this point to better understand electron dynamics in a ringing-θ configuration. Figure 77 displays the results of this simulation, showing a simulated electron's path on the left (starting at a radius of 0.25 cm with no initial energy) and the energy of this simulated electron over time on the right. Note that starting the electron with initial velocities on the order of thermal velocities did not alter these results. An electron impact energy of approximately 10 eV is required to at least excite electrons deuterium atoms to higher energy states so that this is the mimimum interaction energy. As is clear from the right side of figure 77, electrons accelerated by the ringing-θ here are not expected to achieve this energy until just after 300 ns. Figure 78 displays the measured breakdown times of the ringing-θ breakdown studies. Comparing the breakdown times of figure 78 to the expected electron energy from the Boris Pusher on the right side of figure 77, it is clear to see that breakdown is occuring long before maximum electron energies would be expected to be capable of causing breakdown.

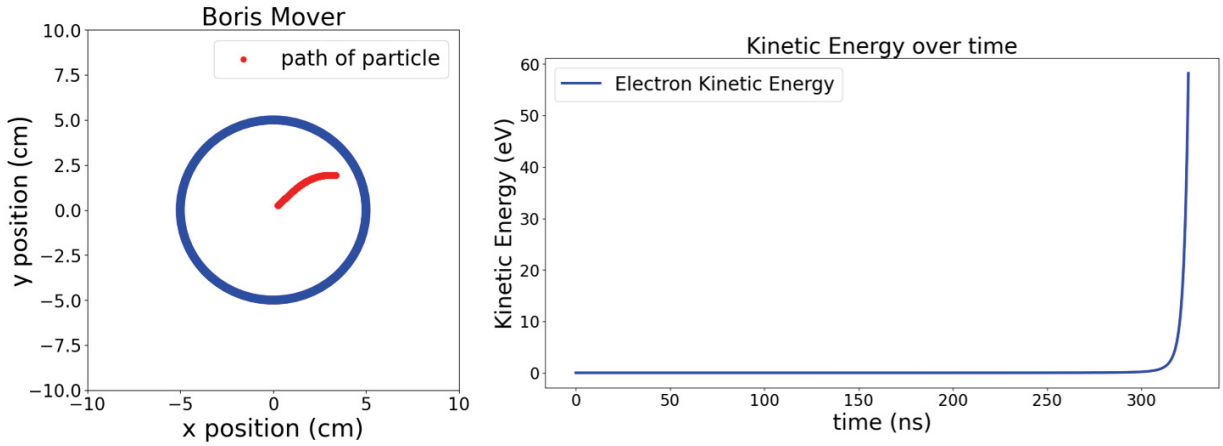

Figure 77: Left: A scatter plot showing the simulated path of an electron under the influence of the MTX ringing-θ system, starting from close to the center of the tube. Right: the kinetic energy of this simulated electron over time.

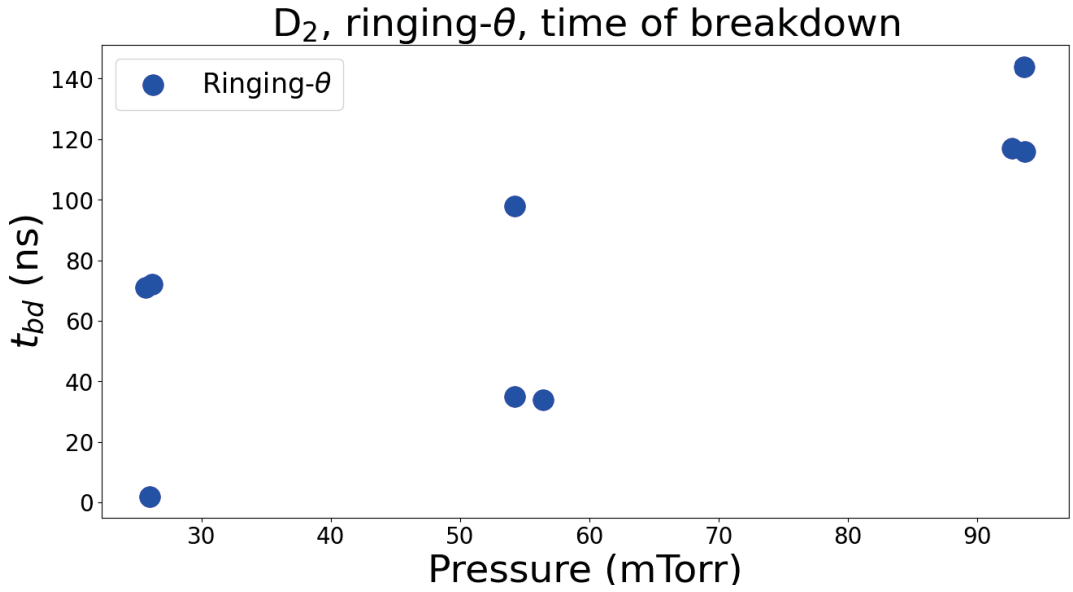

Figure 78: Measured times of breakdown for a ringing-θ discharge with 20 kV on the bias, cusp, and reversal banks.

The end result is that there is either an unaccounted for source of energy in the system or that electrons are able to effectively transfer momentum to the gas below the minimum

interaction energy of 10 eV. Although energy is injected into the gas via the bias and cusp discharges, visible evidence of plasma has subsided by the time the reversal bank is fired and therefore could not serve as an energy source capable of causing this difference. However, it is surmised from the biased dipole results that the presence of seed ionization is significantly reducing electron mean-free-paths and the same should be true in a ringing-θ configuration. This shorter mean-free-path means that electrons accelerated by the induced electric field can more easily transfer energy to the gas but this only happens in electron-neutral or electron-ion collisions. It is possible that electrons are transferring energy to the small population of ions, which then collide with neutrals to cause ionization. Alternatively, one may consider that the single particle motion models no longer apply due to plasma dynamics from the seed ionization becoming non-negligible. However, comparison of measured vacuum field strengths to ringing-θ discharges (see figure 66 in which differences only occur after the field 0 crossing, signficantly later than observation of breakdown) makes this unlikely. These measurements strongly imply that the plasma presence is not significantly altering the field distribution near the time of breakdown. Finally, it is worth noting that the framing camera images taken of ringing-θ discharges (see figure 79) at least qualitatively match the expectation of charged particle drift in the outward radial direction that begin to curve later in time as the background magnetic field becomes weaker. Exploration of this mechanic with different seeding or field strengths may shed light on the problem which is left as an open endeavor for interested future researchers.

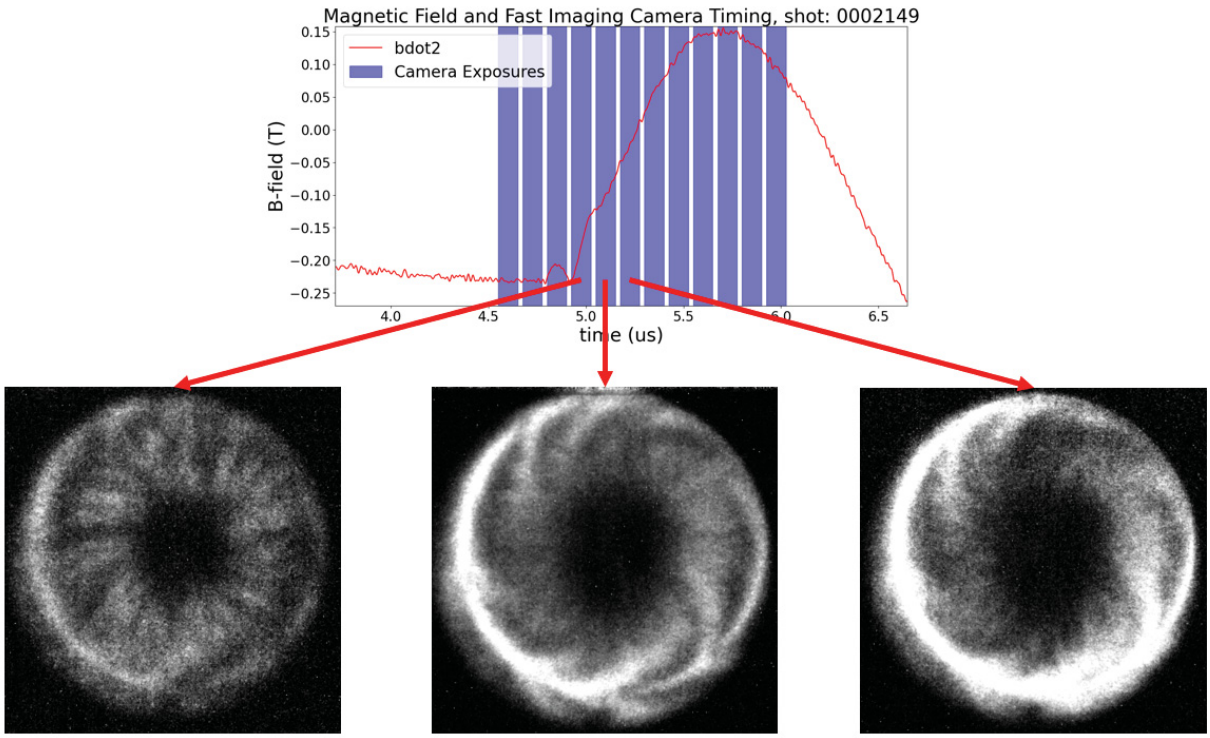

Figure 79: Visible light images of a ringing-θ discharge synchronized to external magnetic field measurements.

Prompt breakdown of the same ringing-θ configuration (20 kV charge on all banks) was observed in Helium for 50 and 100 mTorr as shown in figure 80. In this case breakdown factors much less than 1 are measured for 100 mTorr discharges, but breakdown factors on the order of unity are measured for 50 mTorr. Prompt breakdown could not be observed at 25 mTorr. This presents an interesting case as it is the only seeded configuration tested that actually measures breakdown factors that span unity. This would imply that something about the configuration is fundamentally changing as a function of pressure. If seed ionization is the cause for anonymously early breakdown observed in ringing-θ discharges, it is possible that the 50 mTorr case represents an inflection point in this relation. This field configuration and seeding in Helium gas then would be an appropriate place to begin studies into the early

breakdown of ringing-θ discharges. It should be noted that the error on measurements of α^* near unity are subject high error due to the resonant nature of the ionization cross-section near this point and the rapidly changing electron energy at this point in a θ-pinch discharge.

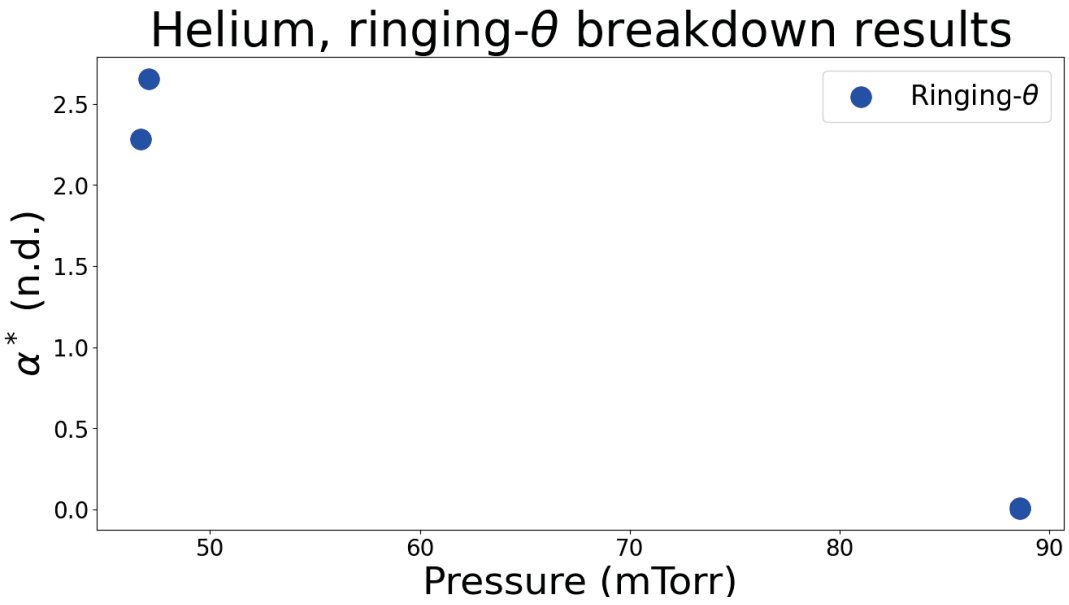

Figure 80: Measured breakdown factors of a ringing-θ system in helium, fired with 20 kV on the bias, cusp, and reversal banks.

6.1.3 Summary of Prompt Breakdown Results

Measurements of breakdown factors for unseeded prompt breakdown configurations (unbiased dipole and θ-pinch) are consistent with the expectations of the proposed breakdown model. This implies the model's potential viability as a useful design tool for inductively-coupled ionization systems. It was determined in the study that electron energy alone is insufficient to appropriately predict inductively-coupled breakdown. The discharge power of a system was also seen to play an important role and future work should elucidate this dependence so that a minimum power requirement for breakdown can also be established.

Measured breakdown factors of seeded configurations show that seed ionization signficantly impacts prompt breakdown characteristics and drastically reduces field strengths required to cause prompt breakdown. Prompt breakdown in the ringing-θ configuration is generally seen well before the model predicts breakdown to be possible. It is possible that plasma formed at the cusp region where bias field strength is weaker is streaming to the formation chamber, causing the observed breakdown. It is noted that a shift in this anomylous behaviour was observed in helium discharges between 25-100 mTorr so that future work would benefit from focusing on this region for further study. The most conclusive result of the prompt breakdown studies is that a staged approach of seeding ionization followed by a higher power preionization discharge signficantly increases the energy coupling between the gas and the preionzation system, particularly for lower pressure gases. Further, measured breakdown factors in a staged pre-ionization system can be used to easily compare efficacy of seed ionization systems without the need for sensitive diagnostic setups for detection of seed ionization characteristics.

6.2 Delayed Breakdown Conditions

Although the primary focus of this research is on prompt breakdown and the models developed for it, it is still worthy to note the conditions unseeded conditions that yielded delayed breakdown as well as prompt breakdown as this information is useful for the general design of inductively-coupled pre-ionization systems. Seeded configurations were capable of prompt breakdown in almost all conditions (see section 6.1.2 for more details) so this section only presents results for unseeded configurations. The tables below list the field configuration, gas pressure, whether prompt breakdown was observed and whether delayed breakdown was observed. The "configuration" column will list either unbiased dipole or θ-pinch as the configuration for a given row. This listing will be followed by listing the

voltages on each bank. For example, an ubiased dipole discharge firing with 20 kV on the dipole bank will list "unbiased dipole: D20" as its configuration. Note that for all unbiased dipoles and θ-pinch configurations, banks are fired and allowed to ring down naturally. The pressure column presents the static fill pressure for the tests (+/- 10 mTorr) and whether prompt and/or delayed breakdown were observed is indicated with either "Y" for yes or "N" for no. Bank parameters are summarized in 5. Note that the field values shown represent the minimum and maximum of the field averaged over the tube area (see section 5.1 for more details on field mapping).

Table 5: This table summarizes the bank parameters. Note that the magnetic field values presented are the tube-area-averaged field strength.

Bank parameters for breakdown studies			
Bank	**Voltage Range (kV)**	**Field Range (mT)**	**Frequency (kHz)**
Cusp	10 to 20	150 to 300	43
Bias	10 to 20	-110 to -225	43
Reversal	20 to 40	300 to 600	320
Dipole	20 to 40	105 to 215	140

θ-pinch delayed breakdown results are represented in table 6. The results here represent the only unique case in which prompt breakdown was observed but breakdown on subsequent rings of the system was not. However, in this particular case the photodiodes that would normally pick up the presence of delayed breakdown were signficantly overfiltered and it is possible that breakdown could not have been observed by them even if present. Of note is the fact that the span of 10 to 20 kV charge on the bias bank spans the ability of the sytem to break down D_2 gas at all. Therefore, this data is directly applicable in the design of a θ-pinch bank intended to ionize deuterium. Systems weaker than the equivalent of this 20 kV charged bias bank should not be expected to reliably ionize D_2.

Table 6: This table summarizes the breakdown observation results of θ-pinch tests in deuterium gas. *Tests on the 15 kV bias discharge had excessively overfiltered photodiodes and may not have detected delayed breakdown, even if present.

Breakdown observations for θ-pinch tests in D_2			
Configuration	**Fill Pressure** (mTorr, $\pm$10)	**Prompt Breakdown**	**Delayed Breakdown**
θ-pinch: B20	100	Y	Y
θ-pinch: B20	50	Y	Y
θ-pinch: B20	25	N	Y
θ-pinch: B15	100	Y	N*
θ-pinch: B15	50	N	N*
θ-pinch: B10	100	N	N
θ-pinch: B10	50	N	N
θ-pinch: B10	25	N	N

Table 7 summarizes the results of θ-pinch testing in helium. In addition to this information, it should be noted that prompt breakdown could be observed with cusp fields alone (see the beginning of section 6.1.2 for details. However, prompt breakdown could not be observed with any standard system of the standard systems that fit the prompt breakdown models presented in this work. Delayed breakdown of helium could be observed with reversal discharges into the formation coils but could not be seen with any other banks discharged through the θ-coils. As such, if breakdown of helium is desired, it is strongly recommended to inject seed ionization prior to firing of a more powerful ionization system.

Table 7: This table summarizes the breakdown observation results of θ-pinch tests in helium gas. *For 40 kV reversal discharges scattered sparks of light could be seen with the framing camera but it could not be confidently considered prompt breakdown.

Breakdown observations for θ-pinch tests in helium			
Configuration	**Fill Pressure** (mTorr, $\pm$10)	**Prompt Breakdown**	**Delayed Breakdown**
θ-pinch: R40	100	N*	Y
θ-pinch: R40	50	N*	Y
θ-pinch: R40	25	N	Y
θ-pinch: R20	100	N	Y
θ-pinch: R20	50	N	Y
θ-pinch: R20	25	N	Y
θ-pinch: B20	100	N	N
θ-pinch: B20	50	N	N
θ-pinch: B20	25	N	N

Table 8 lists observations of breakdown in deuterium gas with the unbiased dipole configuration (i.e., firing the dipole coil by itself with no other systems). The tests performed with a 40 kV charge on the dipole bank did not have diagnostics tuned to observe prompt breakdown. Therefore, prompt breakdown in these cases may have been present but unobserved. At its minimum possible firing settings, the unbiased dipole configuration was still able to cause delayed breakdown at all pressures so that a system design minimum could not be identified.

Table 8: This table summarizes the breakdown observation results of unbiased dipole tests in D_2 gas. *For the 40 kV dipole discharges, photodiodes were not tuned to look for prompt breakdown, so it may have been present and unobserved in this case.

Breakdown observations for unbiased dipole tests in deuterium			
Configuration	**Fill Pressure** (mTorr, ±10)	**Prompt Breakdown**	**Delayed Breakdown**
unbiased dipole: D40	100	Y	Y
unbiased dipole: D40	50	N*	Y
unbiased dipole: D40	25	N*	Y
unbiased dipole: D20	100	Y	Y
unbiased dipole: D20	50	Y	Y
unbiased dipole: D20	25	N	Y

Table 9: This table summarizes the breakdown observation results of unbiased dipole tests in helium gas.

Breakdown observations for unbiased dipole tests in helium			
Configuration	**Fill Pressure** (mTorr, ±10)	**Prompt Breakdown**	**Delayed Breakdown**
unbiased dipole: D40	100	N	Y
unbiased dipole: D40	50	N	Y
unbiased dipole: D40	25	N	Y
unbiased dipole: D20	100	N	N
unbiased dipole: D20	50	N	N
unbiased dipole: D20	25	N	N

Table 9 presents results for unbiased dipole tests in helium gas. At its maximum charge (40 kV), the dipole bank was capable of causing delayed breakdown of helium at

all three pressures tests but prompt breakdown was not observed at any settings. The 20 kV charge was unable to produce delayed breakdown so that the minimum field strength (at this frequency) required to cause delayed breakdown in helium will between these two settings.

In summary, the results imply that the occurrence of prompt breakdown is a strong indicator of whether breakdown will continue later in time for inductively-coupled ionization systems. As induced fields become weaker, prompt breakdown no longer occurs, but delayed breakdown will follow. As the induced fields decrease further in strength, delayed breakdown also becomes impossible for the system. Therefore, the data presented in these tables can help to serve as a rough guide for the minimum design requirements of inductively-coupled pre-ionization systems.

6.3 Preionization Method Comparisons

The second primary focus of this work is to compare and contrast the more classical ringing-θ pre-ionization system to a field-aligned method. The motivation for use of a field-aligned method is that ringing-θ methods have been found in the past to have issues diffusing 100% of the initial bias flux into the plasma prior to the reversal phase (see section 2.2 for more details on prior studies). The field-aligned method chosen here is a dipole coil configuration which should induce electric fields aligned with the existing bias field lines to ionize the plasma, and thereby have better flux diffusion characteristics. See section 4.1.1 for general design information and sections 5.1.1 and 5.1.2 for more detailed field mapping information of these systems.

Table 10 summarizes the pulsed power system's parameters. For the biased dipole data presented here, the bias banks were charged to 20 kV and fired through the formation coils. The cusp banks were also charged to 20 kV and fired through the cusp coils (see figure 81 for

coil locations). The dipole coil's bank was then fired at a 40 kV charge with a 10 μs delay relative to the bias and cusp banks and allowed to ring down naturally. For a ringing-θ shot the bias and cusp banks were fired with the same settings as for a biased dipole shot but the reversal banks would be fired into the formation coils at a 20 kV charge with a 4.6 μs delay relative to the bias and cusp banks and allowed to ring down naturally. Note that with the dipole banks being discharged a 40 kV and and the reversal banks being fired at 20 kV, the dipole bank discharge contains approximately twice the energy of the reversal banks.

Internal measurements of the magnetic field strength at the axial center of the formation chamber at varying radial positions were made using the flux array. Sections 4.2.1 and 5.3 present more details on the flux array's design and implementation, respectively. Note that external magnetic diagnostics were seen to measure the same traces with or without the flux array present. Light-based diagnostics however, were subject to significant alteration during the ringdown of the pre-ionization system. After the ringdown of the pre-ionization system though, when a reversal field would nominally be fired to form an FRC, light-based measurements are unaffected. Therefore, their data can still be used for comparison of the pre-ionization systems at the times of interest. Section 5.3 details these findings in more detail.

Table 10: This table summarizes the bank parameters. Note that the magnetic field values presented are the tube-area-averaged field strength.

Bank parameters for breakdown studies			
Bank	**Voltage Range (kV)**	**Field Range (mT)**	**Frequency (kHz)**
Cusp	10 to 20	150 to 300	43
Bias	10 to 20	-110 to -225	43
Reversal	20 to 40	300 to 600	320
Dipole	20 to 40	105 to 215	140

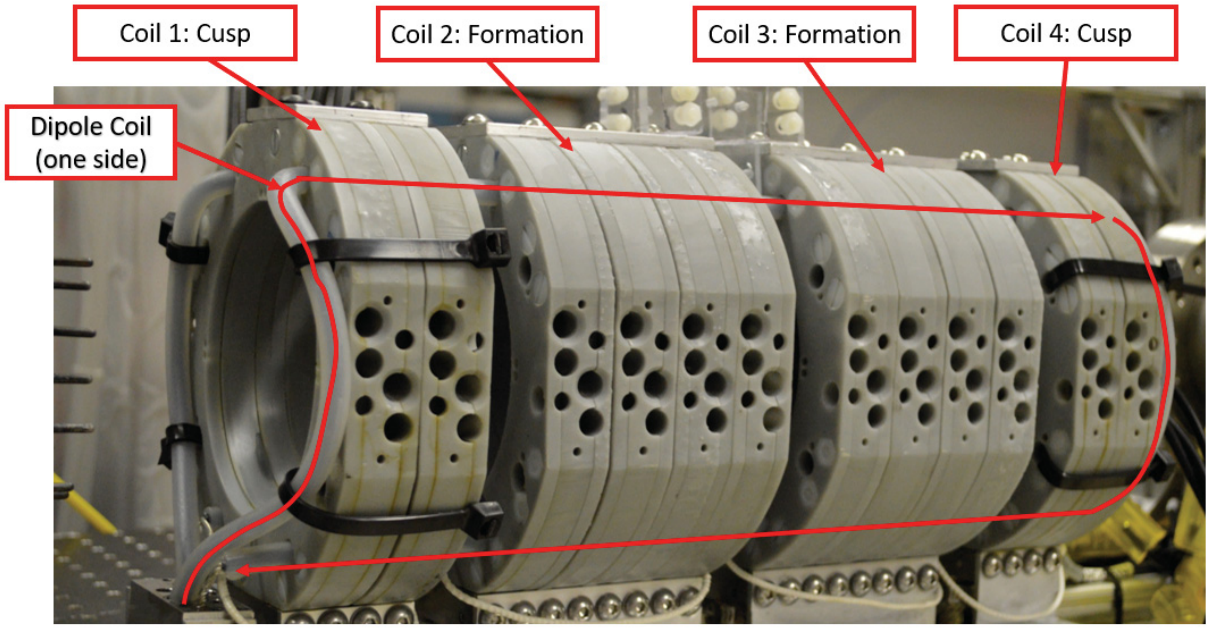

Figure 81: Annotated photo of the MTX coil set.

6.3.1 Pre-ionization Study Results

First note that no significant trace of impurities in either configuration could be observed with the broadband spectrometer, which used a lowpass filter to block the H-α line. A notch filter was not used to block H-β emission and this signal was significantly brighter than any impurity signals that could be measured. Figure 82 presents measurements of internal magnetic field, external flux, and line-integrated density made for ringing-θ shot with a 100 mTorr static fill of D_2 gas. The internal field measurements at the top of the figure indicate that the internal magnetic field of the plasma swings close to the 0 point (passing it at some points) but slowly builds up flux after successive rings. The external flux measurement also displays this behaviour and the line-integrated density (measured through the center of the tube) sees strong peaks during the compressive phases of the ringing-θ as would be expected.

The ringing-θ system has finished ringing down at approximately 25 μs, which in this case would be an appropriate time to fire a reversal field to form an FRC.

Figure 83 presents a zoomed-in view of the time-frame in which reversal fields would likely be fired to form an FRC. The radial field distribution of the internal magnetic field measured at 25 μs agrees with the results observed in field mapping campaign for vacuum conditions in section 5.1.1 within 5%. This strongly implies that the bias field is fully diffused within the plasma. These internal measurements yield a total flux of approximately 1 mWb while the flux loop measures approximately 1.3 mWb. However, the flux coil's position closer to coil 3 yields a measurement of flux approximately 1.3 times that observed in the exact axial center (see section 5.1.1 for details), so that these two measurements are also in agreement. Therefore, it is reasonable to assume that the internal magnetic field strength measurements made later in time are close to the real value and that the field is fully diffused into the plasma at 25 μs. The interferometer measures a line-integrated density of $5.34 * 10^{20}\mathrm{m}^{-2}$ over an integration length of approximately 10 cm. A 100 mTorr fill of deuterium equates to a particle number density of approximately $6.6 * 10^{21}\mathrm{m}^{-3}$ (note there are two deuterium atoms per gas molecule). Therefore, if the plasma is uniformly distributed, this implies an overall ionization percentage of 80% at 25 μs. Unfortunately, images of the plasma were not captured at these times. However, the temporal uniformity of the magnetic field measurements and line-integrated density at these time-scales strongly imply the plasma was uniformly distributed in space.

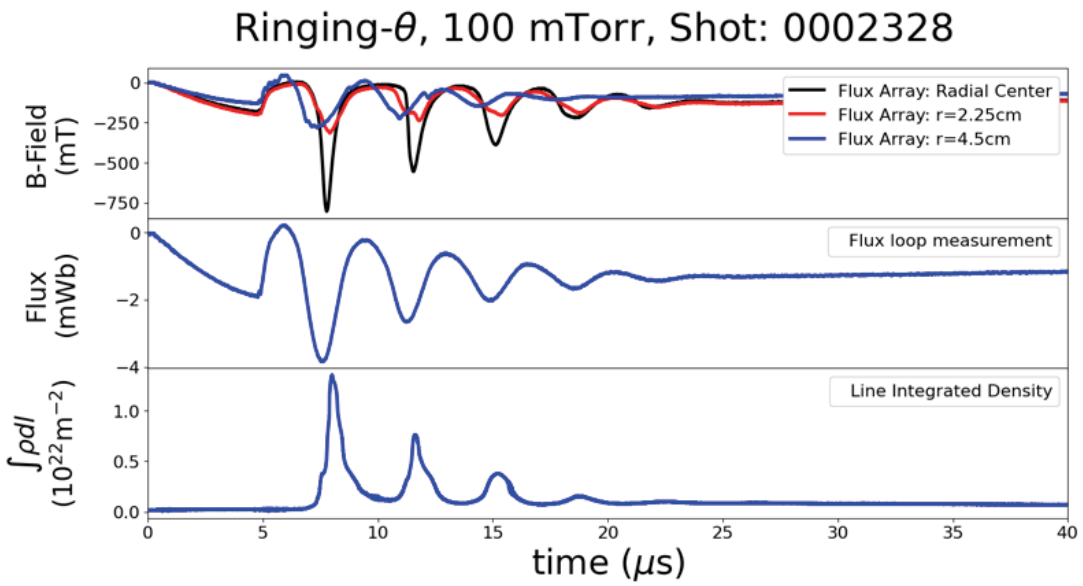

Figure 82: Simultaneous measurements at axial center of formation chamber of internal magnetic field strength(top), external flux (middle), and line-integrated density(bottom) of a ringing-θ pre-ionization shot at 100 mTorr of deuterium.

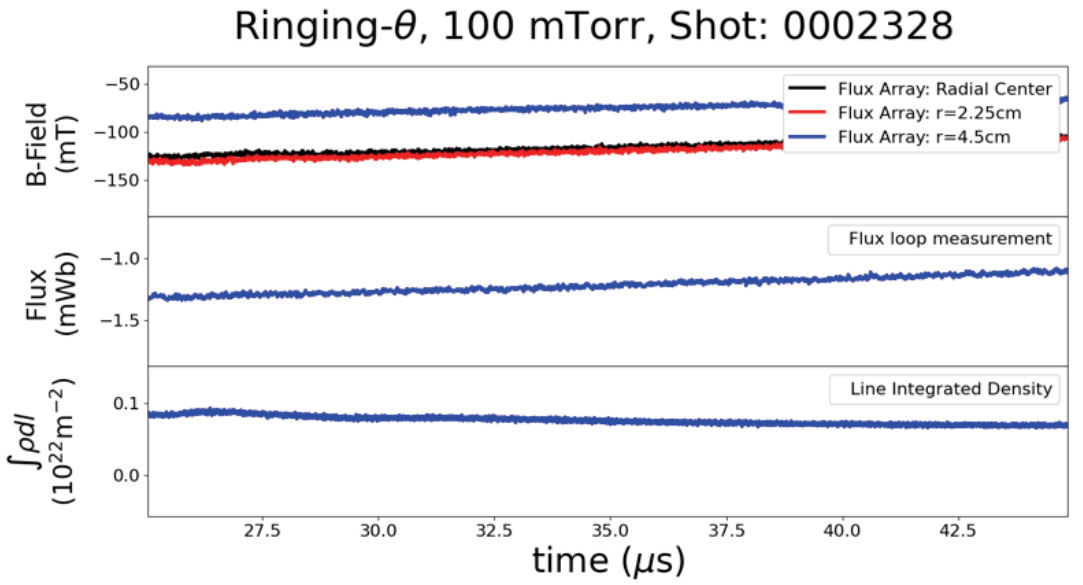

Figure 83: Simultaneous measurements at axial center of formation chamber of internal magnetic field strength(top), external flux (middle), and line-integrated density(bottom) of a ringing-θ pre-ionization shot at 100 mTorr of deuterium, zoomed into the time of interest.

Figure 84 presents similar measurements for a biased dipole pre-ionization shot with a 100 mTorr fill of deuterium gas. The internal field measurements do display fluctation of the axial magnetic field strength (likely due to plasma dynamics) but the measurements tend to remain less than a 100 mT in intensity. This shows that the field-aligned method maintains bias field strength during the pre-ionization process as intended. The flux loop measurement shows signficantly less ringing than the internal measurements, further implying the axial ringing is due to plasma dynamics. Due to the larger inductance of the dipole coil it takes approximately 30 μs longer than the ringing-θ to finish ringing down. Therefore, for this method the time of interest (at which a reversal field would be fired to form an FRC) is approximately 45 μs. Note that the dipole coil is still ringing down at this point but has dispersed approximately 90% of its energy.

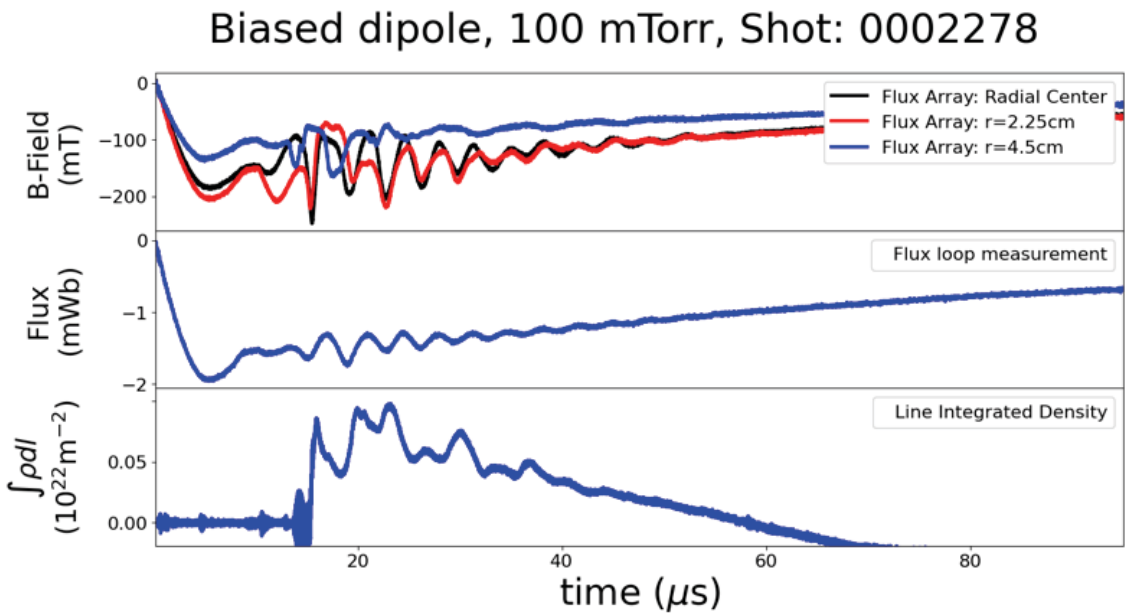

Figure 84: Simultaneous measurements at axial center of formation chamber of internal magnetic field strength(top), external flux (middle), and line-integrated density(bottom) of a biased dipole pre-ionization shot at 100 mTorr of deuterium.

Figure 85 zooms in on the time of interest (45 μs and beyond) for the biased dipole mea-

surements. Again, the field distribution measured by the flux array matches the distribution seen in field mapping studies in section 5.1.1 within 5%. The internal measurements yield an estimated diffused flux of approximately 0.8 mWb while the flux loop measures approximately 1.1 mWb, which is a factor of 1.4 greater than the internal measurements (where a factor of 1.3 is expected based on field mapping studies). It is possible the discrepancy in the measurement is due to plasma dynamics that have not yet ceased, since the dipole coil has only rung down to 90% of its initial energy. Setting this discrepancy of less than 10% aside, the biased dipole coil also achieves 100% of flux diffusion.

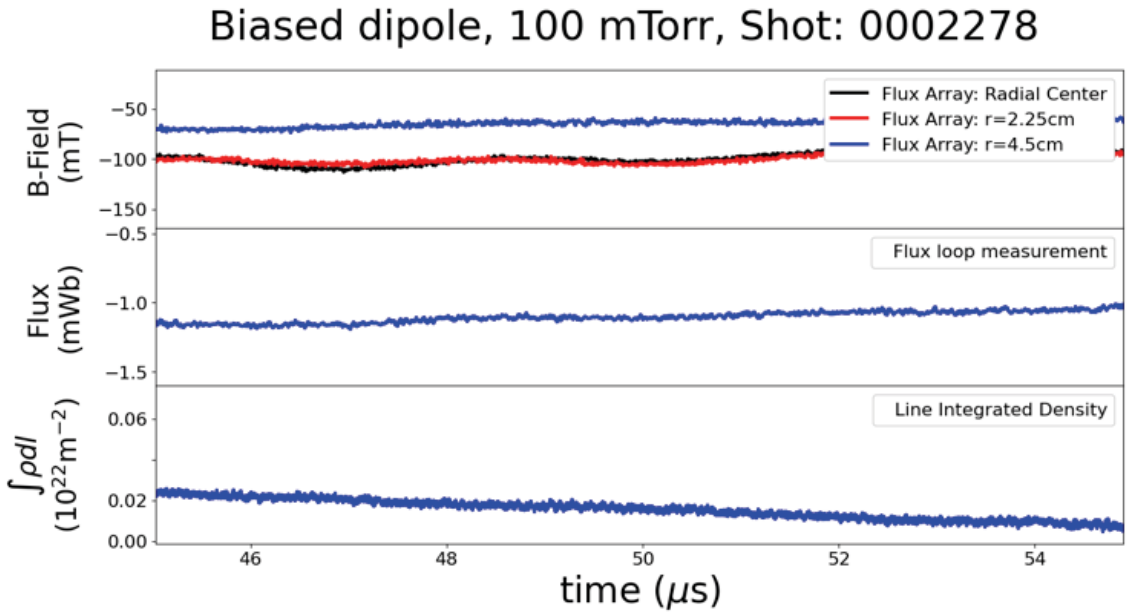

Figure 85: Simultaneous measurements at axial center of formation chamber of internal magnetic field strength(top), external flux (middle), and line-integrated density(bottom) of a biased dipole pre-ionization shot at 100 mTorr of deuterium, zoomed into the time of interest.

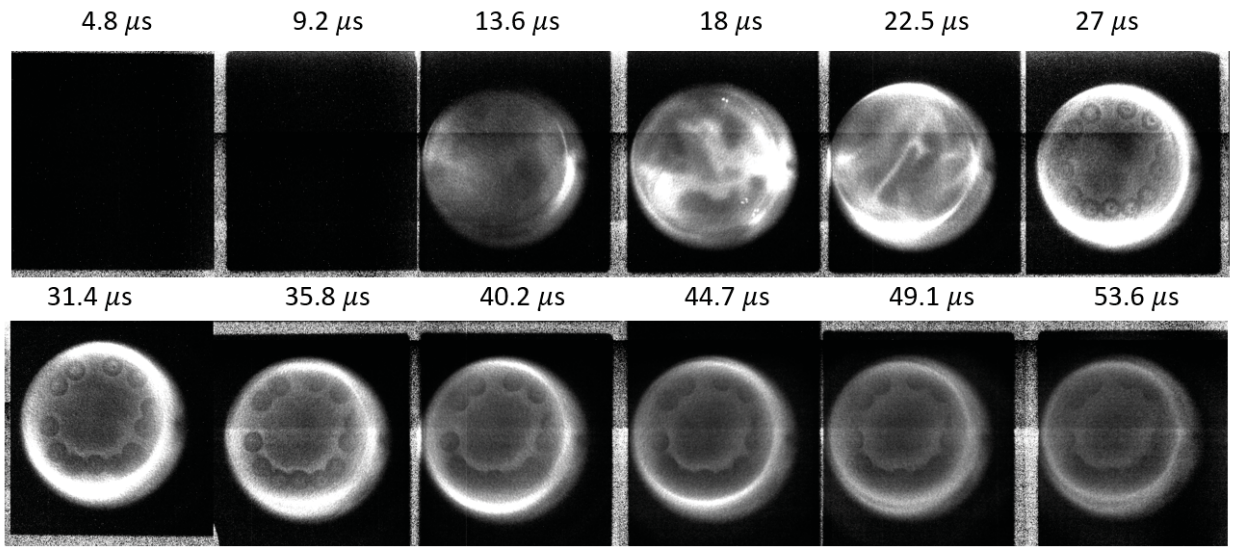

Figure 86: Visible light images captured for a biased dipole shot using the high-speed imaging camera.

The interferometer measures a line-integrated density of $2.4{*}10^{20}\mathrm{m}^{-2}$ over an integration length of approximately 10 cm. A 100 mTorr fill of deuterium equates to a particle number density of approximately $6.6{*}10^{21}\mathrm{m}^{-3}$ (note there are two deuterium atoms per gas molecule). Pictures captured by the high-speed imaging camera on seperate shots of biased dipole pre-ionization are shown in figure 86 with a trace of the dipole current overlayed with camera exposures is shown in figure 87. These images imply that the plasma has a relatively uniform distribution at 45 μs. Therefore, assuming uniform plasma distribution, this implies an overall ionization percentage of 36% at 45 μs.

The lower ionization percentage produced by the biased dipole pre-ionization when compared to the ringing-θ is likely due to the longer ring-down time. Given that the dipole bank contained twice the energy for its discharge when compared to the ringing-θ, this implies that higher power systems more efficiently couple energy to the gas. Given that a plasma loses energy through radiation and particle loss over time, this is a sensible result. Note that

temperature comparison via line ratios could not be made in the region of interest due to H-β signals not being intense enough to detect. However, appendix D does detail the temperature analysis that could be performed in times when H-β was intense enough to be observed. To summarize the pre-ionization performance of the ringing-θ and biased-dipole configurations, both methods achieved full flux diffusion after sufficient ringdown, no significant difference in impurity content was observed between either method, and while the ringing-θ discharge produced a higher ionization percentage than the biased dipole, this is likely due to the lower inductance and therefore higher power of the ringing-θ system. Do note that both of these configurations were provided with ample seed ionization as discussed earlier in this chapter. Therefore, it's possible that in the absence of seed ionization these configurations yield significantly different performance than observed here. Thus, these studies have not uncovered any physical basis for the superiority of one technique over the other, leaving only engineering parameters as the factor determining a choice between the two methods for a given experiment.

Implementation of a ringing-θ pre-ionization system tends to indroduce complexity to the design of the pulsed power system. Since a ringing-θ back is generally discharged through the same formation coils as the bias and reversal banks, each with different firing timings, it is necessary to take precautions to ensure that the banks do not pre-fire one another. Further, since the quality of pre-ionization will be directly dependent on the voltage with which a system is fired, appropriate system isolation with satisfactory performance can rapidly become a complex problem. Additionally, the capacitance of a ringing-θ bank will generally be limited by the capacitance of the reversal bank. Without inductive isolation (which can significantly reduce power), it is generally necessary that the capacitance of the ringing-θ bank be much less than the reversal bank so that current discharges from the reversal bank are not split between the θ-coils and the pre-ionization bank. While field aligned pre-ionization

methods (like the biased dipole configuration studied here) circumvent many of these complexities, they are not without drawbacks. Field-aligned banks tend to fire through separate coil systems and are not integrated into the bias/reversal banks but this does require the design and implementation of a separate coil-set. This introduces complexity to the design of the experimental region, limiting diagnostic access and signficantly reducing the ability to modify coil positions. Given the results observed here and these engineering considerations, it is left to the designer of the experiment to decide which method is appropriate for their purposes.

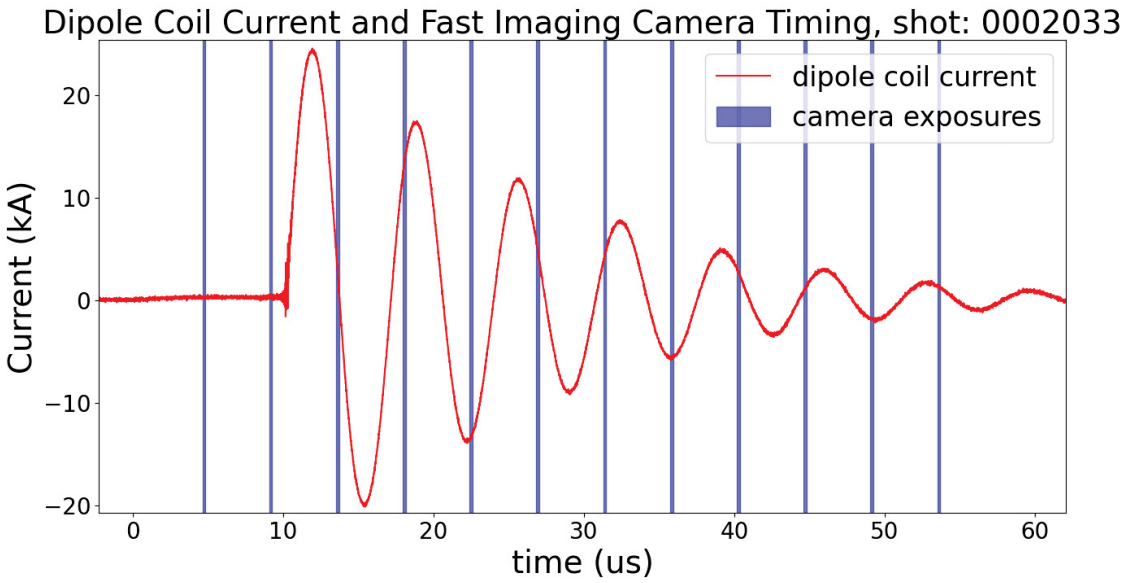

Figure 87: The current in the dipole coil as measured by a Rogowski probe overlayed with camera exposure timings from figure 86.

6.3.2 Pre-ionization Comparisons: Summary

Ringing-θ and biased dipole pre-ionization methods are studied and compared here. Both systems are known to be provided with seed ionization from prior analysis (see section

6.1.2) which likely impact the results observed here. Full flux diffusion was achieved in both configurations after ring down and neither system displayed signficant observable impurity content. The ringing-θ system achieved an ionization percentage of approximately 80% while the biased dipole achieved approximately 36%, despite the biased dipole discharging with twice the energy of the ringing-θ system. This is surmised to be due to the difference in ring-down time between the two systems (with the ringing-θ system being signficantly faster). This implies higher power pre-ionization systems will couple energy more efficiently than lower power systems (likely due to radiative and particle loss time-scales) and should be considered in the design of pre-ionization studies. The power injection of the ringing-θ system was roughly three times that of the dipole coil (see table 3 for bank parameters) so that small factors of power injection can make significant differences in pre-ionization percentages in the regimes studied here. However, no physcial reason for the superiority of either method was observed, which leaves the only practical/engineering considerations for determining a choice between the two for a given system.

Chapter 7

Conclusions and Future Work

One goal of this study was to introduce a semi-empirical model for the prediction and quantitative comparison of breakdown in inductively coupled systems. The second goal was to compare MTX's field-aligned pre-ionization system to that of the more classicly used ringing-θ for FRC applications.

Measurements of breakdown factors for unseeded prompt breakdown configurations (unbiased dipole and θ-pinch) are consistent with the expectations of the proposed breakdown model. Measured breakdown factors of seeded configurations show that seed ionization signficantly impacts prompt breakdown characteristics and drastically reduces field strengths required to cause prompt breakdown. Prompt breakdown in the ringing-θ configuration is generally seen well before the model predicts breakdown to be possible. It is possible that plasma formed at the cusp region (where bias field strength is weaker) streams into the formation chamber, causing the observed breakdown. However, observed emission intensities in the cusp region are significantly weaker than those measured in the formation chamber so that it is unlikely that the total emission of light in the formation region is due energy flowing in from the cusp region. It is noted that a shift in this anomylous behaviour of early breakdown was observed in helium discharges between 25-100 mTorr so that future work would benefit from focusing on this parameter regime for further study. The most imperative result of the prompt breakdown studies is that a staged approach of seeding ionization followed by a higher power preionization discharge signficantly increases the energy

coupling between the gas and the pre-ionization system, particularly for lower pressure gases. Further, measured breakdown factors in a staged pre-ionization system can be used to easily compare efficacy of seed ionization systems without the need for sensitive diagnostic setups that can measure seed ionization characteristics. Thus, a semi-empirical model has been introduced for breakdown in inductively-coupled systems that can be used to aid in design of pre-ionization systems.

Ringing-θ and biased dipole pre-ionization methods were studied and compared. Both systems are known to be provided with seed ionization from the discharging of the bias and cusp fields, which undoubtedly impacted the results observed. Full flux diffusion was achieved in both configurations after ring down and neither system displayed signficant observable impurity content. The ringing-θ system achieved an ionization percentage of approximately 80% while the biased dipole achieved approximately 36% despite the biased dipole discharging with twice the energy of the ringing-θ system. This is surmised to be due to the difference in power injection between the two systems, with the ringing-θ system injecting power roughly three times faster than the dipole coil system. This implies higher power pre-ionization systems will couple energy more efficiently than lower power systems (likely due to radiative and particle loss time-scales) and should be considered in the design of pre-ionization studies. No physical reason for the superiority of either method was observed, which leaves the only practical/engineering considerations for determining a choice between the two for a given system. The primary difference in engineering parameters is that a ringing-θ system tends to introduce complexity to the pulsed power system design while field-aligned pre-ionization systems tend to introduce complexity to the experimental region and limit diagnostic access. As a final note, for dynamic formation of FRCs (i.e., formation of FRCs while also translating them), field aligned methods should be strongly considered. Ringing-θ pre-ionization for dynamic formation must be carefully timed so that the FRC is

formed with sufficient flux, whereas field-aligned methods will be less subject to these issues as they do not ring the axial flux.

The breakdown studies revealed that seed ionization plays a dominant role in effective pre-ionization for plasma. Thus, one avenue of future research is comparison of various seed ionization techniques and their relative efficacy for overall pre-ionization quality. Such studies can now be performed more easily using breakdown factors. Breakdown factors can also be measured for other gases, field configurations, and field parameters. Expansion of the catalogue of available breakdown factors would be a worthy endeavor. It was determined in the study that electron energy alone is insufficient to appropriately predict inductively-coupled breakdown. The discharge power of a system was also seen to play an important role and future work should elucidate this dependence so that a minimum power requirement for breakdown can also be established. As breakdown tended to be observed at much lower discharge powers with the cusp coils, another avenue of future research is to study how field curvature affects prompt breakdown of gases, possibly through the effects of gradient and curvature drifts of electrons in a magnetic field. As it has been established that low collision-rates in these systems are the primary limiting factor, the effects of doping a gas with high-Z elements should be studied. It is possible that small percentages of doping can lead to signficantly earlier breakdown, thereby increasing overall coupling efficiency of pre-ionization systems. Finally, a comparison of ringing-θ and field-aligned methods has not been performed in the absence of seed ionization. Such a comparison may yield physical reasons, rather than purely engineering reasons, for the selection of one method over another.

Bibliography

[1] M. Tuszewski. field-reversed configurations. *Nuclear Fusion*, 28(11), 1988.

[2] Loren C. Steinhauer. Review of field-reversed configurations. *Physics of Plasmas*, 18 (7), 2011. ISSN 1070-664X 1089-7674. doi: 10.1063/1.3613680.

[3] J. T. Slough. Experimental study of the formation of field-reversed configurations employing high-order multipole fields. *Physics of Fluids B*, 2(4), 1990.

[4] T. E. Weber, T. P. Intrator, and R. J. Smith. Plasma-gun-assisted field-reversed configuration formation in a conical -pinch. *Physics of Plasmas*, 22(4), 2015. ISSN 1070-664X 1089-7674. doi: 10.1063/1.4919262.

[5] Chaoqi Hu, Hui Liao, Yilin Li, and Xuan Sun. Experimental study of plasma gun-assisted field-reversed configuration formation. *Physics of Plasmas*, 29(11), 2022. ISSN 1070-664X 1089-7674. doi: 10.1063/5.0097895.

[6] David Hill (Chair) and Richard Hazeltine (Vice Chair). U.s. fusion energy sciences advisory committee: Report of the fesac toroidal alternates panel. Report, 2008.

[7] Alan L. Hoffman, Larry N. Carey, Edward A. Crawford, Dennis G. Harding, Terence E. DeHart, Kenneth F. McDonald, John L. McNeil, Richard D. Milroy, John T. Slough, Ricardo Maqueda, and Glen A. Wurden. The large-s field-reversed configuration experiment. *Fusion Technology*, 23(2):185–207, 1993. ISSN 0748-1896. doi: 10.13182/fst93-a30147.

[8] J. M. Taccetti, T. P. Intrator, G. A. Wurden, S. Y. Zhang, R. Aragonez, P. N. Assmus, C. M. Bass, C. Carey, S. A. deVries, W. J. Fienup, I. Furno, S. C. Hsu, M. P. Kozar, M. C.

Langner, J. Lian, R. J. Maqueda, R. A. Martinez, P. G. Sanchez, K. F. Schoenberg, K. J. Scott, R. E. Siemon, E. M. Tejero, E. H. Trask, M. Tuszewski, W. J. Waganaar, C. Grabaowski, E. L. Ruden, J. H. Degnan, T. Cavazos, D. G. Gale, and W Sommars. Frx-l a field-reversed configuration plasma injector for magnetized target fusion. *Review of Scientific Instruments*, 74(10), 2003. doi: 10.1063/1.1606534 .

[9] S. Nakata. formation of a nearly spherical field-reversed configuration. *Physics of Fluids*, 28(2), 1984.

[10] W. T. Armstrong, D. G. Harding, E. A. Crawford, and A. L. Hoffman. flux-trapping during the formation of field-reversed configurations. *Physics of Fluids*, 25(11), 1982.

[11] W. T. Armstrong, R. K. Linford, J. Lipson, D. A. Platts, and E. G. Sherwood. field-reversed experiments (frx) on compact toroids. *Physics of Fluids*, 24(11):2068–2089, 1981.

[12] S. O. Knox. Reversed-field flux-trapping in a low-compression theta pinch. *Physics of Fluids*, 25(2), 1982. ISSN 00319171. doi: 10.1063/1.863756.

[13] D. O. Campos and H. -J Kunze. Formation of plasma configurations with negative confined magnetic field in different gases of a theta-pinch discharge. *Physics of Fluids B: Plasma Physics*, 5(4):1248–1256, 1993. ISSN 0899-8221. doi: 10.1063/1.860914.

[14] Richard E. Siemon, W. Thomas Armstrong, Daniel C. Barnes, R. Richard Bartsch, Robert E. Chrien, James C. Cochrane, Waheed N. Hugrass, Ralph W. Kewish, Phillip L. Klingner, H. Ralph Lewis, Rulon K. Linford, Kenneth F. McKenna, Richard D. Milroy, Donald J. Rej, James L. Schwarzmeier, Charles E. Seyler, Eugene G. Sherwood, Ross L. Spencer, and Michel Tuszewski. Review of the los alamos frx-c experiment. *Fusion Technology*, 9(1):13–37, 1986. ISSN 0748-1896. doi: 10.13182/fst86-a24698.

[15] Qizhi Sun, Xianjun Yang, Yuesong Jia, Lulu Li, Dongfan Fang, Xiaoming Zhao, Weidong Qin, Zhengfen Liu, Wei Liu, Jun Li, Yuan Chi, and Xiaoguang Wang. Formation of field reversed configuration (frc) on the yingguang-i device. *Matter and Radiation at Extremes*, 2(5):263–274, 2017. ISSN 2468080X. doi: 10.1016/j.mre.2017.07.003.

[16] R. J. Commisso, W. T. Armstrong, J. C. Cochrane, C. A. Ekdahl, J. Lipson, R. K. Linford, E. G. Sherwood, R. E. Siemon, and M. Tuszewski. the initial ionization stage of frc formation. In *Compact Toroid Symposium*.

[17] H. Gota and et. al. Formation of hot, stable, long-lived field-reversed configuration plasmas on the c-2w device. *Nuclear Fusion*, 59, 2019.

[18] C.W. Hartman. *Summary of U.S. Compact Torus Experiments*, pages 441–461. Geneva, Switzerland, 1982.

[19] W. T. Armstrong, J. C. Cochrane, R. J. Commisso, J. Lipson, and M. Tuszewski. theta-pinch ionization for field-reversed configuration formation. *Applied Physics Letters*, 38(9):680–682, 1981. ISSN 0003-6951 1077-3118. doi: 10.1063/1.92477.

[20] C. K. Birdsall and A. B. Langdon. *Plasma Physics via Computer Simulation*. CRC Press, 2017.

[21] PlasmaPy Community and et al. Plasmapy, version 2024.7.0, zenodo, 2024. URL https://doi.org/10.5281/zenodo.12788848.

[22] J. D. Cobine. *Gaseous Conductors: Theory and Engineering Applications*. Dover Publications, Inc., New York, 1958.

[23] J. Yoon and et al. Cross sections for electron collisions with hydrogen molecules. *Journal of Physical and Chemical Reference Data*, 37(2), 2008.

[24] H. R. Griem. *Principles of plasma spectroscopy.* Cambridge University Press, Cambridge, U.K., 2005.

[25] H. R. Griem. Validity of locatl thermal equilibirum in plasma spectroscopy. *Physical Review*, 131(3), 1963.

[26] G. M. Kroesen and et al. The energy balance of a plasma in partial local thermodynamic equilibirum. *IEEE Transactions on Plasma Science*, 18(6), 1990.

[27] T. Fujimoto and R.W.P McWhirter. Validity criteria for local thermodynamic equilibrium in plasma spectroscopy. *Phys Rev A*, 42(11), 1990.

[28] F. Chu and et al. Experimental measurements of ion diffusion coefficients and heating in a multi-ion species plasma shock. *Physical Review Letters*, 130(14), 2023.

[29] T. E. Weber and R. J. Smith. Ultra-high-bandwidth polarization interferometry and optimal quadratic phase detection. *Review of Scientific Instruments*, 90(8), 2019.

[30] I. H. Hutchinson. *Principles of Plasma Diagnostics.* Cambridge Universtiy Press, Cambridge, U.K., 2005.

[31] A. J. H. Donne. High spatial resolution interferometery and polarimetery in hot plasmas. *Review of Scientific Instruments*, 66, 1995.

[32] E. C. Merritt. *Measurements of railgun generated supersonic plasma jet propagation and two jet oblique merging.* Doctoral dissertation, 2013.

[33] W. T. Silfvast. *Later Fundamentals.* Cambridge University Press, Cambridge, U.K., 2012.

[34] A. J. Dixon, A. Von Engel, and M. F. A Harrison. A measurement of the electron impact ionization cross section of atomic hydrogen in the metastable 2s state. *Proceedings of*

the Royal Society of London, Series A, Mathematical and Physical Sciences,, 343(1634), 1975.

[35] Y. Itkawa. Momentum-transfer cross sections for electron collisions with atoms and molecules, 1974.

[36] A. J. Dixon, M. F. A Harrison, and A. C. H. Smith. A measurement of the electron impact ionization cross section of helium atoms in metastable states. *Jounal of Physics B: Atomic and Molecular Physics*, 9(15), 1976.

[37] E. Hintz. Influence of small transverse fields and impurities on theta-pinch stability and confinement. *The Physics of Fluids*, 8(7), 1965. doi: 10.1063/1.1761406.

[38] A. C. Kolb and C. B. Dobbie. Field mixing and associated neutron production in a plasma. *Physical Review Letters*, 3(1), 1959. doi: 10.1103/PhysRevLett.3.5.

[39] E. M. Little, W. E. Quinn, and F. L. Ribe. Effects of ionization and magnetic initical conditions on a magnetically compressed plasma (scylla). *The Physics of Fluids*, 4(6), 1961. doi: 10.1063/1.1706388.

[40] M. Keilhacker. Diffusion of trapped reversed magnetic field in a theta pinch in the presence of a probe. *Nuclear Fusion*, 4, 1964.

[41] A. Eberhagan and W. Grossmann. Thetapinch experiments with trapped antiparallel magnetic fields. *Zeitschrift fur Physik A Hadrons and nuclei*, (248), 1971.

[42] T. S. Green. Plasma containment in the theta pinch. *The Physics of Fluids*, 6(6), 1963. doi: 10.1063/1.1706827.

[43] H. A. B. Bodin, A. A. Newton, G. H. Wolf, and J. A. Wesson. Stability of a bulged theta pinch. *The Physics of Fluids*, 13(11), 1970. doi: 10.1063/1.1692858.

[44] H. A. B. Bodin and A. A. Newton. Rotational instability in the theta pinch. *The Physics of Fluids*, 6(9), 1963. doi: 10.1063/1.1706904.

[45] Loren C. Steinhauer. Plasma rotation in reversed-field theta pinches. *Physics of Fluids*, 24(2), 1980. doi: 10.1063/1.863363.

[46] C. A. Ekdahl, R. Richard Bartsch, R. J. Commisso, R. F. Gribble, K. F. Mckenna, G. Miller, and R. E. Siemon. Rotational instability in a linear theta pinch. *Physics of Fluids*, 23(9), 1980. doi: 10.1063/1.863208.

[47] K. S. Thomas. Measurement of shorting currents from a theta-pinch plasma. *Physical Review Letters*, 23(14), 1969. doi: 10.1103/PhysRevLett.23.746.

[48] M. Tuszewski and et al. Field reversed configuration confinement enhancement through edge biasing and neutral beam injection. *Physical Review Letters*, 108(25), 2012. doi: 10.1103/PhysRevLett.108.255008.

[49] A. I. D. Macnab, R. D. Milroy, C. C. Kim, and C. R. Sovinec. Hall magnetohydrodynamics simulations of end-shorting induced rotation in field-reversed configurations. *Physics of Plasmas*, 14(9), 2007. doi: 10.1063/1.2768017 .

[50] Y. A. Omelchenko. Formation, spin-up, and stability of field-reversed configurations. *Phys Rev E*, 92(2), 2015. doi: 10.1103/PhysRevE.92.023105.

[51] M. Tuszewski and et al. A new high performance field reversed configuration operating regime in the c-2 device. *Physics of Plasmas*, 19(5), 2012. doi: 10.1063/1.3694677.

[52] T. S. Green and A. A. Newton. Diffusion of antiparallel bias magnetic field during the initial stages of a theta-pinch. *Physics of Fluids*, 9(7), 1966.

[53] A. G. Es'kov, R. Kh. Kurtmullaev, A. P. Kreshchuk, Ya. N. Laukhin, I. Malyutin, A. I. Markin, Yu. S. Martyushov, B. N. Mironov, M. M. Orlov, A. P. Proshletsov,

V. N. Semenov, and Yu. B Sosunov. In *Proceedings of the 7th International Conference Innsbruck*, volume 2. International Atomic Energy Association, .

[54] A. G. Es'kov, R. Kh. Kurtmullaev, I. Malyutin, V. N. Semenov, and A. L. Chernyakov. In *Proceedings of the 6th European Conference*. European Physical Society, .

[55] J. M. Finn. Field-reversed configurations with a component of energetic particles. *Nuclear Fusion*, 22(11), 1982.

[56] J. H. Hammer and H. L. Berk. A steady-state beam-driven field-reversed mirror. *Nuclear Fusion*, 22(1), 1982.

[57] Y. Aso, Ch. Wu, S. Himeno, and K. Hirano. End effects on the n=2 rotational instability in the reversed-field theta-pinch. *Nuclear Fusion*, 22(6), 1982.

[58] T. Ishimura. Analysis of stabilization effect of quadrupole field of theta pinch plasmas. Report, Nagoya University, 1982.

[59] S. Ohi, T. Minato, Y. Kawakami, M. Tanjyo, S. Okada, Y. Ito, M. Kako, S. Gotô, T. Ishimura, and H. Itô. Quadrupole stabilization of the n=2 rotational instability of a field-reversed theta-pinch plasma. *Physical Review Letters*, 51(12), 1983.

[60] J. T. Slough, A. L. Hoffman, R. D. Milroy, D. G. Harding, and Loren C. Steinhauer. Flux and particle life-time measurements in field-reversed configurations. *Nuclear Fusion*, 24 (12), 1984.

[61] R. D. Milroy, J. T. Slough, and A. L. Hoffman. Plasma wall sheath contributions to flux retention during the formation of field-reversed configurations. *Physics of Fluids*, 27(6), 1984. doi: 10.1063/1.864787.

[62] J. D. Lawson. Some criteria for a power producing thermonuclear reactor. *Proceedings of the Physical Society. Section B*, 70(1), 1956.

[63] A. L. Hoffman and R. D. Milroy. Particle lifetime scaling in field-reversed configurations based on lower-hybrid-drift resistivity. *Physics of Fluids*, 26(11), 1983. doi: 10.1063/1.864087.

[64] Y. Ito, M. Tanjyo, S. Ohi, S. Gotô, and T. Ishimura. Ion rotational velocity of a field-reversed configuration plasma measured by neutral beam probe spectroscopy. *Physics of Fluids*, 30(1), 1987. doi: 10.1063/1.866165.

[65] A. L. Hoffman and J. T. Slough. Flux, energy, and particle lifetime measurements for well formed field reversed configurations. *Nuclear Fusion*, 26(12), 1986.

[66] U.S. Department of Energy. Strategic plan for the restructured u.s. fusion energy sciences program. Report, Office of Energy Research, 1996.

[67] A. L. Hoffman, H. Y. Guo, and J. T. Slough. The tcs rotating magnetic field frc current-drive experiment. *Fusion Science and Technology*, 41, 2001. doi: 10.13182/FST02-A205.

[68] H. Y. Guo, A. L. Hoffman, and R. D. Milroy. Rotating magnetic field current drive of high-temperature field reversed configurations with high zeta scaling. *Physics of Plasmas*, 14(11), 2007. doi: 10.1063/1.2801481 .

[69] C. Brunkhorst, B. Berlinger, N. Ferraro, and S.A. Cohen. The princeton frc rotating-magnetic-field-experiment rf system, 2007.

[70] K. Miller, J. T. Slough, and A. L. Hoffman. An overview of the start thrust experiment. In *AIP Conference Proceedings*, volume 420. doi: 10.1063/1.54907.

[71] Z. A. Pietrzyk, G. C. Vlases, R. D. Brooks, K. D. Hahn, and R. Raman. Initial results from the coaxial slow source frc device. *Nuclear Fusion*, 27(9), 1987.

[72] W. S. Harris, E. Trask, T. Roche, E. P. Garate, W. W. Heidbrink, and R. McWilliams. Ion flow measurements and plasma current analysis in the irvine field reversed configuration. *Physics of Plasmas*, 16(11), 2009. doi: 10.1063/1.326596110.1063/1.3265961 .

[73] J. T. Slough, S. Andreason, H. Gota, C. Pihl, and G. Votroubek. The pulsed high density experiment: Concept, design, and initial results. *Journal of Fusion Energy*, 26 (1), 2006. doi: 10.1007/s10894-006-9058-x.

[74] G. Votroubek, J. T. Slough, S. Andreason, and C. Pihl. Formation of a stable field reversed configuration through merging. *Journal of Fusion Energy*, 27, 2007. doi: 10.1007/s10894-007-9103-4.

[75] G. Votroubek and J. T. Slough. The plasma liner compression experiment. *Journal of Fusion Energy*, 29, 2010. doi: 10.1007/s10894-010-9335-6.

[76] A. Shiokawa and S. Goto. Dynamic property of spontaneous toroidal field in field-reversed configuration plasmas. *Physics of Fluids B*, 5, 1993. doi: 10.1063/1.860538.

[77] T. Takahashi, K. Inoue, N. Iwasawa, T. Ishizuka, and K. Yoshiomi. Losses of neutral beam injected fast ions due to adiabaticity breaking processes in a field-reversed configuration. *Physics of Plasmas*, 11, 2004. doi: 10.1063/1.1724832 .

[78] T. Asai, Y. Suzuki, T. Yoneda, F. Kodera, M. Okubo, S. Okada, and S. Goto. Experimental evidence of improved confinement in a high-beata field-reversed configuration plasma by neutral beam injection. *Physics of Plasmas*, 7, 2000. doi: 10.1063/1.874121.

[79] T. P. Intrator, G. A. Wurden, P. E. Sieck, W. J. Waganaar, L. Dorf, M. Kostora, R. J. Cortez, J. H. Degnan, E. L. Ruden, M. Domonkos, P. Adamson, C. Grabowski, D. G. Gale, M. Kostora, W. Sommars, M. Frese, S. Frese, J. F. Camacho, P. Parks, R. E.

Siemon, T. Awe, A. G. Lynn, and R. Gribble. Field reversed configuration translation and the magnetized target fusion collaboration. *Journal of Fusion Energy*, 28(2), 2008.

[80] J. H. Degnan, D. J. Amdahl, M. Domonkos, F. M. Lehr, C. Grabowski, P. R. Robinson, E. L. Ruden, W. M. White, G. A. Wurden, T. P. Intrator, J. Sears, T. Weber, W. J. Waganaar, M. H. Frese, S. D. Frese, J. F. Camacho, S. K. Coffey, V. Makhin, N. F. Roderick, D. G. Gale, M. Kostora, A. Lerma, J. L. McCullough, W. Sommars, G. F. Kiuttu, B. Bauer, S. R. Fuelling, R. E. Siemon, A. G. Lynn, and P. J. Turchi. Recent magneto-inertial fusion experiments on the field reversed configuration heating experiment. *Nuclear Fusion*, 53(9), 2013.

[81] Y. Aso, Ch. Wu, S. Himeno, and K. Hirano. End effects on the n = 2 rotational instability in the reversed-field theta-pinch. *Nuclear Fusion*, 22, 1982.

[82] J. M. Finn. Stochastic behavior of particle orbits in field reversed geometries. *Plasma Physics*, 21, 1979.

[83] Ronald H. Cohen, David V. Anderson, and Carolyn B. Sharp. Quadrupole-coupled orbital resonances in the cornell electron-ring experiment. *Physical Review Letters*, 41 (19), 1978.

[84] H. Gota, M. W. Binderbauer, T. Tajima, S. Putvinski, M. Tuszewski, S. Dettrick, E. Garate, S. Korepanov, A. Smirnov, M. C. Thompson, E. Trask, X. Yang, L. Schmitz, Z. Lin, A. A. Ivanov, T. Asai, I. Allfrey, R. Andow, M. Beall, N. Bolte, D. Q. Bui, M. Cappello, F. Ceccherini, R. Clary, A. H. Cheung, K. Conroy, B. H. Deng, J. Douglass, A. Dunaevsky, P. Feng, D. Fulton, L. Galeotti, E. Granstedt, M. Griswold, D. Gupta, S. Gupta, K. Hubbard, I. Isakov, J. S. Kinley, K. Knapp, R. Magee, V. Matvienko, R. Mendoza, Y. Mok, A. Necas, S. Primavera, M. Onofri, D. Osin, N. Rath, T. Roche, J. Romero, T. Schindler, J. H. Schroeder, L. Sevier, D. Sheftman,

A. Sibley, Y. Song, L. C. Steinhauer, T. Valentine, A. D. Van Drie, J. K. Walters, W. Waggoner, P. Yushmanov, and K. Zhai. Achievement of field-reversed configuration plasma sustainment via 10 mw neutral-beam injection on the c-2u device. *Nuclear Fusion*, 57(11), 2017.

[85] H. Gota, M. W. Binderbauer, T. Tajima, A. Smirnov, S. Putvinski, M. Tuszewski, S. A. Dettrick, D. K. Gupta, S. Korepanov, R. M. Magee, J. Park, T. Roche, J. A. Romero, E. Trask, X. Yang, P. Yushmanov, K. Zhai, T. DeHaas, M. E. Griswold, S. Gupta, S. Abramov, A. Alexander, I. Allfrey, R. Andow, B. Barnett, M. Beall, N. G. Bolte, E. Bomgardner, A. Bondarenko, F. Ceccherini, L. Chao, R. Clary, A. Cooper, C. Deng, A. Dunaevsky, P. Feng, C. Finucane, D. Fluegge, L. Galeotti, S. Galkin, K. Galvin, E. M. Granstedt, K. Hubbard, I. Isakov, M. Kaur, J. S. Kinley, A. Korepanov, S. Krause, C. K. Lau, A. Lednev, H. Leinweber, J. Leuenberger, D. Lieurance, D. Madura, J. Margo, D. Marshall, R. Marshall, T. Matsumoto, V. Matvienko, M. Meekins, W. Melian, R. Mendoza, R. Michel, Y. Mok, M. Morehouse, R. Morris, L. Morton, M. Nations, A. Necas, S. Nicks, G. Nwoke, M. Onofri, A. Ottaviano, R. Page, E. Parke, K. Phung, G. Player, I. Sato, T. M. Schindler, J. H. Schroeder, D. Sheftman, A. Sibley, A. Siddiq, M. Signorelli, M. Slepchenkov, R. J. Smith, G. Snitchler, V. Sokolov, Y. Song, L. C. Steinhauer, V. Stylianou, J. Sweeney, J. B. Titus, A. Tkachev, M. Tobin, J. Ufnal, T. Valentine, A. D. Van Drie, J. Ward, C. Weixel, et al. Overview of c-2w: high temperature, steady-state beam-driven field-reversed configuration plasmas. *Nuclear Fusion*, 61(10), 2021.

Appendices

Appendix A

History of FRC Experiments

Theta-pinch experiments were being explored in 1950s at a variety of institutions including the U.S. Naval Research Laboratories[37][38], Los Alamos Scientific Laboratory[39], the Institute for Plasma Physics in Garching Germany[40][41], and Culham Laboratories in the United Kingdom[42][43] as a method of producing thermonuclear plasmas. Researchers noted in these experiments that application of a reversed bias field prior to the theta-pinch firing would produce a compact toroid with lifetimes exceeding the Alfven transit time. However, interest began to wane in these field-reversed theta-pinch experiments due to rotational and tearing instabilities that lead to short life-times[1][2]. Tearing instabilities caused "magnetic islands" to manifest post formation of these toroids but the rotational instability was the most significant hindrance to longer lifetimes. Compact toroids formed with a reversed-field theta-pinch tended to become elliptically shaped and develop a bulk rotation in the azimuthal direction. As the toroid became more elliptical, impact with the vacuum tube's walls would cause complete destabilization. Significant effort was made early on by researchers to understand the exact cause of this instability and the cause is still under investigation to this day over 50 years later[44][45][46][47][48][49][50]. Most work seems to agree that disruption of a radial electric field that exists in an FRC [51] leads to the spin-up of the rotational instability but what exactly disrupts the radial electric field remains to be proven. Regardless, due to these issues interest in field-reversed theta-pinch research began to wane in the 70s as lifetimes could not exceed a few microseconds and no solutions were

projected to counteract these instabilities.

In the mid and late 1970s, experiments at the Kurchatov institute in the Soviet Union had shown that the use of higher intensity bias and lower intensity reversal fields coupled with independently controlled mirror coils that could control where magnetic reconnection occurred significantly reduced the generation of instabilities during formation. These mirror coils were positioned on either both axial ends, producing fields an opposite polarity of the bias field. Further, a pulsed quadrupole magnetic field (which consisted of four conductors carrying current in the axial direction outside of the vacuum tube, thereby producing azimuthal magnetic field near the tube wall) was fired during reversal in order to limit flux and particle loss to the wall when the axial magnetic field crossed the zero field strength point as predicted by the Green-Newton limit [52]. This pulsed quadrupole field was also shown to significantly delay the startup of the rotational instability. These experiments reported a final plasma life time of 100 μs [53][54]. It should be noted here that published work from the Kurchatov experiments could not be found by the author and references used in older works only cite presentations at conferences (whose works have not been digitized) so that all discussion of the Kurchatov work here comes from secondary sources. The rest of this historical review will focus primarily on FRC experiments that use/used the reversed theta-pinch formation method, as the pre-ionization work in this document applies most directly to this type of formation method.

Due to the success of the Kurchatov experiments, the 1980s saw a "boom" in FRC research with multiple experimental programs being generated in short order, particularly in the United States. The combination of using independently driven cusp coils and another technique to inhibit the growth of the rotational instability became a standard adopted by nearly all other field-reversed theta-pinch experiments, launching research into FRCs as they're known today. Indeed, the term "Field Reversed Configuration" appears to have

been first published in 1982 as several other experiments began exploring FRCs[2][55][56]. Following the Kurchatov results, Los Alamos Scientific Laboratory began its own campaign of FRC research with the "Field Reversed theta-pinch eXperiments" A and B (FRX-A and FRX-B) and their primary results were published in 1981 [11]. The two experiments were operated in concert with one another with FRX-A being used to study particle loss and different operational approaches (like the independently driven cusp coils of the Kurchatov studies) while FRX-B, with its more powerful reversal bank, was used to study scaling of equilibrium FRC stability and lifetime. FRX-A compared independently driven to passively driven cusp coils and showed that independently driven cusps yielded longer lived FRCs. However, even without using this technique, FRX-B was able to use lower compression fields to achieve FRCs with lifetimes up to 50 μs. The lifetime was limited by the rotational instability, which was theorized to be caused by cross-field transport loss of ions with a preferential angular momentum, causing spin-up of the FRC due to conservation of angular momentum. Further, researchers here were beginning to draw connections between ion gyro-radius and FRC stability (later to be called the "s" parameter, a central factor for FRC stability). It was theorized that more flux trapping should lead to longer lifetimes and the Field Reversed theta-pinch eXperiment C (FRX-C) was proposed which would have a larger diameter fill tube to trap more flux (from 25 cm diameter to 40 cm diameter).

Complimentary to the particle loss studies performed on FRX-A and their relation to the rotational instability, the Staged Theta-Pinch (STP) experiment at Nagoya university investigated the theory of end-shorting as the potential cause of rotational spin-up[57]. An FRC that has any ion velocity in the azimuthal direction and a pressure gradient in the radial direction will form an electrostatic field in the outward radial direction[51]. End-shorting occurs when axial magnetic field lines outside of the FRC terminate in the conductive ends of the machine which tends to short out the radial electric field produced in the FRC.

Two primary theories exist that explain why this end-shorting leads to spin-up[45][49] but studies on the STP experiment in 1982 strongly indicated that spin-up is strongly dependent on end-shorting effects. This determination becomes important in later FRC experiments that electrically bias the ends of their machines to maintain a radial electric field as an alternative method of suppressing the rotational instability. In 1982 a 2D MHD study of the FRC's rotational instability indicated that quadrupole fields could mitigate the growth of the instability[58]. Shortly after this in 1983 notable results were published from the PIACE experiment at Osaka university in Japan[59]. It was reported that use of quadrupole fields had completely suppressed the growth of the rotational instability. In fact, significantly weaker fields than predicted by the computational work were actually required to mitigate the instability's growth. The results clearly indicated a direct suppression of the elliptical deformation and spin-up of the FRC. It should be noted that the quadrupole fields were not actually turned on until after the firing of the field reversal coil, in contrast to the Kurchatov experiment where the quadrupole fields were pulsed during the field reversal stage. This was the first time that complete suppression of the rotational instability had been achieved.

Primary findings of the Triggered Reconnection eXperiment (TRX-I) were published in 1984[60] by Mathematical Sciences NorthWest (MSNW) in Washington state. This experiment further investigated equilibrium FRC scaling using the now-termed "programmed formation" approach (using independently driven cusp coils to control where magnetic reconnection occurs during FRC formation as pioneered in the Kurchatov studies). Additionally, octupole fields were used to suppress the growth of the rotational instability[3]. Using these techniques, lifetimes up to 150 μs were achieved. Studies on this experiment also showed the development of a sheath during field reversal so that flux loss to the wall occurred on diffusive time-scales[61] rather than the Alfven time-scale as predicted by Green and Newton[52]. Notably, FRC lifetime was shown to scale with higher s parameters, indicating that a machine

exploring higher s FRCs should be considered.

In the following year of 1985 a summary of results on the FRX-C and FRX-C/T (T for translation) were published. The large tube diameter (40 cm) allowed for higher trapped flux in the FRC which, when coupled with quadrupole stabilization to suppress rotational instabilities, yielded FRC lifetimes of up to 300 μs. FRX-C/T demonstrated the ability to translate equilibrium FRCs and showed that the process was reasonably adiabatic, increasing the appeal of the FRC for a fusion reactor as this could significantly simplify reactor design. On FRX-C it was observed that the strength of the axial contraction increased with trapped flux, and beyond a certain level of trapped flux the FRC did not survive the axial contraction. This became a limiting factor for longer lifetimes in these studies but particle confinement was still considered a primary focus for increasing lifetimes and getting closer to the Lawson criterion[62]. Better particle confinement had recently been predicted by numerical studies[63] to scale with higher s parameter which was now corroborated by both the FRX-C and TRX experiments. Again, the next step was to explore higher s parameters in FRCs.

Two concurrent studies occurred in 1986. In Osaka Japan studies on the Osaka Compact Toroid (OCT-L1) machine studied quadrupole suppression of the rotational instability using neutral beam spectroscopy to determine azimuthal velocities of hydrogen ions[64]. Results indicated reduced azimuthal velocity of ions with stronger quadrupole fields, cementing the use of quadrupole fields as a valid method of suppressing ion spin-up. TRX-II was also reported on in this year, which was a slightly modified version of TRX-I[65]. Since it had been shown on TRX-I that the Green-Newton limit was not, in fact, a true limit of reversal speeds due to sheath formation during field reversal, the main coil on TRX-I had been replaced with a slower multi-turn coil to study slower formation on the now called TRX-II machine. It should be noted that MSNW had now become Spectra Technology Incorporated (STI).

With slower formation it became apparent that non-uniformities/asymmetries in pre-ionized plasma prior to reversal could propagate and lead to poor FRC formation and stability. This experiment is also notable for the fact that it showed FRCs could be formed by slower methods which encouraged the exploration of other formation methods in the near future.

The next major result in reverse-theta-pinch formed FRCs came in 1993 when preliminary results from the Large-s eXperiment (LSX) were published by STI[7]. LSX was the response to the call for studying FRCs with larger s parameter, as its name would imply. LSX was a major effort in FRC research that incorporated results from many previous experiments. The results of TRX-II showed that LSX could use a slower reversal field (25 μs quarter-cycle time) which relaxed the engineering requirements and made it easier to form FRCs with a larger s. It used a larger diameter tube (80cm) scaling up from that of FRX-C to trap more flux, octupole fields to protect the tube wall during field reversal (as studied on TRX-II)[3], and quadrupole fields to suppress growth of rotational instabilities as many experiments had used at this point. A suite of seed-ionization and pre-ionization systems were installed (see section 2.1 for more details). LSX was able to form FRCs with s parameters up to 8. The primary results indicated that for FRCs with $s \leq 4$ post formation deformations such as fluting would decay away and yield a stable FRC but for $s \geq 4$ these deformations would not decay fast enough and caused shorter FRC lifetimes. It is notable that in 1990, the U.S. DOE made the decision to change its approach to fusion energy and drastically reduced support for alternate fusion concepts (which FRC research fell under)[66]. Due to this, the LSX experiment was only operated for one year before funding was no longer available. Due to this, researchers could not conclude whether $s \approx 4$ was a physical limit or if better formation techniques could create a more stable FRC with fewer deformations at higher s. However, it was recommended that Neutral Beam Injection (NBI) should be explored in an approach where an FRC could be formed with lower s parameter, allow deformations to

decay, and then use NBI to inject energetic particles to increase the s parameter.

The U.S. DOE's decision to effectively stop funding alternative fusion concepts brought an end to the flurry of FRC research that occurred from 1983 to 1993. However, over the next 20 years several university projects were able to continue work with smaller grants and studied topics including Rotating Magnetic Field (RMF) formation[67][68][69][70], Coaxial Slow Source formation[71][72], as well as collision merging and FRC compression using leftover equipment from LSX experiment[73][74][75]. Japanese efforts in FRC research continued at Osaka University with the FRC Injection eXperiment (FIX). In operation since 1992[76] (about the same time-frame as LSX), the researchers at Osaka were now studying the use of NBI to sustain an FRC. Particular attention was given to the capture efficiency between the NBI and the FRC plasma as a function of injection angle and beam energy[77]. FRC lifetimes on FIX were increased by approximately a factor of 2 (from 300μs to 600μs) using NBI sustainment, indicating that this is a valid approach to increasing FRC lifetimes[78].

The next major FRC experiment was the Field Reversed theta-pinch eXperiment - Liner (FRX-L) at Los Alamos[79] and its sister project, the Field Reversed Configuration Heating eXperiment (FRCHX) at the U.S. Air Force Research Laboratory (AFRL) in New Mexico[80]. Publications for these twin projects spanned from 2005 to 2013. They were funded as a Magnetized Target Fusion (MTF) study to form and accelerate an FRC into a metal liner which would then be imploded by the Shiva Star capacitor bank at AFRL to compress the FRC to high density and temperature. The role of FRX-L was to study production and translation of a high density FRC suitable for liner compression, and it achieved the highest reported FRC densities in literature to date with measurements of $n_e \approx 5 \times 10^{16}\text{cm}^{-3}$. Because the translation and compression of the FRC requires much less time than a standard lifetime no suppression of the rotational instability was expected to be required. Liner implosion tests were conducted at AFRL with results that showed

weak plasma compression. This was determined to be due to insufficient lifetimes (20 μs) and researchers proposed a closer analysis of pre-ionization could yield higher trapped flux and longer lifetimes. Further, FRCHX scientists decided to test a new method of rotational suppression that was suggested in the early 80s by a researcher on the STP experiment[81]. Researchers explored supporting the radial electric field of the FRC using electrodes at appropriately biased field potentials in locations where the external magnetic field lines terminated. However, results on their use were only preliminary at the time of the FRCHX publication and their viability as a suppression mechanism for the rotational instability was not determined. A final note on the LANL efforts is that the use of plasma guns for seed ionization was explored on the Magnetized Shock eXperiment (MSX)[4] in 2015. The MSX machine was an upgraded version of the FRX-L device that used an annular array of plasma guns to produce seed ionization in an annular configuration prior to a ringing-theta pre-ionization stage. A 350% increase in trapped flux was reported at typical operating pressures (50 mTorr) as well as allowing operation at lower fill pressures than were previously possible. More details on this device are discussed in section 2.2.

In 2012 (just before the summary of efforts on the FRCHX project were published), Tri Alpha Energy published a summary of work on their new C-2 machine[51]. It should be noted here that Tri-Alpha Energy (now TAE Technologies) has performed and published a significant number of detailed studies on FRC physics, all of which are available from their website. The vast majority of work performed on FRC physics over the last decade (time of writing this is 2023) has come from TAE technologies such that covering the extent of their work is beyond the scope of this historical review. Therefore, only their seminal publications on their main experiments will be discussed. The C-2 experiment was constructed to study FRC equilibrium and life-times using collision merging formation of two field-reversed theta-pinch formed FRCs, which were then sustained using NBI. Suppression of the rota-

tional instability was explored by using both quadrupole fields as well as end-biasing of the machine. Specifically it was noted that the presence of quadrupole fields inhibits the effectiveness of NBI[82][83]. Siginificant work was done comparing quadrupole suppression to end-biasing suppression with the overall result that end-biasing was a viable approach and to stabilizing the FRC against this mode. On the C-2 device lifetimes of up to 3000 μs were achieved. C-2 was upgraded to the C-2U machine and results were published in 2017[84]. The upgrades consisted of enhancements to both the power of the NBIs as well as more variable control of the machine's end-biasing. These upgrades allowed researchers to achieve FRC lifetimes up to 5000 μs. Further, results from C-2U displayed encouraging confinement scaling with electron temperature, prompting construction of the C-2W machine. Initial results of the C-2W machine were published recently in 2021[85]. This new machine features almost universally upgraded systems including higher voltage and pulse duration end-biasing electrodes, higher energy NBIs with tunable energies during plasma shot, higher energy main bank systems, as well as active control systems to assist in FRC shape and position. Further, the use of Google's machine-learning framework has been applied to determine operational parameter regimes that consistently produce hot and stable plasmas. On this new machine FRC lifetimes have been reported of up to 30 ms, which is limited by pulse duration of the NBIs.

In recent years, efforts have been made by researchers in China to explore the properties of FRCs and their potential application to fusion energy. Yingguang-1 was an experiment fielded by the China Academy of Engineering Physics in Mianyang China and preliminary results were published in 2017]citeRN13. The machine itself is similar in nature to the FRX-L device with its stated goal as exploring the viability of MTF using an injected FRC as the target. Efforts thus far have been primarily focused on stable FRC formation, however, as of the most recent publication FRC lifetimes are limited by the fact that the reversal field is

not being crowbarred. Researchers state that this will be upgraded in future work. In this study significant attention was given to the pre-ionization system which will be discussed in more detail in section 2.2. Very recently in 2022 initial studies on the Keda Mirror with AXissymmetry (KMAX) experiment fielded at the University of Science and Technology in Hefei China have been published[5]. KMAX is a collision merging formation machine similar in nature to the C-2 device fielded by TAE Technologies. Researchers explored the use of plasma guns as seed ionization to increase the trapped flux of the FRC post-formation as reported by Weber on the MSX machine[4]. An increase in trapped flux of 30% was observed in the study when comparing plasma gun seed ionization to no seed ionization.

Research into FRCs as effectively began with the Kurchatov experiments in the mid and late 1970s, spurring a flurry of publicly funded research in the U.S. and Japan in the 1980s culminating with studies on the LSX machine in 1993. At this point public funding for FRC fusion research was drastically reduced and led to a significant decrease in research performed for two decades. In the last decade there has been a significant surge in private funding for fusion energy research which includes FRC work like that being published by TAE technologies. Helion energy is another company exploring FRC fusion applications but as of yet little has been published on their efforts so it is difficult to say more. The state of FRC research in the U.S. at this point is inexorably tied to private funding due to public policy on fusion energy research. Where FRC research goes from this point on will depend heavily on these two private fusion energy companies but the dedication of the researchers at TAE Technologies to publishing their work in extensive details means that whatever the future brings, their work will undoubtedly contribute to further the understanding of FRC physics.

Appendix B

Collisions and Rate Equations

Particle collisions can be either elastic or inelastic. Elastic collisions occur when two particles collide and transfer momentum but no change in either particle's internal energy or identity occur (e.g., a scattering collision between an electron and neutral). Inelastic collisions occur when one or both particles involved in a collision become excited, fractured (disassociation of a molecule for example), ionized, or recombine. Even for electrons in a hydrogen gas a plethora of inelastic collisions are possible. Table 11 shows some of the more common examples. For each of these collisions a collision cross section can be defined and each is a function of the kinetic energy of the collision.

Table 11: An abbreviated list of inelastic collisions for electrons in hydrogen gas (Note that there are multiple possible levels of excitation

Collision description	Reaction
Excitation of H_2	$H_2 + e^- \longrightarrow H_2^* + e^-$
Ionization of H_2	$H_2 + e^- \longrightarrow H_2^+ + 2e^-$
Dissociation of H_2	$H_2 + e^- \longrightarrow 2H + e^-$
Ionization of H	$H + e^- \longrightarrow H^+ + 2e^-$
Ionization of excited H	$H^* + e^- \longrightarrow H^+ + 2e^-$

Due to the wide range of possible collisions and their energy dependencies, it is often convenient to use equivalent cross sections that represent a general type of reaction or summation of reactions. A common example which is often used for an introduction to the cross-section concept is analyzing how far an electron passes through a gas before colliding

with a particle and losing all momentum in the direction of interest. In fact, equation 3.1.8 from the Townsend derivation represents exactly this where the effective cross section of a momentum absorbing collision occurring in a gas is instead represented as a mean-free-path. Note here that a mean-free-path is defined as the average distance traveled by a particle before a collision in which its momentum is significantly altered. So, while a cross section can be defined for any type of specific or general collision, mean-free-paths are usually defined in terms of a particular particle. The equivalent of 3.1.8 in terms of cross section is defined as

$$n_e(x + dx) = n_e(x) - (\sigma_{\text{ion}} n_n) n_e(x) dx \tag{B.0.1}$$

where the subscripts e and n represent electron and neutral populations respectively and the cross section of interest in this case is the electron impact ionization cross section, represented as σ_{ion}. The same result is also obtained as equation 3.1.12 now in terms of cross section as

$$n_e(x) = n_{e0} e^{(\sigma_{\text{ionization}} n_n) x} \tag{B.0.2}$$

Further, the rate of electron growth due to electron impact ionization in such a system can be defined by simply taking the time derivative of equation B.0.2 (noting the general chain rule: $d/dt[e^u] = u' e^u$) which yields

$$\frac{dn_e}{dt} = \left(n_n \sigma_{\text{ion}} \frac{dx}{dt} \right) n_{e0} e^{\sigma_{\text{ion}} n_n x} \tag{B.0.3}$$

Noting that the term outside of the parentheses in equation B.0.3 is simply the electron density from equation B.0.2, the rate of electron population growth due to electron impact ionization can be rewritten as

$$S_I = \frac{dn_e}{dt} = n_e n_n \sigma_{\text{ion}}(v_e) v_e \tag{B.0.4}$$

where v_e is the electron velocity (recall as stated above that cross section is generally a function of electron energy). Note that while this has been derived for the electron impact ionization cross section, the same general process may be used for any electron impact interaction like those listed in table 11.

Appendix C

Magnetic Diagnostics Details

The term “magnetic pickup diagnostics” refers to diagnostics that measure magnetic fields using voltages induced on electric circuits (Faraday’s law). Our three major types of magnetic diagnostics are flux loops, which measure magnetic flux through a large region, $\dot{B}$-probes, which measure magnetic field over a small region (ideally a point location compared to the system scale), and Rogowski coils, which allow for measurement of currents passing through a wire. The purpose of this document is to provide a thorough explanation of the physics, calibration, and post-processing of basic magnetic diagnostics.

First, we will cover basic physical modeling of the three primary forms of magnetic pickup diagnostics used on the experiment. Then, we will discuss the design requirements and overview of potential challenges of each diagnostic. We will then cover some basic circuit modeling with notes on parasitics, followed by transmission line treatment notes, and finishing with development of a general analytic model that can be applied to each magnetic diagnostic as well as accompanying LTSpiceXVII models. We will then detail the construction and calibration methods of each diagnostic and their results followed by some basic notes on digital filtering.

Part 1: Physics of flux loop, $\dot{B}$-probes, and Rogowski coils

Flux loop physics:

Out of the three main types of our magnetic diagnostics, flux loops are the most basic implementation of Faraday’s law. When a magnetic flux normal to the plane of the loop changes in time, a voltage will be induced on the coil as shown in figure 1. (provided the loop is un-shorted). They are used to measure the total flux in a certain region (usually a large one compared to $\dot{B}$-probes).

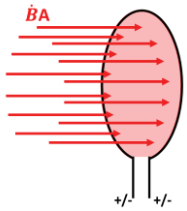

Figure 1: Flux measurement region of a flux loop

The voltage induced by the normally-directed, time-varying flux can be deduced using Faraday’s law as shown,

$$V(t) = \frac{d\Phi(t)}{dt}$$

$$\boxed{\phi(t) = \int_0^t V(t)dt}$$

The self-inductance of a flux loop can be estimated using

$$L_{fluxloop} \approx \mu \left(\frac{D_{FL}}{2}\right) \ln\left[\left(\frac{8D_{FL}}{d_{FL}}\right) - 2\right]$$

Where D_{FL} is the diameter of the loop and d_{FL} is the diameter of the wire used to make the loop.

$\dot{B}$-probe physics:

A $\dot{B}$-probe is just a slightly different implementation of a flux loop. Whereas a fluxloop usually measures magnetic field over a large area, the goal of a $\dot{B}$-probe is to measure the magnetic field strength at a point. Therefore, $\dot{B}$-probes are usually much smaller in diameter and may have more than one turn as shown in figure 2.

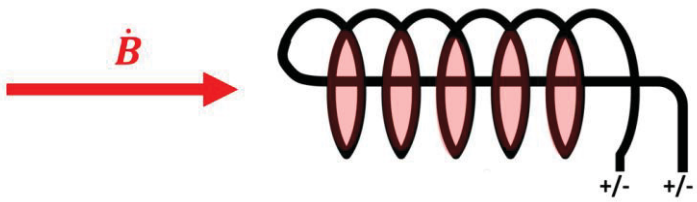

Figure 2: $\dot{B}$ – probe field measurement region, pickup loop area highlighted in pink

More turns in a $\dot{B}$-probe will mean a stronger signal but it will also mean that the measurement may be more distributed in space (depending on the density of the windings) or that parasitic effects could become less negligible (winding capacitance for example). This is a standard trade-off made based on the measurement's needs. The physics are the same as shown for the flux loop above with minor modification. To get the field strength at the $\dot{B}$-probe from a voltage measurement, we use

$$V(t) = \frac{d\Phi(t)}{dt} = N_{\dot{B}} A_{\dot{B}} \dot{B}(t),$$

Solving for magnetic field, we get

$$B(t) = \frac{1}{N_{\dot{B}} A_{\dot{B}}} \int_0^t V(t) = \frac{1}{\kappa_{\dot{B}}} \int_0^t V(t)$$

Where $N_{\dot{B}}$ is the number of turns in the $\dot{B}$-probe and $A_{\dot{B}}$ is the area of those turns. We use $\kappa_{\dot{B}} = N_{\dot{B}} A_{\dot{B}}$ which we call the "area-turns" factor of the $\dot{B}$-probe. It is common to measure this value during a calibration procedure, which we will cover later.

The self-inductance of a $\dot{B}$-probe can be estimated using an ideal solenoid equation with a Nagaoka correction factor for finite solenoids (plot shown in figure 3).

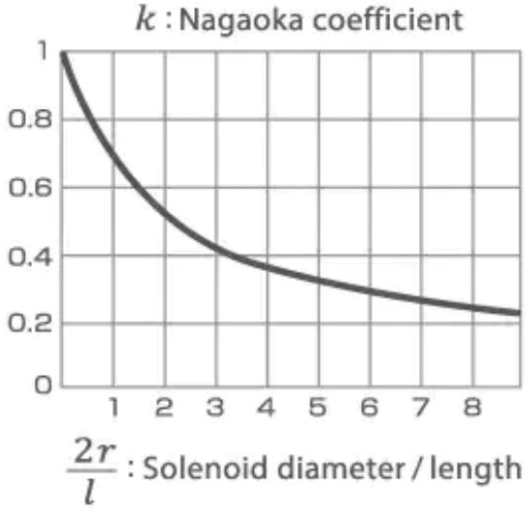

Figure 3: Plot of Nagaoka coefficient for determining inductance of finite length solenoids (note we do not use k for the Nagaoka coefficient in this writeup)

So we will have

$$L_{\dot{B}} = C_{NF}\frac{\mu N_{\dot{B}}^2 A_{\dot{B}}}{l_{\dot{B}}}$$

Where l is the length of the $\dot{B}$-probe's solenoid and C_{NF} is its corresponding Nagaoka factor. Although this is useful for design, once the $\dot{B}$-probe is constructed, it is best to measure the probe's inductance using an LCR meter.

Rogowski coil physics:

Rogowski coils are used to measure currents (usually on a pulsed power system). A Rogowski coil is a solenoid that has its length curved into the shape of a loop and is wrapped around a current carrying wire (see figure 4 below). When current is passing through the wire of the pulsed power system, it generates a magnetic field that is then picked up by the Rogowski coil. In many laboratories, Rogowski coils are commonly made using coaxial cable by soldering a length of insulated magnet wire to the tip of the cable and wrapping it around the inner insulator in a coiled fashion.

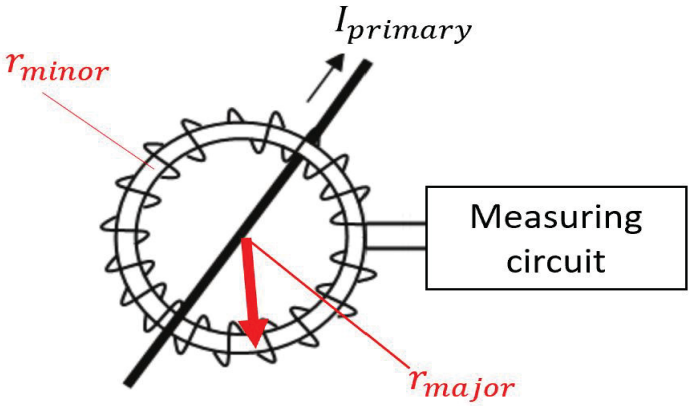

Figure 4: Rogowski coil diagram

The voltage measured in a Rogowski coil can be related to the current in the primary line it is wrapped around through mutual inductance. Mutual inductance is defined as the magnetic flux present in one system due to the current in another and vice versa. For our case mutual inductance is

$$M_{Rog} = \frac{\Phi_{\mathrm{Rog}}}{I_{prim}}$$

Where Φ_{Rog} is the flux present in the Rogowski coil due to the current (I_{prim}) present in the line of interest. If r_{maj} (the diameter of the Rogowski coil as it is wrapped around the primary) is much greater than r_{min}(the diameter of the individual pickup loops of the Rogowski solenoid) then we can approximate the magnetic field in the Rogowski coil using the Biot-Savart equation for the magnetic field at a point far away from a wire. So provided $r_{maj} \gg r_{min}$ then the magnetic field in the Rogowski coil due to the current in the primary line is approximately constant across the area of the Rogowski's individual loops and is given by

$$B_{Rog} = \frac{\mu I_{prim}}{2\pi r_{maj}}$$

The flux in the Rogowski coil then is just the magnetic field in the Rogowski coil's loops multiplied by the area of the turns (A_{Rog}) in the coil and the number of turns (N_{Rog}), so that

$$\Phi_{Rog} = N_{Rog} A_{Rog} B_{Rog}$$

Where $A_{Rog} = \pi r_{min}^2$. So now we can get the mutual inductance between a Rogowski coil and the primary line as

$$\boxed{M_{Rog} = \frac{\mu N_{Rog} A_{Rog}}{2\pi r_{maj}}}$$

Here, as with the $\dot{B}$-probe earlier, we lump geometric values of the Rogowski coil into a geometric coefficient that we will call the "area-turns-per-length" factor of the Rogowski coil so

$$\kappa_{Rog} = \frac{N_{Rog} A_{Rog}}{r_{maj}}$$

Using this factor, we can describe the mutual inductance between the primary line and the Rogowski coil as (it should be noted that some versions of this derivation include the 2π factor in the κ_{Rog} term but here we do not)

$$\boxed{M_{Rog} = \frac{\mu \kappa_{Rog}}{2\pi}}$$

To determine the current going through the primary line, we start again with Faraday's equation as

$$V(t) = -N_{Rog} \dot{\Phi}_{Rog}(t) = -N_{Rog} A_{Rog} \dot{B}_{Rog}(t)$$

To relate the field in the Rogowski coil to the current in the primary line, we use the Biot-Savart law again to get

$$\dot{B}_{Rog}(t) = \frac{\mu \dot{I}_{prim}(t)}{2\pi r_{maj}}$$

And we can see that the voltage induced on the Rogowski coil is given as

$$V(t) = \frac{\mu N_{Rog} A_{Rog} \dot{I}_{prim}(t)}{2\pi R_{maj}} = \frac{\mu \kappa_{Rog} \dot{I}_{prim}(t)}{2\pi} = M_{Rog} \dot{I}_{prim}(t)$$

Thus, the voltage induced on the Rogowski coil is the change in current multiplied by the mutual inductance factor. Solving for the primary current, we get

$$\boxed{I_{prim}(t) = \frac{2\pi}{\mu \kappa_{Rog}} \int_0^t V(t)}$$

Provided again that $r_{maj} \gg r_{min}$, we can treat the Rogowski coil as a solenoid (a Nagaoka correction factor is less likely to be needed for a good inductance estimate here) and get an estimate of the inductance as

$$\boxed{L_{Rog} = \frac{\mu_0 N_{Rog}^2 r_{min}^2}{2 r_{maj}}}$$

Part 2: Design requirements and non-ideal effects

Here we will discuss our specific design requirements, followed by some general notes and discussion of non-ideal effects to account for, and finish with a discussion on how to appropriately approach modeling of transmission lines.

Parameter range for MTX magnetic diagnostics

Presently, there are two primary pulsed discharges on MTX. One is ~60 kA at 40 kHz (a bias discharge) and the other is ~200 kA at 350 kHz (a reversal discharge). Because there are plasma dynamics that may occur at faster frequencies than this, we will say that our goal frequency range is ~40-1000 kHz. So our Rogowski coils will be measuring 1-100 kA signals at frequencies of 40-1000 kHz.

The main coils supply field to a 10 cm diameter tube, and we expect to get a maximum of ~2 T fields from a reversal discharge into a vacuum. When an FRC is formed, these values can increase as the FRC excludes field (although the overall flux is not expected to increase) so we may see fields up to 6T. A field of 2T on a 10cm diameter tube can produce a maximum of ~20 mWb of flux. At 350 kHz, this will produce about 50 kV on the flux loop itself so we must take special care with insulation on it. The $\dot{B}$-probes will be measuring 0-6 T fields at frequencies of 40-1000 kHz.

A note on inductively coupled systems:

First, we note that for inductively coupled systems (like what we're working with here), even though mutual inductance is symmetric, the complete circuit system is not symmetric. What this means is that (in our Rogowski case for example) if we drive 100 kA through the primary line we may get 5A on our Rogowski circuit. However, if we drive 5A through our Rogowski circuit, we will certainly NOT get 100 kA through our primary circuit.

Modeling the magnetic pickup diagnostics in a circuit:

First note that the voltage generated in an element of a circuit due to mutual inductance is entirely separate from the voltage dropped across that same element. For example, if a Rogowski is put in series with a resistor whose impedance is larger than that of the Rogowski itself, then most of the voltage generated by the Rogowski will actually be dropped across the resistor. So in our case (because the presence of the Rogowski does not significantly affect the impedance of the primary line and the circuits are effectively decoupled), the Rogowski coil acts as a voltage source of $j\omega M I_{prim}$ with a source impedance of $j\omega L_{Rog}$.

Notes on parasitic capacitances:

Parasitic capacitances are capacitances in the system that are unintended and often difficult to model properly but may not be negligible depending on the signal frequency.

One case of this is "winding-to-winding" capacitance. Both $\dot{B}$-probes and Rogowski coils can have multiple windings (i.e. loops) of wire that can be densely packed. The capacitance between windings can become non-negligible at higher frequencies. It will typically manifest as a drop-off in magnitude response at higher frequencies as well as phase discrepancy.

Another example is the capacitance between high-voltage electrodes/wires and the diagnostics. For example, a Rogowski coil is often wrapped closely around the wire it is measuring current in. If this wire also gets to high voltage and the frequency of the signal is high enough, signal from the high-voltage line can capacitively couple onto the Rogowski coil. A simple way to test for this is to obtain a signal with the Rogowski coil, then reverse its orientation, and obtain the same signal again. Since the coupled signal will have the same polarity regardless of the Rogowski coil's orientation, a distinct difference in signal strength depending on orientation will be present if the capacitive coupling is non-negligible.

These are just a couple of examples of parasitic capacitance that one must watch out for and is by no means a complete list.

Notes on skin-depth effects:

It is common for Rogowski coils and $\dot{B}$-probes to be constructed by winding the loops of the solenoid back over a central wire. Figure 5 below shows that this core wire is often in the plane of the loop through which a changing flux induces a voltage.

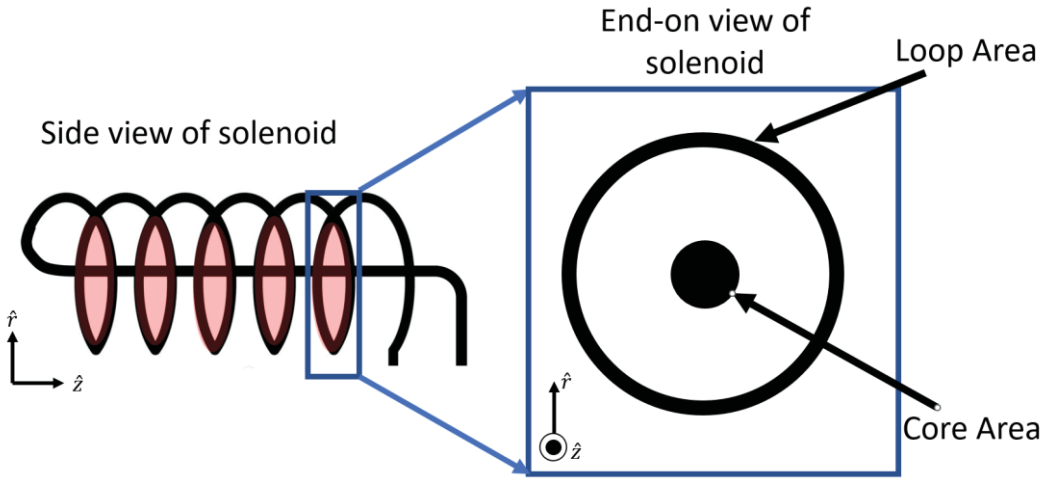

Figure 5: Diagram showing first a side view of a solenoid and then an end-on view down the solenoid to describe the core area (from which flux can be excluded due to skin-depth effects) relative to the loop area.

Magnetic field will only penetrate radially into the core up to about a skin-depth. Therefore, at higher frequencies, the loop area is actually reduced by some fraction of (or the entirety of) the core's area. This will manifest purely as a drop in magnitude response at higher frequencies. To approximate this change, we assume that magnetic field will penetrate exactly one skin depth, radially inward towards the core. We can approximate skin depth as

$$\delta \approx \sqrt{\frac{2\rho}{\omega\mu}}$$

Where ρ is the resistivity of the core's material (usually copper is a good assumption). When the skin-depth is less than the core's radius, flux will start being excluded and the magnitude response of the diagnostic will decrease. This can be modeled as a decrease in the effective area of the diagnostic as

$$A_{eff}(\omega) = A_{loop} - \pi\big(r_{core} - \delta(\omega)\big)^2$$

This can be accounted for in the geometric factor of the diagnostic by using an effective area ratio so that

$$\kappa_{eff} = \kappa_0 \left(\frac{A_{eff}(\omega)}{A_{loop}}\right)$$

Transmission line notes:

There are 2 primary effects introduced by a transmission line. The first is the potential for signal reflections (we will NOT have a matched source/line/termination system). This determines whether or not we need to do a fully distributed transmission line model. Second, the actual circuit parameters of the transmission line itself become relevant to the circuit depending on the length of the line and the frequency of the signal (note that the circuit parameters of the transmission line are also a determining factor in reflection considerations). As a first approximation, we can use the ratios of the transmission line's circuit parameters' impedances to the source and termination impedance to determine whether we can use a single lumped model for the line or if we have to distribute it. For intermediate cases we can get an accurate model by using a few distributed elements but again at higher frequencies it is necessary to use a fully distributed transmission line for an accurate model.

Consequently, there are 4 primary ways to treat a transmission line; resistive, lumped element, multi-element, and fully distributed. Which method is appropriate will depend on the relative impedances of the source, transmission line, and load in the targeted frequency range.

In many cases transmission lines can be ignored and this can easily be checked for by seeing if; A: the inductive impedance of the transmission line is very low compared to termination and source impedances, B: the capacitive impedance of the transmission line is high compared to termination and source impedances C: verifying that the wavelength of the

signal is much greater than the transmission line's physical length. Intermediate situations are detailed below but deciding what type of treatment is necessary is ultimately up to the designer and their requirements for accuracy.

Resistive treatment

If the transmission line's capacitive impedance is high compared to the termination impedance, and the inductive impedance is low compared to the termination impedance, then the transmission line can be treated as a resistive element (this is akin to a DC treatment) or ignored entirely if the transmission line's resistance is low enough.

Lumped element treatment

This treatment means modeling the transmission line using its bulk parameters. It is customary to model the transmission line as a "pi circuit" (we use this treatment later for our model validation in the analysis section). For example, for a 10' cable with 100 nH/ft and 100pF/ft, use a 1000 nH inductor in the circuit model with 500 pF capacitors on either side. For our requirements, this treatment is appropriate for cases where the cable's inductive impedance and/or capacitive impedance are of the order of 2% or more of the termination impedance.

Multi-element Treatment

This treatment is an intermediate case between the lumped element and fully distributed treatments. For a single element model, it was necessary that the cable's circuit impedances were a non-negligible fraction of the termination impedance. As a transmission line model is distributed, each element's capacitive impedance increases. If distributing the transmission line into a few elements can achieve the necessary ratios, then a multi-element treatment can be appropriate. Note that the accuracy of the circuit model will increase with additional elements.

Fully Distributed Treatment

In this case, the cable's capacitive impedance is of the order of the cable's inductive impedance. This can mean that the cable is attenuating the source signal in a non-negligible fashion. Here it is necessary to distribute the transmission line into many elements (usually done using a circuit modeling software like LTspice unless you write your own). In practice we use a fully distributed model as opposed to the analytic model, even though both are appropriate for our use case here.

Reflection Considerations

Another method of determining whether reflections must be considered depend on the time it takes for your signal to propagate across the transmission line and back compared to your signal's wavelength. If your signal's wavelength is much greater than the length of your transmission line, then you can ignore reflection effects and treat the transmission line using one of the reduced element models mentioned above. (Note that this is referred to as being an

"electrically short" line). Propagation velocity in a transmission line is given as $u_p = \frac{c}{\sqrt{\epsilon_r}}$ where ϵ_r is the relative permittivity of the transmission line's insulator (usually polyethylene where $\epsilon_r = 2.25$) and c is the speed of light in a vacuum. So for our case with RG-223, our wavelength for a $1MHz$ signal is

$$\lambda = \frac{u_p}{f} = \frac{2E^8\left(\frac{m}{s}\right)}{1Mhz} = 200m = 656\ ft$$

And if we have <u>at most</u> a 20 ft bnc cable, then for our case we should be well within the range to use one of the reduced model elements described above.

<u>Lossy transmission lines</u>

Cable resistance for RG-223 is given as approximately 0.015Ω/ft but because multiple connections can further increase resistance it is best to measure the actual resistance of the cable at DC. For skin effects in our analytic model (we do not use a lossy transmission line in the LTSpice software), we're currently using a relation I found on-line which, when compared to measurements seemed accurate enough beyond 200 kHz. The relation gives resistance per meter of a bnc cable as

$$R' = \frac{R_s}{2\pi}\left(\frac{1}{a} + \frac{1}{b}\right)$$

Where

$$R_s = \sqrt{\frac{\pi f \mu_0}{\sigma_{cu}}}$$

a (.445 mm) is the radius of the cable's inner conductor, b (1.475 mm) is the radius of the cable's insulator, f is frequency, and σ_{cu} (5.96e7 S/m) is the conductivity of copper. Note though that the cable's resistance is 0 at DC, which is clearly not correct. We should find or derive a better approximation of coax resistance at some point.

Part 3: Circuit modeling

<u>Integrator/probe analytic modeling:</u>

Here, we present an analytic model of the Rogowski coil. The model is easily adapted to work for both Rogowski coils and bdot probes. It is common to use passive integrators for these types of circuits, primarily to help eliminate high frequency noise and obtain a cleaner signal. Further, while the response of magnetic pickup diagnostics response varies proportionally with ω, the response of a standard integrator is inversely proportional to ω (for certain ranges) so an integrator can help maintain a more consistent signal strength over a range of frequencies. Therefore, the circuit model shown in figure 6 includes an integrator on

the measurement side. The induced voltage on the left side of the circuit is given by $\tilde{V}_{EMF} = \tilde{V}_{Rog} = -M\dot{\tilde{I}}_{prim}$ or in the frequency domain, $\tilde{V}_{Rog} = -j\omega M\tilde{I}_{prim}$, where $M = \frac{\mu\kappa_{Rog}}{2\pi}$ is the mutual inductance of Rogowski/primary line coupled system.

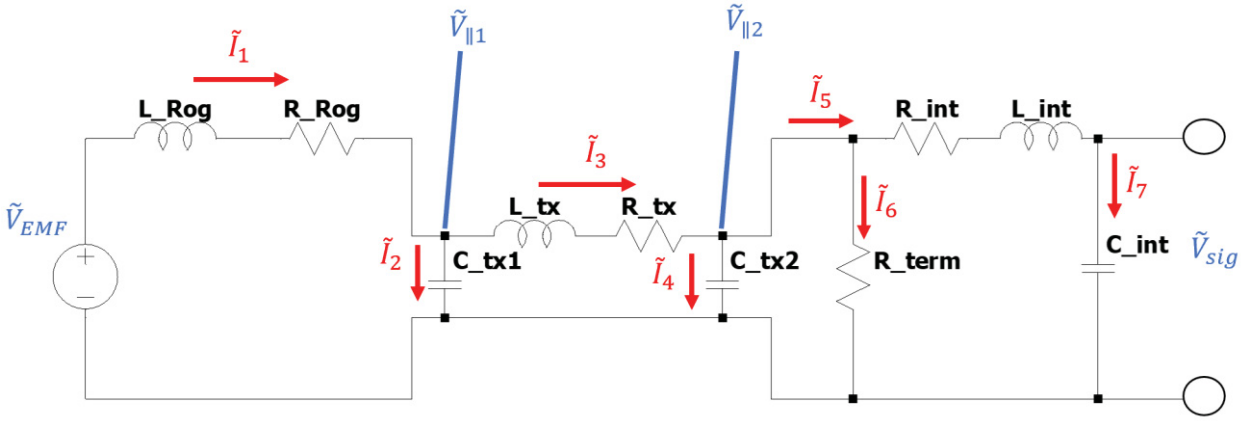

Figure 6: Circuit diagram for the analytic response derivation

Our goal is to get $\tilde{V}_{sig}/\tilde{V}_{EMF}$ so we can properly deconvolve our signal where $\tilde{V}_{sig}$ is the voltage signal picked up at the scope and $\tilde{V}_{EMF}$ is the voltage signal induced at the probe. We begin by defining some convenient equivalent impedances ($Z_{\|_1}$ and $Z_{\|_2}$) as labeled on the above diagram.

$$Z_{\|2} = \left[\frac{1}{Z_{C_{int}} + Z_{L_{int}} + R_{int}} + \frac{1}{R_{term}} + \frac{1}{Z_{C_{tx2}}}\right]^{-1}$$

$$Z_{\|1} = \left[\frac{1}{Z_{L_{tx}} + R_{tx} + Z_{\|2}} + \frac{1}{Z_{C_{tx1}}}\right]^{-1}$$

Using voltage division we can determine the signal voltage on the integration capacitor as

$$\tilde{V}_{sig} = \frac{\tilde{V}_{\|_2} Z_{C_{int}}}{R_{int} + Z_{L_{int}} + Z_{C_{int}}}$$

We continue to work backwards using voltage division again to define $V_{\|_1}$ and $V_{\|_2}$ as

$$\tilde{V}_{\|_2} = \frac{\tilde{V}_{\|_1} Z_{\|_2}}{Z_{L_{tx}} + R_{tx} + Z_{\|_2}} \qquad \tilde{V}_{\|_1} = \frac{\tilde{V}_{EMF} Z_{\|_1}}{R_{\dot{B}} + Z_{L_{\dot{B}}} + Z_{\|_1}}$$

Plugging in our definitions of $\tilde{V}_{\|_1}$ and $\tilde{V}_{\|_2}$ into the relation for $\tilde{V}_{sig}$, we can obtain the response function as

$$\frac{\tilde{V}_{sig}}{\tilde{V}_{EMF}} = \frac{Z_{\|_1} Z_{\|_2} Z_{C_{int}}}{\left(R_{\dot{B}} + Z_{L_{\dot{B}}} + Z_{\|_1}\right)\left(Z_{L_{tx}} + R_{tx} + Z_{\|_2}\right)\left(R_{int} + Z_{L_{int}} + Z_{C_{int}}\right)}$$

At this point the models for $\dot{B}$-probes and Rogowski coils diverge slightly due to the different interpretations of induced voltage. For Rogowski coils, the current in the primary line can be determined as

$$\tilde{I}_{prim} = \frac{2\pi}{\mu\kappa_{Rog} j\omega}\tilde{V}_{EMF} = \frac{2\pi}{j\omega\mu\kappa_{Rog}}\tilde{V}_{sig}\left(\frac{\tilde{V}_{EMF}}{\tilde{V}_{sig}}\right)$$

And for $\dot{B}$-probes, we get

$$\tilde{B} = \frac{1}{j\omega\kappa_{\dot{B}}}\tilde{V}_{EMF} = \frac{1}{j\omega\kappa_{\dot{B}}}\tilde{V}_{sig}\left(\frac{\tilde{V}_{EMF}}{\tilde{V}_{sig}}\right)$$

Where $\left(\frac{\tilde{V}_{EMF}}{\tilde{V}_{sig}}\right)$ is just the inverse of the integrator's response function derived above.

Integrator/probe spice modeling:

If analytic modeling is not accurate enough for a given frequency range/circuit setup, then a spice analysis may be necessary. We use LTSpice XVII for the following analysis. Below we see a spice model in figure 7 where the transmission line has been modeled using Spice's built-in lossless transmission line.

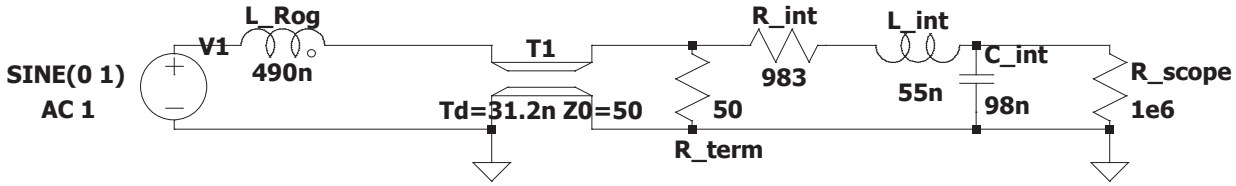

Figure 7: LTSpice XVII model for a rogowski/integrator combo

The values used are the measured values from a Rogowski/integrator combination used in the lab. Note for this model that we neglect Rogowski coil and transmission line resistance. The process of getting the response from LTSpice XVII into a useable form for signal deconvolution can be somewhat unintuitive, so here we will go into some detail on the process.

The first step is obviously to create the circuit model in spice. The settings for the voltage source should be set as seen in figure 8. Once the circuit is created and the voltage source settings are input, the simulation command settings must be input. To access them, either click "edit" on the upper bar and then select SPICE analysis, or right-click on the simulation object in the circuit diagram (as shown in figure 9).

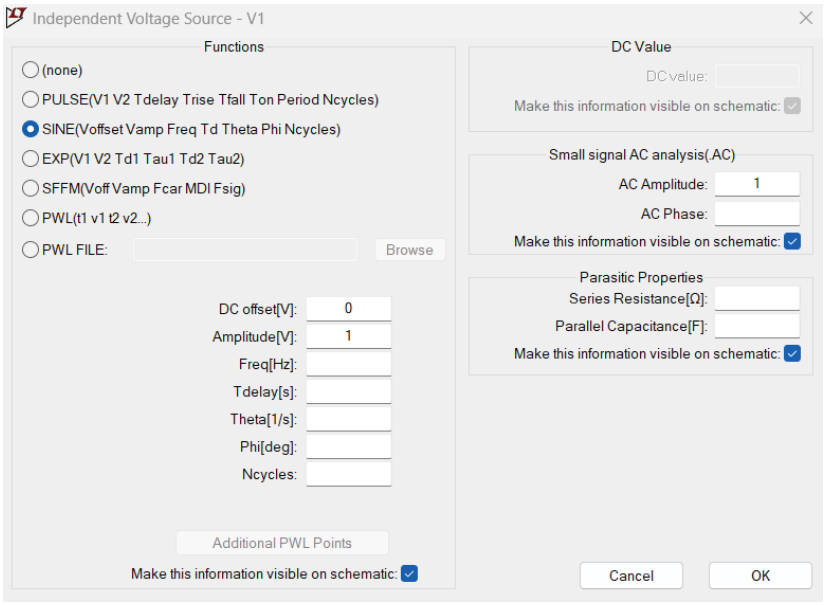

Figure 8: Settings for the supply voltage in the SPICE simulation

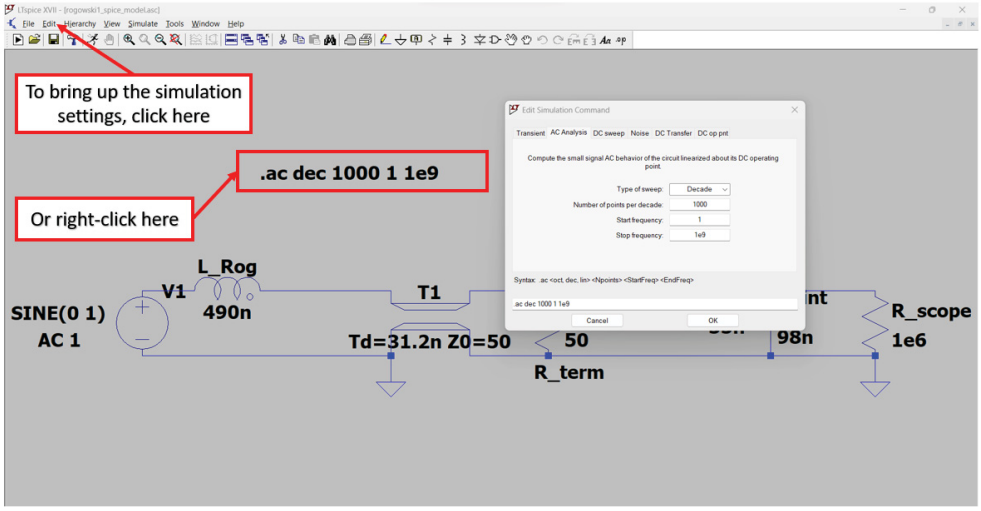

Figure 9: How to edit the simulation command in LTSpice XVII

This brings up the "edit simulation command" box. To get the response function equivalent to the analytic version derived above, select "AC Analysis" from the upper bars in the box. Typically for these purposes, using a "decade" sweep with 1000 points per decade from 1 to 1e9 Hz is sufficient. Note that incorrect settings will results in incorrect circuit analysis. Insufficient resolution (number of points per decade) or improper frequency range (setting too high of a start frequency or too low of a stop frequency) can be troublesome to diagnose so ensure that these are correctly set.

Once the circuit is properly constructed and the simulation commands are set, the simulation can be run by clicking the little running guy icon below the upper-most selection bar or by selecting "simulate" in the upper-most selection bar and selecting "Run". Once this is

done a blank plotting screen should appear (if the simulation ran without issue). Clicking on the node that joins the integration capacitor and scope resistor (C_int and R_scope in figure 6) should yield a curve similar to the one seen in figure 10 (assuming the circuit parameters are similar).

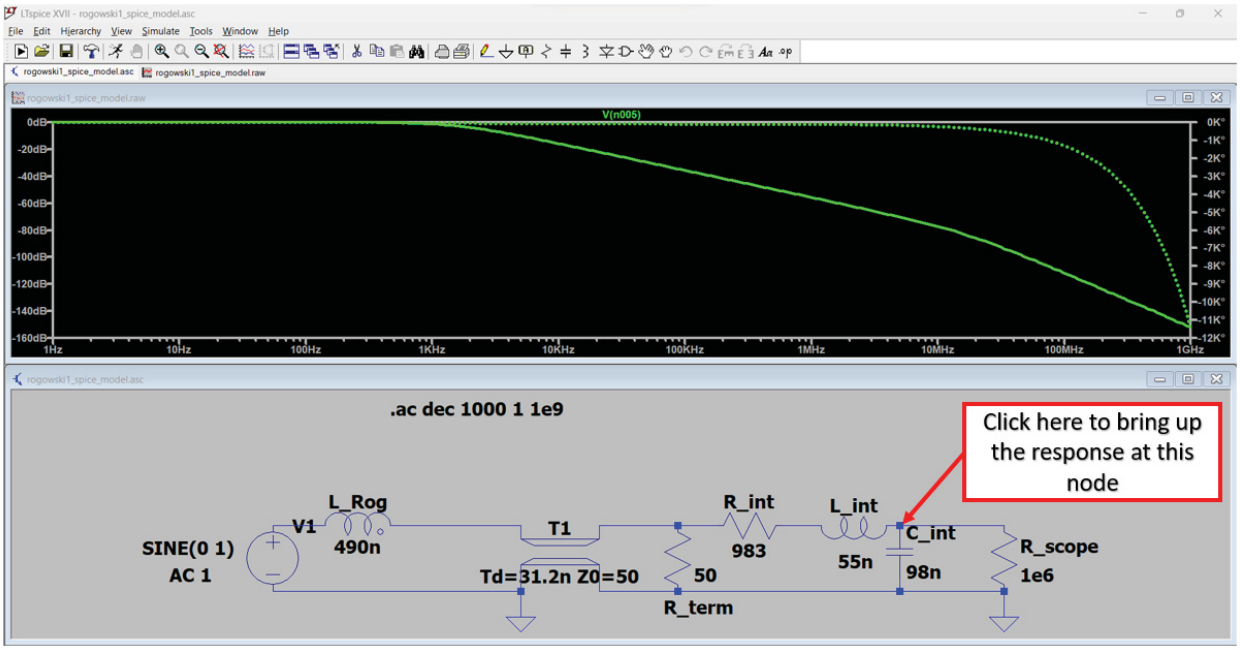

Figure 10: Click on the node at the scope's measurement point to get the circuit's response so the induced voltage on the probe

Once this is done it is time to export the response. FIRST CLICK ON THE PLOTTING WINDOW (otherwise the following commands will not be available). Once the plotting window is selected, click “File” in the upper selection bar and select “Export data as text”. This will bring up the window seen in figure 11. It will automatically select the trace in the plotting window as the data to export. Use the “Polar” format as this will be much easier to interpolate than the complex response. Select the name for the data file in the top bar on the window. Once this is done the data will be written to a text file with the selected name.

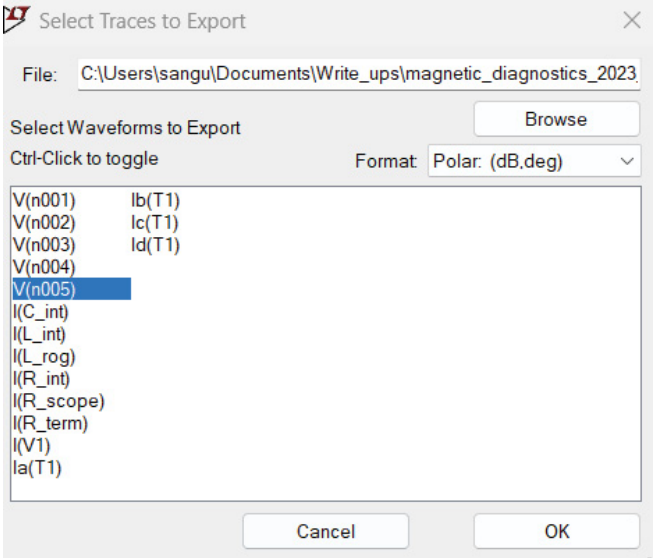

Figure 11: Data exportation window

The output format of the data will be as shown in figure 12. Due to the odd choices (I don't know why they didn't choose to simply use a comma-separated format with a descriptive header) the data will have to be carefully parsed. The first column is the frequency value in Hertz, the second column is the magnitude response in decibels, and the third column is the phase angle in degrees. The reference value for the magnitude response's decibel format is the voltage amplitude of the voltage source in the spice simulation (if you've been following this guide, $V_{source} = 1\ V$). Therefore, to get the voltage value, the relation is

$$\frac{V_{sig}}{V_{src}} = 10^{\frac{V_{dB}}{20}}$$

if your voltage amplitude was properly set in the spice simulation then $V_{src} = 1$

```
Freq.    V(n005)
1.00000000000000e+000   (-8.85699281678731e-003dB,-3.59804550855129e-002°)
1.00230523807790e+000   (-8.85700170100759e-003dB,-3.60633985698254e-002°)
1.00461579027840e+000   (-8.85700963519070e-003dB,-3.61465332740502e-002°)
1.00693166885180e+000   (-8.85701859248989e-003dB,-3.62298596064321e-002°)
1.00925288607668e+000   (-8.85702462711897e-003dB,-3.63133780475147e-002°)
1.01157945425990e+000   (-8.85703365816795e-003dB,-3.63970889985723e-002°)
1.01391138573668e+000   (-8.85704173986128e-003dB,-3.64809929338271e-002°)
1.01624869287070e+000   (-8.85704985886100e-003dB,-3.65650902846585e-002°)
1.01859138805412e+000   (-8.85705801533411e-003dB,-3.66493815024621e-002°)
1.02093948370768e+000   (-8.85706620945534e-003dB,-3.67338670259147e-002°)
1.02329299228075e+000   (-8.85707542788963e-003dB,-3.68185473053877e-002°)
```

Figure 12: Example of polar data output for a trace from LTSpice XVII

Once parsed the data normally must be interpolated for a specific set of frequencies to be useful. For example, the frequency array obtained when taking the Fourier transform of a voltage over time data set recorded by an oscilloscope or other digitizer is a commonly used set of frequency values. Since there is a negative half of the frequency array created in the interpolation script, fully understanding the interpolation script requires a basic understanding of the discrete Fourier transform, so refer to the signal processing section of this write-up as needed.

We now have the polar format of the circuit's response from the SPICE simulation at the desired set of frequencies. The final step is to convert it back to its complex form. The response is given to us in the polar format so that

$$\frac{\tilde{V}_{sig}}{\tilde{V}_{Source}} = \left|\frac{\tilde{V}_{sig}}{\tilde{V}_{Source}}\right| e^{\left(\frac{i\theta\pi}{180^{\circ}}\right)}$$

Where $\frac{\tilde{V}_{sig}}{\tilde{V}_{Source}}$ is our desired complex response, $\left|\frac{\tilde{V}_{sig}}{\tilde{V}_{Source}}\right|$ is the magnitude response given by SPICE (after converting from decibels as detailed above), and θ is the phase angle in degrees given by SPICE. In order to get the complex form, we simply perform the calculation shown in the above equation. Note that for the negative portion of the frequency array, the complex conjugate of the above relation is used. With this done, the final product should be a more accurate circuit response when compared to the analytic derivation above (provided transmission line resistance is negligible).

Comparison of analytic and spice models:

Here we use data taken by a bdot probe on the machine for comparison. The bdot probe is measuring the field produced by a bias discharge in the radial and axial center of the coil set. Plotted below are the interpreted field strength from the signal voltage for both analytic and spice simulation deconvolution using a digital 1, 25, and 35 MHZ low-pass filter (shown in figures 13, 14, and 15 respectively). As would be expected, the analytic solution becomes less accurate when interpreting high frequency values. This is due to its low-resolution approximation of the transmission line. It should be noted though that for 1MHz the solutions are identical so that this analytic approximation can likely work for many conditions in this lab and others.

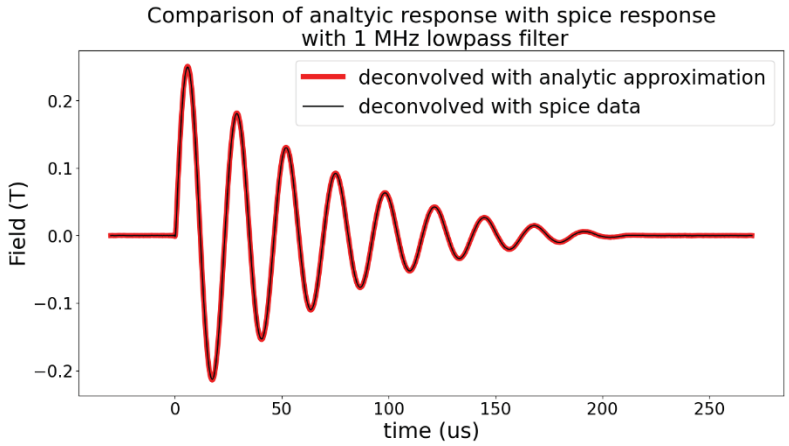

Figure 13: Analytic vs spice signal deconvolution with 1 MHz digital low-pass filter

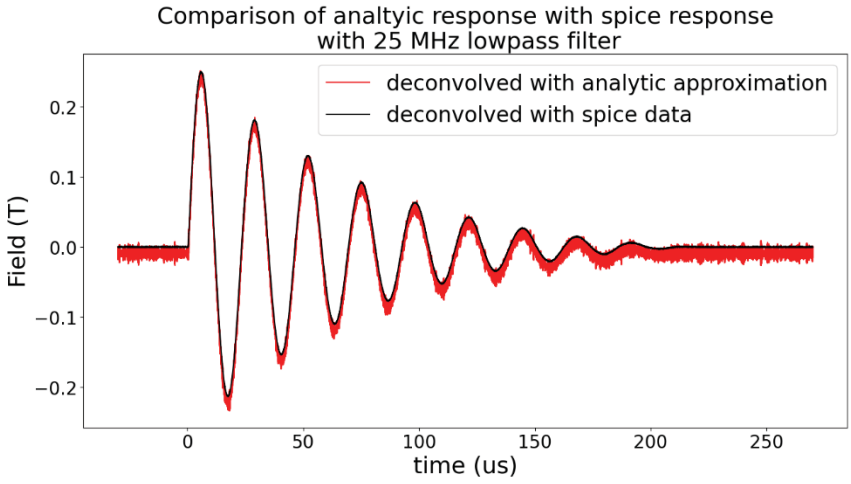

Figure 14: Analytic vs spice signal deconvolution with 25 MHz digital low-pass filter

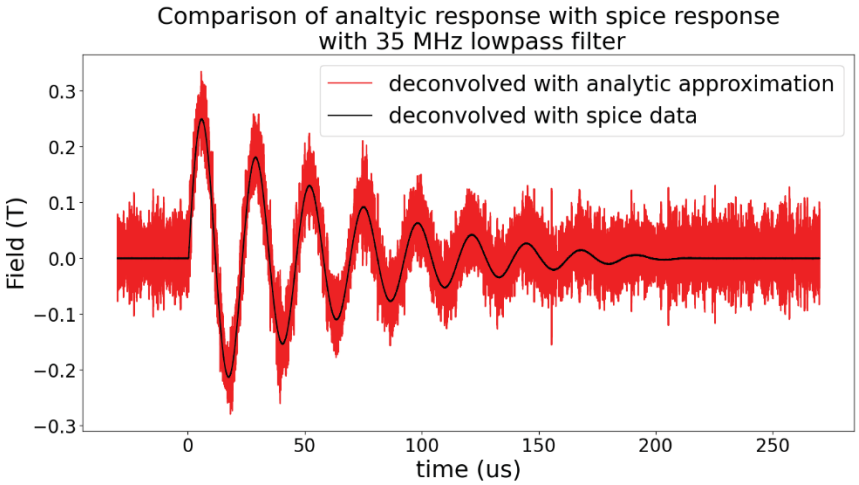

Figure 15: Analytic vs spice signal deconvolution with 35 MHz digital low-pass filter

Part 4: $\dot{B}$-probe design and calibration procedure

Isolating and measuring $\kappa_{\dot{B}}$

Here we cover the calibration process of a $\dot{B}$-probe. Our goal is to experimentally determine $\kappa_{\dot{B}}$ (the area-turns value) of the $\dot{B}$-probe. First, we look mathematically at how to isolate $\kappa_{\dot{B}}$. From our analysis in the physics section above, we know that $V_{EMF}(t) = \kappa_{\dot{B}}\dot{B}(t)$. If we use phasor notation (assuming that $\dot{B}(t)$ is sinusoidal) then we can equivalently state

$$\tilde{V}_{EMF} = \kappa_{\dot{B}} j\omega \tilde{B}$$

Where the tilde indicates a sinusoidally varying value such that

$$\tilde{V} = V_0 e^{j(\omega t+\phi_1)} \text{ and } \tilde{B} = B_0 e^{j(\omega t+\phi_2)}.$$

However, during the actual calibration process, we will only be measuring real magnitudes and potentially phase difference if desired. It is prudent to briefly analyze the circuit formed by the probe and scope before proceeding. In practice, measuring a signal from a $\dot{B}$-probe using a high impedance termination on a scope can tend to amplify high-frequency noise, making the intended signal more difficult to isolate. Therefore, in the calibration process we generally use a 50 Ω termination on our scope. If the transmission line between the probe and the scope is negligible (use the appropriate transmission line treatment from the section above to determine if it is, for the calibration setups used for MTX probes the transmission line is negligible), then the circuit can be approximated as shown below in figure 16.

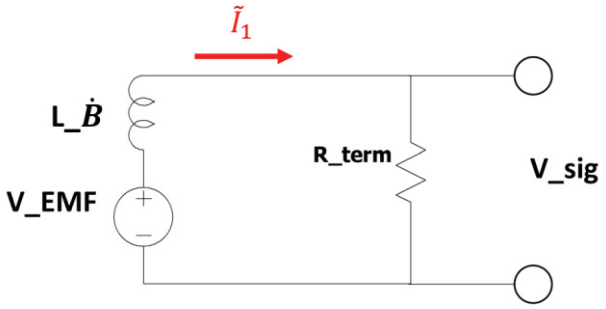

Figure 16: Circuit diagram of a probe/scope combination, neglecting transmission line components

To obtain the EMF voltage from the signal voltage we use the following relations

$$\tilde{V}_{sig} = R_{term}\tilde{I}_1, \qquad \tilde{V}_{EMF} = Z_{tot}\tilde{I}_1, \qquad Z_{tot} = j\omega L_{\dot{B}} + R_{term}$$

Eliminating $\tilde{I}_1$ between the first two equations yields a simple response function.

$$\frac{\tilde{V}_{EMF}}{\tilde{V}_{sig}} = 1 + \frac{j\omega L_{\dot{B}}}{R_{term}}$$

Here we can note that the response function is quite simple indeed. The real part of the response is just 1, and the inductance of the probe only serves to introduce a frequency dependent phase shift relative to the source voltage (the imaginary part of the response). It's worth noting that for those without an LCR meter available for measuring inductances, the above relation can be used to determine the probe's inductance by measuring the phase difference and applying the full complex response. Since we have an accurate LCR meter for measuring probe inductance, we can dispense with the phasor notation since we will only be measuring magnitudes and state more simply that

$$V_{0_{EMF}} = V_{0_{sig}} = \kappa_{\dot{B}} \omega B_0$$

Where V_0 represents a peak magnitude value. In practice, a more accurate value of the average peak signal voltage can be obtained by using the RMS measurement on a scope, so keeping that in mind and rearranging the above to solve for $\kappa_{\dot{B}}$, we then say that

$$\kappa_{\dot{B}} = \frac{V_{RMS_{sig}}}{\omega B_{RMS}}$$

A final note on this is that if the wire in the core is of non-negligible diameter compared to the loop diameter, then flux exclusion (as discussed in the section above) must be accounted for. This effect makes it such that $\kappa_{\dot{B}}$ becomes frequency dependent but its frequency dependence can be isolated in the "effective area" term so that

$$\kappa_{\dot{B}}(\omega) = \kappa_{0_{\dot{B}}} A_{eff}(\omega)$$

If this term is separated out then one can also say that

$$\kappa_{0_{\dot{B}}} = \frac{V_{RMS_{sig}}}{\omega B_{RMS} A_{eff}(\omega)}$$

Where $A_{eff}(\omega)$ is defined in the earlier flux exclusion section. On the $\dot{B}$-probes primarily used for MTX this effect accounts for ~10% variation in the probe's response and is therefore vital to account for.

Helmholtz coil theory:

The relation above indicates how to determine $\kappa_{0_{\dot{B}}}$. V_{RMS} and ω can be determined by measuring the voltage wave-form induced on the $\dot{B}$-probe but this still leaves the determination of B_{RMS}. For this, we use a Helmholtz coil, a diagram of which is shown in figure 17.

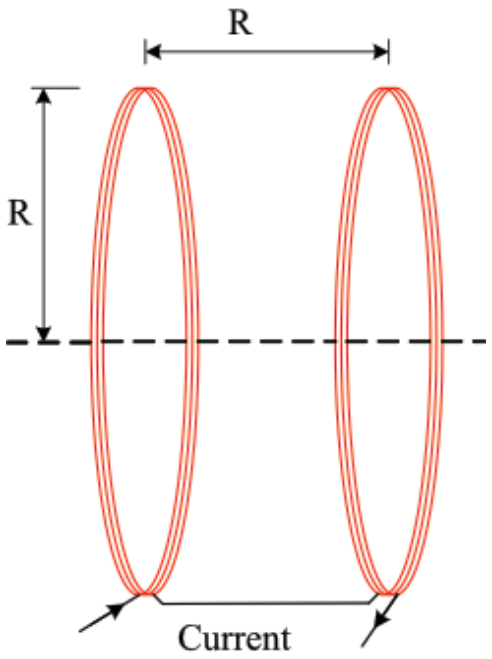

Figure 17: Basic diagram of a Helmholtz coil

A Helmholtz coil is an assembly of two axially collocated coils connected in series. Their loops have a radius R and they are separated by that same distance R. Helmholtz coils are useful because they produce a relatively uniform magnetic field in the center between them. If a constructed Helmholtz coil is close enough to the ideal model, the field strength at the axial and radial center of the two coils can be considered a known value. A Helmholtz coil will produce an axial field that has a very uniform field over a large axial range at its radial center. Specifically, the magnetic field strength along the coil's radial center (along z at $r = 0$) is given by the following relation.

$$B_z(z) = \frac{\mu_0 I N R^2}{2}\left(\frac{1}{\left(R^2 + \left(\frac{R}{2} + z\right)^2\right)^{\frac{3}{2}}} + \frac{1}{\left(R^2 + \left(\frac{R}{2} - z\right)^2\right)^{\frac{3}{2}}}\right)$$

Where I is the current in the coil, and N is the number of turns on each side of the Helmholtz coil (not their combined total). Generally, it is prudent to design a Helmholtz coil that suits the needs of the $\dot{B}$-probe(s) to be calibrated. When it comes to determining whether the above relation is applicable, the assumptions of an ideal Helmholtz must be analyzed to determine if they apply to the Helmholtz design being considered. First is the assumption that the field is radially uniform over the area that the $\dot{B}$-probe is measuring the field. Provided the radius of the Helmholtz coil's loops is much greater than the radius of the $\dot{B}$-probes loops, this assumption is valid. Second, it is assumed that the wires forming the loops of the Helmholtz coil are infinitely thin. If the radius of the Helmholtz coil's loops is much greater than the

diameter of its wires (and the wires are tightly wound over a small area) this assumption is valid. Finally, it is assumed that winding-to-winding capacitance of the Helmholtz coil's loops is negligible. Whether this assumption is valid or not is difficult to say based on a design but it straightforward to determine experimentally. The frequency range in which the winding-to-winding capacitance of the Helmholtz coil must be characterized.

It is important to note that at higher frequencies, driving the necessary current for calibration can require high voltages that may punch through the magnet wire's insulation or exceed power supply output capability. The inductance of the Helmholtz coil can be estimated (it's always better to measure if possible though) by approximating it as two ideal solenoids connected in series, where each coil's inductance is modified by the Nagaoka coefficient as described in Part 1 above. Therefore, we can approximate the inductance using

$$L = 2C_{NF}\frac{\mu N^2 \pi R^2}{l}$$

Where C_{NF} is the Nagaoka coefficient, N is the number of turns on EACH side of the Helmholtz (not their combined total), R is the radius of the Helmholtz coil's loops. And l is the length of each solenoid (not the length between them).

Helmholtz coil characterization:

Because Helmholtz design will often be iterative at first, we describe the characterization process and its necessity before discussing design. Characterizing a Helmholtz coil is a process in which the functional frequency range (where winding-to-winding capacitance is negligible) is determined. The characterization process is relatively straightforward. Using a resistive load in series with a Helmholtz coil, the voltage output of both the RF supply and the voltage drop across the resistive load are measured. The physical setup is shown in figure 18 below. The results from these measurements are compared to the results of a simple spice simulation the circuit for which is shown in figure 19 (see Part 3 for information on how to use SPICE simulation outputs). It is assumed that winding capacitance is the first most dominant parasitic not included in the circuit diagram so that deviation of measured values from the simulated response will indicate the presence of non-negligible winding capacitance effects.

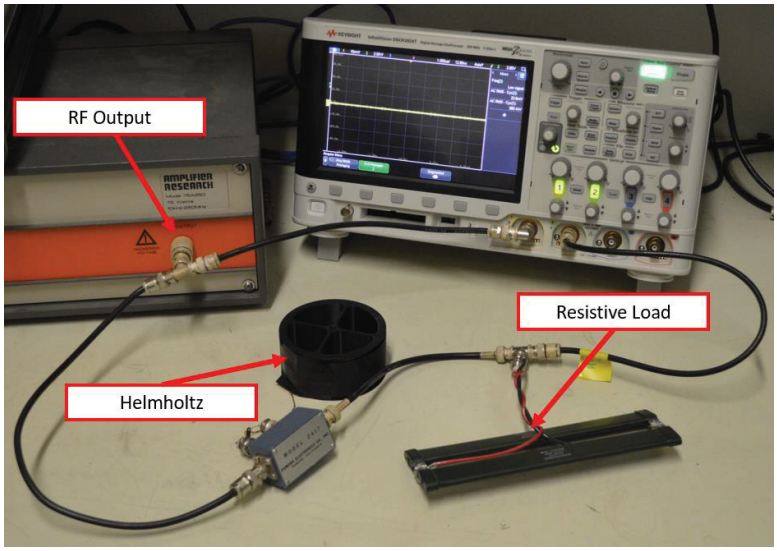

Figure 18: setup for helmholtz coil characterization

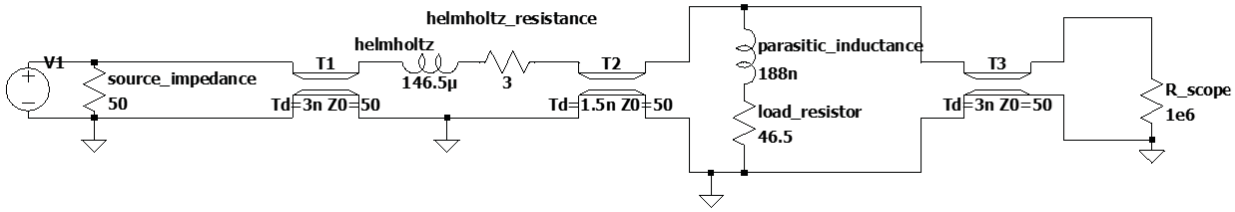

Figure 19: SPICE circuit against which measured results are compared

The resistance and inductance of the Helmholtz coil was determined using an LCR meter. The same was done for the resistive load, yielding the values seen in the circuit diagram above in figure 19. Two different Helmholtz coils were compared, each with the same nominal diameter and number of turns but with different thicknesses of insulation. The Helmholtz coil on the left of figure 20 uses thinly insulated magnet wire while the one on the right uses thickly insulated jumper wire.

Figure 20: Left - a helmholtz coil made using thinly insulated magnet wire, right - a helmholtz coil of the same dimensions as the one on the left but made with thickly insulated jumper wire

The comparison of the measured results vs. their respective spice simulations are shown in figure 21. (Note that the lower experimental frequency range is limited by equipment). Close inspection of the magnitude responses will show significant deviation for the magnet wire Helmholtz at around 500 kHz while the jumper wire Helmholtz doesn't significantly deviate until around 2 MHz. In practice it is prudent to set a "safety-factor" on the coil's upper frequency limit to minimize error (the next section shows that using a limit 40% below the frequency determined with this method is sufficient). This process determines the upper frequency limit to which a Helmholtz coil may be used. The primary advantage of using the lower frequency magnet wire Helmholtz is because it actually produces a field strength much closer to that of ideal Helmholtz coil field predictions (the assumption that the Helmholtz's windings are not spatially distributed is more valid for the magnet wire version). Therefore, the low-frequency Helmholtz will provide a more accurate calibration for probes (provided it is used within its operational frequency).

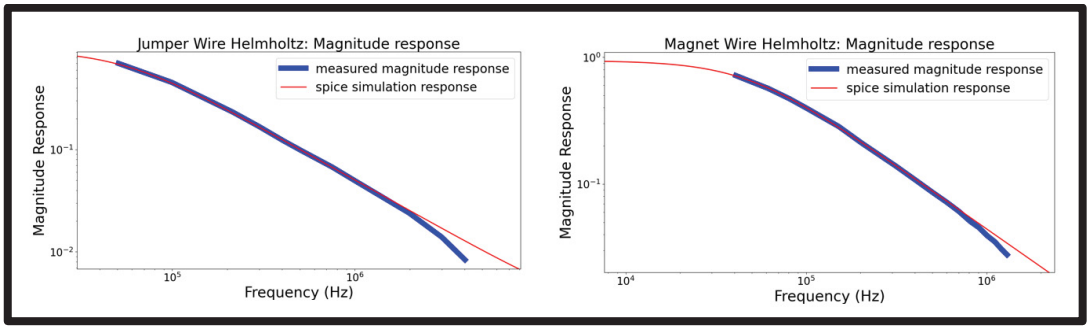

Figure 21: Measured Helmholtz response vs. ideal simulated response for: left- thickly-insulated jumper wire Helmholtz coil, right - thinly-insulated magnet wire Helmholtz

$\dot{B}$-probe and Helmholtz coil design:

Used as an example here are the $\dot{B}$-probes designed for mapping the distribution of the OMF field (producing tens of mT field strengths at ~350 kHz). Since the probes are measuring a relatively low signal compared to those produced by the main system and are not constrained by the coils' 3D-printed frame geometry, larger diameter probes were designed which required a corresponding Helmholtz coil design.

The new bdot probes were made using about 12 turns of 26 AWG magnet wire over a length of ~0.45 inches and with a diameter of approximately 0.165", yielding a theoretical area-turns constant of ≈ 1.65·10^(-4) m^2. To calibrate these new probes, a Helmholtz coil was made using a 3d printed frame. The Helmholtz coil was made with 20 turns of 24 AWG magnet wire, has a 3.165" loop diameter, theoretically produces a uniform 0.447 mT/A over an inch of length, a Nagaoka coefficient of ~ 0.12, and has a measured inductance of 167 uH. Figure 22 displays pictures of both the $\dot{B}$-probe (left) and the Helmholtz coil (right).

The Helmholtz coil was designed so that; 1: its loop diameter was much greater than the the loop diameter of the Bdot probe (~20 times greater), its windings don't occupy a significant cross-sectional area (20 turns of 26 AWG magnet wire has a cross-sectional area of ~$4E^{-6}\ m^2$ compared to the $\sim 1.6E^{-3}\ m^2$ cross section area of the Helmholtz's loop and separation plane), and its region of uniform axial field spans a length twice that of its associated $\dot{B}$-probe length. Its absolute current limit will be approximately 0.577 A based on its wire thickness and its voltage limit specified by the manufacturer is 4850V. In practice, significant safety factors are used for both of these limits.

The ideal field distribution of the Helmholtz coil (using the equation from the Helmholtz theory section) calculated for these parameters is shown in figure 23 (left shows the ideal field strength produced while right shows the normalized variation in field strength). An ideal Helmholtz coil made with the above parameters will produce approximately 0.447 mT/A and its field strength will vary less than 0.5% over the 0.45" length of the $\dot{B}$-probe to be calibrated. It should be noted that the Helmholtz coil used here is the same magnet wire one characterized in the previous section, so that it's upper operable frequency limit is 200 kHz.

Figure 22: Left - Probe made for field mapping, Right-Helmholtz coil made to calibrate the new probes

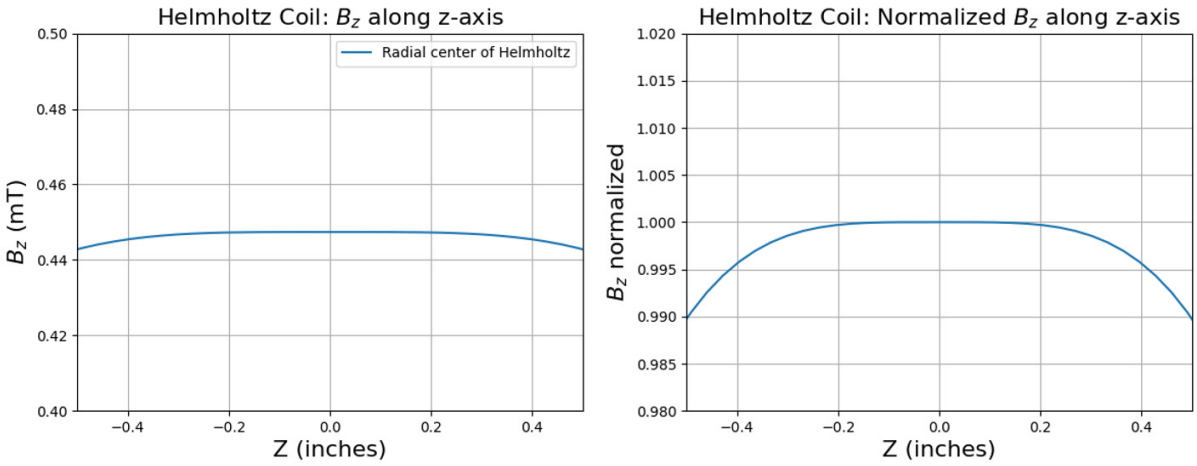

Figure 23: Left - Field strength ideally produced by Helmholtz coil with 1 Amp of current, Right - Normalized variation in field strength.

$\dot{B}$-probe calibration process:

We continue to use the field mapping probes as an example in how the calibration process is performed. The calibration setup is shown in figure 24 and its corresponding circuit diagram of the helmholtz portion of the circuit is shown in figure 25. One may note that this is the same circuit setup as the characterization process of a helmholtz coil but without measuring RF supply output (and now measuring the voltage induced on a bdot probe inserted into the Helmholtz coil).

The steady state calibration signal is produced by a Hewlett-Packard 3312A function generator which is amplified to higher signal strength using a Model 75A250 RF amplifier made by Amplifier Research which has a nominal output impedance of 50 Ω. The output of the amplfier is connected to the Helmholtz coil in series with a 47.2 Ω load resistance whose parasitic inductance was measured with an LCR meter. The bdot probe is inserted into the center of the Helmholtz coil. The scope was set to use $1\ M\Omega$ inputs and measure the voltage across both the resistive load and the B-dot probe.

From here, the data of frequency, load voltage, and probe voltage are gathered for varying frequencies. We can determine current through the Helmholtz coil from the voltage on the resistive load and field produced for the given current using the previously determined value of 0.447 mT/A of the Helmholtz coil. Then, we can use the relation for determining $\kappa_{0_{\dot{B}}}$ of a $\dot{B}$-probe derived above as

$$\kappa_{\dot{B}} = \frac{V_{RMS_{sig}}}{\omega B_{RMS}}$$

Noting that the core area is much smaller than the loop area for these particular probes so the effective area correction factor discussed earlier is not necessary.

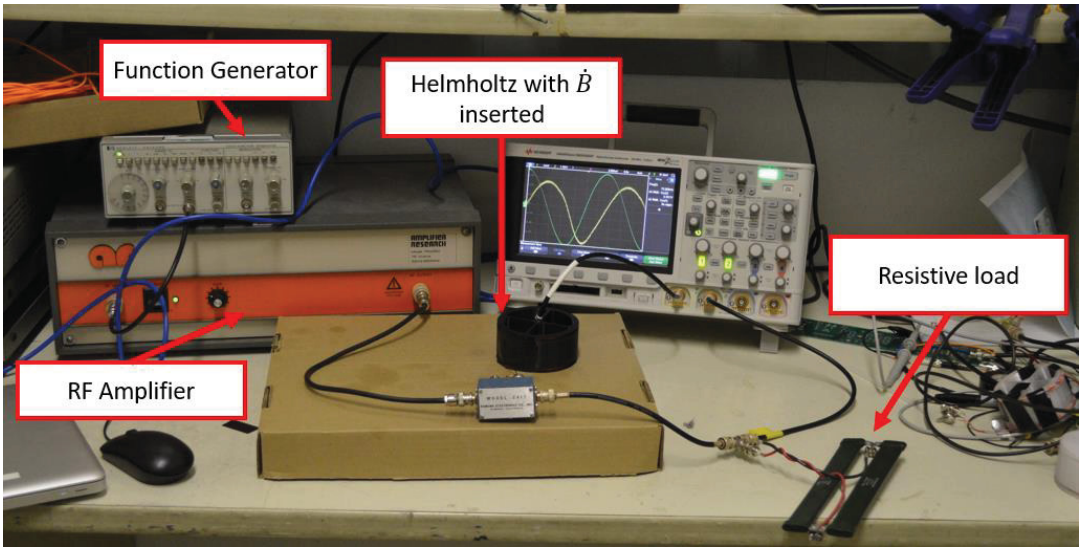

Figure 24: Physical setup of the calibration process for a B-dot probe

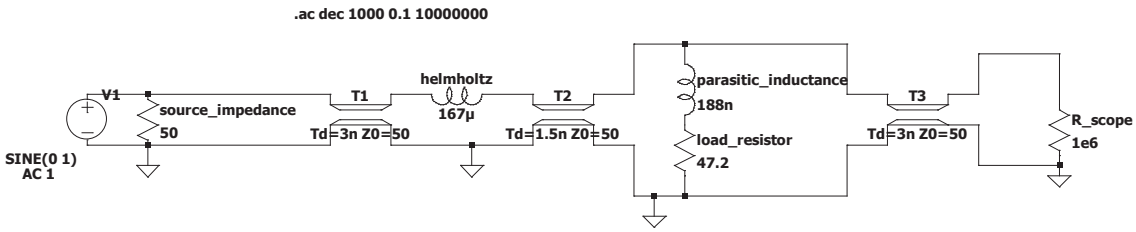

Figure 25: Circuit diagram of the Helmholtz coil portion of the circuit

Figure 26 displays the results of calibrating "Bdot-11" (one of the $\dot{B}$-probes made for the field mapping procedure) using both the magnet-wire Helmholtz and the jumper-wire Helmholtz. First noted is the off-set between the two calibration curves. This is expected as the thickly insulated wire Helmholtz is expected to deviate significantly from its ideal field distribution because the assumption of infinitely thin wire and their distribution is violated. However, the calculated calibration constant for it varies less than 0.5% across the measured frequency range. The calibration curve produced by the magnet wire Helmholtz varies across the entire measured frequency range but this is also expected due to the results of its characterization process which determined that beyond 500 kHz the winding capacitance becomes a significant factor. Still, a variation of ~3% of the calibration constant is seen between 40-500 kHz with a trend matching that shown above 500 kHz which implies the 3% variation is linked to winding capacitance effects on the Helmholtz coil. This shows that it is prudent to use a "safety factor" when setting the upper limit of Helmholtz coils. Closer inspection here reveals that the calibration constant varies less than 0.5% between 40 kHz and

200 kHz so setting the actual frequency limit of the Helmholtz coil to approximately 40% of that determined in the characterization process should be sufficient.

Given the above analysis, we obtain the calibration constant of the bdot probe by taking the average of the measured points between 40 and 200 kHz for the thinly insulated $\dot{B}$-probe to be the here as $\kappa_{0_{\dot{B}}} \approx 1.553E^{-4}\ m^2$ (recall that the theoretically predicted constant was of $\kappa_{\dot{B}_{ideal}}$≈ 1.65·10^(-4) m^2 which serves as a good sanity check). Further, we can reasonably expect this calibration value to be accurate up to at least $1\ MHz$, satisfying the stated design requirements Part 2. In order to account for any other unquantified errors in the calibration process we state that the probe is accurate to at least 5% in magnetic field measurements up to $1\ MHz$.

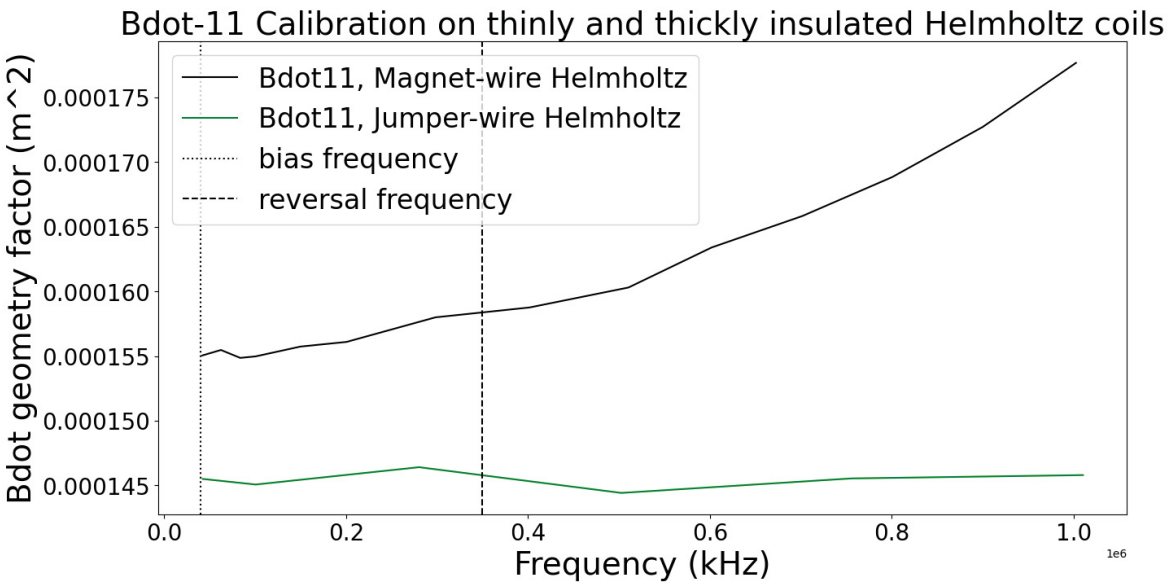

Figure 26: Calibration curves determined for Bdot11 using the thinly insulated magnet wire Helmholtz (black) and the thickly insulated jumper Helmholtz (green)

Part 5: Flux Loop Design

As stated before, the flux loop is conceptually the simplest diagnostic. The voltage induced on the loop is directly related to the rate of change of flux in it as

$$V(t) = \frac{d\Phi(\mathrm{t})}{dt} = A_{fluxloop}\frac{dB(t)}{dt}$$

Or in phasor notation as

$$\tilde{V} = j\omega\tilde{\phi} = A_{fluxloop}j\omega\tilde{B}_z$$

Fluxloop calibration and sources of error:

Although a flux loop can technically be calibrated using a known time-varying flux, producing a well-known flux on the size scale of a flux loop can be cumbersome. Further, the dimensions of a flux loop are usually easily measured so that the error in the flux loop's "calibration" ($\kappa_{fluxloop} = A_{fluxloop}$) will be on the scale of the error in its radius($r_{fluxloop}$) measurement squared, i.e.

$$\delta\kappa_{fluxloop} = O\left(\left(\delta r_{fluxloop}\right)^2\right)$$

Therefore, rather than having any calibration procedure for flux loops, its error in area is simply estimated using the above based on the radial measurement uncertainty. Additional sources of error in the area measurement can exist if one is not careful though. For example, if a twisted wire pair with thick insulation is used to lead back to a transmission line, they can form unintended pickup loops near the measurement point that increase error. Proper shielding of any such twisted pairs can help minimize this source of error.

High voltage division and voltage coefficients

Flux loops on the MTX machine are presented with a unique challenge due to the fact that the reversal discharge is both high field strength and high frequency (~2.5 T at ~350 kHz) over the area of the flux loop which has a diameter of ~10 cm. Simple calculation will show this can induce voltages on the order of 50,000 V. Accurately measuring a 50,000 V signal at ~350 kHz can be difficult to put it bluntly. It should be noted that using a loop with no resistance and measuring the current through it is not a valid option since the flux loop will then act as a flux conserver and change the field distribution produced by the main coils.

The primary difficulty of measuring such a signal is that the circuitry used to divide out the signal must maintain a well-known impedance value under the application of high voltages. Capacitive division is an option but capacitance actually varies as a function of applied voltage (particularly at high voltages) as the dielectric material has voltage dependent permittivity and the capacitor itself may even flex due to electrostatic forces. Inductors do NOT have any voltage dependent characteristics but it turns out in practice that designing an inductive divider

with sufficiently high inductive impedance that does not arc through insulation at high voltage or suffer from parasitic capacitance effects is a challenging design problem. Resistors also tend to have voltage dependent characteristics but there are a large variety of resistor materials available in market so it was decided to test some high voltage resistors for this application. Several varieties of resistors were tested on MTX to find suitable resistors.

Resistive divider testing on MTX

The change in the resistance value of a resistor due to the application of voltage is referred to as its "voltage coefficient of resistance" or VCR. The simplest way to determine if VCR effects are negligible is to test a flux loop divider with two or more of the same resistors in series and obtain data for both a ringing bias and a ringing reversal discharge. Then use only one of the resistors and obtain the same data. If VCR effects are negligible, then the processed flux measurement from each test should match. If the processed flux measurement does not match then VCR effects are non-negligible. (Note that parasitic inductance may also need to be accounted for depending on the divider's resistance, size, and the frequency of the applied pulse). Examples of this testing are included below.

HVRAPC resistor testing for Flux Loop

Testing was first performed on January 30th, 2023 using the same high-voltage resistors used for charging and dumping capacitor banks on MTX. Specifically, these are HVRAPC brand resistors with model number T2530C683K-O, with a voltage rating of 52,000 Volts and a resistance value of 68.3 $k\Omega$ (+/- 10%) shown below in figure 27. A divider was constructed using two of these resistors in series and a spice model of the entire circuit is shown in figure 28.

Figure 27: One of the HVRAPC resistors tested for VCR

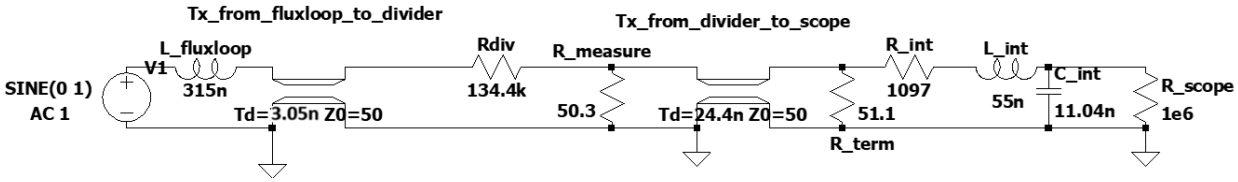

Figure 28: Circuit model of the HVRAPC resistive divider for flux loop

In series the resistors measured 134.4 $k\Omega$ and with one shorted the resistance used was 72.3 $k\Omega$. According to the spice model above, the change in voltage signal magnitude from using 72.3 $k\Omega$ (one resistor) to 134.4$k\Omega$ (two resistors) is different by a factor of 1.86 and the change in phase response between the different resistance values is negligible. Therefore, if

VCR effects are negligible then the difference in voltage signal between the two setups should be different by a factor of 1.86. Figure 29 below displays the results with the voltage from the 134.4 $k\Omega$ resistive divider scaled up by 1.86 for a bias discharge. The two traces clearly do not match and it is concluded that for these resistors VCR effects are non-negligible. In particular, note that the voltage induced on the flux loop for the bias discharge shown is only about 600 volts (0.3T peak field at 40 kHz). Since these resistors are designed primarily for use as energy dissipation in capacitor charging/dumping this result was not entirely unexpected.

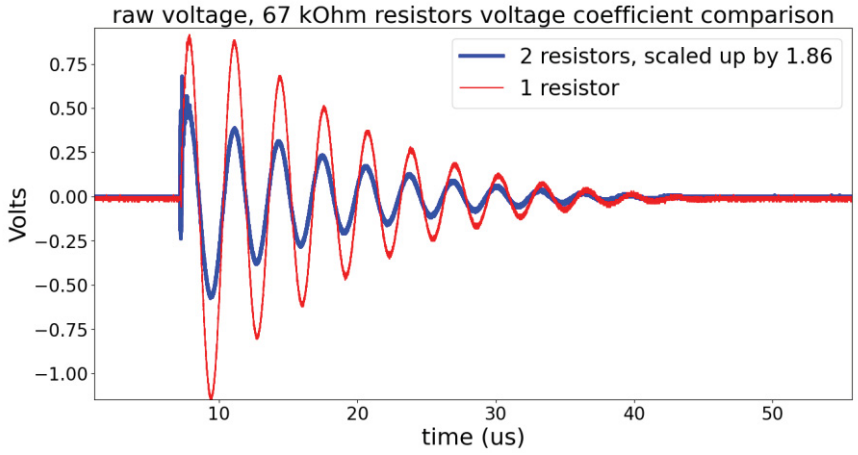

Figure 29: VCR effects on the HVRAPC brand resistors

Ohmite model 500 series testing for flux loop

The next set of tests was performed on February 21-22nd using Ohmite brand resistors model 508AS101KDG2 with a voltage rating of 50,000 Volts and a resistance value of 100 Ω (+/-10%) shown in a series assembly below in figure 30. The resistive divider was constructed to minimize inductance and a 20 Ohm measuring resistor was used for direct voltage measurement. Note that in the image, two of the 4 resistors are shorted (part of the tests to determine if voltage coefficients are negligible). Too high value of a measuring resistor means too large of a voltage signal sent back to the scope but too low means that parasitic inductance becomes more relevant (which it's best to avoid). A 20 Ohm measuring resistor (upper right portion of figure 30) was chosen as a compromise between these two extremes for this set of tests.

The parasitic inductance of the divider was measured using an LCR meter and by shorting the resistors using aluminum wire (not pictured). The value measured was 1.3 uH, which should be an overestimate because the shorting wire used was much smaller area than the resistors themselves.

In order to determine whether voltage coefficients are a concern for this setup, a bias shot (957) and a reversal shot (959) were performed using a single coil that was fully isolated from all other coils (to ensure that energy from the discharge was not transferred to other

banks via mutual inductance). A spice model of the divider circuitry and backend integrator is shown in figure 31. A 20dB attenuator was used between the integrator and the divider which is not shown in the circuit. Two of the resistors of the divider were then shorted out for a nominal resistance of 232 Ohms and another bias shot (961) and reversal shot (960) were performed.

The resulting interpreted flux of these tests are shown in figure 32 below. Reversal shots 959 and 960 unintentionally produced a plasma in the low pressure vacuum tube late in time which was only roughly pumped down during the tests. Regardless, the results in early time prior to breakdown are still viable and show no significant VCR effects. Therefore these resistors were deemed viable for use as voltage dividers in the present operational range (~10 kV induced on the flux loop).

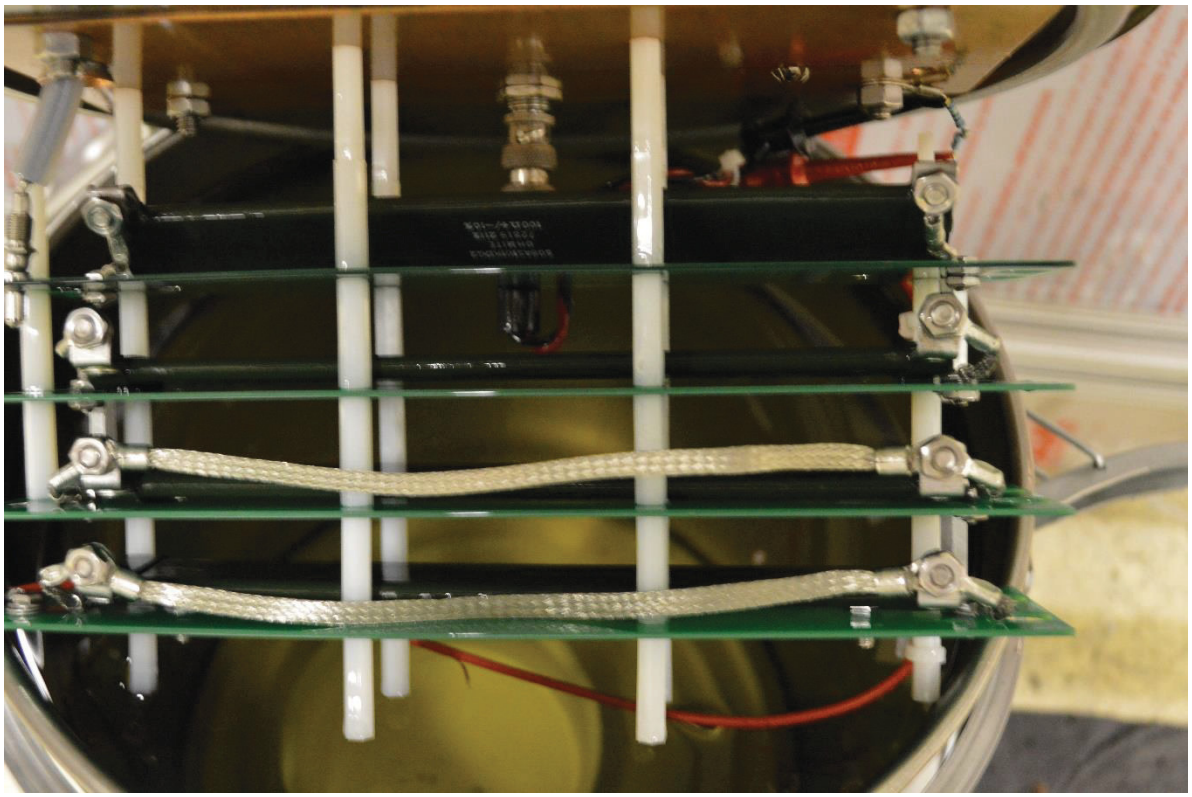

Figure 30: series assembly of the 500 model ohmite resistors with 2 of the 4 resistors shorted out for VCR tests

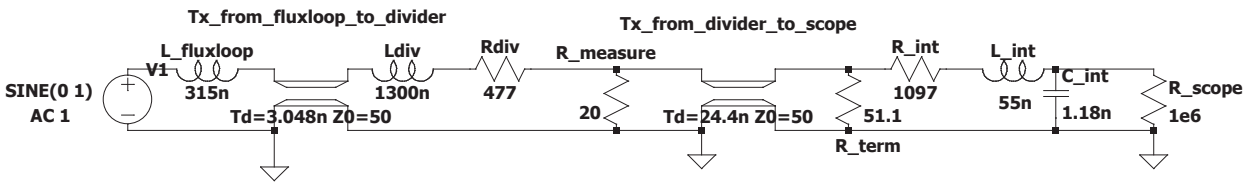

Figure 31: Divider and integrator circuit model of the 500 model Ohmite resistor test

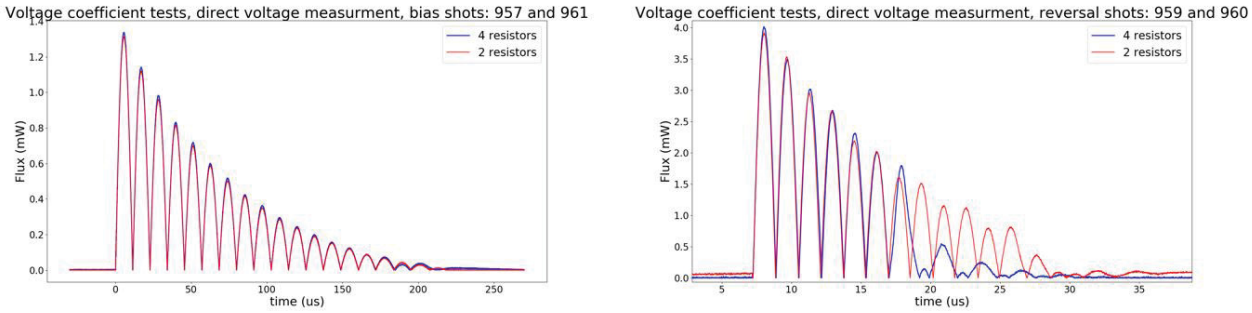

Figure 32: Results of testing for VCR effects on 500 model Ohmite resistors for Bias and Reversal discharges

Final flux loop design:

The final flux loop design is a simple one shown in figure 33 below. The wire loop itself is made of wire insulated up to 30 kV and forms a twisted pair at its junction point that leads back to a 100 kV coaxial cable where it is soldered. The twisted wire pair is shielded using braid and the 100 kV coax cable connects to the resistive divider (un-shorted now) shown in figure 30 above. The loop itself has been measured to have a diameter of $0.114\ m \pm 0.001\ m$ so that its area accuracy should be on the order of 1%. Although the exact inductance of the resistive divider is not known, we know that it is **not more than** 1.3 uH, which can account for up to 5% of the impedance of the divider so that we can say with confidence our flux measurement is accurate for a loop diameter of 0.114 m to approximately 5%.

Figure 33: Image of the final flux loop design presently used on the MTX machine

Part 7: Rogowski Coil Calibration

Dipole coil Rogowski probe calibration

A Rogowski coil was made for measuring current waveforms on the dipole coil. It consists of approximately 35 turns of 0.2" loop diameter and can be seen in figure 34 below installed on one of the OMF coils. The Rogowski was calibrated on the benchtop using the setup shown in figure 35 (with a corresponding circuit diagram shown in figure 36). Figure 37 presents a plot from the LTSpice simulation of figure 18's circuit depicting the response of the measurement at the scope compared to the voltage produced at the power supply. Barring any effects not accounted for in the simulation, it shows that the calibration setup should be effective up to at least 1 MHz calibration.

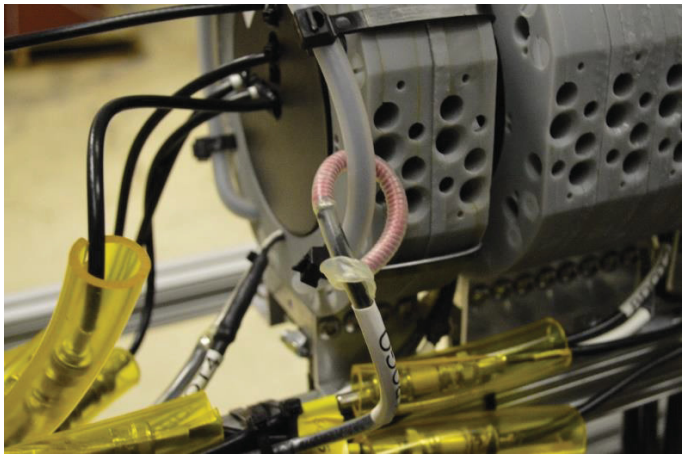

Figure 34: Rogowski coil installed on one of the OMF coils

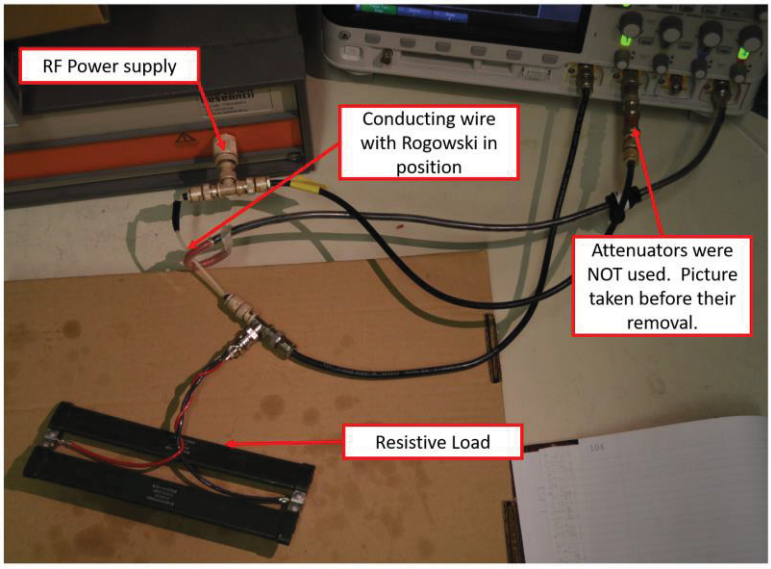

Figure 35: Calibration setup for the Rogowski coil. Note that the 50 Ohm attenuators shown in the picture were NOT used.

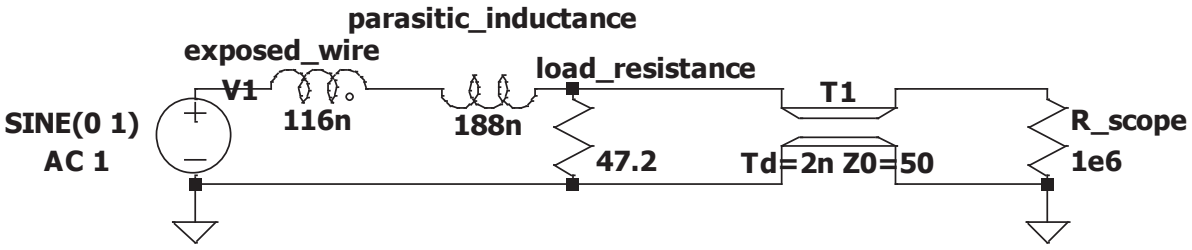

Figure 36: LTSpice XVII circuit for the Rogowski's calibration setup

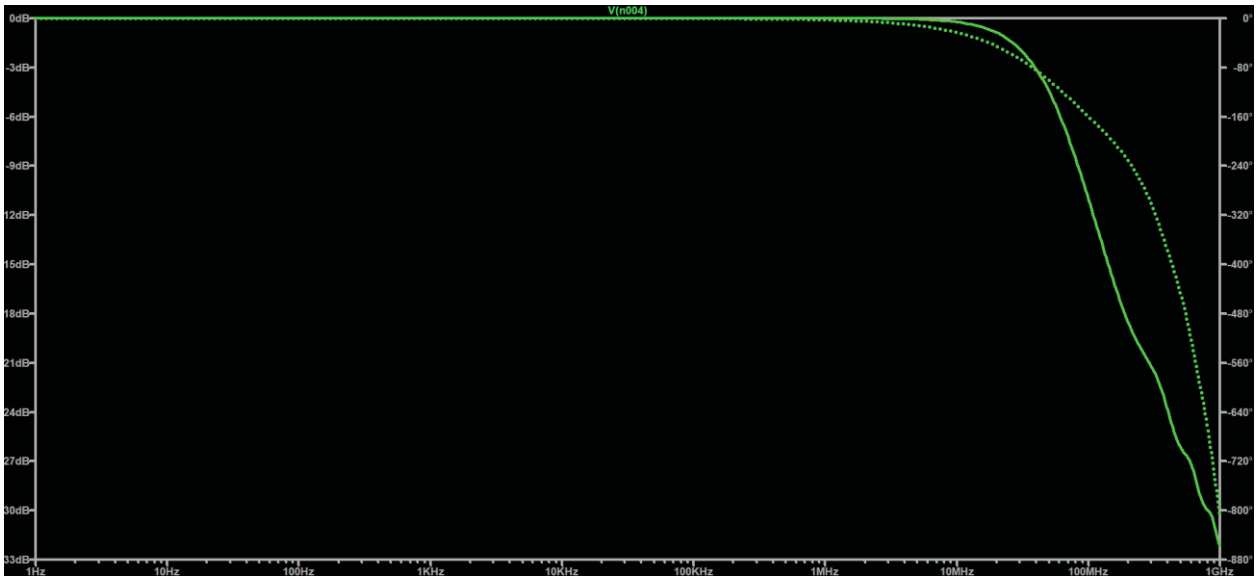

Figure 37: Response from the circuit in figure 18 comparing measurement at the scope to voltage output by the RF device. Indicates that the measurement can be considered accurate up to at least 1 MHz.

The results of the obtained data have been used to obtain a calibration curve for the Rogowski coil that can be seen in figure 38. The curve shows unexpected results where the Rogowski's response appears to decrease as a function of frequency. This data was obtained by eye instead of using a laptop to capture instant values so at least some of this data is lent an unquantified error by that (the RF power supply can drift in frequency and power over the several seconds it takes a human to record the values displayed on the scope. A second calibration should be done for more accurate results. For now, the given calibration curve indicates that the Rogowski should yield accurate values within 10% of the true value.

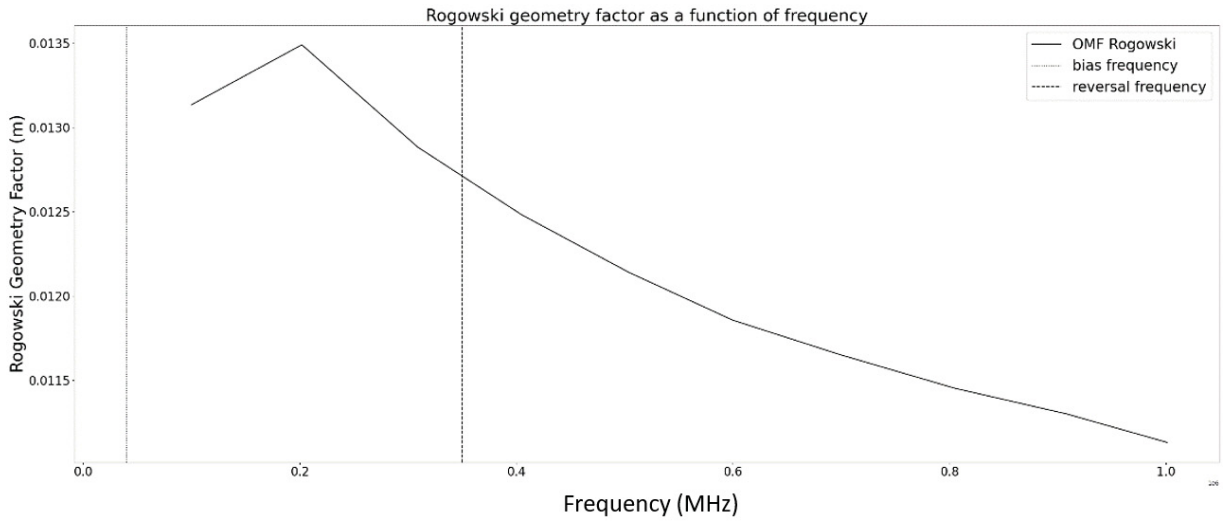

Figure 38: Calibration curve for the OMF Rogowski

The Rogowski coil is used with an analog integrator as described in the magnetic diagnostics writeup with nominal values of 1000 Ω and 100 nF. Using the above calibration and an analog integrator, data was obtained with the Rogowski coil for OMF currents shown below in figure 39. Peak currents are 13.5 kA at 30 kV and 18.1 kA at 40 kV, displaying an expected ~33% increase in current for the increase in voltage. Again, these values can be expected to be accurate within 10% of the true current.

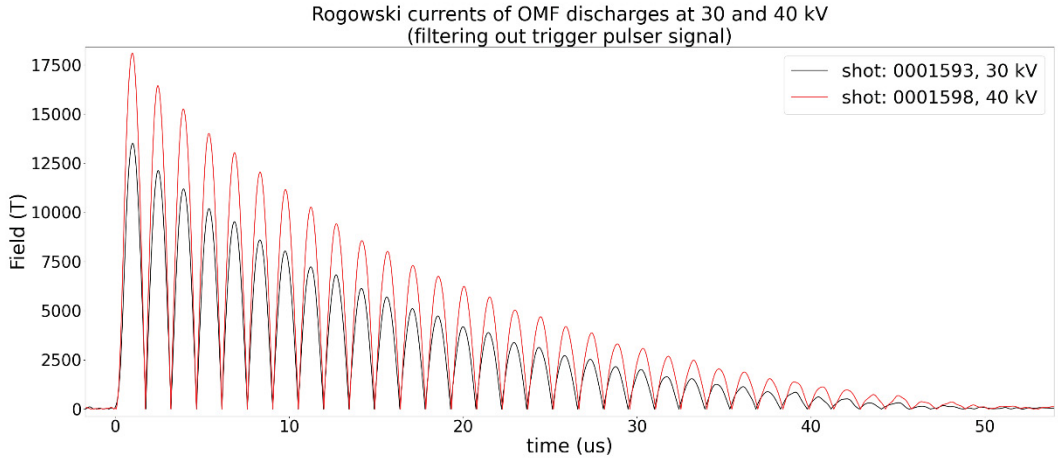

Figure 39: Comparison of current measurement firing the bank at 30 and 40 kV.

θ-coil Rogowski probe calibration

Although these Rogowski probes were created and calibrated after the data taken for this dissertation document, it is still worth presenting the calibration process for these probes. The author would like to thank Evan Loftin for his efforts in this section of the study. The probes and calibrations represented here were performed entirely by Evan. In order to properly calibrate a Rogowski probe for the MTX θ-coils, a calibration coil was created. An annotated photo of the calibration setup can be seen in figure 40 below.

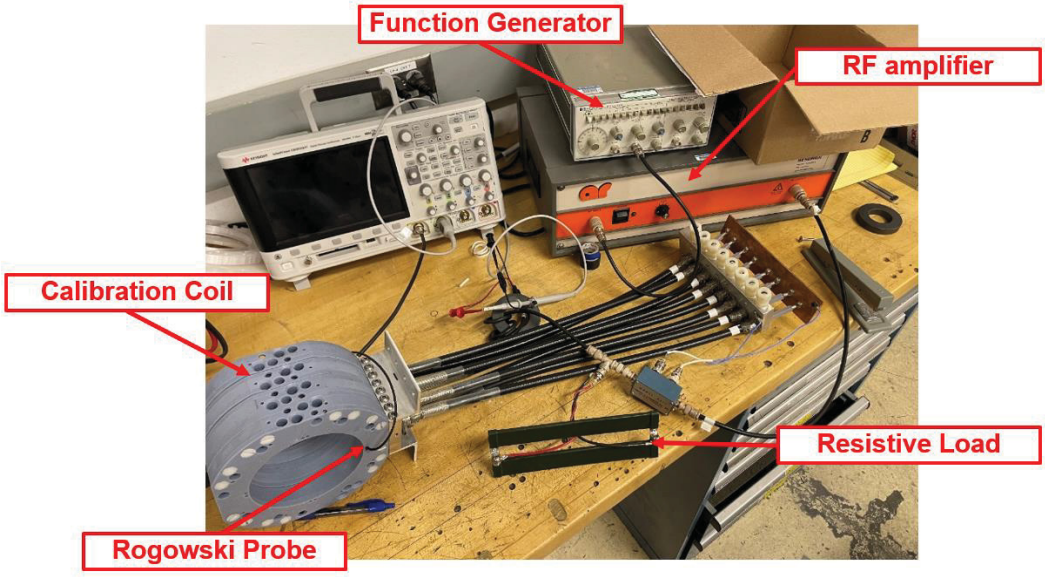

Figure 40: An annotated photo showing the calibration setup for Rogowski probes to be installed on θ-coils.

This calibration circuit setup is the same as in the previous section with two exceptions: The calibration coil is used here instead of the bare wire in the previous section; The resistor used for the data presented here is not the one pictured in figure 40 and not the one used in the previous Rogowski probe calibration section. For calibration of these Rogowski probes a more powerful signal could be used due to the higher current capability of the calibration coil, and thus a higher power resistor was used as the load. Specifically, an Ohmite brand model 889SP500k was used, which was measured to have a resistance of 47.4 Ω. Data was obtained in a similar fashion as the previous section.

The probes themselves were made using 26 AWG magnet wire, which was passed through clear heat-shrink tubing, then wrapped around on the heat shrink (after heating) for a loop diameter of approximately 2.5mm. Probes were made with either 100 or 150 turns and once all turns had been made, another layer of heat shrink was used to hold windings in place (see figure 41 below). The probes were then coupled to RG-223 BNC cable to transmit the signal.

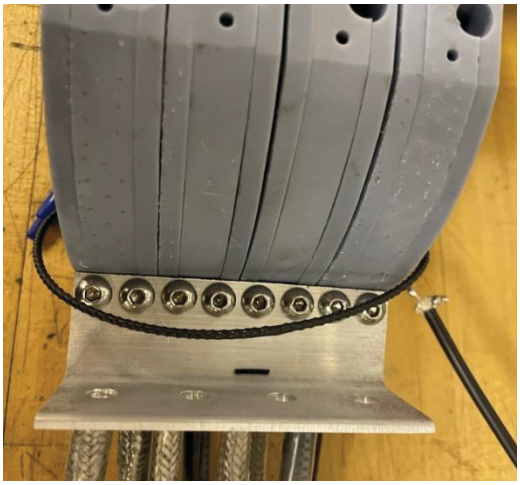

Figure 41: A photo showing a closer image of a Rogowski probe installed on the calibration coil.

Calibration proceeded in a similar manner as specified in the previous section, with the results shown in figure 42 below. . 100 turn and 150 turn probe calibrations are compared in order to determine if winding-to-winding capacitance of the Rogowski probe is an important factor. Over the frequency range of interest (10-400 kHz), the calibration is seen to vary less than 5% and by less than 10% up to 1 MHz. Therefore, the Rogowski coils now installed on the MTX machine are expected to be accurate to better than 5% for frequencies up to 400 kHz.

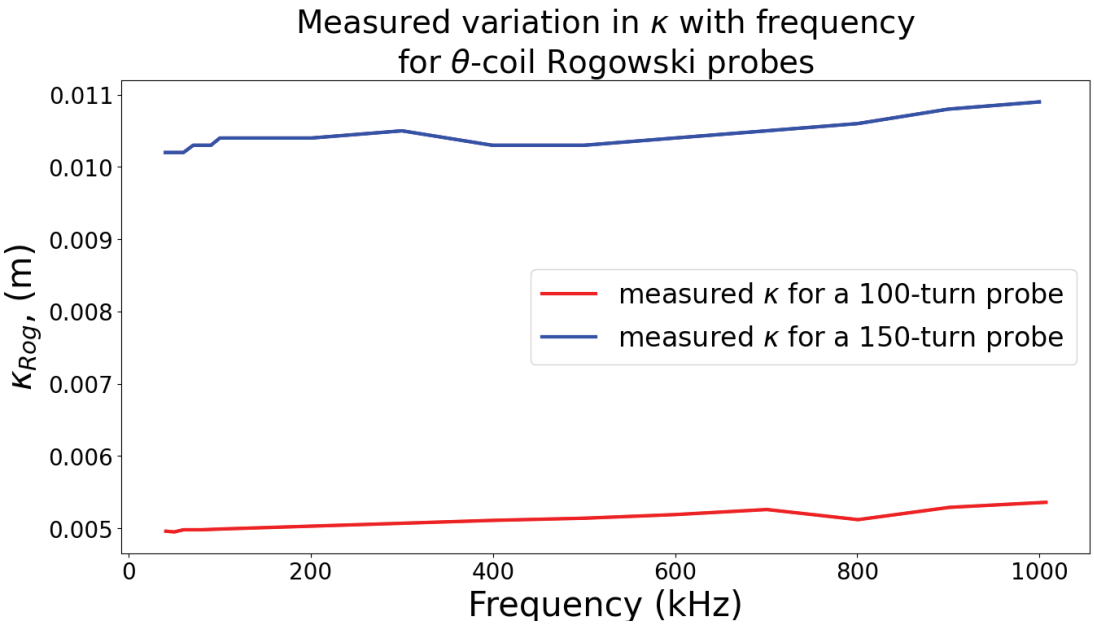

Figure 42: A plot showing the measured calibration coefficient of two separate Rogowski probes, one made with 100 turns, and the other made with 150 turns.

Part 7: Signal-processing

In this section we describe how to obtain a current trace from the voltage data of a Rogowski coil with an integrator. The approach described below is easily translated to use with $\dot{B}$-probes and flux loops. Note that this section is NOT intended to provide the reader with a full understanding of Fourier transforms, only how to use a Discrete Fourier Transform for these specific applications.

Processing with The Discrete Fourier Transform

We measure the voltage at the capacitor of the integrator, and from that we wish to determine the current passing through the primary line that the Rogowski coil is measuring. Basically, with our analytic model or the spice simulation, we have the response (or transfer function) of the integration circuit **in the frequency domain**. This allows us to calculate the primary current from the voltage at the integrator's capacitor **in the frequency domain** but frequently we are more interested in looking at signals **in the time domain.** The simplest way to get the primary current **in the time domain** is to transform the voltage measurement on the integrator's capacitor from the time domain into the frequency domain, apply the circuit response, then transform the data back into the time domain. The general process is shown in the flow chart in figure 43 below where $H(\omega)$ represents the circuit response in the frequency domain.

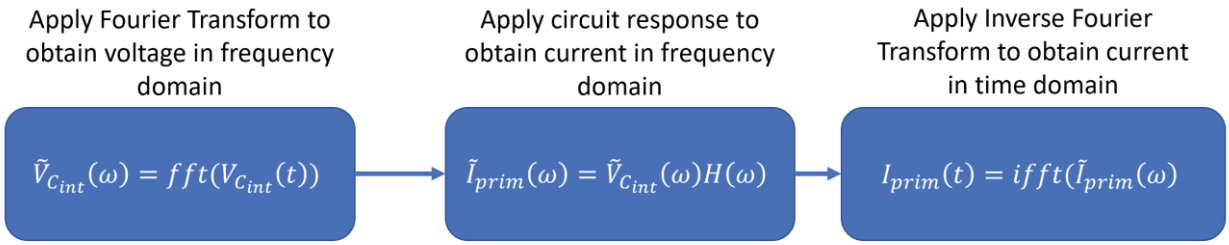

Figure 43: Basic flow chart of how to apply a frequency response to a time varying signal

Python's numpy package is well equipped to help us do this easily, but there are some finer points to cover to apply these well. In Python, we use the "fft" function which performs a discrete Fourier transform on a data set (a voltage trace in our case). This transforms our voltage data set from being a purely real function of time to a complex-valued function of frequency. It is imperative that we understand the structure of this complex-valued data set to properly apply the circuit response and filtering properly.

The Discrete Fourier Transform outputs a very specific structure of information. First, the output values correspond to specific frequency bins (ranges of frequency). The size of these frequency bins (i.e. the "frequency step" of the domain) is determined by the minimum resolvable frequency of the signal. This is defined as the period of the total sample time

$$f_{min} = \frac{1}{t_{end} - t_{start}}$$

The maximum resolvable frequency is dependent on the number of samples taken between the start and end times (i.e. the sampling frequency). For the Discrete Fourier Transform (DFT), it is defined as one frequency bin below the Nyquist frequency or

$$f_{max} = f_{Nyquist} - f_{min} = \frac{\#\ of samples}{2(t_{end} - t_{start})} - f_{min}$$

With these terms defined, we can describe the corresponding frequency structure of the output of the Discrete Fourier Transform for an **even number of data samples** and it is

$$[0,\ f_{min}, 2f_{min},\ \ \ldots\ \ f_{max} - f_{min}, f_{max}, f_{Nyquist}, -f_{max}, -f_{max} + f_{min},\ \ \ldots\ \ -2f_{min}, -f_{min}]$$

What this means is that the first value returned by the DFT corresponds to the DC offset of the signal. The second value AND LAST VALUE corresponds to the contribution of signals with a frequency around f_{min}, the third and second to last values correspond to $2f_{min}$, etc. When we apply a circuit response to the output of the DFT, we must be sure to properly apply the response to both the positive frequency and negative frequency components correctly (more on this after a note on filtering).

Frequency Filtering using DFT

It is worth noting several more things here. First, we can now easily filter out signals we're not interested in analyzing. For example, it is common to see noise spikes at the firing of the banks due to EMI from gap firings. The frequency of this noise signal is much higher than the frequency of interest. To filter it out, we artificially set to 0 the values of the DFT in those frequency ranges. For example, we commonly filter out any signals higher than 50 MHz on our signals. Note here that we must also filter out the negative frequency contributions but take care not to filter out the low frequency contributions of the negative end. i.e. do not simply find the target frequency and filter out everything above it, as this will also eliminate the negative frequency contributions for frequencies of interest. For example, a proper 50 MHz filter will only 0 out contributions **above** 50 MHz and **below** -50 MHz. Finally, any DC offset in a trace can be removed by artificially setting the first value of the DFT (whose frequency corresponds to 0 Hz) to 0. After the filtering process, the circuit response can be applied to the DFT data-set to obtain current in the frequency domain.

Applying Circuit Response using DFT

Once we have the filtered voltage signal in the frequency domain it's time to apply the circuit response. If you're using an analytic model (like the one derived above), then simply calculate the response using the full frequency domain of the FFT (negative frequencies included) and apply it to the FFT data. You may have to take care when using square roots in

Python's numpy to get an output (when taking the square root of a negative value, just add "+0j" to define it as imaginary so the sqrt function will behave.

If using a spice model, the process is different and a bit more complex. LTSpice XVII can output response as either Cartesian/complex (real and imaginary values) or polar (magnitude and phase). Interpolating complex-valued sets can be difficult (if you know how to do it then more power to you) so we output the magnitude and phase of the response from spice. We then interpolate these using numpy's "interp" function for the corresponding frequency values of your DFT. Note that spice also doesn't output this information for 0/DC frequency so you will have to artificially add that response value at the beginning of the array. For our case with magnetic diagnostics, response at DC frequency is simply 0. Then we use Euler's equation to obtain the complex response (i.e. the complex valued response) for the positive frequency range.

$$x + iy = |mag|e^{j\phi}$$

Where we have obtained "mag" and "ϕ" from the Spice's polar output. Now we have the complex response for the positive frequency portion of the DFT. To get the complex response for the negative frequency portion of the DFT, just take the complex conjugate of the positive portion of the response. Remember to structure your response array correctly before applying it to the DFT and then you're finally good to go.

Appendix D

Line Ratio Temperature Measurements

Under certain conditions it is possible to estimate a plasma's electron temperature by analyzing ratios of line emission coming from electron transitions within the plasma. Care must be taken to apply appropriate assumptions about the statistical state of the plasma. Therefore, this topic is covered in detail here so that the methods used for temperature estimates in this study are clear.

Theory

Electron Configuration Basics

Line emission refers to the spontaneous emission of photons when an electron de-excites from a higher energy shell of an atom. When an atom gains energy (for example through a collision or photon absorption), its electrons can become "excited" and occupy a higher-level energy state. The excited state tends to be unstable and the electron will "de-excite," transitioning to a lower energy shell and emitting a photon in the process. Figure 1 displays an example of two commonly observed transitions, the Hydrogen-α and Hydrogen-β (parts of the Balmer series) transitions.

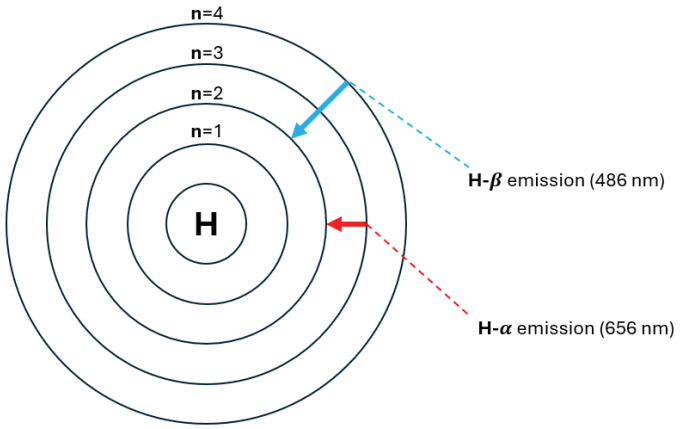

Figure 1: Basic diagram of hydrogen energy shells

The emitted photon energy is equal to the change in energy of the electron as it transitions to a lower energy state. For a hydrogen (or deuterium) plasma, the ratio of intensities of these two colors of emission can be analyzed to determine electron temperature in a plasma, provided the assumption of Partial Local Thermodynamic Equilibrium (PLTE) within the plasma is valid, which will be defined later.

It is also worth reviewing basic electron structure terminology so as to easier understand contemporary charts of information that must be used in the calculation of the electron temperature. First reviewed is the basic configuration of electron shells in an atom which will provide a context for understanding the "quantum numbers" of an electron. Recall the standard shell description as shown in figure 2 below. 1s represents the lowest energy state, 2s and 2p represent the next highest energy state, and so on. The letters s, p, and d (f not shown in diagram) represent the "sub-shells" within each shell.

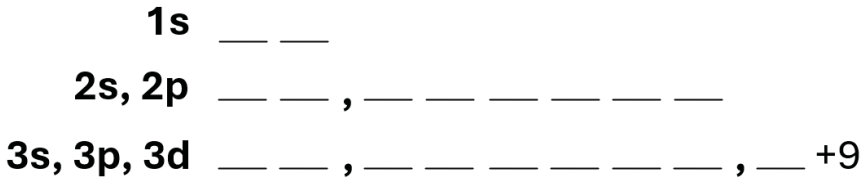

Figure 2: Standard definition of energy shells for electron configuration

Quantum numbers are used to specify an electron's state when bound to an atom and there are four of them in total. The first one is the "principal quantum number," which defines the energy level an electron is bound to and it is usually represented as "n". In figure 2, the principal quantum number is equivalent to the shell's energy level so that for the 1s shell n=1, for the 2s/2p shell n=2, and so on. The second quantum number is the is referred to as the "azimuthal quantum number" and is represented as l. The number defines the subshell that an electron is in, so that for an electron in the s sub-shell $l = 0$, for an electron in the p sub-shell $l = 1$, for an electron in the d sub-shell $l = 2$, and so on. Under certain conditions this spin value can affect the emitted photon energy and will be discussed a bit later. The third quantum number is the "magnetic quantum number" and is represented as m_l. This quantum number will not be relevant to the models used in this analysis. Finally, the fourth quantum number is the "spin magnetic quantum number" which defines the spin angular momentum of an electron and has the value of either $+\frac{1}{2}$, or $-\frac{1}{2}$. Like the azimuthal quantum number, the spin value can also affect the emitted photon energy under certain conditions and will be discussed a bit later next.

So as to avoid confusion with external literature it is worth noting the "fine-structure" model of a hydrogen atom. Let it be noted here that this model is not necessary for the temperature estimations performed here but due to its prevalence in literature on the topic it is worth defining here so that the reader is clear when reading other literature. This becomes especially important when determining the statistical weight of an electron's energy state. When the emission spectrum of a specific transition is closely observed, the spectrum actually has the shape of a doublet. This is because the energy of the transition has a dependence on the spin of an electron. As such, the fine-structure shell model of the hydrogen atom is modified as shown in figure 3 below. The subshells are now given by the "total angular momentum quantum number" which is defined as

$$j = |l + s|$$

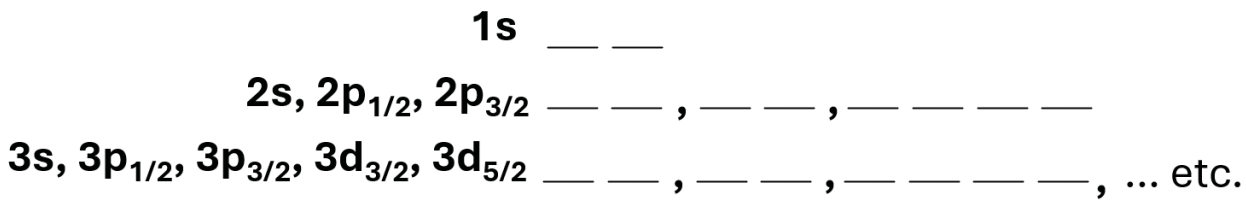

Figure 3: Diagram of subshells in the Hydrogen fine structure model

Note that the subscripts in the subshell designations correlates to the total angular momentum quantum number and electrons bound to different subshells in this model actually have slightly

different energies. This model is commonly assumed in much literature regarding emission spectra so the reader should be aware of which model between the two shown above the material is using.

Radiation model for LTE plasmas

For a plasma that is in Local Thermodynamic Equilibrium (LTE), the relative population of two energetic electron states can be assumed to be thermally distributed (see section on "ionization equilibrium ratios" in the chapter on "thermodynamic equilibrium relations" in Griem[1]), so that

$$\frac{N_m}{N_n} = \frac{g_m}{g_n} \mathrm{e}^{-\frac{\mathrm{E_m} - E_n}{kT_e}} \qquad 1$$

Where N_i is the population of the i'th energy state, g_i represents the statistical weight of that energy state (this will be discussed in more detail later), E_i is the energy associated with that electron state, k is the Boltzmann constant and T_e is the electron temperature. LTE in a plasma requires that the plasma be dominated by collisions and that radiative absorption in the plasma is negligible. This is valid for plasmas of $n_e \geq 10^{16}\ cm^{-3}$ and $kT \leq 5\ eV$ (see Griem[2]) which is close to values being explored on the MTX machine (note that for LTE, the assumption that $T_i \approx T_e$ is valid) but not always true. However, the relation can still hold accurate to better than 10% for plasmas in Partial Local Thermodynamic Equilibrium (PLTE). The energy difference between various excited states is small when compared to the energy difference between ground level and higher energy states. These excited states are more likely to be validly described by a thermal distribution and in this state a plasma can be said to be PLTE (this effectively means that ion temperatures and electron temperatures are allowed to differ) (see Kroesen[3]).

The plasma parameters and electron energy states for which PLTE can be assumed have been studied intensively and thus the range of validity for PLTE is relatively well understood. In general, the higher the electron density and the lower the principal quantum number, the more valid a PLTE assumption is for a plasma, as demonstrated by Fujimoto and McWhirter[4] (see figure 6 of their publication). Using Fujimoto's plot, it becomes apparent that for electron densities greater than 10^{15} cm^{-3} and temperatures less than 10 eV, PLTE should be valid for comparison of H-α and H-β lines and any higher energy level transitions. Therefore, equation 1 above may be used to represent energetic electron state populations.

Now that the validity of equation 1 has been established (within 10% accuracy), note that emission intensity of a given energetic electron population in a plasma can be determined as (see section on "relative intensities of lines of the same atom or ion" in the chapter on "spectroscopic temperature measurements" in Griem[1])

$$i_{mn} \approx \frac{\hbar \omega_{mn}}{4\pi} A_{mn} N_m l \qquad 2$$

Where i_{mn} is the total intensity produced by a line emission of an electron transitioning from state m to n and integrated over spectral length of l, $\hbar$ is the reduced Planck's constant, ω_{mn} is the

frequency of the emitted radiation (assumed constant over spectral integration, i.e. line spectrum is narrow), A_{mn} is the Einstein coefficient for the transition, and N_m is the population of the given energetic state. Direct substitution for two arbitrary energized states of equation 2 into equation 1 will yield

$$\frac{i_{m_1n_1}}{i_{m_2n_2}} = \frac{\omega_{m_1n_1}A_{m_1n_1}g_{m_1n_1}}{\omega_{m_2n_2}A_{m_2n_2}g_{m_2n_2}}e^{-\frac{E_{m_1}-E_{m_2}}{kT_e}} \quad 3$$

Where the lefthand side represents the ratio of two spectrally integrated line intensities and the other variables are consistent with those specified in equations 2 and 3. If the emission wavelength, Einstein coefficients of the transitions, statistical weight, and bound energy of both transition types are known, then electron temperature can be calculated as

$$T_e = \frac{E_{m_2} - E_{m_1}}{k\ln\left(\frac{i_{m_1n_1}\omega_{m_2n_2}A_{m_2n_2}g_{m_2n_2}}{i_{m_2n_2}\omega_{m_1n_1}A_{m_1n_1}g_{m_1n_1}}\right)} \quad 4$$

Do note that a method using a linear fit that increases accuracy by using multiple line ratios (useful for heaver gases) is outlined in the supplemental materials of Chu's publication[5]. For a single ratio, error can also be estimated using the method suggested by Griem[1] so that

$$\frac{\Delta T_e}{T_e} = \frac{kT_e}{\left(E_{m_2} - E_{m_1}\right)}\left|\frac{\Delta X}{X}\right| \quad 5$$

Where X represents the value in the natural logarithm of equation 4. If it is assumed that the error in the emission frequency, Einstein coefficients, and statistical weights is negligible compared to the intensity ratio measurement (a likely scenario for this situation), then the time independent error of the estimate will be equal to the uncertainty in the intensity ratio measurement plus another 10% due to the PLTE model. It must also be noted that when using fast time resolution photodiodes, one must also take into account the statistical decay time (inverse of the Einstein coefficient) and account for error in time-varying measurements as well. For example, the Einstein coefficient for H-β for hydrogen is given by NIST as $A_{ki} = 8.4193 * 10^6 s^{-1}$, the inverse of which means on average it takes $\approx 120\ ns$ for the emission event to occur. This means that changes in intensity occurring on timescales faster than this are subject to additional error proportional to the rate of change of intensity and the Einstein coefficient. This can be modeled by dividing the rate of change of intensity by the Einstein coefficient and the instantaneous intensity value. Since there are two events being measured, each one is calculated separately and contributes to the total error in intensity ratio. Finally, bit noise tends to add an additional 1% overall uncertainty. Therefore, the overall error can be estimated as

$$\frac{\Delta T_e}{T_e} \approx \frac{kT}{E_{m_2} - E_{m_1}}\left|0.11 + \frac{\Delta \mathrm{I}_{\mathrm{ratio}}}{I_{ratio}} + \left(\frac{\left|\frac{1}{A_1 I_1}\left(\frac{dI_1}{dt}\right)\right|}{\left|\frac{1}{A_2}I_2\left(\frac{dI_2}{dt}\right)\right|}\right)\right| \quad 6$$

Temperature Analysis

Temperature comparisons here could only be performed within a very specific range, due to two primary factors. Two perform a line-ratio calculations, two detectable intensities of line emission are required. In many cases H-β emission could not be detected with the diagnostics at hand. This implies that the plasma temperatures in these tests are generally very cold. Additionally, using the ratios of H-α to H-β generally only work up to approximately 10 eV. This is because once the electron temperature reaches this value, the emission of H-α tends to cease as the majority of electrons in hydrogen orbitals are in the n=4 shell. However, some analysis of electron temperature can still be performed in the pre-ionization studies.

Figure 4 below shows the camera images taken from a ringing-θ discharge in 50 mTorr of deuterium gas. The image shows a much brighter spot on the 4th frame (7.55-7.65us) which directly coincides with the temperature going off-scale what this method can measure as shown in figure 5. It's worth noting that the average temperature increased by ~0.1 eV from before vs. after the compression, implying a small degree of shock heating.

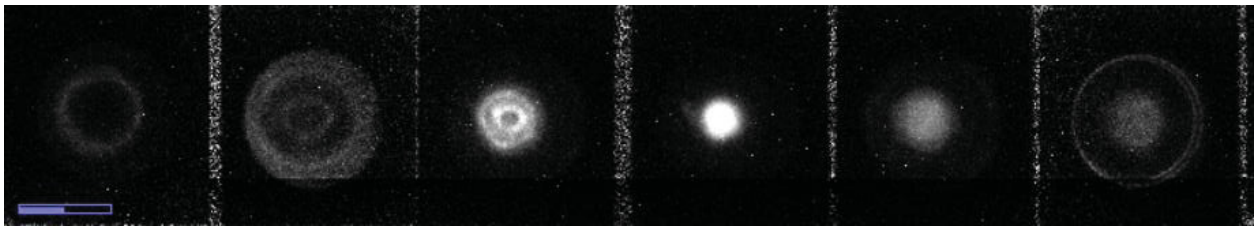

Figure 4: Images taken of a ringing-θ discharge in 50 mTorr of deuterium.

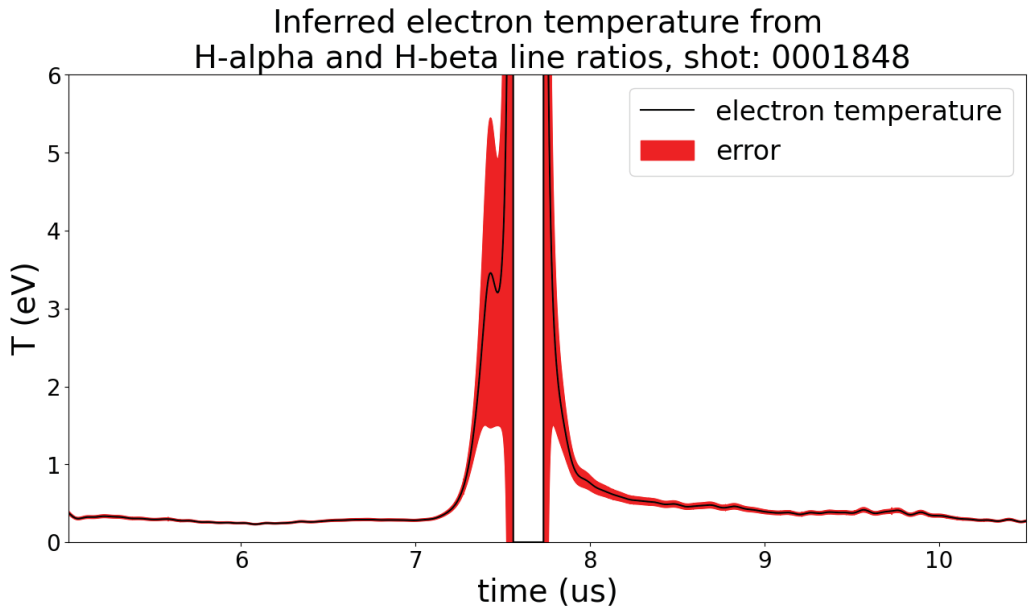

Figure 5: Line ratio temperature of a ringing-θ discharge in 50 mTorr of deuterium gas.

Temperature measurements in the biased-dipole configuration could be performed over a longer span of time due to the fact that the maximum variation of line intensity was not as high as seen in the ringing-θ configuration due to the plasma compression. Figure 6 displays the measured temperature of a biased-dipole discharge in 100 mTorr of deuterium gas. The temperature tends to stay consistent of the timescale shown at ~0.4 eV. However, by the time the reversal field would be fired for formation (~50 μs), H-β emission is no longer detectable, implying a very cold plasma.

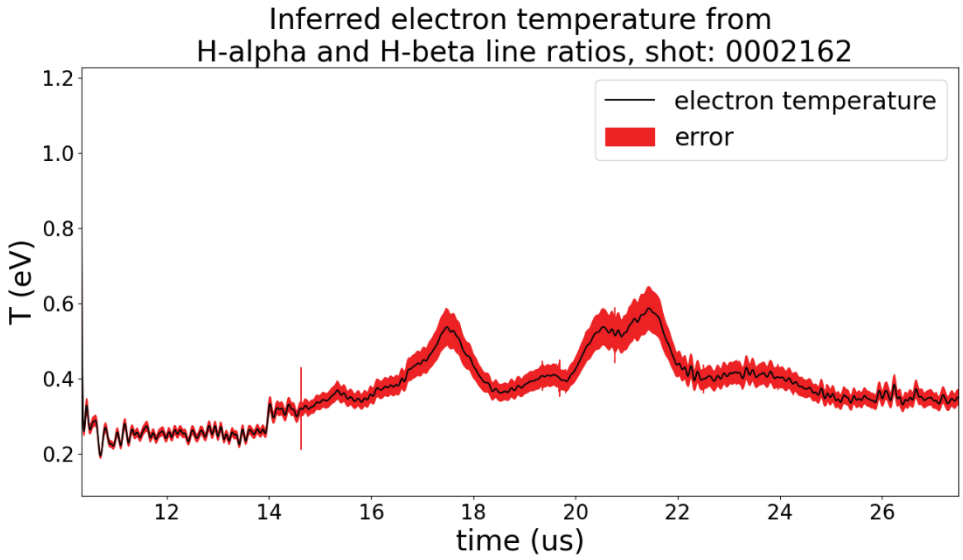

Figure 6: Line ratio temperature of a biased-dipole discharge in 100 mTorr of deuterium gas.

References for temperature by line ratio appendix section

*Note that these references are also included in the main bibliography of this dissertation. They are presented here for ease of printing this particular appendix section.

[1] Griem, H. R. (2005). *Principles of plasma spectroscopy*. Cambridge University Press.

[2] Griem, H. R. (1963). Validity of local thermal equilibrium in plasma spectroscopy. *Physical Review*, *131*(3), 1170.

[3] Kroesen, G. M., Schram, D. C., Timmermans, C. J., & De Haas, J. C. M. (1990). The energy balance of a plasma in partial local thermodynamic equilibrium. *IEEE Transactions on Plasma Science*, *18*(6), 985-991.

[4] Fujimoto, T., & McWhirter, R. W. P. (1990). Validity criteria for local thermodynamic equilibrium in plasma spectroscopy. *Physical Review A*, *42*(11), 6588.

[5] Chu, F., LaJoie, A. L., Keenan, B. D., Webster, L., Langendorf, S. J., & Gilmore, M. A. (2023). Experimental measurements of ion diffusion coefficients and heating in a multi-ion-species plasma shock. *Physical Review Letters*, *130*(14), 145101.

Appendix E

Interferometer Details

Plasma density measurements on the MTX machine are obtained using interferometry. Interferometry is a technique that refers to the use of an interference pattern between two beams for measuring parameters of a system such as path length or refractive index. A plasma's refractive index is a direct function of its electron density (subject to some conditions discussed later) and thus, interferometry can be used to measure electron density in a plasma. If an average charge state is also known then an average ion density can also be determined. A general overview of interferometry with regards to plasmas can be viewed in Hutchinson[1].

Interferometry Introduction

The speed of light in a plasma is different than that of air (due to its refractive index or permittivity). This causes a change in the phase of the beam after it exits the plasma that is directly related to the plasma's density. If this "scene" beam is then superimposed with a "reference" beam that has not passed through a plasma, the changing of phase between the two beams will be seen as a variation in beam intensity. This variation is referred to as an interference pattern. It should be noted that interference of the beams requires that they are coherent (i.e. they have the same wavelength in air). Mathematically, the interfered beams can be represented as the superposition of the electric fields of each beam as given by Hutchinson[1]

$$E_t = E_1 e^{i(\omega t)} + E_2 e^{i(\omega t + \phi)}$$

Equation 1

Detectors will generally measure the "power" of a beam incident on it and the power of two superimposed beams is given again by Hutchinson[1] as

$$|E_t|^2 = [E_1^2 + E_2^2]\left[1 + \frac{2E_1E_2}{E_1^2 + E_2^2}\cos(\phi)\right]$$

Equation 2

Given that E_1 and E_2 are constant, it is evident that the detected power of the beam will vary only with the phase change of the scene beam. For example, if the two waves are completely out of phase ($\phi = \pi, 3\pi, 5\pi$ …) the combined beam will be at its minimum power due to complete destructive interference and if the two waves are perfectly in phase then the combined beam will be at its maximum power ($\phi = 0{,}2\pi, 4\pi \ldots$) due to constructive interference. Figure 1 plots the variation in power with ϕ of the superimposed beam with $E_1 = E_2$ (if $E_1 \neq E_2$ then the minimum power does not reach 0)

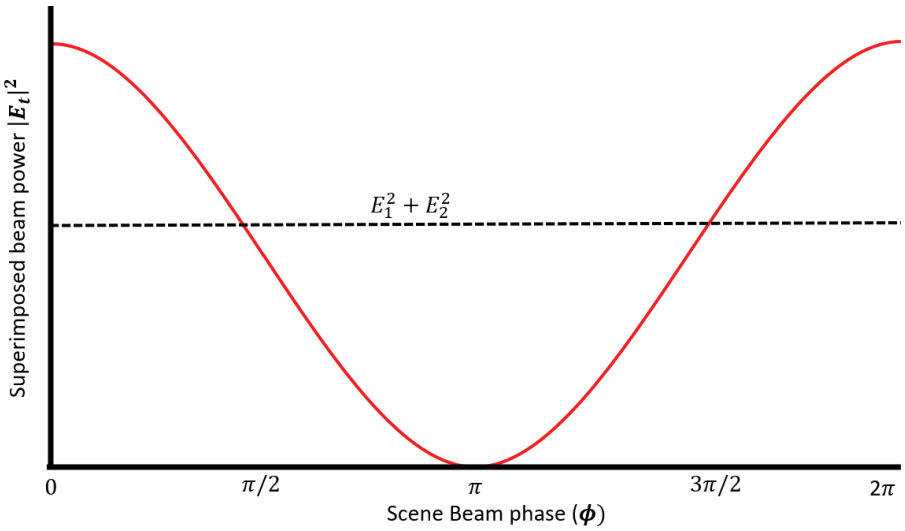

Figure 1: Variation in total beam power with phase difference of two superimposed beams

Thus, the measured power of two coherent interfering beams (one of which passed through a plasma) can be used to determine the phase change between the two beams. In order to relate this to the plasma's refractive index and thus its electron density, several assumptions are made. First it is assumed electron velocities do not approach the phase velocity of the laser beam (~speed of light) so that the plasma can be considered cold with respect to the beam[2]. In addition, if the magnetic field in the direction of beam propagation is negligible and if the wavelength of the beam is much smaller than the gradient scale of the plasma (i.e. if $\frac{1}{\lambda} \gg \frac{1}{\rho}\frac{d\rho}{dx}$ where x is the direction of the beam's propagation) then the following equation can be used to relate plasma density to the measured change in phase (a thorough derivation of this is given by Merritt[3]).

$$\Delta\phi = -\frac{\omega}{2cn_c}\int_0^l n_e dl$$

Equation 3

Where ω is the beam frequency, c is the speed of light, n_e is the electron density, l is the path length of the beam through the plasma, and $n_c = \frac{\omega^2 m_e \epsilon_0}{e^2}$ is the critical density at which the beam begins to get absorbed into the plasma rather than propagating through. The $\Delta\phi$ calculated with this represents the change in phase of the scene beam due to the presence of a plasma compared to the phase state with no plasma present, i.e. $\Delta\phi = \phi(t) - \phi(0)$.

Phase Ambiguity

The problem of phase ambiguity in this form of measurement arises when the combined beam reaches its minimum or maximum power. Figure 2 displays an example of this problem. The green line represents the density of a plasma that the scene beam is passing through while the red line represents the detected intensity of the interfering beam. Between t_0 and t_1, no plasma is present and so the phase difference between the scene and reference beams does not change and there is no variation in beam intensity. Between t_1 and t_2 the plasma is formed and begins to increase in density, causing a phase lag in the scene beam which is detected as a change in beam intensity. However, at t_2 the beams are perfectly out of phase and the plasma begins to decrease in density. At this point, an increase or decrease in plasma density looks exactly the same on the power detector, i.e. it is impossible to tell whether the phase lag of the scene beam continued to increase or decrease, i.e. the sign of $\Delta\phi$ cannot be determined. Figure 3 displays how a positive or negative change in phase will yield the same result in detected power. Thus, if a change in sign of $\Delta\phi$ occurs when the beams are at complete constructive or destructive interference, it cannot be detected. This issue is referred to as "phase ambiguity."

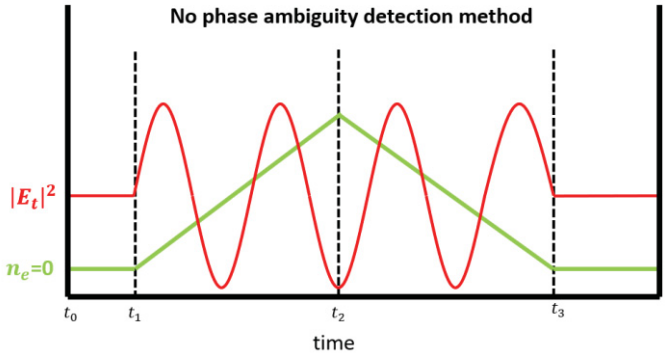

Figure 2: The green line represents plasma density changing over time. The red line represents the associated phase shift from an intensity measurement. At time 2 the change to decreasing density cannot be detected by the intensity variation.

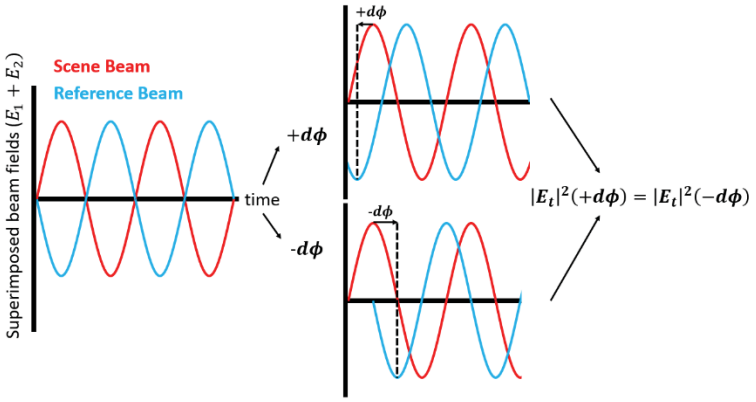

Figure 3: Displaying how a negative or positive frequency shift from two beams that are 180° out of phase yields the same total intensity.

Frequency Modulation for Phase Discrimination

Historically, the problem of phase ambiguity has been solved through the application of frequency modulation. In this method either a vibrating mirror or acousto-optic modulator (AOM) are used to introduce a high frequency (10s of MHz) oscillation in the measured value of $\Delta\phi$. With the measured signal oscillating an arbitrary frequency, changes in the scene beam's effective path length now manifest as a frequency shift of the measured signal. If $\Delta\phi$ changes positively, the frequency of oscillation is increased and if $\Delta\phi$ changes negatively, the frequency of oscillation is decreased. It should be noted that for this approach to work it is necessary that the "carrier" frequency (the oscillation frequency introduced by the vibrating mirror or AOM) be much higher than the rate of change of plasma density.

This approach is shown graphically in figure 4 for clarity. First, note that because another frequency is super-imposed on the signal that the detected power is no longer directly proportional to $\Delta\phi$ so the red line specifically represents $|E_t|^2$. Between t_0 and t_1 with no plasma present, the detected power oscillates at the carrier frequency of the vibrating mirror or AOM. As the plasma density increases between t_1 and t_2 the frequency of the signal oscillation increases relative to the plasma density's rate of change. As the plasma density decreases between t_2 and t_3, the frequency of the oscillation decreases below that of the carrier frequency. Finally, once the plasma density reaches 0, the frequency of the oscillation returns to that of the carrier frequency.

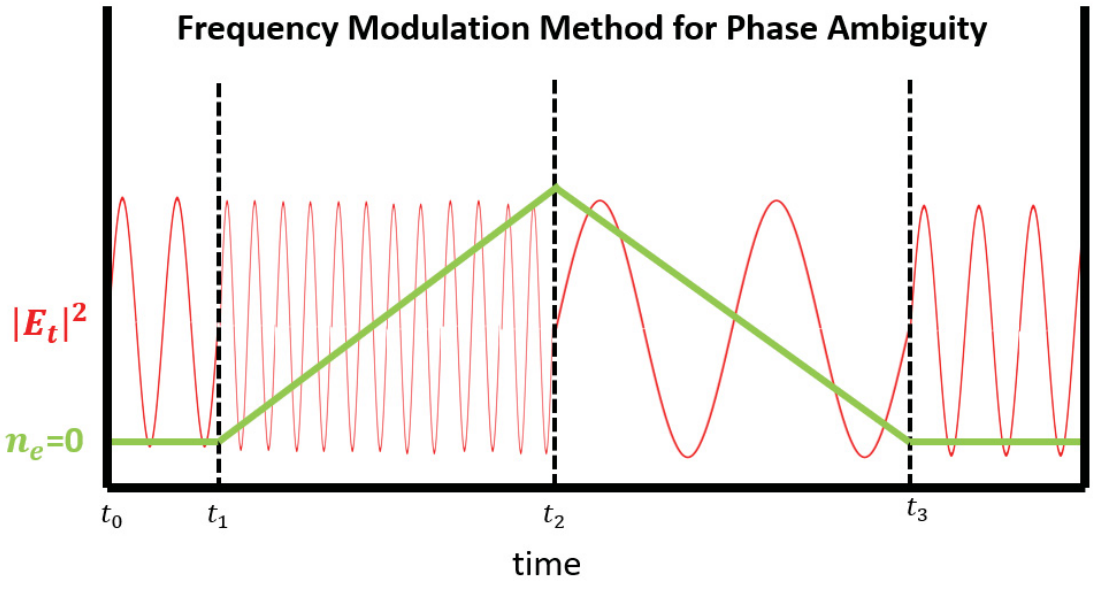

Figure 4: Green represents a changing plasma density in time. Red represents the measured intensity of an interference beam that is using frequency modulation to detect the sign of ϕ

Quadrature Method for Phase Discrimination

Recently an alternate solution to the phase ambiguity problem was introduced by Weber[4]. The fundamental concept behind the approach is to split the recombined beam into orthogonal s and p polarizations while having the polarizations 90 degrees out of phase with one another (see the Interferometer Setup and Tuning section below for more details on how this is done). As a result, neither beam's intensity will reach peak amplitude at the same phase shift of the scene beam. Figure 5 displays the resulting power measurements graphically. The s polarization in red ($|E_s|^2$) has the same phase ambiguity problem as shown in figure 2 above. However, the p polarization in blue is out of phase with the s polarization and the change in sign of $\frac{dn_e}{dt}$ is clearly observed at time t_2 where it is ambiguous for the s polarization. Because these two polarizations are 90 degrees out of phase with one another a change in derivative of the measured value will always be observed in one polarization or the other.

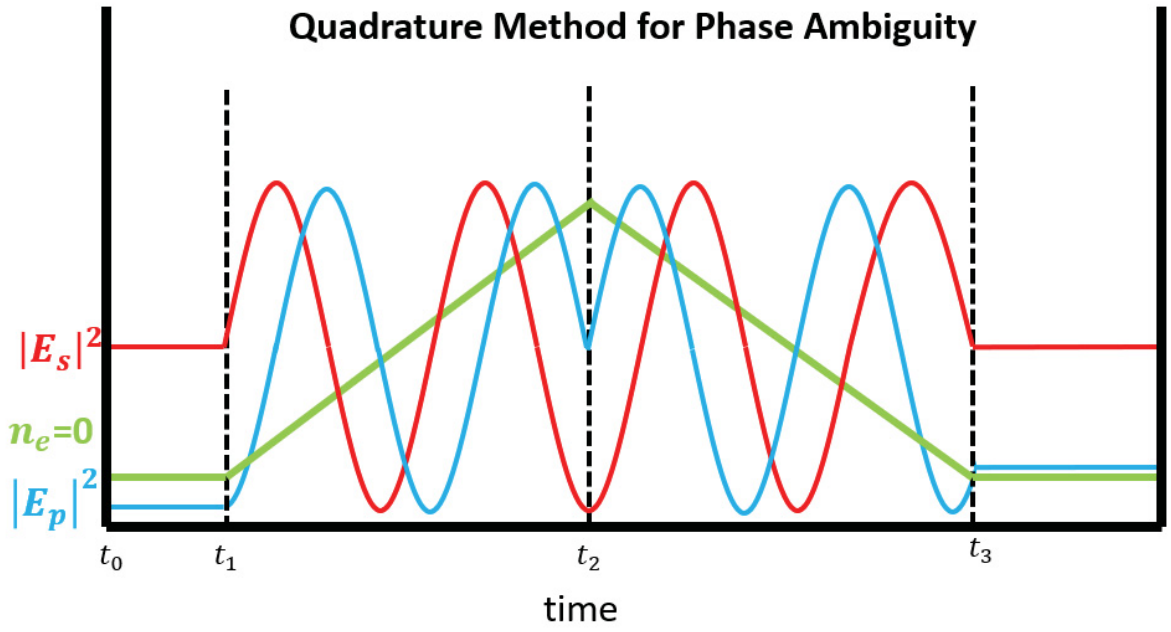

Figure 5: Green represents changing plasma density over time. Red represents variation in intensity of the s polarization and blue represents variation of the p polarization's intensity which is 90° out of phase with s.

The quadrature discrimination method's time resolution is only limited by the sampling rate/time resolution of the photo detectors used (whereas the frequency modulation method is limited by the selected carrier frequency). Further, the quadrature method minimizes the use of electronic components in the diagnostic (no AOM's or high frequency demodulators are needed) which allows for easier implementation on experiments that produce high levels of ElectroMagnetic Interference (EMI) like MTX. For these reasons it was chosen to use this style of interferometer on MTX.

Interferometer Construction

The MTX project was already in possession of many of the necessary optical components required to build a 532 nm (green) laser interferometer using the quadrature phase discrimination method introduced above. Therefore 532 nm was selected as the laser wavelength to use for this diagnostic. It is important to estimate how effective this wavelength will be for detecting the plasmas being studied. The static fill gas pressure range to be explored prior to ionization is 10-100 mTorr and using D_2 as an example, the associated electron density at full ionization can be determined as

$$n_e = \frac{2PN_A}{RT}$$

Equation 4

Where P is the gas pressure in Pascals, $N_A = 6.022 * 10^{23} \frac{particles}{mole}$ is Avogadro's number, $R = 8.314 \frac{J}{mol*K}$ is the universal gas constant, $T = 293K$ is the ambient temperature of the gas, and the factor of 2 is due to the diatomic nature of D_2. Using a green laser and conservatively assuming ~1 cm integration length (since a torus will be a common ionization structure in these experiments), equation 3 above can be used to estimate a phase shift due to the plasma. Figure 6 below shows estimated phase shifts for several pressures and degrees of ionization.

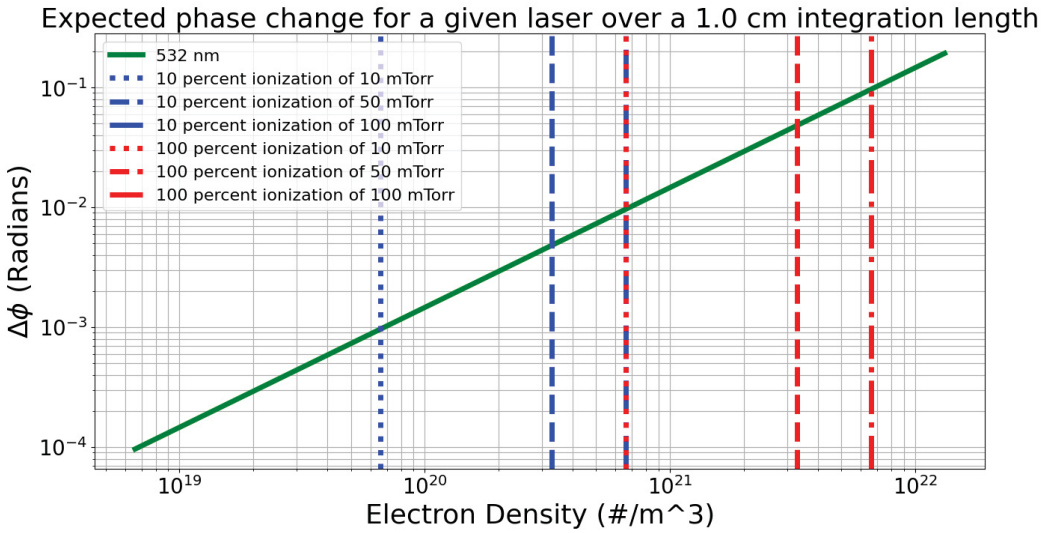

Figure 6: Estimated phase shift using a 532 nm laser on a plasma annulus ~1cm in total width for various ionization states and pressures.

It is clear to see that for these assumptions only a few to tens of milliradians of phase shift will be induced at the most for a deuterium plasma (depending on the length integration, assumed 1 cm here for plotting). Ultimately, measurement sensitivity will depend on noise levels which will be determined during the experimental campaigns but it is unlikely that this

interferometer will be able to determine electron densities in early time during the pre-ionization process. However, the integration length may increase up to an order of magnitude later in the ionization process (the tube diameter is 10 cm), so the design will be capable of measuring final plasma density after the pre-ionization process prior to field reversal (and certainly capable of measuring FRC densities post-formation). Taking into account the fact that the beam will pass through the plasma twice, it can be calculated that depending on integration length and assuming full ionization, 1-10° of phase shift can be induced for a 10 mTorr fill, 5-50° for 50 mTorr, and 10-100° for 100 mTorr.

Interferometer Parts

The laser used for the interferometer is a Thorlabs model DJ532-10 laser diode. It is stated to have a center wavelength of 532 ± 1 nm. Its coherence length can be approximated using[5]

$$L_{coh} \approx \frac{\lambda^2}{\Delta\lambda}$$

Equation 5

Where $\Delta\nu$ is the FWHM of the beam's spectrum profile which was determined by calling Thorlabs technical support who provided a value of $\Delta\lambda \approx 10.3$ fm. This yields a coherence length of $L \approx 30$ m which is more than sufficient for the present task.

The diode is contained in a Thorlabs TCLDM9 laser diode mount which is equipped with an AD592AN temperature sensor to allow for temperature control of the laser to ensure ideal performance. Power is provided to the laser using a Thorlabs LDC205C laser diode controller and temperature control is provided by a Thorlabs TED200C temperature controller. A Coherent brand LabMax_TOP optical power meter was used to tune the laser power to ~5 mW for safety reasons (this corresponds to a supply current of 133.3 mA at 24° C).

The photodetector selected for use is the Thorlabs DET10A model which outputs a voltage relative to incident beam intensity. Its measurement bandwidth capability is dependent on its termination impedance (noting that higher termination impedance yields higher voltage signals). Because the interferometer will be unable to provide strong signal during the pre-ionization process, the bandwidth (i.e time-resolution) requirements on the detectors are relaxed and lower bandwidth capability is acceptable to allow for stronger signal strength. The manual for DET10A photodetectors states that termination resistance can be calculated for a desired bandwidth resolution using

$$R_{term} = \frac{1}{2\pi f_{BW} C_{junc}}$$

Equation 6

Where C_{junc} is the photodetectors junction capacitance, given as $C_{junc} = 6$ pF in the manual. Presently a termination of $5\ k\Omega$ is being used which yields a bandwidth resolution of ~5 MHz (meaning rise times of ~100 ns are resolvable). In the interferometer's present state this yields a signal with a 30 mV average with a peak-to-peak oscillation of 20 mV, which is considered sufficient for measurement (provided EMI shielding performs well enough).

Interferometer EMI Shielding

The optical table for the interferometer is bolted onto an 80/20 cart that can be moved into position and mounted to the machine's frame for stability. The entire assembly can be viewed in figure 7. A higher quality ground connection is provided between the machine and table through a thick grounding braid (not pictured).

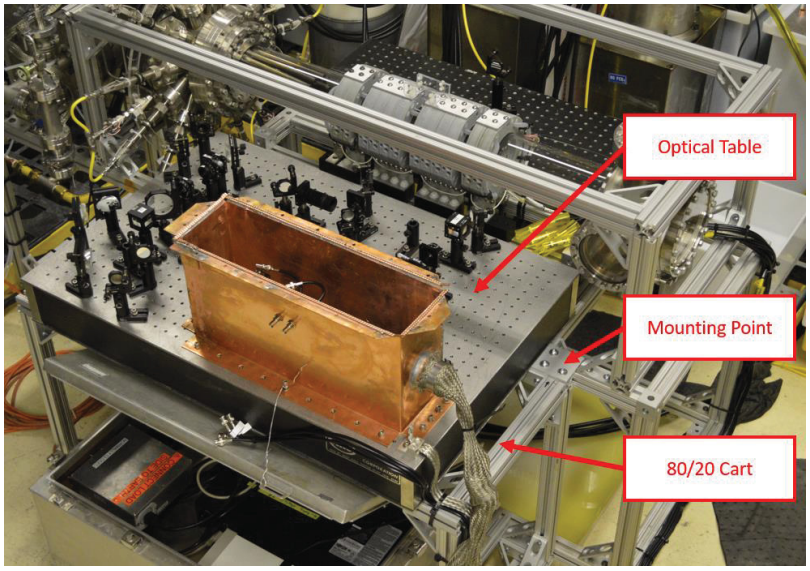

Figure 7: Image showing the interferometer table and cart setup.

In order to provide sufficient electrical shielding the power and temperature controllers are contained in an EMI shielded box with an internal battery powered UPS that is disconnected from wall power during operation using a custom contactor box shown in figure 8.

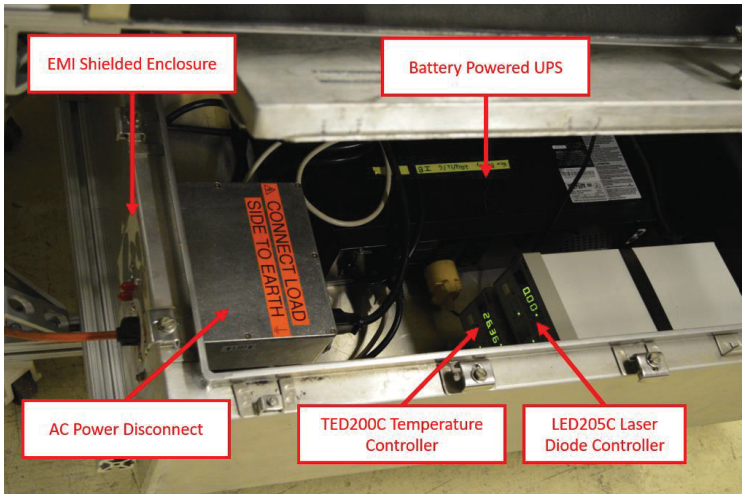

Figure 8: Image showing the diode controller's and their battery UPS in an EMI enclosure on the bottom of the cart under the optical table.

Power to the laser diode and its solid-state cooling system is channeled through a shielded braid to a copper box that sits on the optical table with the interferometer and provides EMI shielding for both the laser diode and the photodetectors. Three small holes are drilled into the enclosure to allow the laser to get out and the two photodetectors to receive signals. Shielded BNC throughputs are bolted into the copper box and the photodetectors send their signals through these to another EMI shielded data acquisition unit through 25' of RG-223 coaxial cable (21' to the enclosure and another 4' inside the enclosure). The laser and photoreceiver enclosure can be viewed in figure 9.

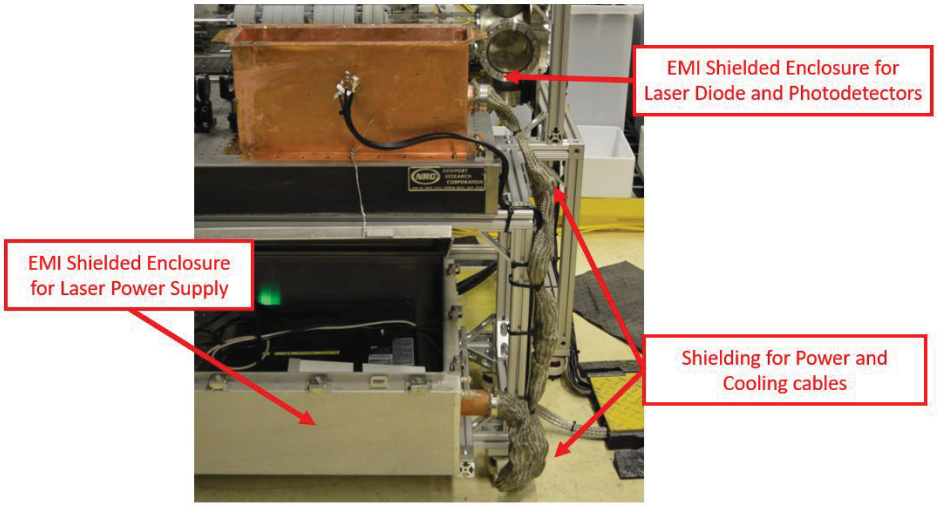

Figure 9: Image showing the EMI enclosures for both the laser power supply and the laser/photodetectors, as well as their cabling.

Interferometer Setup and Tuning

A diagram of the interferometer can be seen in figure 10 and an annotated top-down photo of the overall setup can also be seen in figure 11. The laser is initially emitted (elliptically polarized) from the laser diode inside of the EMI enclosure. It passes through lens L1 which focuses the beam to a small diameter profile over the length of the interferometer. The beam then passes through polarizer P1 and half-wave-plate HWP1 and is then split by polarizing beam splitter PBS1. The combination of P1, HWP1, and PBS1 allow for tuning of laser intensity between the scene and reference beams by rotating the polarization. Extra mirrors are included at multiple points in the interferometer to allow for better tuning of both beam position and angle.

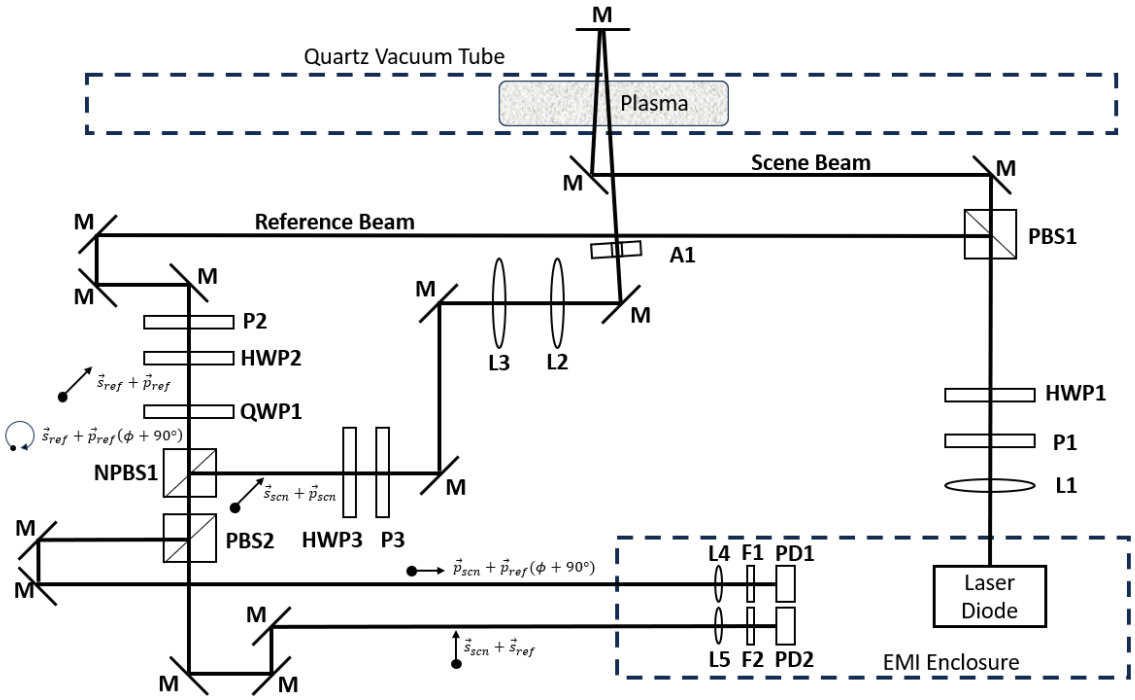

Figure 10: Diagram of the interferometer as it is currently setup. L=Lens, P=Polarizer, HWP = half-wave-plate, PBS = polarizing beam splitter, M = mirror, A = aperture, QWP = quarter-wave-plate, NPBS = non-polarizing beam splitter, F = spectral filter, PD = photodetector

The scene beam passes through the quartz vacuum tube and is bounced off a mirror on the other side of the tube to pass through the plasma again. The quartz tube tends to refract the beam in a vertically striated pattern as seen in figure 12. Therefore, the scene beam is passed through aperture A1 to reduce static background light intensity before being collimated by lens L2 and L3. The scene beam then proceeds through polarizer P3 which is tuned to allow maximum beam intensity. The beam then has its polarization rotated so that it is 45° relative to PBS2 “after” passing through NPBS1 (the reference beam was blocked during this tuning process).

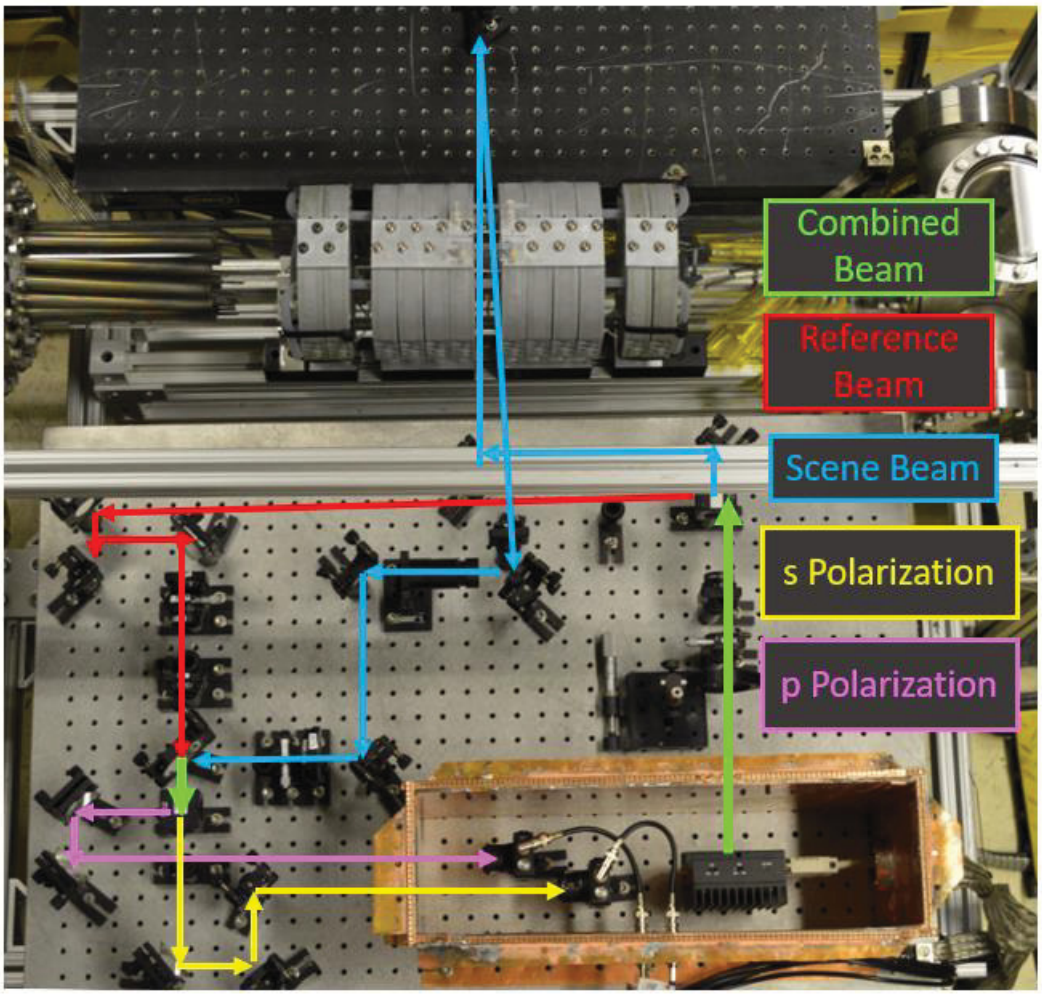

Figure 11: Top down photo of the interferometer labeling out various beam paths

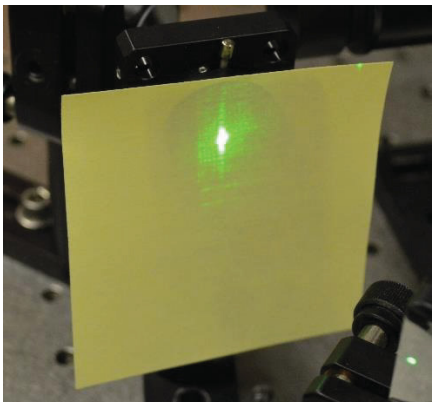

Figure 12: Image of the refraction that occurs when the beam passes through the quartz vacuum tube.

The reference beam passes through polarizer P2 to retain maximum intensity and is then rotated to 45° relative to PBS2 “after” passing through NPBS1 (the scene beam was blocked

during this tuning process). After this was tuned, quarter-wave-plate QWP1 was used to delay the reference beam's $\vec{p}$ component by 90° so that the reference beam was circularly polarized. QWP1 was tuned by temporarily placing a polarizer before the beam impinged on photodetector PD1. QWP1 was tuned until there was less than 2% variation in detected signal strength for any polarization state of the reference beam.

After the beams have recombined at NPBS1, they are then split into their $\vec{s}$ and $\vec{p}$ components where the $\vec{p}$ component is 90° out of phase with the $\vec{s}$ component due to the reference beam's circular polarization. Each photodetector is equipped with a lens which focuses the beam down onto the detector's surface and a spectral filter with a center wavelength of 532 nm with a $\pm$ 10 nm FWHM. Once tuned, a forced mechanical vibration (i.e. tapping table with a screwdriver) was introduced and a snapshot was taken with a Tektronix scope. The resulting signal which can be viewed in figure 13. Comparison with figure 5 above indicates that the signal looks as expected. Where a change in direction of the path length (i.e. phase angle for a plasma) is somewhat ambiguous in the yellow signal 1 (from PD1), it is clearly evident in the blue signal 2 (from PD2).

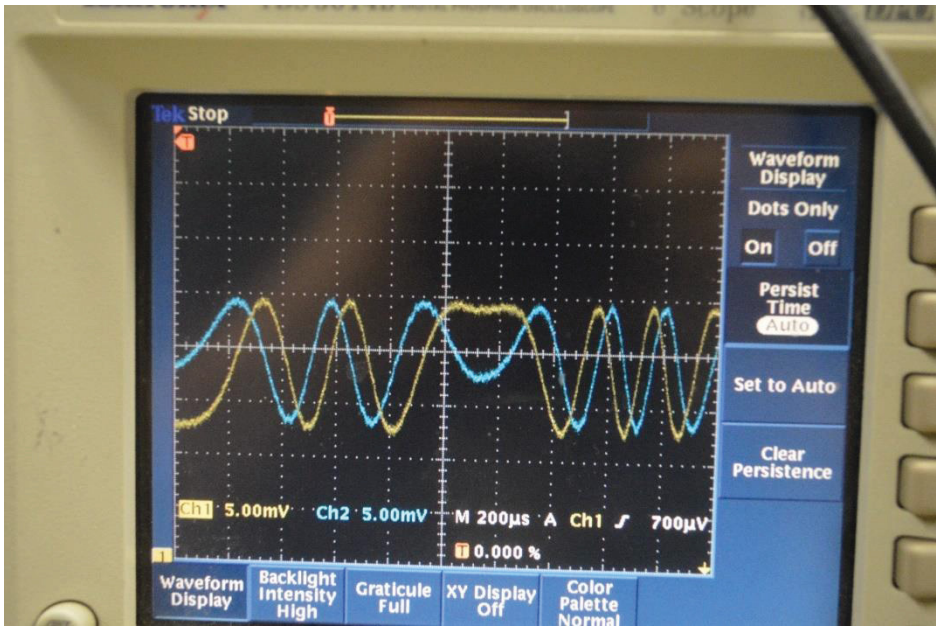

Figure 13: Photo of the DET10A signals on a Tektronix oscilloscope from the quadrature interferometer. The yellow line represents the s polarization and the blue represents the p polarization. Change in path lengths of the beams was introduced by tapping the table to yield the signal shown here.

Interferometer Testing and Modification

During initial testing of the interferometer, it was revealed that signals were dominated by electrical noise from firing the pulsed power system. Reflection issues arose when using higher termination impedances for the DET10A photo-diodes to increase signal strength. In order to overcome this additional shielding was placed around the BNC cables going from the interferometer table to the shielded oscilloscope enclosure. Additionally, two transimpendance amplifiers were installed (Femto brand, model DHPCA-100) which are able to amplify the signal strength of the DET10As and allow for an impedance matched transmission at 50 Ohms. These modifications can be viewed in figure 14 below.

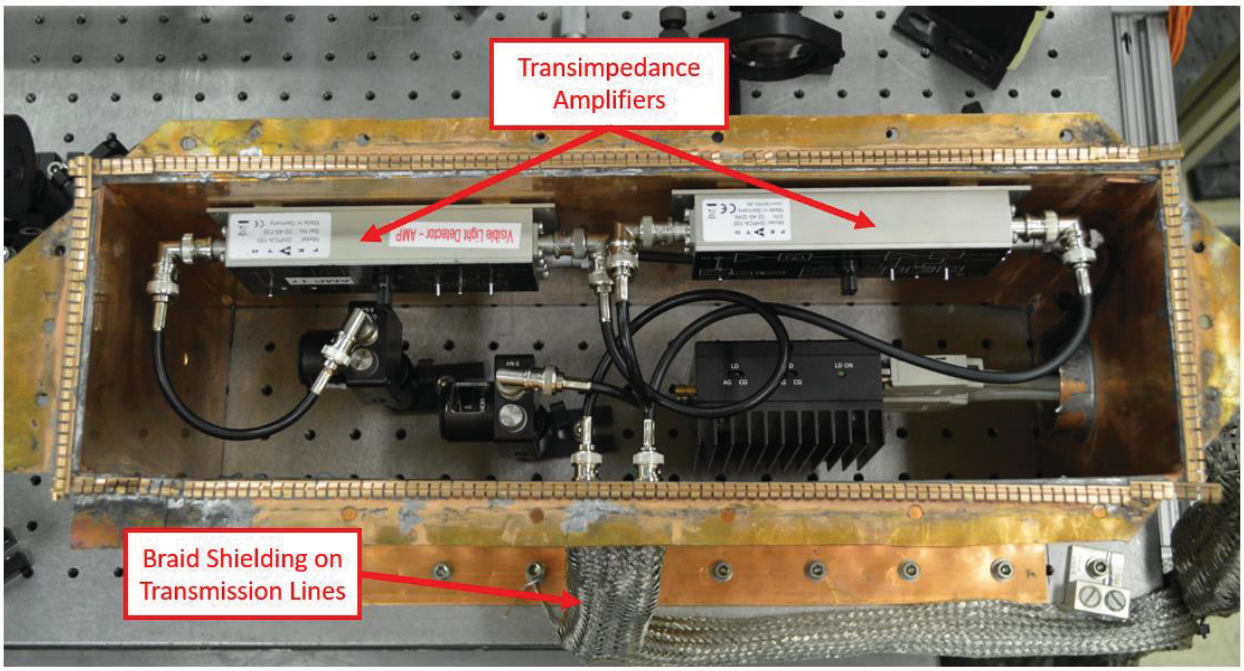

Figure 14: Modifications made to the interferometer after testing. Transimpedance amplifiers for stronger signal and shielding braid for reduce electrical noise

The transimpedance amplifiers did put out periodic high frequency noise signals so 15 MHz lowpass filters (mini-circuits brand, model BLP-15+) were installed at the oscilloscope signal input. The transimpedance amplifiers were set to grounded mode with an amplification of 10^4, DC-coupled, and using a 10 MHz bandwidth output filter (strong noise signals were seen when firing the machine using a full bandwidth setting. These settings can also be seen in figure 15 below. Finally, vibrations from the vacuum pumps were strongly coupled to the machine in frequency ranges that may be of interest (~ 1 kHz). Kneeling pads placed underneath the vacuum pumps helped to damp this vibration down to approximately 30 Hz, far below frequencies of interest.

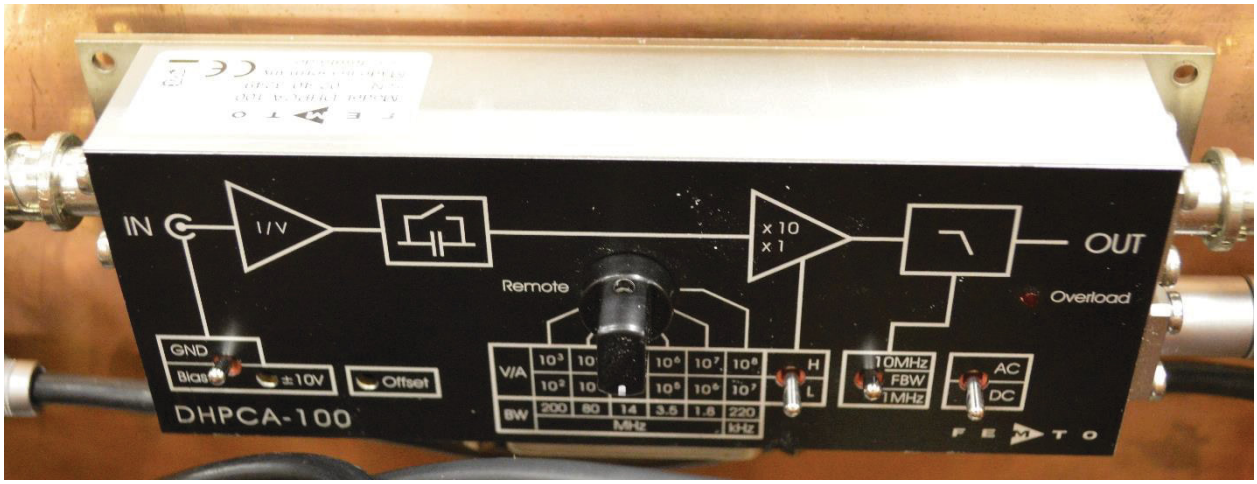

Figure 15: Settings on the transimpedance amplifier

Interferometer Post-Processing

Here we briefly summarize the necessary algorithms given in Weber's paper[4] that are necessary to determine plasma density from the measured intensities. The overall process consists of scaling the sensors' voltages to one another, followed by determining the intensity of the reference beam. With this information in hand (assuming the reference beam is of constant intensity), variation in beam intensity is assumed to be in the scene beam and this variation can be calculated using the constant reference beam intensity. Finally, since the interfering beams are 90° out of phase the sine and cosine components are each solved for using the intensity measurements and the overall phase change is determined using Euler's equation. With the phase change in hand, the determination of plasma density follows simply.

In order to perform the intensity scaling/calibration process, it is necessary to obtain the maximum and minimum voltage signals of each detector. On the present machine vibrations from the vacuum pumps transmitted to the optical table provide sufficient path length changes to see full minimum and maximum signals of the interfering beams. Once a long time scale dataset has been taken (pump vibrations occur at ~30 Hz so a few 100ms is usually sufficiently long timescale), the minimum and maximum voltage signals can be used for the following equation set to determine scaling ratios.

$$\eta_p = \frac{\eta_s\left(V_{p\,max} - V_{p\,min}\right)}{V_{s\,max} - V_{s\,\min}}$$

Where $\eta_s = 1$ (since the intention is only to scale one sensor to the other). Intensities are then calculated using

$$I = \frac{V - V_0}{\eta}$$

Where V_0 is the channel dc offset from the oscilloscope (in practice oscilloscopes usually have a small voltage offset on their channels). Using this, minimum and maximum intensities of both the s and p polarizations can be calculated. Using the s polarization, the reference beam intensity can be calculated using the following equation set,

$$I_{ref} = \frac{I_{s\,max} - I_{s\,min}}{2\sqrt{I_{ratio}}}$$

Where

$$I_{ratio} = \xi \pm \sqrt{\xi^2 - 1}$$

(see Weber's paper for more information on which sign to use) and

$$\xi = 2\left(\frac{I_{s\,max} + I_{s\,min}}{I_{s\,max} - I_{s\,min}}\right)^2 - 1$$

Finally, the variation in scene beam (again, assuming constant reference beam intensity) can be calculated as

$$I_{scn} = I_s + I_p - \sqrt{2I_{ref}\left(I_s + I_p\right) - I_{ref}^2 - \left(I_s - I_p\right)^2}$$

Using the time varying scene beam intensity, constant reference beam intensity, and the measured s and p polarization intensities, cosine and sine of the phase are calculated as

$$\kappa = \cos(\phi) = \frac{I_s - 0.5I_{ref} - 0.5I_{scn}}{\sqrt{I_{ref}I_{scn}}}$$

$$\sigma = \sin(\phi) = \frac{I_p - 0.5I_{ref} - 0.5I_{scn}}{\sqrt{I_{ref}I_{scn}}}$$

Finally, using Euler's equation, $e^{i\phi} = \cos(\phi) + isin(\phi)$, the phase can be determined as

$$\phi = Re\left[\frac{\ln(\kappa + i\sigma)}{i}\right]$$

It should be noted here that once the phase value has been obtained, the "unwrap" function in Python's Numpy library is very handy for getting total phase shift from cycled phase shift.

Error Estimation

The first source of error comes from Weber's paper, stated as

$$error \approx \sqrt{\Phi\Phi^*} - |Re\{\Phi\}|$$

However, when calculated, this yields 0 error. In his python scripts, he has used

$$error \approx Im\{\Phi\}$$

which practically yields 0 error ($O(10^{-12})$). Bit noise error alone is far more significant than this error estimation.

Tests were performed to determine the noise levels coupled from the pulsed power machine onto the photo diodes during operation. By blocking the reference beam and observing only the power of the scene beam (no interference pattern) it became clear that little electrical noise was coupled. However, a clear shift in the average laser power occurs as seen in figure 16 below (note that the periodic noise spikes are due to noise coming from the transimpedance amplifiers and this noise is generally filtered out digitally during post-processing). The cause of the shift remains unknown but since the interferometry method used accounts for shifts in scene beam intensity, the present solution has been to recalibrate the interferometer every shot (which has been automated and takes approximately 5 seconds).

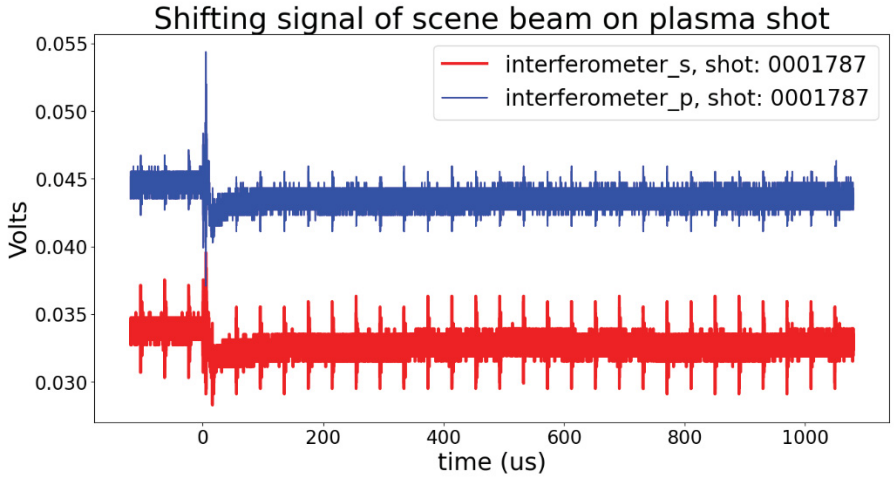

Figure 16: Raw voltage photodiode traces taken during a ringing theta plasma shot with the reference beam blocked.

It must also be noted that the intensity ratio calculation (I_{ratio}) from the equations above yields values that seem incorrect (very small scene beam intensity compared to reference beam intensity usually) but the algorithm correctly reconstructs shifts in scene beam intensity and all other values when back-calculated. Therefore, it is believed that the process still works overall and yields reasonable answers, but it is something to take note of and return to if things seem off later.

For a cylindrical plasma, Hutchinson gives an approximation of beam deflection as

$$\theta \approx \frac{n_0}{n_c}$$

Where n_0 is the peak electron density. Initial rounds of testing have shown a deuterium ringing theta plasma to have a peak electron density of $n_0 \approx 4e16$ cm^{-3}. For a green laser, $n_{crit} \approx 4e21$ cm^{-3}. Therefore, an angular deflection of at most $\theta \approx 6e-4°$. This can lead to a total movement of the final beam on the detector lenses of about 20 μm, which is presently not expected to be a significant source of error. For later experiments with helium and argon that have higher electron densities, this may become a more significant source of error.

Given that a shift of ≤ 5mV occurs every shot and factoring in bit noise (a total spread of ~ 2.5 mV), and the fact that the total signal strength measured is on the order of 100 mV, it is reasonable to claim that the interferometer's line integrated density measurement is accurate to approximately 15% or better.

References for interferometer appendix section

*Note that these references are also included in the main bibliography of this dissertation. They are presented here for ease of printing this particular appendix section.

[1]Hutchinson, I. H. "Principles of Plasma Diagnostics," Textbook, 1987

[2]Donne, A. J. H. "High spatial resolution interferometry and polarimetry in hot plasmas," Review of Scientific Instruments, Vol. 66, 1995

[3]Merritt, E. C. "Measurements of railgun generated supersonic plasma jet propagation and two jet oblique merging" Doctoral Dissertation, University of New Mexico, 2013

[4]Weber, T.E. "Ultra-high-bandwidth polarization interferometry and optimal quadratic phase detection," Review of Scientific Instruments, Vol 90, 2019.

[5]Silfvast, W. T. "Laser Fundamentals," Textbook, 1996